SEPTEMBER 2021 M.Sc. in Electrical and Electronic Engineering YOUSIF MUSTAFA SADEQ AL-KHDHAIRI

REPUBLIC OF TURKEY

GAZİANTEP UNIVERSITY

GRADUATE SCHOOL OF NATURAL & APPLIED SCIENCES

1MWh BATTERY ENERGY STORAGE SYSTEM CONNECTED TO DISTRIBUTION NETWORK: DESIGN, MODELING, AND CONTROL

M.Sc. THESIS

IN

ELECTRICAL AND ELECTRONIC ENGINEERING

BY

YOUSIF MUSTAFA SADEQ AL-KHDHAIRI

SEPTEMBER 2021

1MWH BATTERY ENERGY STORAGE SYSTEM CONNECTED TO DISTRIBUTION NETWORK: DESIGN, MODELING, AND CONTROL

M.Sc. Thesis

in

Electrical and Electronic Engineering

Gaziantep University

Supervisor

Assoc. Prof. Dr. Ahmet Mete VURAL

by

Yousif Mustafa Sadeq AL-KHDHAIRI

September 2021

1MWH BATTERY ENERGY STORAGE SYSTEM CONNECTED TO DISTRIBUTION NETWORK: DESIGN, MODELING, AND CONTROL

submitted by **Yousif Mustafa Sadeq AL-KHDHAIRI** in partial fulfillment of the requirements for the degree of Master of Science in **Electrical and Electronics Engineering, Gaziantep University** is approved by,

Prof. Dr. Mehmet İshak YÜCE
Director of the Graduate School of Natural and Applied Sciences ………….............

Prof. Dr. Ergun ERÇELEBİ
Head of the Department of Electrical and Electronics Engineering ………….............

Assoc. Prof. Dr. Ahmet Mete VURAL
Supervisor, Electrical and Electronics Engineering
Gaziantep University ………….............

Exam Date: 09 September 2021

Examining Committee Members:

Assoc. Prof. Dr. Ahmet Mete VURAL
Thesis Supervisor, Electrical and Electronics Engineering
Gaziantep University ………….............

Assoc. Prof. Dr. Mehmet Ali ÖZÇELIK
Vocational School of Technical Science
Gaziantep University ………….............

Assist. Prof. Dr. Murat Mustafa SAVRUN
Electrical and Electronics Engineering
Adana Alparslan Türkeş Science & Technology University ………….............

I hereby declare that all information in this document has been obtained and presented in accordance with academic rules and ethical conduct. I also declare that, as required by these rules and conduct, I have fully cited and referenced all material and results that are not original to this work.

Yousif Mustafa Sadeq AL-KHDHAIRI

ABSTRACT

1MWH BATTERY ENERGY STORAGE SYSTEM CONNECTED TO DISTRIBUTION NETWORK: DESIGN, MODELING, AND CONTROL

AL-KHDHAIRI, Yousif Mustafa Sadeq
M.Sc. in Electrical and Electronic Engineering
Supervisor: Assoc. Prof. Dr. Ahmet Mete VURAL
September 2021
177 pages

Battery energy storage system (BESS) is recently becoming a strong candidate for being a system component of modern smart grids. In this thesis, a two-stage 1MWh BESS connected to a 34.5 kV distribution grid is designed and simulated. The power stage of the system consists of a three-phase wye-connected 11-level cascaded H-bridge (CHB) converter and a DC-DC converter for each submodule of CHB converter. At first, a recent literature survey is given about BESS components focusing mainly on the battery storage unit in hierarchal order from cell to pack in terms of modeling, design, and wiring diagrams. Then, CHB converter topology is compared with other power electronic interfaces in terms of storage capacity and switching elements. It is shown that CHB converter topology minimizes the number of series connected batteries. The modeling details of the power circuit of the BESS as well as its control system based on decoupled current control to exchange active and reactive power between the BESS and the grid are described. Finally, a nonlinear state feedback exact linearization controller is designed to control the bidirectional buck-boost converter in each submodule to charge/discharge the batteries. It is also shown that this controller can stabilize the dc-link capacitor voltage. Simulation tests is then performed to test the capability of the designed system to exchange active/reactive power with the distribution grid while charging and discharging the battery.

Key Words: Battery Energy Storage System, Cascaded H-Bridge Converter, DC-DC Converter, Feedback Linearization Control, Vector Control.

ÖZET

DAĞITIM ŞEBEKESINE BAĞLI 1 MWH BATARYA ENERJI DEPOLAMA SISTEMI: TASARIM, MODELLEME VE DENETIM

AL-KHDHAIRI, Yousif Mustafa Sadeq
Yüksek Lisans Tezi, Elektrik ve Elektronik Mühendisliği
Danışman: Doç. Dr. Ahmet Mete VURAL
Eylül 2021
177 sayfa

Batarya enerji depolama sistemi (BEDS), son zamanlarda modern akıllı şebekelerin sistem bileşeni olmak için güçlü bir aday haline gelmektedir. Bu tezde, 34,5 kV'luk bir dağıtım şebekesine bağlı iki aşamalı 1MWh kapasiteli bir BEDS tasarlanmış ve benzetim çalışmaları yapılmıştır. Sistemin güç katı, üç fazlı yıldız bağlantılı 11 seviyeli bir kaskat H-köprü (KHK) dönüştürücü ve KHK dönüştürücüsünün her bir alt modülüne bağlı bir DC-DC dönüştürücüden oluşmaktadır. İlk olarak, modelleme, tasarım ve kablo şemaları açısından hücreden pakete hiyerarşik bir düzende esas olarak batarya depolama birimine odaklanan BEDS bileşenleri hakkında güncel bir literatür taraması sunulmuştur. Daha sonra, KHK dönüştürücü topolojisi, depolama kapasitesi ve anahtarlama elemanları açısından diğer güç elektroniği arayüzleri ile karşılaştırılmıştır. KHK dönüştürücü topolojisinin seri bağlı batarya sayısını en aza indirdiği gösterilmiştir. BEDS ile şebeke arasında aktif ve reaktif güç alışverişi yapmak için ayrılmış akım kontrolüne dayalı bir denetim sisteminin yanı sıra BEDS'nin güç devresinin modelleme detayları açıklanmıştır. Son olarak, bataryaları şarj/deşarj etmek için her bir alt modüldeki çift yönlü buck-boost dönüştürücüyü kontrol etmek amacıyla doğrusal olmayan bir durum geri beslemeli kesin doğrusallaştırma denetleyicisi tasarlanmıştır. Ayrıca bu denetleyicinin da-bağı kapasitör gerilimini stabilize edebildiği de gösterilmiştir. Daha sonra, tasarlanan sistemin aküyü şarj ederken ve deşarj ederken dağıtım şebekesi ile aktif/reaktif güç alışverişi yapma kabiliyetini test etmek için simülasyon testleri yapılır.

Anahtar Kelimeler: Batarya Enerji Depolama Sistemi, Kaskat H-Köprü Dönüştürücü, DC-DC Dönüştürücü, Geribeslemeli Doğrusallaştırılmış Denetim, Vektör Kontrolü.

''Dedicated to my family''

ACKNOWLEDGEMENTS

I would like to thank my supervisor, Assoc. Prof. Dr. Ahmet Mete VURAL for his guidance and support throughout the study. I am thankful for his encouragement and motivation.

I would like to express my love and gratitude to my family for their support, always best wishes.

TABLE OF CONTENTS

LIST OF TABLES

Page

LIST OF FIGURES

Page

LIST OF SYMBOLS

$\boldsymbol{P}$	Active power
$\boldsymbol{\alpha}$	Alfa (temperature coefficient)
$\boldsymbol{m_a}$	Amplitude modulation index
$\boldsymbol{C_b}$	Battery bank capacity
$\boldsymbol{E_b}$	Battery bank voltage
$\boldsymbol{I_b}$	Battery current
$\boldsymbol{R_i}$	Battery internal resistance
$\boldsymbol{V_T}$	Battery terminal voltage
$\boldsymbol{E_{bess}}$	BESS total energy
$\boldsymbol{\beta}$	Beta
$\boldsymbol{f_{cr}}$	Carrier wave frequency
$\boldsymbol{i_{HB}}$	CHB SM output current
$\boldsymbol{V_{dc}}$	Dc-link voltage
$\boldsymbol{dq0}$	Direct-quadrature-zero coordinates
$\boldsymbol{d}$	Duty cycle
$\boldsymbol{\eta}$	Efficiency
$\boldsymbol{e}$	Error
$\boldsymbol{L_f}$	Filter inductance
$\boldsymbol{R_f}$	Filter resistance
$\boldsymbol{m_f}$	Frequency modulation
$\boldsymbol{f_m}$	Fundamental frequency
$\boldsymbol{V_i}$	Inverter voltage
$\boldsymbol{s}$	Laplace function (Complex frequency)
$\boldsymbol{ad_f g}$	Lie bracket operator
$\boldsymbol{L_x}$	Lie derivative operator
$\boldsymbol{C_{LC}}$	Life-cycle cost

$\boldsymbol{\varphi}$	Linearized state vector
$\boldsymbol{m}$	Modulation index
$\boldsymbol{V_{LL}}$	Line-to-line voltage
$\boldsymbol{\omega_o}$	Natural vibration frequency
$\boldsymbol{\Omega}$	Ohm
$\boldsymbol{\omega}$	Omega (angular velocity)
$\boldsymbol{E_0}$	Open-circuit voltage
$\boldsymbol{V_o}$	Output voltage
$\emptyset$	Phase shift
$\boldsymbol{\pi}$	Pi
$\boldsymbol{C_p}$	Polarization capacitance
$\boldsymbol{R_p}$	Polarization resistance
$\boldsymbol{v_p}$	Polarization voltage
Q	Reactive power
$\boldsymbol{S_i}$	Switching function
$\boldsymbol{T_s}$	Switching time
$\boldsymbol{T}$	Temperature
$\boldsymbol{\theta}$	Theta (phase angle)
$\boldsymbol{i_{abc}}$	Three-phase current
$\boldsymbol{V_{abc}}$	Three-phase voltage
$\boldsymbol{\tau}$	Time-constant

LIST OF ABBREVIATIONS

BESS	Battery energy storage system
BMS	Battery management system
BPM	Battery power module
CAES	Compressed air energy storage
CC	Constant current
CC-CV	Constant current – constant voltage
CHB	Cascaded h-bridge converter
CHB-BESS	CHB based BESS based CHB
CHBDCDC	Double-stage CHB including DC-DC converter
CMC	Current mode control
CV	Constant voltage
DAB	Dual-active bridge
DHB	Dual-half bridge
DISCO	Distribution networks and companies
DOD	Depth of discharge
DP	Dual-polarization
ECM	Equivalent circuit model
EKF	Extended Kalman filter
ES	Energy source
ES-FBL	Exact state feedback linearization
ESS	Energy storage system
EV	Electric vehicle
FBL	Feedback linearization
FC	Flying capacitor
FESS	Flywheel energy storage system
GNL	General nonlinear model
HESS	Hydrogen based energy storage system
IEA	International energy agency

KCL	Kirchhoff's current law
KF	Kalman filter
KVL	Kirchhoff's voltage law
LFP	Lithium iron phosphate
Li-ion	Lithium-ion
LS-SPWM	Level shifted SPWM
MBESS	Mobile battery energy storage system
MLI	Multi-level inverter
MMC	Modular multilevel converter
MMLCFB	Modular multi-level cascade full-bridge
MMLCHB	Modular multi-level cascade half-h-bridge
MSCC	Multi-stage constant current
MV	Medium voltage
NAS	Sodium-sulfur
NPC	Neutral-point clamped
OCV	Open-circuit voltage
PCC	Point of common coupling
PCM	Parallel cell module
PCS	Power conversion system
PHS	Pumped hydro energy storage
PI	Proportional-integral
PLL	Phase locked loop
PNGV	Partnership of new generation of vehicles
PSB	Polysulfide bromide battery
PS-SPWM	Pulse shifted SPWM
PV	Photovoltaic
PV-BESS	Photovoltaic integrated with BESS
PWM	Pulse width modulation
Q	Capacity
RES	Renewable energy resource
SC	Super capacitor storage
SCM	Series cell module
SM	Sub-module

SMES	conducting magnetic field
SOC	State of charge
SOE	State of energy
SOH	State of health
SOL	State of life
SPWM	Sinusoidal pulse width modulation
T&D	Transmission and distribution
THD	Total harmonic distortion
UPS	Uninterruptible power supply
VMC	Voltage mode control
VRFB	Vanadium redox flow battery
VSC	Voltage source converter
ZBB	Zinc bromine battery
ZSI	Z-source inverter

CHAPTER I

INTRODUCTION

1.1 Motivation of the Study

The continuous growth of the electrical power demand is proportional with the economic and industrial growth which requires an equal electrical power generation and consumption in return. The imbalance between the electrical power generation and demand causes deviations and fluctuations in the grid voltage and frequency which eventually negatively affect the resilience and stability of the electrical grid. Most electrical power generation comes from fossil fuel and nuclear generation facilities that is a major source of carbon dioxide emission and considered as a global threat to the environment and a main contributor to the global warming phenomena [1][2]. As a result, the penetration of renewable energy resources (RES) such as solar energy and wind energy has acquired more attention globally to replace diesel distribution generators to reduce the CO2 eruption and generate more eco-friendly energy in both centralized and decentralized way [1]. However, the intermittent nature of the RES and its dependency on the unpredicted weather conditions might introduce several problems in the power quality, stability, and reliability of the grid. Therefore, the introduction of energy storage system (ESS) can be a practical solution for the aforementioned issues. The key principle of the ESS is to store excess electrical energy of the grid in different forms of energy and release this energy as electrical energy when it is needed. The ESS is categorized based on the form of the stored energy such as electro-mechanical, electro-magnetic, thermal storage, and electro-chemical storage systems as shown in Figure 1.1. The main benefits of the ESS integration are to save energy by storing it for later usage, improve the power quality and efficiency of the grid by decoupling the generated energy from the demand, and defer the expensive upgrades of electrical infrastructure for transmission and distribution systems [3][4].

Regarding the intermittence issue of the RES, the ESS can be considered as a convenient solution by storing the excess energy generated by the RES and release it when the RES cease generation occurs. This can fill the energy gaps and intermittence making the RES more reliable and steady energy resource. Additionally, ESS can provide different kinds of ancillary services to the power grid and applications. Energy ratings, application power, weight, volume, operating temperature, and response time are considered as key factors in deciding the application of the ESS [2][5][4].

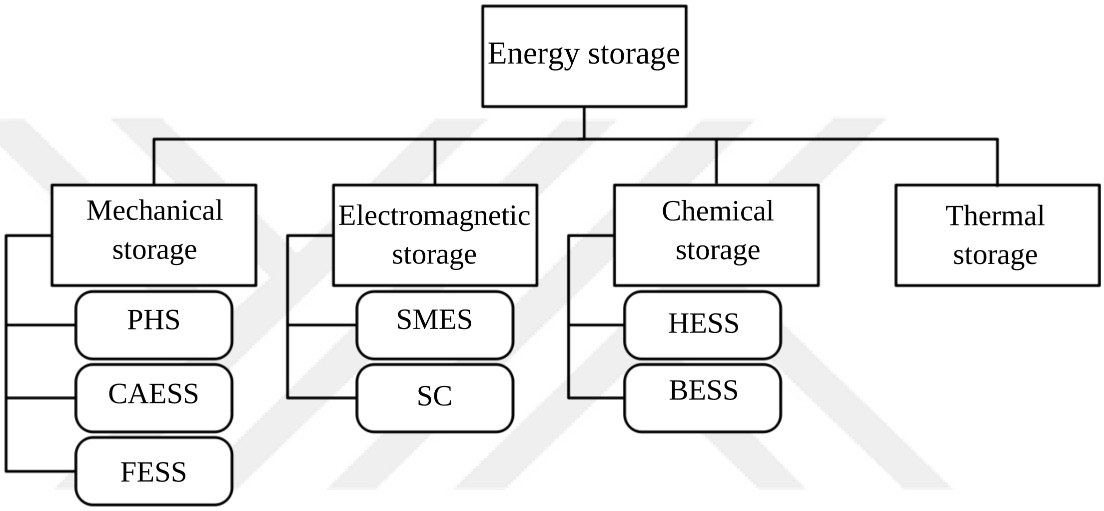

Figure 1.1 ESS category.

This chapter gives a brief introduction on ESS technologies and their working principles, also it describes the applications of ESS in different power sectors. This chapter also mentions the key parameters that could differentiate between each ESS technology and its appropriate application.

1.2 The Purpose of the Study

The main focus of this study is BESS in term of its structure and components, operating principle, design, modeling, and control. BESS generally comprises several battery modules, one or more power conversion modules (for example, AC/DC-DC/AC power converters), optionally power transformers, harmonic filters and the magnetic interface (for example, coupling reactor and power transformer) based on the AC/DC and DC/DC converter topology used. Besides these details, the charging/discharging stage controller must be relatively fast to fulfill the dynamic performance required for the battery energy storage system. Therefore, in this thesis all the aforementioned components topologies and different battery models will be reviewed in order to choose the appropriate battery model and PCS topology that will be used later in this study. Accordingly, a 1 MWh energy capacity battery energy storage system will be designed, modelled, and tested in a computer simulation environment. It will be connected to the distribution network under 34.5 kV (line-to-line) at 50-Hz medium voltage level. The thesis will include a survey of the current literature. Real and simulated large-scale battery energy storage systems that have been constructed and are still in operation will be investigated, with the type of battery technology chosen based on capacity, cost, charging and discharging qualities, and other factors.

1.3 ESS Background

1.3.1 ESS Technologies

The key principle behind the concept of ESS is the charging and discharging processes. In the chagrining process the energy is stored at a time when an excess amount of energy is available. By contrast, the discharging process is the release of the stored energy when it is needed. There are different kinds of technologies that are used to store energy and each uses different materials and operates in a different manner. Mainly ESS is classified into electrical and thermal energy type. Moreover, this study focuses only on electrical ESS. Generally electricity cannot be stored directly unless it is converted into a more stable form of energy that can be transformed back to electrical form. The ESS technologies vary based on the form of energy stored and can be categorized as follows: mechanical storage (pumped-hyrdo, flywheel), electrochemical (battery, super-capacitor), electromagnetic energy storage (super-conducting magnetic energy storage SMES). Figure 1.1 shows the each energy form and its compatible energy storage technology. The choice of the storage technology depends on the technological, economic or environmental performance characteristics of available technologies [5][6].

1.3.1.1 Mechanical ESS

Mechanical ESS stores the energy in the form of mechanical energy and converts it into the electrical energy when needed. The examples of mechanical ESS include pumped hydro storage (PHS) and flywheel which will be discussed individually in the following subsections.

1.3.1.1.1 Pumped Hydro Storage (PHS)

PHS is considered as the most mature energy storage technology and in fact it is the most used ESS especially for large scale power applications. More than 99% of the global large scale energy storage reserve is actually PHS. The PHS operates by manipulating the gravitational potential energy of water storing electrical energy from the power grid by pumping water from a lower reservoir higher to an upper reservoir (charging). The stored water at the upper reservoir can be later released downward to the lower reservoir while driving an electrical generator to generate electrical energy (discharging). The capacity of the energy stored has a proportional relationship with the height of the upper reservoir and the volume of the water contained in it [5][6]. PHS can provide reliable power in a short time lapse (less than one minute) with high efficiency up to 87%. However, since PHS can only be integrated with natural water structures such as waterfalls, rivers, and natural lakes. Hence, due to this geographical constraint, PHS cannot be installed easily anywhere and can only be installed in locations of specific geological features [5].

1.3.1.1.2 Flywheel ESS (FESS)

FESS comprises of a rotatory disk coupled with mote/generator machined through a shaft and often includes magnetic brackets that help to reduce the high speed friction and self-discharge losses [2][5][6]. Originally, the flywheel was designed to improve the power quality and solve some issues incorporated with short-voltage disturbances [5]. Also, it was utilized to improve the output voltage stability of the synchronous generators [2]. Moreover, due to the advancement in power electronics, FESS have received more attention in other applications like transportation [2]. The maximum rotational speed of the flywheel is considered as a key factor that can classify the FESS and determine its type FESS [2]. Typically, the flywheels are ranged into high speed flywheels that rotates over 10,000 rpm and low speed ones that rotate at a rate less than 10,000 rpm [5]. The energy capacity of the FESS is decided by the maximum rotational speed of the flywheel. The maximum torque produced at the shaft of the machine limits the power capacity of the FESS that produces the electric current. Hence the maximum power of the FESS is constrained by the ratings of the electrical equipments [6]. High speed flywheels are capable of discharging for longer time but with low energy capacities, the exact opposite is applicable for low speed flywheels [2][5]. When the rotating mass of the flywheel starts to accelerate using the electrical energy, the machine operates as a motor that transfers angular momentum to the rotating mass through the rotating of the shaft that stores the kinetic energy and hence charging the FESS. In contrast, when FESS starts discharging, the machine acts as a generator as the rotating mass decelerates and the stored kinetic energy drives the generator via the shaft to generate the electrical energy thereby discharging the FESS [5][6]. The high-efficiency, incredibly long life cycle, and high power and energy densities are the main features of FESS. However, FESS can be only limited to short term energy storage due to the presence of frictional forces that cause a self-discharge of around 20% of the stored capacity in an hour [5][6].

1.3.1.1.3 Compressed Air Energy Storage (CAES)

CAESS system is based on a similar concept of the gas turbine technology [6]. The CAESS consumes the excess off-peak electricity to compress air and store it in storage units located either above the ground in tanks or in underground caverns (charging). When the energy is needed, the compressed air stored in the storage caverns or tanks is released to be heated and expanded in a turbine to convert the stored energy into kinetic energy that later drives an electrical generator [6]. The CAESS is characterized for its long lifetime that reaches up to 40 years with an approximated efficiency of 70% [5]. In term of large capacity energy storage installation, CAESS is next to PHS similarly, CAESS installation is dependent on the availableness of suitable geographic locations (underground caverns) [6].

1.3.1.2 Electromagnetic Storage Systems

1.3.1.2.1 Super Conducting Magnetic Energy Storage (SMES)

SMES stores energy in the form of magnetic energy in a super conducting coil by inducing dc current through the coil to produce a strong magnetic field. Fundamentally, a SMES comprises of three main components; these are, super conducting coil with a magnet, cryogenically cooled refrigerator, and the power conditioning system [5][7]. In order to charge the SMES, first, all resistive property in the coil has to be removed by using cryogenically cooling refrigerator to cool the coil below its super conducting temperature [7]. Normally, the super conducting coil is either solenoid or toroid type. The solenoid design is simpler, cheaper, and easier to control. Whereas, the toroid design provides a low stray field that can be useful in SMES applications [5]. A dc current is necessary to generate the magnetic field that can be obtained using a power converter. During the charging process, the current increases. On the other hand, the current decreases during the discharging phase. [5]. The power density provided by SMES is considered as the greatest amongst the other energy storage technologies [2]. In addition to its long lifetime, SMES is fit for applications that require large power in short-time due to its high storage efficiency (up to 90%) and incredibly fast response (in the range of milliseconds) [2][5][7]. However, the drawback of the SMES is that it requires large power and high cost to cool the superconducting coil to its cryogenic temperature [5][7].

1.3.1.2.2 Super Capacitor ESS

Super capacitor (SC) (ultra-capacitor) is an electrochemical double-layered capacitor that stores energy electrostatically by moving ions between two electrodes through a separating porous membrane [6][8][9]. Compared to conventional capacitors, a SC outclasses the other capacitors in terms of energy density, compactness, and larger capacitance. The SC replaces the solid dielectric located between the two electrodes in the conventional capacitors with an electrolyte solution [5][8]. SCs have large cycle life that is capable of charging/discharging nearly million number of times. Thus, they are virtually maintenance free [9]. Unlike the batteries that store energy in their cells by performing chemical reactions for few hours to fully charge/discharge, SC is capable of rapid charging/discharging by handling larger rate of electrical currents [8][9]. However, with all the aforementioned features, SC suffers from daily short self-discharge of nearly 5%. As a result, SC is mainly utilized in power quality applications such as frequency regulation [5][9].

1.3.1.3 Electro-Chemical Energy Storage

1.3.1.3.1 Battery Energy Storage System (BESS)

BESS is considered as one of the oldest energy storage techniques [5]. It converts the electrical energy into potential chemical energy and stores it in an electro-chemical cell. The charging and discharging of BESS are performed based on reversible chemical reactions called “reduction” and “oxidation” reactions (Redox term in short). The Redox reactions take place between two electrodes called as cathode and anode. [1]. A BESS consists of the battery units, power conditioning system, and control system [10][11]. BESS is used widely in power system applications. Additionally, due to its mobility and flexible small size, it is commonly used in portable devices such as phones, laptops, and even electrical vehicles (EV) [5]. There are too many types of batteries that vary in size, chemistry, and capacity. each BESS type has different response time, power, and energy characteristics. The most common battery types in the literature as well as in the industry is lead-acid, Li-ion, and sodium-sulfur [1]. The BESS is the main focus of this thesis, thus BESS will be explained in more detail regarding its operation, structure, and types in Chapter 2.

1.3.1.3.2 Hydrogen Based Energy Storage System (HESS)

HESS stores the electric energy drawn during off-peak hours and produces hydrogen via water electrolysis. The produced hydrogen is then stored in high pressure cylinders. The prime components of the HESS is the water electrolysis unit that produces the hydrogen and the fuel cells [12]. Fuel cell is an electrochemical device that consumes the chemical energy stored in the hydrogen to produce electrical energy and water [2][12]. HESS is an eco-friendly technology that has high-energy density. Besides, providing electricity during times of high-demand, HESS also serves as a fuel for hydrogen vehicles [5][12]. Still, the considerable energy losses in each cycle is the huge disadvantage for HESS applications [5].

1.3.2 ESS Applications

ESS can provide different kind of services in addition of boosting the performance of various types of applications in different scales and aspects. ESS can be applied for both stationary utility-scale and transportation based applications. Generally, ESS applications are categorized into two groups based on the application’s time-scale as listed in Table 1.1 [3][4]. This section defines these applications and gives an example for each one. It is also mentioned about the deciding factors for each type of ESS application.

Table 1.1 Major ESS application categories.

Energy Applications	Power Applications
Energy arbitrage	Frequency regulation
RES time-shifting	Voltage support
Peak shaving	Black start
Transmission and distribution (T&D) network upgrade deferral	Spinning reserves
	Power quality and reliability
	RES capacity firming

1.3.2.1 Energy Applications

Energy applications are long-term applications that operate over long periods of time of several-hours and require large charge/discharge cycles. Such applications require high capacity ESS in the range of MWh. Arbitrage, renewable energy time-shifting, peak shaving and upgrade deferral of transmission and distribution networks are some examples of energy applications which will be discussed in the following sections [4].

1.3.2.1.1 Energy Arbitrage

The tariffs in the electricity market differ based on times of demand. At times of high demand, the prices surge compared to the times of low demand. Furthermore, energy arbitrage is a profitable approach to buy and store cheaper electricity at time of low demand and sell it during high-demand periods when the prices are higher. Aside from the economical profit, arbitrage can also enhance the system efficiency by influencing the consumers end to mitigate the peaks in demand via the exploit of real-time pricing [2][14]. The daily arbitrage activities and potential profit depend on the number and shape of the peaks along with the road trip efficiency of ESS [4]. Energy arbitrage requires ESS that can handle long charge/discharge cycles with considerably large capacity such as PHS and CAESS. PHS has a huge participation in energy arbitrage due to its incredibly large capacity of hundreds of MWs and its capability to function for long periods form 100 up to 1000 minutes [2].

1.3.2.1.2 RES Time-Shifting

The penetration of RES such as solar and wind energy has been growing rapidly as a more environmentally clean energy source (ES). However, the unpredicted cloud movement and the wind gusts cause intermittence and fluctuations in the generation. This situation may cause instability in the power system and imbalance between generation and demand [2]. Instead of supporting RES with traditional utility-power plants RES can be integrated with ESS to manage these issues. Time-shifting of RES is an application with similar concept to energy arbitrage. ESS stores all of the energy generated from RES plants at time of low demand, and if necessary, cheap energy can be bought from the grid. Later on, the stored energy is discharged and sold at peak demand periods. As a result, the intermittent generation of the RES is compensated and the reliance on peak utility-power plants can be avoided [6]. In order to perform RES time-shifting, ESS can be placed anywhere near the load or the source [14].

1.3.2.1.3 Peak Shaving

Peak shaving is a similar concept like energy arbitrage. Except, it operates to mitigate the peaks in the load curve instead of making economical profit [14]. Peak shaving operates in a time-lapse between 1 to 10 hours. Commonly, the application is installed near consumer’s end, while the arbitrage is placed near the source [6].

1.3.2.1.4 Transmission and Distribution (T&D) Networks Upgrade Deferral

The upgrade of T&D networks requires an incredible amount of investment and work. Usually transmission lines require upgrades when transmission congestion occurs during high-demand times that limit the electric current flow on the transmission lines. Also expensive upgrades are needed when equipment in T&D network starts wearing due to exceeding their power ratings. Some of these equipments are power transformers, transmission lines, and distribution lines. ESS can be utilized to avoid the equipment of T&D network from exceeding their power rating and delay the expensive upgrades for few more years by utilizing relatively small energy storage energy to meet the excess demand. The energy storage size used in T&D network deferral is related to the anticipated load growth and the required time to delay the upgrade investments [5][15].

1.3.2.2 Power Applications

Power applications include the applications that exchange active and reactive power between ESS and the power grid over short period of time (seconds to minutes scale). Some of these applications are frequency regulation, voltage support, black start, spinning reserves, RES capacity firming, power quality, and reliability that will be discussed in the upcoming sections [4].

1.3.2.2.1 Frequency Regulation

Frequency regulation is a short-time scale (in seconds) ancillary service provided by the ESS to stabilize the power system and maintain the nominal grid frequency at 50/60Hz. The system frequency deviates from its nominal value due to the imbalance between supply and demand. When the demand surpasses the power supplied by the system, the grid frequency falls below its nominal value this could cause black-outs. On the contrary, if the supplied power exceeds the demand, the grid frequency rises above its nominal value that could cause damage to the electrical equipments [14][16]. ESS can be applied for frequency regulation to achieve balance between generation and demand. Frequency regulation is divided into three types as follows: primary, secondary, and tertiary reserves [6][14]. The function of primary regulation is to maintain the stability and the frequency of the grid during transients within small time-lapse (5-30s). For that reason, it is usually directly incorporated with a power conversion system (PCS) to ensure fast response [17]. For secondary regulation, it acts as a standby reserve for the primary reserve with a response time of 5-15 minutes. The tertiary reserve serves as a standby reserve to maintain the system synchronized by keeping the generation and load balanced in case of any disturbance. Tertiary reserve is controlled manually with a response time of 15-60 minutes while the other reserves are controlled by automatic generation control signals [4][14]. The types of ESS with high efficiency and fast response are suitable for frequency regulation such as SMES, FESS, and BESS.

1.3.2.2.2 Voltage Support

Voltage support is important to maintain the voltage levels of the power system at its desired limits in order to preserve the voltage stability. This can be realized by proper control of the reactive power in the electrical network. Normally, it is difficult to transfer reactive power over long distances. Therefore, ESS is placed locally near large loads in order to maintain the system stability and the desired voltage levels by applying voltage support [14][15]. ESS provides voltage support to the electrical network by managing the amount of reactive power injected and drawn from the grid depending on the corresponding voltage level. This requires the ESS to incorporate proper control over power electronic devices with suitable size and rating in order to exchange reactive power efficiently. Also, the power electronic components must be capable of operating at non-unity power factor and be able to mitigate voltage ripples [4][6].

1.3.2.2.3 Black Start

In case of unexpected large disturbances in the power system, it may be necessary to completely shut down or reduce the generation. In this case, the power system should be eventually restarted through black start operation to restore the system stability. Therefore, ESS can be employed to supply the power required for black start operation to restart the power plants. For this kind of application, ESS technology should have fast response. Thus, ESS such as BESS or SC are considered suitable for black start application [5][14][15].

1.3.2.2.4 Spinning Reserves

Spinning reserve is the unused capacity of the generated energy of the source during normal operation. Moreover, the spinning reserve can be utilized as an online reserve to responds in short-time (within 10 minutes) to unexpected blackouts in generation or transmission systems by injecting power for certain time until the power shortage is compromised and the system regains its stability [14][18]. Therefore, this application requires ESS with large capacity and ability to discharge over long time periods (at least 15-60 minutes) [14][15].

1.3.2.2.5 Power Quality and Reliability

Downstream loads can be exposed to quality problems such as variations in the nominal frequency/voltage, and unwanted harmonics caused by short-term events in the power system. ESS can be used to cover these variations in the power quality. ESS can be also installed near sensitive loads to support power reliability purposes. During outages, both the load and the ESS are disconnected from the power grid and are required to operate in islanded mode until the power is restored and the islanded system is resynchronized with the main grid [14][15]. Power reliability is similar to the power quality in principle, but it takes longer time to restore power as it occurs after power quality. Thus, the ESS type used for this kind of application should support high reliability power with best quality [14].

1.3.2.2.6 RES Capacity Firming

Short-term fluctuations in the generated power from the RES could introduce variations in the system frequency and voltage, which leads to degradation in the power quality. ESS can be used to carry out the capacity firming application by injecting power simultaneously with the RES to feed the load demand. Consequently, the output power of the RES is smoothed and the power quality is improved [6][14][17].

1.3.3 ESS Characteristics

The diversity in the ESS technologies brings about different types of applications to be carried out to provide multiple services to the power system. Moreover, each type of application requires specific requirements such as specific time response, specific energy, and specific efficiency, and etc. Thus, the fundamental characteristics of the ESS has to be studied in order to create a selection criterion to implement each ESS technology for its appropriate application. In this section the main characteristics of the ESS will be discussed briefly.

1.3.3.1 Energy/Power Density

Power density of the ESS device can be defined as the ratio of the rated power output to the weight or volume of the storage device. In other words, this ratio denotes the maximum power provided by the ESS device relative to its weight (Watt/Kg) or volume (Watt/l). Likewise, the energy density is the ratio of the actual energy stored in the ESS device to its corresponding weight (Wh/Kg) or volume (Watt/l). Commonly, ESS having high power density has low energy density and vice versa. The size and weight of the ESS device is inversely proportional to the power and energy density, as the power and energy increase the size of the ESS device. ESS technologies with high power density are typically used in applications that demand high power efficiency, large discharge currents, and quick response time. PHS and flow-batteries are example of low energy density ESS. Alternatively, BESS and HESS exhibit high energy and power density particularly Li-ion batteries are commonly used in portable devices and mobile applications due its extremely high energy density.

1.3.3.2 Lifetime

Naturally, after a certain amount of time, all ESS devices degrade. The lifespan of the ESS can be defined by both calendar life (the time elapsed since its operation in term of years) and cycle life (the total number of charge/discharge cycles until the storage device cease to function [18]. The ESS lifetime is determined by the ESS technology used, operating parameters such as depth of discharge, charge/discharge cycles, and other environmental factors [16][18]. As the lifetime of the ESS is directly correlated to its cost-efficiency, it is considered a major factor in determining which application is feasible for the corresponding ESS technology. ESS technologies that have long lifespan are more recommended for applications that involve economical investments. Electro-mechanical based ESS such as PHS, CAES, and FESS often have long lifetime that are basically dependent on the life span of their corresponding mechanical parts. On the other hand, electro-chemical based storage devices such as batteries usually have short lifetime due to the chemical degradation over time [5].

1.3.3.3 Time Response

Time response is defined as the time needed for the storage device to reach full discharge from no discharge state in order to meet the power demand. Each type of application requires time-response in specific range. For instance, applications that deal with power quality issues and fluctuation damping require the time response to be in the range of milliseconds. Thus, the ESS technology adopted is bounded by the time response requirement of the application. SMES, flywheels and SC have rapid response in milliseconds, while the secondary batteries have response in seconds, while PHS and CAES have slower time response in minutes [5][18].

1.3.3.4 Round-Trip Efficiency

Efficiency is an oversimplified term that is denoted as the ratio between the discharge energy to the stored energy over single point of operation [19]. Therefore, the term round-trip efficiency or cycle-efficiency is introduced as a more general term to characterize the efficiency of the ESS. It is defined as the ratio between the output and the input energy of the ESS over a whole charge and discharge cycle [5][18]. In addition to the losses associated with the energy storage device, round-trip efficiency takes into account all the losses that result from the supplementary devices (e.g. power electronic converters) and other patristic loads throughout the operation of the ESS. Hence, it is considered as a key factor for ESS cost-effectiveness. Among the ESS with high round-trip efficiency such as SMES, BESS, FESS, SC, Li-ion batteries, have the highest reported efficiency (87-94%). Comparably CAES has the lowest efficiency (40-55%) [5][16].

1.3.3.5 Cost of ESS

The investment in ESS for commercial use is economically rewarding. Moreover, the cost of ESS is a critical factor which has to be analyzed thoroughly to determine whether or not it can be commercially deployed [5]. The cost of the ESS is divided into capital and operating costs. The capital cost involves the energy cost of storage devices ($/kWh) as well as the subsystem's power costs ($/kW) that covers the cost of the PCS and other equipments [18]. Operating costs include all the costs related to operating and maintenance of ESS. It also includes the costs of spare parts. For long-term consideration, other costs such as disposal and recycling costs might be considered [19]. Storage systems with low-efficiency and low-cycling capacity typically has the lowest capital costs, being CAES as an example. Hence, it is critical to assess the durability of the storage system. SMES, FESS, and SC have high power density with low capital cost of kWh per cycle, making them ideal for applications that demand high power outputs for short periods of time [5][19]. The cost of the ESS is a function of total annual costs, and the cost of the energy discharged annually [18].

1.3.3.6 Self-Discharge

Following the charging of the ESS, if the ESS does not discharge for long duration, the unused stored energy will start discharging which means that the energy will tend to dissipate over time. The scales of self-discharge vary based on the type of energy storage technology and its principle of operation. Electro-chemical energy storage systems such as batteries, exhibit self-discharge losses due to chemical reaction when the batteries are inactive. FESS self-discharges at large rate on daily basis at 20-100%, thus it is preferred for short-term application so that the stored energy is discharged as soon as it is get charged to minimize the losses from self-discharge. On the other hand, self-discharge is almost non-existent in PHS and CAES technologies [18][19].

1.3.3.7 Technical Maturity

Technical maturity of ESS is essential in deciding if it should be used for a specific energy storage application. Matured technologies are normally favored because they have gained more operational experience than their less matured counterparts. Furthermore, as technology matures, the price of the it decreases. The maturity of ESS can be categorized into three levels; fully, medium, and early technological maturities. Examples of fully matured storage technologies are lead-acid batteries and PHS. Whereas, technologies such as CAES, FESS, and Li-ion batteries fall between high and medium maturity levels. Early matured technologies include flow batteries. If mobile applications and portable devices is considered, Li-ion and Ni-Cd can be regarded as fully matured energy storage technologies [5][18].

1.3.3.8 Storage Capacity

This is the amount of energy that can be stored in the storage unit. To put it another way, it refers to the total amount of energy contained in the energy storage unit. It is measured in units of Wh. Since discharge is normally incomplete, it differs from the energy recovered from the storage unit. Energy storage systems with large storage capacities typically used for commercial scale operations. Because of the self-discharging issue, storage period is also regarded as an important factor to consider when selecting an energy storage technology for a specific application. Another factor that affects the recoverable stored energy is how fast the storage system charge/discharge. Incase of fast charge/discharge the efficiency drops and recovered energy becomes lower than the original stored energy as efficiency. The massive energy capacity of PHS and CAES makes them suitable for grid-scale applications. [5][19].

1.3.3.9 Recharge and Discharge Time

Recharge and discharge time is defined as the time necessary for the energy storage device to get charged and discharged, respectively. Normally ESS has equal charging and discharging rates. However, it is not always the case as charge/discharge rate varies based on PCS capacity and control as well as energy storage technology. If ESS is not charged or discharged fast enough, it is not possible to be able to supply power for the next service cycle. If it is too fast to charge and discharge, the efficiency of the ESS might decline [18][19]. The installation of ESS can be at different voltage levels and capacities based on its position with regard to the power system to overcome certain challenges in different power sectors as simplified in Figure 1.2. ESS can be installed at distribution networks to maintain the power system stability at transmission networks to relief electrical congestion at the time of high demand, and also ESS can be used in power generation to participate in energy arbitrage.

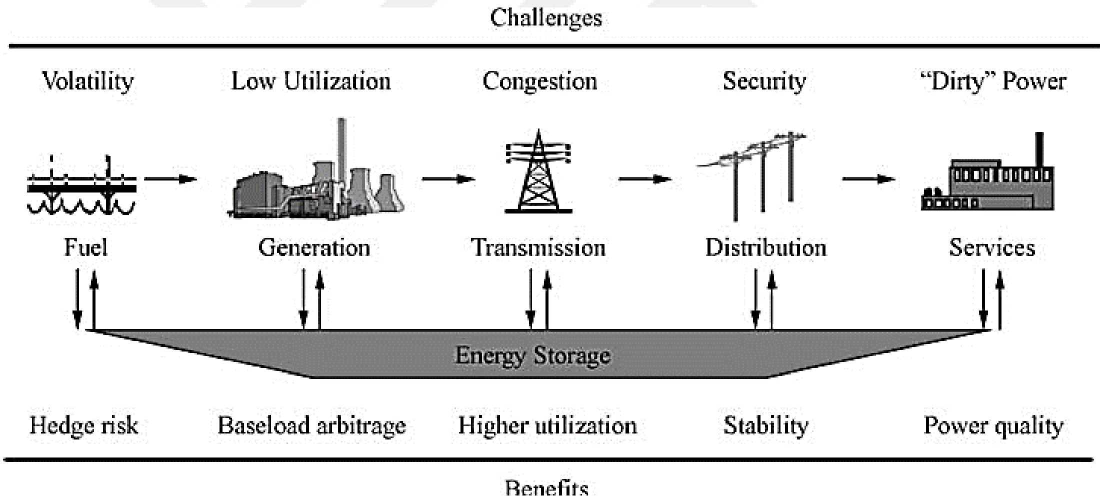

Figure 1.2 Utilization of ESS at different power sectors [20].

The power output and energy density of ESS is used to define the performance of ESS in such manner that can be derived for each energy storage technology and their befitting application which is based on the power requirement and according to the respective location in the power system. The ESS applications versus ESS technology are shown in Figure 1.3. Observably, power to gas, PHS, and CAES are used for applications that require tremendous power and capacity over time duration from hours to months which makes them more fitting for applications implemented at generation side of the power system. As mentioned before, FESS and SC have short discharge duration from fraction of seconds up to few hours making them a proper choice for providing ancillary services such as frequency regulation and voltage support at T&D networks. Whereas, BESS can be applied for a broad range of applications and installed anywhere in the power system. This flexibility comes from the flexible design as it can be small enough to deliver 1 kW or big enough to supply hundreds of GW of electrical power.

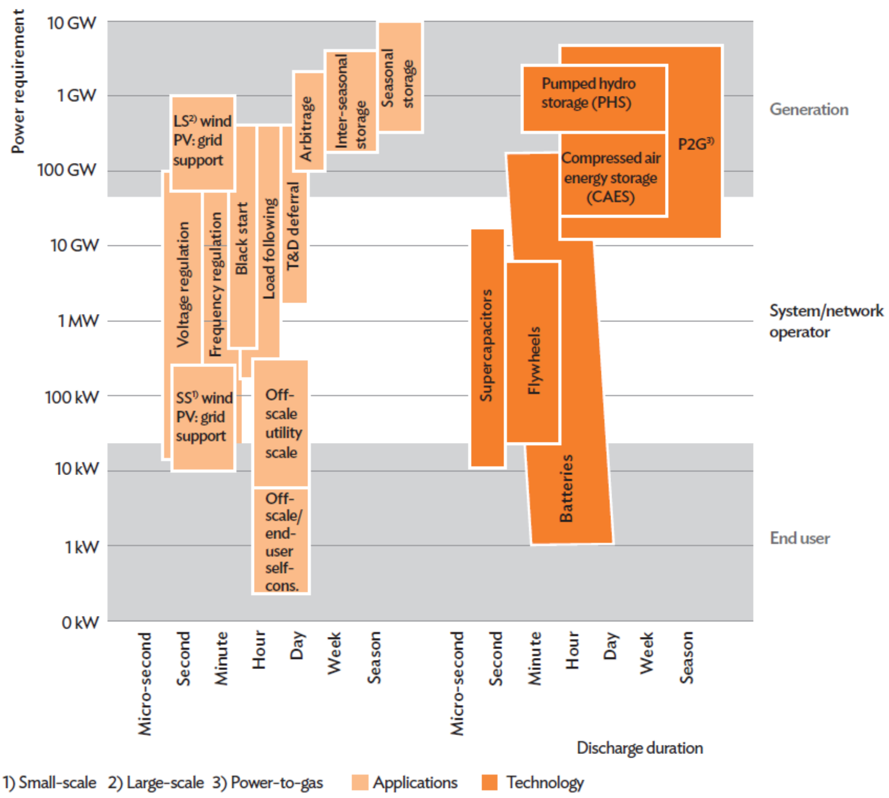

Figure 1.3 ESS applications versus ESS technology [16].

Over the last two decades, the installation and usage of BESS facilities have swiftly increased for both stationary applications (e.g. grid utility, RES integration) and mobile applications such as EV. Stationary BESS applications play a key role in utility-grid applications. Nearly half of stationary BESS installations are mainly equipped in T&D networks to perform frequency regulation owing to the fast response characteristics of BESS. While the rest of installations provide other ancillary services such as voltage support or participate in electrical market for energy arbitrage. Stationary BESS is frequently integrated with RES to minimize the fluctuations associated with the intermittent nature of the RES [21][22][23]. According to the reports of International Energy Agency (IEA), the total capacity of utility-scale BESS is installed globally nearly peaked 25 GW in 2020, as shown in Figure 1.4.

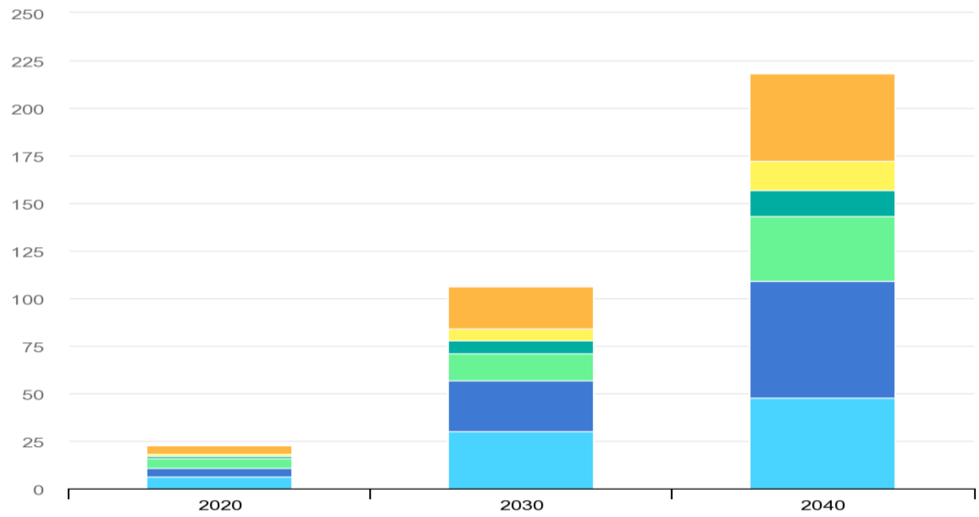

Figure 1.4 BESS capacity installation prediction over the next 20 years [24].

1.4 Thesis Description and Methodology

As the price of batteries (Li-ion in particular) is on a continuous decline, BESS installation has attracted the attention of researchers and industrial investors to setup more BESS projects in the power systems, portable devices as well as transportation applications. This study aims to review stationary BESS by giving a full review of its structure, operation, components, and control. Previous studies available in the literature were conducted on the BESS related to different fields of operations such as RES (e.g. PV and wind turbines) integrated micro/smart grids. Also, some studies focused on finding the optimum sizing and allocation of the BESS project installation. After a general review of the most essential aspects of the BESS, this thesis aims to give model, design and simulate a 1MWh BESS connected to a 34.5 kV distribution network. The general review is given in Chapter 2 that includes the modeling topologies, design assessments, and control strategies available in the literature. The Lithium iron phosphate (LifePO4) battery type is selected in this study to build the BESS. The dc-side behavior of the BESS is modelled using a non-linear model to capture the battery and dc-link dynamics well. Thus, a non-linear state feedback exact linearization (ES-FBL) controller is proposed to control the bidirectional DC-DC converter connected to each storage unit to regulate the charging and discharging of the batteries and maintain a stable dc-link voltage. By adopting a multi-level cascaded H-bridge converter, the battery banks are divided among the multiple power modules to be connected to the distribution grid. The ac side of the BESS contains a cascaded H-bridge (CHB) inverter that can be modeled as a voltage source coupled with the distribution network through a coupling transformer. The design of the BESS is highly dependent on the voltage and the capacity requirements. In order to meet these requirements the BESS has to be sized properly without over or under sizing the system to avoid impractical design. Thus, including additional hardware such as a DC-DC converter and CHB can improve the flexibility and robustness of the design in such a manner that multiple options can be acquirable. Moreover, the BESS will be more fault tolerant in case of any failure in a battery unit. Vector oriented control scheme is adopted at the ac side of the BESS to control the power flow by regulating the current components in the rotating reference frame. The simulations are carried out to demonstrate the performance of the BESS design with different case studies. Due to the large scale of the BESS model in this study and the adaptation of the CHB converter, the battery banks are modelled using single battery cell model with the required capacity and voltage specifications assigned to the individual block. In this study, the temperature effects and other aspects related to the chemical nature of the batteries are ignored. The battery dynamics involve the voltage, current, state of charge (SOC), and the dc-link voltage of each CHB power module. Implementation and control of the battery management system (BMS) are beyond the scope of this study such that SOC and other parameter estimations are excluded but only reviewed in Chapter 2.

1.5 Thesis Structure

This chapter has presented a general background on the ESS including the technology, application areas, as well as the services provided for the power system. Later on, the characteristics and parameters that distinguish each ESS technology are clarified. Accordingly, a selection criterion is reviewed for each ESS technology. The motivation as well as the purpose of the study are given in this chapter. Also, the methodology used in this study and the limitations are clarified.

Chapter 2 is related with BESS. The concept of the BESS is explained alongside its core components. At the beginning, the operating principle of a simple battery cell and its fundamental parameters are defined. The different kinds of battery technologies available in the literature are reviewed and compared. Next, the modeling topologies for the battery cells and the battery pack as well as different connection configurations are reviewed. Later on, a review on the common PCS and other components are given. Lastly, the design process of a large-scale BESS and its control scheme are outlined together with the design options and control strategies available in the literature.

In Chapter 3, the BESS is modeled and designed using a non-linear model to describe the dc side of the BESS. The ES-FBL control scheme is designed to regulate the DC-DC converter to charge/discharge the batteries. The BESS design is based on CHB converter to interface the batteries with the distribution grid. Vector oriented current control strategy is used to exchange the active and reactive power with the network.

In Chapter 4, the simulation studies are conducted with different case studies to verify the designed BESS model. Different control tasks are considered under different circumstances. At the end, the simulation results are presented and discussed.

Finally, Chapter 5 includes the conclusion of this work and future prospects related with this thesis. The findings are summarized and the contribution of the study is underlined

CHAPTER II

BATTERY ENERGY STORAGE SYSTEM (BESS)

2.1 Introduction

This chapter starts by reviewing the previous successful BESS installations in the world and the previous simulation studies related to different aspects of BESS. Later, a literature review is presented covering multiple research materials related to different aspects of BESS starting by giving a general overview of the BESS structure and components. The battery modeling is also reviewed from single cell to multi-cell battery pack perspective as well. The different types of connections topologies and power conditioning system topologies for interfacing BESS with the grid are reviewed thoroughly. Next, the design procedures and design options for implementing utility-scale BESS available in the literature and industrially are reviewed in detail. Finally, the control strategies available in the literature to control and optimize the performance of BESS for different applications are reviewed.

2.2 Previous BESS Installations and Simulations

The majority of the current BESS installations are distributed in China, India, and United States. Furthermore, the global total capacity of BESS will keep increasing at a pace of nearly 100 GW over 10 years peaking approximately 105 GW capacity in 2030 and almost reaching 225 GW total installations by 2040. An example of successful BESS implementation that has been operating for over a decade is Aomori, Rokkasho-Futamata wind farm BESS since August 2008 incorporating 245 MWh sodium-sulfur BESS which mainly operates to smoothen the output power fluctuations of the wind turbine farm and solve low-voltage ride through and reactive power compensation problems. Other examples of utility-scale BESS operating at grid side is the Henan 100.8 MW/125.8 MWh Li-ion BESS and Jiangsu Zhenjiang 101MW/202 MWh Li-ion BESS in China which participate in peak shaving and provide ancillary services to the grid such as frequency and voltage regulations and also function as emergency resource. The SDG&E Escondido Li-ion 130 MW/120 MWh BESS project in United States is one of the examples of economic profitable BESS projects that performs energy arbitrate to participate in the electrical energy market. An example of hybrid BESS projects that consists of multiple different battery technologies in the energy storage facility is Zhangei wind-PV project in China which comprises of 14 MW/63 MWh Li-ion battery, 2 MW/8 MWh redox flow battery, 2 MW/12 MWh lead-acid battery, and Lithium-titante battery 2 MW/1 MWh [17]. As BESS is getting on the trend line, a variety of studies in the literature is focusing on the modeling, control, and simulation of BESS from different perspectives and for different applications and purposes. In [93] a large-scale BESS that adopts Y-connected CHB for PCS was modeled and controlled based on a real BESS of 10 kV/2 MW constructed in Shenzhen, China. The system proved by experiment splendid performance in realizing decoupled power control for active and reactive powers, very fast step response at millisecond time scale, and full-load shutdown was achieved in microsecond timescale. Ref [127] performed a simulation study on a grid-tied 2 MW/968 kWh Li-Ion BESS that employs a VSC with vector control strategy to provide frequency regulation while meeting the standards of UK primary national distribution network operator based on real frequency data. In [123] grid-scale BESS was modeled as grid-supporting converter and controlled to provide primary- secondary frequency response and voltage support for the grid. The model effectiveness was verified through simulation studies. BESS is considered as a splendid countermeasure for the grid fluctuations in frequency, voltage, and power that is associated with the rapid penetration of RES. The 21 MW/21 MWh and 16 MW/16 MWh BESS developed by EGAT in Thailand Chai Badan and Bamnet Narong respectively are examples of grid-scale BESS that performs RES capacity firming by providing large power and energy under short periods of time in order to reduce the fluctuations caused by weather condition and stabilize the power system [25]. Another similar existing BESS projects are the Futamata-Aomori 34 MW NAS BESS that is integrated with 51 MW wind farm and the Wakkanai-Hokkaido 1.5 MW NAS BESS integrated with 5.02 MW PV farm. The main objectives of those projects are to optimize the power control and mitigate the fluctuations associated with the intermittent operation of wind turbines and PV [128]. In [129], a mathematical model for large scale grid-tied BESS which provides high accuracy in estimating the energy flow characteristics and battery SOC were developed. Also, a model was proved to be capable of simulating 20-50 faster than conventional equivalent circuit models. The study of the sizing and allocation for the BESS is considered as a critical factor to efficiently participate in the electric market of distribution networks and companies (DISCO). Ref [130] proposed a practical model for the optimum BESS allocation based on particle swarm optimization (PSO) algorithm in distribution system. The method demonstrated effective results by saving costs for DISCO by finding an appropriate plan for buying energy. Different benefits can be obtained based on BESS location corresponding to the distribution line. For example, the placement of BESS at the end of the distribution line provides better end voltage regulation, while allocating the BESS in the middle of the line helps to reduce the losses associated with the power transmission from distribution generators or PV panels along the distribution line [131]. From economical perspective, BESS installation in T&D systems can save the high investment costs related to the network upgrades required when congestion occurs. The network upgrade cost analysis in [3] for the Pattaya Tai Thailand 115/22 kV distribution network proved that BESS installation is more cost saving and feasible than the conventional network reinforcement method. Moreover, BESS installation is not only limited to differing investments, it is also capable of reducing the line losses and improving load curve by injecting power to the grid at peak demand times in the evening [131]. Mobile battery energy storage system (MBESS) is a practical technology that allows the BESS to be transported to areas with high power demand or utilized for emergency cases to compromise for blackouts and faults in micro grids. MBESS can be used for seasonal demands in such a way that it moves to areas with high demand or requirement to perform different kinds of applications such as network reinforcement or peak-shaving. When it has fulfilled its purpose, it can be easily assigned and moved to other demand area [132][133]. Ref [134] used three different modeling methods namely average, ideal-dc link, and detailed models to model and simulate 1 MWh two-stage BESS connected to a micro grid in both grid-forming mode and grid-supporting mode. Reference [135] presented a control strategy for charging and discharging batteries in distribution system in order to optimize the energy transaction cost by performing a forecasting the wind and PV powers, and the short-term load profile. The control strategy for managing the BESS plays a vital role in providing the most benefits of the BESS and delivery the maximum operating efficiency in distribution systems. Reference [136] simulated low-voltage distribution network using coordinated control scheme for controlling multiple BESS to reduce the overvoltage associated with PV generation. The method proved efficient in improving the BESS reliability and robustness. In [137], an optimization algorithm based on linear programming was adopted to manage the operation of 500 kW/1440 kWh Lead-acid BESS connected to 2 MW islanded micro grid comprised of PV and diesel units power generators. With the proposed algorithm, the BESS improved the utilization of PV power and reduced the fuel consumption in diesel generators without forecasting. Ref [138] simulated the addition of 100 kWh capacity BESS in a low-voltage distribution network located to provide power to end-user (elementary school) in Kinmen Island Taiwan. This installation shows that implementation of BESS and RES can save costs for end-users and solve the voltage reliability issues in islanded micro grid. Ref [139] performed a simulation study on low-voltage active distribution network in Denmark using BESS controlled by optimization control based on single step model predictive control to improve the PV peak shaving and reduce the network power losses. Ref [140] modeled and simulated a 0.5 MWh BESS to provide voltage and support and peak shaving for 10 kV distribution system using distinctive active and reactive power support algorithms. In [141], a two-stage BESS connected to PV micro grid was modeled and controlled using PQ control strategy to control the active/reactive power flow between the BESS and grid, while voltage/frequency control was adopted to maintain the stability of the micro grid. Due to the asymmetrical nature of distribution systems, unbalance voltage is more common to transpire causing severe damage to the system components. [142] proposed a two-stage scheduling strategy based nonlinear programming for BESS to reduce the voltage unbalance in the network.

2.3 BESS Structure and Components

BESS consists of several components such as the battery banks which are the main energy storage units that use reversible electrochemical reactions to store excess energy in the form of chemical energy when the battery is charging and discharge it as electrical energy when there is a demand for energy at the load or grid. These battery packs are formulated from several battery cells connected either in series or parallel. Subsequently the battery banks are connected to a PCS that provides a four-quadrant power conversion between both ac and dc systems. PCS may include a dc/dc converter to regulate charging and discharging operations of the battery and able to step up the battery voltage to provide higher voltage levels at the dc-link capacitor. dc/ac bidirectional converters convert the dc current to ac current or vice versa that serve to exchange the energy between the battery packs and the electrical grid or load depending on the charging and discharging state. At the ac side of the BESS, choke filters are utilized to filter the harmonics associated with high frequency switching of the power electronic converters. Also, a coupling transformer can be added to synchronize the voltage levels of BESS and grid. Furthermore, a control system or an energy management system to coordinate the operations of charging/discharging processes, besides a BMS is also employed in each battery module to control the battery cells and protect them from thermal and voltage instabilities such as over-voltage or under voltage problems. As well as the control and estimation of the SOC of the batteries are required to provide a longer lifetime. Figure 2.1 shows a general overview of a grid-tied BESS structure. Many other structures and connection topologies of BESS are available depending on the utilization type and objective [25].

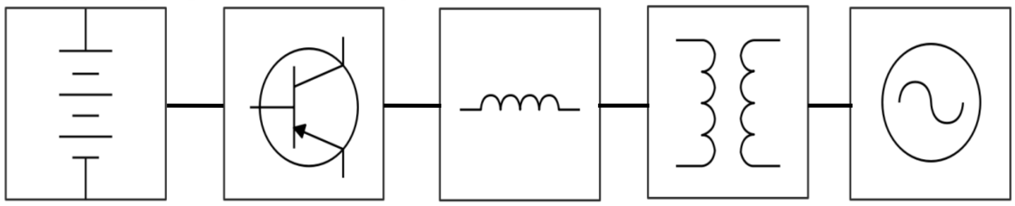

Figure 2.1 A general overview of a grid-tied BESS.

2.3.1 Battery

BESS is composed of several battery cells connected either in series or parallel, however the most traditional batteries are connected as series strings to accumulate the voltage to a specific level. On the other hand, further several series strings of battery cells are connected in parallel to increase the current capacity [26][27]. Batteries use electrochemical reactions known as Redox reactions (which is a short term for reduction and oxidation reactions) to convert electrical energy and store it in the form of potential chemical energy in battery cells [6]. Figure 2.2 shows a schematic of the electrochemical cell in both charging and discharging operations

[28]. Observably, once battery discharges, oxidation occurs at the anode and an electron is released and transferred through the electrolyte and accepted by the cathode through reduction. This electron transition leads to the generation of electrical current. Moreover, during charging operation, the same principle is applicable with reversed reactions while the battery is supplied by an external source [28].

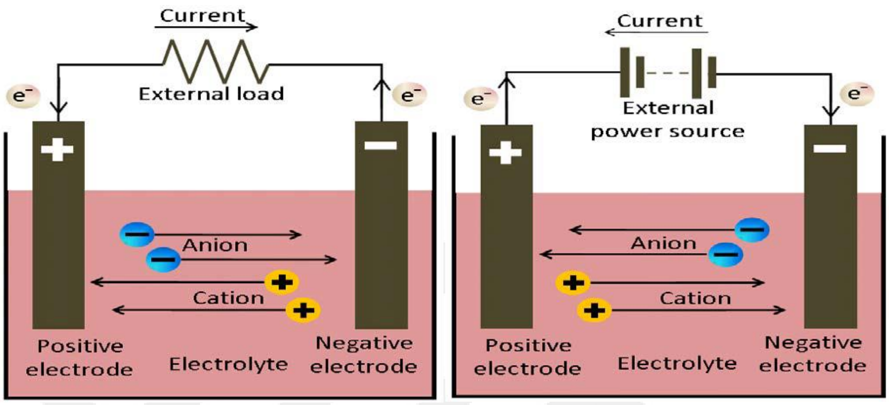

(a) Discharging (b) Charging

Figure 2.2 The electrochemical cell structure and reactions during: (a) discharging, (b) charging [28].

Basically, a battery cell consists of two circuits; an internal circuit that allows the movement of the resultant ions, and an external circuit (load or ES) which closes the electrical circuit and allows for the current flow. However, an energy difference between the electrochemically active substances is essential for the flow of electrons and ions to exist. The battery cell discharges when an external circuit (load) is connected between the electrodes. The redox reactions occur simultaneously at the anode and the cathode yields an electrical current such that the electrons flow from the anode to cathode. This operation reverses for charging where the external circuit added is an ES [6].

2.3.1.1 Battery Characteristics

The battery can be characterized by its capacity (Q) which is given in Equation (2.1) where I_b is the battery current and open-circuit voltage (OCV). Q is the highest possible energy quantity which is measured in coulombs. Q is a function of the battery volume, mass, and the material type being used. On the other hand, OCV it is the potential difference between the battery electrodes when the battery is neither charging nor discharging. However, during charging and discharging, the measured voltage can be above or below the OCV due to polarization effect which is caused by chemical reactions and the internal components. Thus, the battery terminal voltage is a more precise characteristic parameter that accounts for the polarization effects.

$$Q = \int I_b \, dt \tag{2.1}$$

There are other battery parameters that should be monitored and estimated throughout the operation of the BESS. These parameters are used to characterize the battery performance and how the BESS operates by setting a stopping/starting criterion for the charging/discharging processes. These parameters are SOC, given in Equation (2.2), depth of discharge (DOD), state of health (SOH), and round-trip efficiency. SOC is a significant reference parameter in a BESS which indicates the available remaining electric charge capacity of the battery cell compared to its rated nominal capacity (Q_{max}). The SOC is measured in percentage units of amber-hour (Ah) of the battery's energy drawn until it is fully discharged. Moreover, the exact value of SOC or the chemical energy cannot be calculated or monitored directly by using sensors due to battery's chemical nature. Therefore, SOC is estimated by implementing a BMS that uses different SOC estimation algorithms and approaches to give an accurate estimation of the current SOC value. Having information on SOC protects the battery from overvoltage and under voltage, also SOC information provides better capacity utilization to have better management over the battery energy. There are multiple ways for estimating the SOC value which differ in accuracy and complexity. Columb-counting and OCV estimation methods are considered as the most basic commonly used SOC estimation approaches [27][25][29][30]. Columb-counting method is a straightforward estimation approach in which SOC is calculated as a function of initial SOC value $SOC_{(k_0)}$ given in Equation (2.3), where $I(t)$ is the charging/discharging current, n is the charging/discharging efficiency, and Q_n is the battery nominal capacity.

$$SOC = 100 * \left(1 - \frac{Q}{Q_{max}}\right) \tag{2. 2}$$

$$SOC_{(k)} = SOC_{(k_0)} + \int_{k_0}^{k} \frac{nI(t)dt}{Q_n} \tag{2.3}$$

Since this method highly relays on the current measurements, any error in current measurement will have great impact on the SOC estimation accuracy. Also, obtaining prior information on the initial SOC value is difficult as battery SOC is usually charged between certain ranges depending on the type of the battery used [31]. The OCV of the battery share a non-linear relationship with battery SOC such that SOC value could be estimated with high accuracy based on the measured battery OCV following battery resting. Other popular estimation methods are Kalman filter (KF) based estimation, extended KF (EKF), and adapted KF. Originally, KF filters out statistical noise and other forms of inaccuracies from measured data to provide an optimal estimation of the unknown variables in a dynamic system in term of minimum variance. KFs are more befitting for linear system. However, Li-ion battery exhibits a non-linear behavior adding more challenge in estimation due to polarization parameters related to the equivalent circuit models which vary over time under different operating conditions. Hence, EKF or unscented Kalman filter is considered as a solution to improve SOC accuracy in nonlinear systems [32][33][34][35]. More accurate SOC estimation can be acquired using adaptive methods which employ different neural network algorithms but the estimation complexity is considerably increased [36][37][38]39]. Effects like temperature and capacity have considerable impact on the SOC of the battery. During the modeling and simulation of the BESS the following factors should be considered;

1- **Charging and discharging rate:** The capacity and SOC vary among the cells when the battery is charged or discharged at different rate. Peukert Equation given in Equation (2.4) demonstrates a relation between the battery capacity and the charging/discharging current. C is the capacity, i is the charging current, n and K are the battery constants, respectively [30].

$$C = Ki^{1-n} \tag{2.4}$$

2- **Temperature:** The temperature affects the SOC. For example, uneven temperature among the battery packs can influence the cell aging and may cause capacity fade. The influence of the temperature on the SOC can be described by a common model, given in Equation (2.5),

$$Q = C_{25}\,[\,1 - \alpha(25 - T)] \tag{2.5}$$

where, $Q$is the battery capacity under temperature T, Q_{25} is the battery capacity when the battery operates under a temperature of 25°C, α is the temperature coefficient that varies in different temperature intervals, and T is the actual temperature [30][40].

3- **Capacity fade:** The capacity will continuously fade throughout the aging of the battery and eventually negatively affect the SOC [30].

4- **Self-discharging:** Self-discharging occurs due to the chemical reaction within the battery without being connected to any external circuit. This phenomenon differs according to the battery type and technology and some batteries do not exhibit this effect such as Zn-Br or flow batteries. Relevant data regarding this phenomenon is commonly provided by the battery manufacturer [30].

5- **Internal resistance:** The internal resistance continually increases throughout the aging of the battery resulting in a slight decrease in discharge voltage and battery capacity. Moreover, in the equivalent circuit model, the internal resistance manifests a strong influence on the SOC, or rather becomes a function of SOC [30][41].

6- **Cell-to-cell variation:** This is another major factor which could have a significant impact on SOC estimation and on the capacity of BESS. In [41], the effect of cell-to cell variation along with the deterioration and inconsistency is tested and discussed in detail implying how the deterioration of a single cell could limit the capacity and functionality of the whole battery back.

7- **State of energy (SOE):** SOE is a similar to SOC. The SOE indicates the ratio of the remaining energy of the battery. However, SOE is a more general term which can be used for any storage device [29].

8- **Depth of discharge (DOD):** DOD is the ratio of the battery capacity that has been discharged in relative to the maximum capacity of the battery which is expressed in Equation (2.6);

$$\mathrm{DOD} = \frac{\int_0^t i_b(t)\cdot dt}{Q_{max}} \tag{2.6}$$

Looking at Equations (2.1), (2.2), and (2.6), one can conclude that DOD is a complement of SOC and can be written as follows;

$$SoC = 1 - DOD \tag{2.7}$$

Both SOC and DOD are expressed as percentage of the battery maximum capacity. For example, if SOC is 20%, this value indicates that the current energy capacity available is 20% of the maximum battery capacity. Oppositely, a 20% DOD means that 20% of the maximum capacity is being discharged while 80% remains. The deeper the DOD the faster the battery life-time decays. Similarly, if the SOC exceeds 100% when charged or fall below 0% when discharged, it could cause degradation in the battery cells that could shorten the life span of the battery. This situation is called as "over-charging" and "over-discharging". In case of Li-ion battery, the SOC is preferred to be in range of 20%-80%. Therefore, the appropriate monitoring and control of SOC and DOD are essential for safe and efficient operation of the BESS [25].

9- **State of Health (SOH):** SOH is the ratio of the current maximum capacity of the battery to its initial maximum capacity. SOH is used to express the deterioration rate of the battery. However, SOH is commonly described by an attenuation index of the battery due to the difficulty to estimate the number of the remaining cycle of the battery in an accurate manner. A common way to estimate SOH is the capacity fading rate formula which can be expressed as:

$$\text{SOH} = \frac{Q - Q_{EOL}}{Q_{BOL} - Q_{EOL}} \tag{2.8}$$

where Q_{BOL} is the begin of life capacity or initial maximum capacity of the battery, and Q_{EOL} is defined as the end-of-life capacity. In addition, end of life refers to the time when the battery capacity is reduced to 80% of its original capacity [25][41].

10- **Energy efficiency:** The operation of the BESS is not ideal, consequently there are losses accompanied with the charging and discharging processes. Apart from the losses from the PCS, there are losses in the battery cell due to the chemical reaction in the battery cells which vary with the type of the battery technology used, and the self-discharge nature of the battery cell [23]. The energy efficiency is proportional to the net energy change of the battery, energy acquired during charging, and energy drained from the battery during discharging. The charging and discharging efficiencies can be described as follows:

$$\eta_{charge} = \frac{\Delta Q_n}{Q_{in}} \tag{2.9}$$

$$\eta_{discharge} = \frac{Q_{out}}{\Delta Q_n} \quad (2.10)$$

where ΔQ_n is the net energy change of the battery, Q_{in} and Q_{out} stand for the energy acquired by the battery and the energy drained from the battery, respectively [42]. The energy efficiency of the battery cell can also be studied as a function of the cell voltage and the thermodynamic voltage which is the maximum voltage attained from the chemical reaction in the battery cell. Because of the effect of the internal resistance of the cell, the cell voltages are higher than that of the thermodynamic voltage during discharging but lower when charged. Additionally, the voltage cell is dependent on the SOC and it is possible to derive a relation between the energy efficiency and the SOC in a linear manner such that the discharging efficiency increases with the SOC. On the contrary, the charging efficiency decreases with SOC [6]. The charging/discharging current also has an influence on the efficiency, since the energy consumed in the internal resistance increases proportionally with the charging and discharging current [42]. Therefore, an optimum average SOC should be considered to optimize the overall efficiency of a cycle [6].

11- **Round-trip efficiency:** This parameter is deemed to be a major factor in determining the cost-effectiveness of the energy storage system that is defined as the ratio of the energy regained from discharging to the spent energy when the battery is charged calculated through an entire charging/discharging cycle. The round-trip efficiency takes into account the losses from power conversion and other losses that accompany the operation of the energy storage device [16][29]. CAES has the lowest round-trip efficiency of around 40%-55%. Li-ion batteries hold the highest round-trip efficiency up to 95% [16][43].

2.3.1.2 Battery Types

There are many different battery technologies that use different chemical substances in their electrodes and electrolytes. These technologies can be characterized based on several factors such energy density, round-trip efficiency, cycle life, effective cost, and self-discharge. Batteries in general are characterized into primary cells and secondary cells, primary cells are batteries that can be only used once with no rechargeable capability. while secondary batteries have cells capable of reversible reaction that allow it to be recharged continuously. The most common secondary battery types available in the literature as well as in the industry are Lead-acid, Li-ion, NAS, Ni-Cd, and the flow batteries. These battery types are discussed and compared in the next section.

2.3.1.2.1 Lead-acid (Pb-acid) Battery

Lead-acid battery is considered as one of the first rechargeable battery type introduced for commercial use in the mid of the 18th century. Lead-acid battery technology is deemed to be one of the most mature battery technologies, commonly used in EVs and other applications requiring high-discharge currents, Lead-acid batteries are well known for their low-cost compared to other battery types which are highly dependent on lead price, capability of deep current discharge, efficient recycling, and good performance at low and high temperatures [6][16][44]. Lead-acid battery cell is made of parallel arrangement of lead plates that is alternatively polarized such that the cathode plates are coated with lead dioxide (PbO_2) and the anodic plates with porous lead are immersed in a sulfuric acid electrolyte [6]. Lead sulfate is produced with an excess electron from a chemical reaction between the porous lead at the anode (negative electrode) and the sulfuric acid during discharging. This electron is then transmitted to the cathode (positive electrode) and reacts with the lead dioxide resulting in a potential of 2.04 V between the two electrodes and water [6]. Lead-acid has a non-linear power output and the life time of lead-acid batteries change significantly upon usage ratio, discharge rate, number of deep discharge cycles, ambient temperature, and the frequency at the charging and discharging state [44][45]. Lead-acid batteries have low energy and power density, slow charging, and periodic maintenance. Another drawback of this battery type is that it suffers from low life-cycle, around 200-1800 cycles based on DOD and operating temperature. Hence it is more commonly used in power quality management and backup power applications [6][16][44][45]. There are several types of Lead-acid batteries. Flooded battery is the most common topology among other traditional Lead-acid batteries. Flooded batteries may suffer from water loss in case of overcharging and might require frequent water maintenance. Therefore, the utilization of valve-regulated Lead-acid batteries in utility scale system might be a better consideration regarding this issue, since they ensure no electrolyte or gas leakage. However, they fall behind in terms of life and reliability [6][16][44][46].

2.3.1.2.2 Nickel-Cadmium (Ni-Cd) Battery

Nickel-cadmium battery consists of electrodes of nickel oxide hydroxide at the cathode and metallic cadmium at the anode immersed in an electrolyte of potassium hydroxide solution. The chemical reactions in this kind of battery produce an electrical potential of around 1.2 V which is less than the 2.04 V electrical potential of Lead-acid batteries [6]. There are two forms of Nickel-cadmium batteries: sealed form which is used in portable applications such as drills, razor, portable computers, and other electronic devices and the flooded form which is utilized in industrial applications [6][16][46]. Nickel-cadmium is also applied for hydro-EVs and tested for aviation battery technology [47]. Nickel-cadmium batteries exhibit great characteristics regarding the durability. Also, they are better resistant to harmful effects like, over-charging and over-discharging that cause sulfation and life reduction observed in Lead-acid batteries. The low maintenance for Nickel-cadmium batteries can make them operate for up to 15 years without the need for any water addition. Nickel-cadmium deems to be a great choice in PV applications due to its remarkable reliability and its long-life of 20-25 years performance. Nickel-cadmium is also known for its high-ramp rates, cyclability (3500 and max cycles of 50000 at 10% DOD), environmentally safe (75-100% recyclable), and has the lowest cost per cycle [6][16][46][48]. However, the disadvantages of Nickel-cadmium hinder it for becoming commercially feasible. First reason is the requirement of high number of cells to obtain high voltage due to its low cell voltage of 1.20 V. Second one is the high cost of Nickel-cadmium batteries compared to Lead-acid (ten times of Lead-acid price). Third, the toxicity of cadmium and nickel expose human to danger and health risks. Last one is the memory effect which is considered as the capacity drop caused by repeatedly recharging before reaching fully discharged state. This problem causes Nickel-cadmium batteries to exhibit sudden voltage drop. This effect is only limited to the in-sealed (portable sintered plate) type Nickel-cadmium batteries [6][16][46].

2.3.1.2.3 Sodium-sulfur (NAS) Battery

A NAS is a promising energy storage technology which was first introduced in 1966 by Ford Company for vehicle applications. NAS is a molten metal battery composed of sodium (anode) and sulfur(cathode). In contrary to other batteries, the electrodes in NAS are liquid separated by a solid electrolyte of beta-alumina ceramics. The electrical potential between the two electrodes attained from the electrochemical reactions is around 2.075 V at 350℃. NAS offers high energy density (151 kWh/m3, as three times that of Lead-acid), long cycle life, and no self-discharge. Thus, a 100% columbic efficiency is achievable. Its high dc conversion efficiency of around 85% is a promising subject of interest for further research on dc distribution systems [6][16][44][49]. NAS batteries operate under high temperature such as 300℃-350℃ limiting them for stationary grid-scale energy storage systems and high-power storage applications. The combustible nature of the sodium which behave explosively, the corrosion due to sulfur, and the extra costs for building an enclosing structure for leakage prevention could be the drawbacks for this type of batteries technology [6][16][44][49][50].

2.3.1.2.4 Redox Flow Battery

Redox flow battery is a new promising energy storage technology adapting a different operating technique than other conventional batteries. It stores the positive and negative electrolytes in two separated tanks. These electrolytes are pumped through an ion-selective membrane. Meanwhile oxidation and reduction take place in the anode and cathode respectively during charging process resulting in flow of electrons. This process is reversed in case of discharging. The sizing and calculation of the electrochemical cell and the external storage tank determines both the power rating and capacity rating, respectively. Vanadium redox flow battery (VRFB), Zinc–bromine battery (ZBB), and Polysulfide bromide battery (PSB) are the major types of VRFB technology [6][16][51]. VRFB is a type of redox flow batteries that store and provide chemical energy through the use of distinct oxidation states of vanadium ions in the electrolyte solution. The electrodes of the cell at the anode and cathode are both made of catalyzed graphite. A polymer membrane separates the anodic and cathodic regions which both has an aqueous electrolyte based on sulfuric acid solution. The cell potential of VRFB is reach up to 1.6 V. VRFB can reach a splendid number of life-cycles up to 20000 cycles which is still limited to the lifetime of ion exchange membrane that is easily replaceable. VRFB can reach a splendid number charge and discharge cycles up to 13000 cycles at 100% depth of charge with an efficiency of 78% [6][51][52].

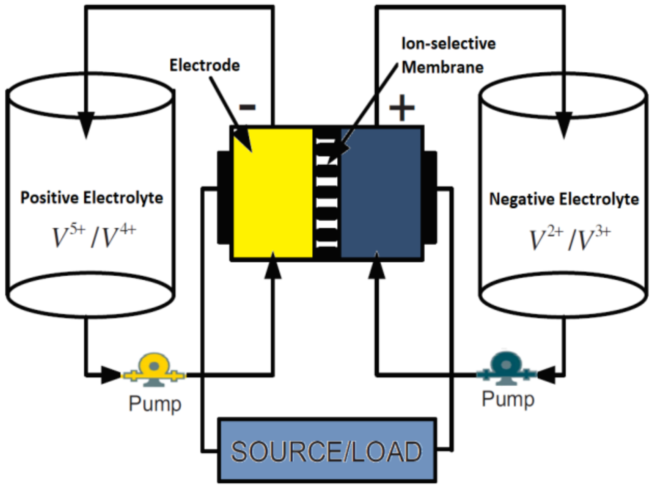

Figure 2.3 VRFB block diagram [51].

ZBB is another redox flow battery technology that operates in the same manner as VRFB. But as for the ZBB, the anode and cathode are composed of solutions of Zinc and complex bromine respectively which is separated by a polyolefin sheet that prevents the battery from self-discharge caused by the direct reaction of Zinc and Bromide. The electrolyte is an aqueous solution of dissolved Zinc-bromide in different oxidation states. During charging, the oxidization of Zinc leads to the conversion of Bromide into Bromine, yielding a cell voltage of around 1.7 V. The rated life time of ZBB is about 2500 cycles [6][44]. PSB is considered as the least mature redox flow battery technology among the rest of others. Similar to the Zinc-bromine, a polyolefin sheet separates the anode and cathode regions which are composed of aqueous electrolytes of Sodium sulfide and Sodium tribromide, respectively. The Sodium sulfur at the anode is oxidized during discharging, losing electrons in which support the reduction at the cathode. The electrical potential between the electrodes reaches up to 1.5 V [6][16]. The common characteristics of the aforementioned redox flow battery technology is the low cost of production, environment friendly for its high-recyclability, low self-discharge, capability of charge and discharge over long intervals, fully discharging property at 100% DOD without any issues. The flaws of this technology is the low energy density, complexity, and immaturity of the technology which limits it to stationary applications [6][16][51].

2.3.1.2.5 Lithium-ion Battery

Lithium-ion battery is one of the most developed and common battery energy storage technology which is traditionally used in consumer mobile electronic devices such as laptops, smartphone, and cameras etc. Recently it has been highly preferred in the field of modern EV and grid-connected applications. The working principle of Li-ion battery is defined by the motion of Lithium ions between the positive and negative electrodes which produces a flow of electrical current. A cell potential of 3.7 V can be reached. This potential is the he highest cell voltage among other batteries technologies. Li-ion batteries offer significantly high round trip efficiency, long cycles, high energy density (170-300 Wh/l), and high specific energy (75-125 Wh/kg). Moreover, its light weight is a considerable factor for its popularity in mobile applications. The fast charging and discharging capability along with the significant reliability make Li-ion batteries a preferred candidate in frequency regulation and power quality applications. However due to the scarceness of Lithium, Li-ion battery costs are roughly higher than the rest of the traditional battery technologies. Other drawbacks are high sensitivity to over-charging and over-discharging which could slightly decrease the life-time and the rated capacity of the battery. Moreover, Li-ion battery requires additional circuits for protection to prevent thermal-runaway [6][16][44][51][52]. Lithium cobalt oxide (LiCoO2), Lithium manganese oxide (LiMn2O4), Lithium nickel manganese cobalt oxide (LiNiMnCoO2, or NMC), LiFePO4, and Lithium titanate (Li4Ti5O12) are the common commercially established forms of Lithium-ion batteries. It should be noted that each type of these batteries has different formation and chemistries. Therefore, each type provides different energy/power density, safety/reliability assessment, as well as different cost [16].

2.3.1.2.6 Comparison of Battery Types

There are several battery technologies which are commercially used in the industry of energy storage systems. So far, we have discussed some of the most commercially used batteries technologies in energy storage applications. The selection of these batteries for certain applications relies mainly on the assessment of their specific energy, specific power, energy density, cell voltage, capacity, power density, life time, life cycles, and their cost per kWh. Other traits like the greenness and maintenance requirement can also play a part in the comparison in some sort of cases. However, this diversity between battery technologies comes from different chemistry and operation technique. Table 2.1 presents the comparison metrics for the aforementioned battery types [6][16][45]. There are other attributes that nominated the battery type for its specific application in energy storage applications. For instance, fast response and the extremely high charge of Li-ion batteries are major reasons for its utilization in power quality and load leveling applications. Regarding high discharging rate, Li-ion batteries suffer from degradation when charged above 80% SOC or discharged at SOC less than 20%. Redox flow batteries can be fully discharged at 100% DOD without harming the battery. VRFB, for instance, could reach up to 13000 charge cycles and discharge cycles at 100% DOD exhibiting an efficiency of 78 %. Nevertheless, Li-ion battery has still the superiority in terms of highest specific energy/power, and high energy density over all other battery technologies [6][44][52]. When it comes to the battery price, Lead-acid batteries hold the lowest case among all the kinds of other batteries (50-110$ per kWh), whereas Li-ion battery has the highest cost among the rest of the batteries (200-4000$ kWh) [16]. As we have mentioned so for, each battery technology has its own uniqueness, pros and cons. Therefore, a selection criterion amongst battery technologies depends on their cost-effectiveness and functionality in a specific application [6][16][45]. Table 2.1 compares each battery technology based on different characteristics. Table 2.2 summarizes the pros and cons of each battery technology and as well as their corresponding befitting applications.

Table 2.1 Comparison metrics between different battery types [1, 6, 16, 43, 53-54].

Battery technology	Specific energy (Wh/kg)	Specific power(W/kg)	Self-discharge (%)	Cycle life (cycles)	Energy efficiency (%)	Capital Cost($/kWh)	Life-time (yr)
Lead-acid	25-50[1][43]	25-415[16]	<0.2 [1,14]	500-3000 [1]	70-85[1][6]	50-150[43]	5-15[1,6]
Ni-cd	30-80[43][53]	100-150[6]	0.2-0.3[1,14]	3500[6,43]	70[43]	400-2400[43]	10-20 [43]
NAS	100-175[1,43]	115[6]	No [1,14]	2000-5000[1]	75-85[1, 6]	200-600[43]	10-20[43][6]
VRB	16-35 (Wh/L)[52,43]	160(W/kg)[6]	Negligible [1,14]	13000-20000 [6,52]	65-85[6,43]	600[43]	10-20[43]
ZBB	60-85[6,43]	45[6]	No	2000-2500[43]	65-85[6][43]	500[43]	8-10[6, 43]
PSB	-	-	No	100-13000[43]	60-75[6,43]	300-1000[43]	15[6, 43]
LI-ion	100-200[6,43]	1500-2500[52]	1-5[1,14]	500-10000[1, ,54]	75-95[14]	900-1300[43]	14-25[1,6,43,45]

Table 2.2 Comparison of battery technologies in terms of pros/cons, application type, and discharge time

Battery type	Pros	Cons	Applications	Discharge time
Lead-acid [1,43,55,56,57]	Low cost Highly Mature technology High cycle efficiency Fast response Slow-charging	Poor cycle life Low power density Environmentally harmful Maintenance requirement	Uninterruptible power supply (UPS) Electric Energy Time Shift Renewable smoothing Frequency regulation	sec-hrs
Ni-cd [6,43,48,55,57]	Low-maintenance Long life and high reliability	Memory effect High toxicity materials High cost	Renewable integration Spinning reserve (UPS)	sec-hrs
NAS [43,44,52,55,56,57]	high energy capacity good power density good efficiency high recyclability	High operating temperature and thermal management Low safety High operating cost	peak shaving renewable integration power quality reserves (UPS)	sec-hrs

Table 2.2 (Continued)

Battery type	Pros	Cons	Applications	Discharge time
VRB [1,6,16,51,52, ,55,57]	Low maintenance and material cost Fast response Large storage capacity Long life cycles safe	Low energy density Low power density High total cost	Renewable Capacity Firming Power quality enhancement Load leveling	sec-10 hrs
ZBB [43,55,57]]	No self-discharge High recyclability Deep discharge capability	Material corrosion Low cycle efficiency Low power	(still in early stage of demonstration) Mainly for grid support applications	sec-10 hrs
PSB [6,55,56, 57]	Fast response Scalable Abundant electrolyte materials Cost effective	Low efficiency Low energy density Low performance Electrolyte cross-contamination	still in early stage of demonstration) Bridging power Frequency control Voltage regulation	sec-10 hrs

Table 2.2 (Continued)

Battery type	Pros	Cons	Applications	Discharge time
Li-ion [1,16,44,45,54 ,58]	High efficiency Long life time fast charge and discharge. High energy and power density No memory effect Low maintenance	High cost Degradation Need of additional circuit for protection Sensitive to ambient temperature	Frequency regulation Peak shaving Energy arbitrage Black start Renewable Capacity Firming	min-hrs

2.3.1.3 Battery Models

The modeling process of the battery cell is essential as a means to capture the battery dynamics and extract and estimate the aforementioned crucial parameters such as SOC, SOH, and DOD. The battery modeling is crucial to monitor the battery performance and maintain an efficient control over the battery charging and discharging ensuring safe operation and long life for the battery. Since the battery stores electrical energy in the form of chemical energy and due its non-linear performance, no direct approach is available to estimate those parameters. Thus, battery models are built and analyzed through different modeling approaches and from different perspectives. Accordingly, battery modeling is classified into four main models such as mathematical models, electrochemical models, equivalent circuit models, and data-driven models. Each modeling method will be discussed in detail in the following section [44].

2.3.1.3.1 Electrochemical Model

Electrochemical model is formulated in order to describe the chemical reactions inside the battery, enhance the physical design aspects of the battery, and characterize the mechanics of charge generation. In addition to these, battery voltage and current can be identified. The electrochemical model is the basis of the other kinds of battery models and considered as the foundation of some significant physical laws, such as Ohm’s Law, Faraday’s Law, and Fick’s Law of diffusion. The pseudo-2D model and the single particle model are the two common electrochemical models in the literature. The active materials in the electrode are considered as spherical particles that are equal in size and volume in the pseudo-2d model. On the other hand, the electrode is considered as a single particle in the single particle model. Regardless of the high accuracy of the electrochemical model, the complexity and time-consuming computation hinder it from becoming a preferable model. The main reasons behind this complexity of the electrochemical model are that the electrochemical model is expressed in the form of nonlinear partial differential equation which requires numerical methods to change the equations into ordinary differential equation and obtain a direct analytical solution. Another reason for the complexity of this model is the difficulty to obtain the real parameters of the models which require the use of heuristic methods such as PSO and genetic algorithm for parameter identification of the model and therefore increasing the computation time [59][60].

2.3.1.3.2 Mathematical Model

The mathematical model simplifies the electrochemical model by adopting the empirical equations that represent the battery terminal voltage as a function of the current, SOC, and dc gain to predict system behavior (battery run-time, efficiency, and capacity). The parameters of this model are acquired through minimizing the mean square error between the model voltage and real voltage. Hence for these parameters to be found, a prior data set must be available. Three traditional common empirical models are available: Shepherd model, Nernst model, and Unnewehr universal model, described by the Equations (2.11), (2.12), and (2.13), respectively.

$$V_T = E_o - K\left(\frac{Q}{Q-\int i dt}\right) i - R_i i \tag{2.11}$$

$$V_T = E_0 - R_i \cdot i_k - K_2 \cdot \ln(SOC) + K_3 \cdot \ln(1 - SOC) \tag{2.12}$$

$$V_T = E_0 - R_i \cdot i_k - K_1 \tag{2.13}$$

V_T the terminal voltage, E_0 is the OCV when the battery is fully charged, R_i is the internal resistance, K is the polarization resistance, and i_k is the cell instantaneous current. This current is positive when charging and negative when discharging [60][61]. Both the Nernst and Unnewehr universal models show better performance and accuracy than the Shepherd model. However, Nernst model has the best accuracy and performance compared to other models. The traditional empirical models lack in terms of accuracy. Each model holds a kind of deficiency, so including more effects inside the battery and adding more parameters can improve the accuracy of model to fill the model deficiency. But the tradeoff between computation and complexity is increased. For example, Nernst model can describe the dynamic terminal voltage in an improved manner by adding additional constants $\tau_1$and τ_2. As well as considering the hysteresis effect of the battery voltage the term $s \cdot M$ can be added to the Nernst equation to achieve that [60][61].

2.3.1.3.3 Data-driven Models

The extensive development in the field of artificial intelligence and machine learning utilizes a data-driven model to approximate the electrochemical model through training a sample dataset and establishing a relationship between battery variables directly without any prior knowledge of the battery. The process of this model is as follows: Firstly, a set of data or training sample is attained from the applications. In the second step, the sample data set goes on a training process of machine learning algorithms, and finally the data-driven model is established and the battery parameters are predicted. These parameters are current, SOC, temperature, and the terminal voltage V_t. The data-driven models are based on the machine learning and artificial intelligence algorithms that make the modeling process easier, however the accuracy and usage of the data-driven model are limited by the training dataset. Examples of data-driven models are neural network based model and radial basis function neutral network-based model [60].

2.3.1.3.4 Equivalent Circuit Model (ECM)

The ECM simplifies the electrochemical reactions of the battery by using electric circuits that comprise of voltage sources, resistances, and capacitors that capture an electrical relationship with different inputs such as SOC, current, temperature, and terminal voltage. The ECM is a moderate model that falls between the empirical model and the electrochemical model in terms of accuracy and computational requirements which makes it favorable in battery modeling. There are variety forms of ECM in the literature that differ in the circuit elements included in the model. The traditional models available in the literature are the simple R_i model, Thevenin based model, partnership of new generation of vehicles (PNGV) model, and general nonlinear model (GNL). Other models are multi-purpose comprehensive model and a specific battery type model such as flow-batteries that have unique characteristics than other conventional batteries [60]. Simple model (R_i model) is the most basic ECM as shown in Figure 2.4 where V_b indicates the battery OCV.

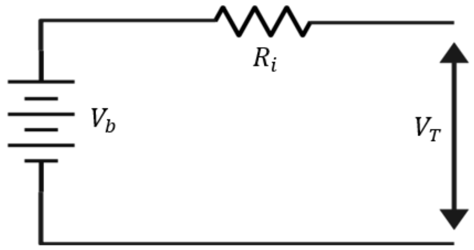

Figure 2.4 R_i model

The internal resistance can be obtained by measuring the OCV and the terminal voltage when a load is connected between the battery terminals at full charge. The main reason behind the poor accuracy as well as the inability to reflect the transient processes of charging and discharging in this model goes back neglection of the relationship between SOC and the internal resistance. Also, as the internal resistance is assumed constant, the energy drawn-out from the battery is assumed limitless [41][59]. This model can be modified and improved by taking into account the variation of internal resistance in regard to the varying SOC and the varying internal resistance [44][59]. Thevenin model is considered as the most common battery model used for parameter identification, and for SOH and SOC estimation, frequently used in the modeling of Li-ion battery. This model circuit is shown in Figure 2.5.

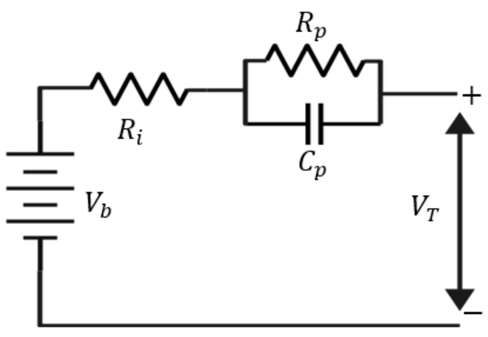

Figure 2.5 Thevenin model [30].

This model comprises of constant open circuit voltage V_b, internal resistance R_i, polarization resistance R_p, and polarization capacitance C_p. The addition of the RC network helps to predict the battery response to a transient load at a certain SOC and captures the terminal voltage dynamics related to polarization effect [30][41][59][60][62][63]. The parameters of this model can be found by using the voltage respond to current excitation [64]. A general expression of the polarization voltage v_p and terminal voltage for Thevenin model are described by Equation (2.14) and (2.15), respectively [30][38].

$$\frac{dv_p}{dt} = -\frac{v_p(t)}{R_p C_p} + \frac{i(t)}{C_p} \tag{2.14}$$

$$V_T = V_b - R_i i(t) - v_p(t) \tag{2.15}$$

The drawback of this model is that it is unable to capture neither the battery voltage variations in steady-state nor the runtime information [59]. However, connecting additional RC circuits can improve the accuracy and capture additional terminal voltage dynamics, but increases the complexity and the computation burden [60]. The dual polarization (DP) model is shown in Figure 2.6.

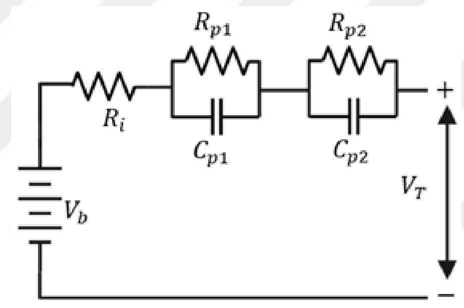

Figure 2.6 Improved Thevenin model (DP model) [30].

An improved Thevenin model that connects one additional RC circuit to increase the accuracy and capture the polarization characteristics more accurately is also available [30][64]. The PNGV model shown in Figure 2.7 is established by connecting a capacitor C_b to the ordinary Thevenin model which expresses the OCV variation with the accumulation of load current [30][59]. Compared to simple R_i model and Thevenin models, PNGV model has generally better accuracy [59]. The GNL model is obtained by adding an additional RC network to the PNGV model. This model shows high accuracy as it is able to reflect the polarization effects in more detail in which it sub divides the battery polarization effect into ohmic polarization, electrochemical polarization, and concentration polarization. However, this model is not convenient for large-scale energy storage systems due to the complexity in identifying the parameters which comes from the large number of nonlinear model links [41][59][65]. Compared to the ordinary Thevenin model, the high order models such as PNGV and GNL are more accurate in reflecting the multi-state response process. Nevertheless, it is difficult and complicated to model their parameters in large scale BESS [65].

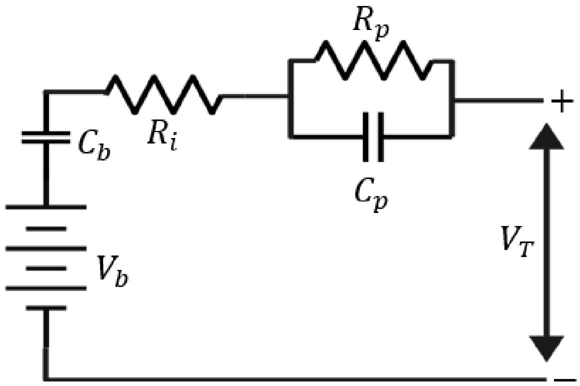

Figure 2.7 PNGV model [30].

Comprehensive models are types of models that utilize complex circuits to simulate multiple characteristics of the battery. The comprehensive model given in Figure 2.8 splits the model into two parts. The left part simulates the life time of the battery, whereas the right part simulates the current-voltage characteristics of the battery. The capacitor C_c and current-controlled current source i_b is used to model the run-time, SOC, and the capacity of the battery. The SOC is bridged with the OCV by using a voltage-controlled voltage source. In addition, an RC network on the right side simulates the transient response. The comprehensive model is known for its high accuracy in predicting run-time, steady state, and transient response. In addition, this model also considers other dynamic electrical characteristics of the battery such as the usable capacity C_c, OCV, and the self-discharge characteristic. The comprehensive model can be further improved by adding an additional RC network on the right side, and R_{cf} resistance on the left side, as displayed in Figure 2.9 to improve the polarization characteristics and include the capacity fade [30][59].

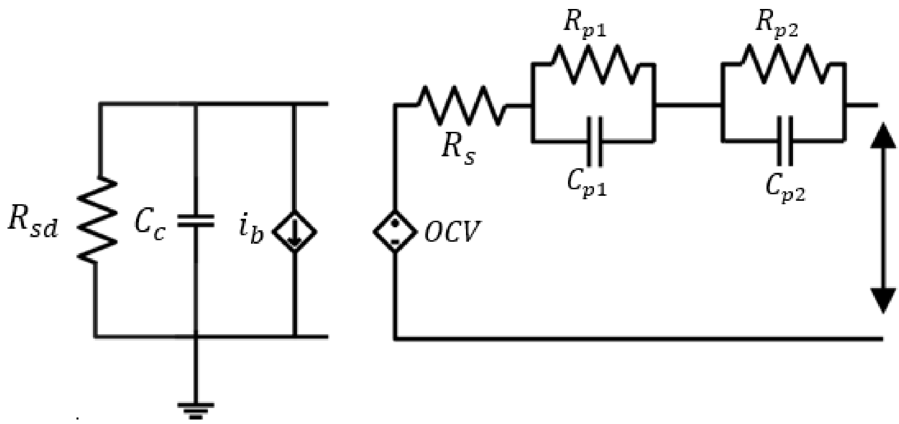

Figure 2.8 Comprehensive model [30].

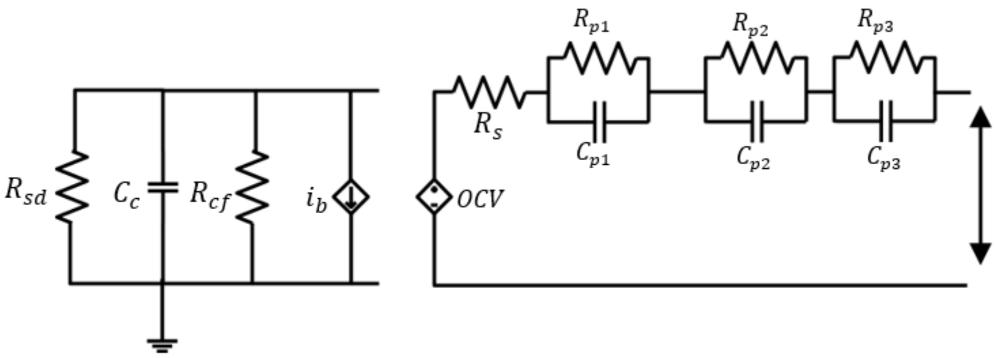

Figure 2.9 Modified comprehensive model [30].

The impedance-based model is based on electrochemical impedance spectroscopy which is a measurement method used to model the ac equivalent impedance in frequency domain over a wide range of frequency impedance spectroscopy in order to study the electrode system. The equivalent circuit model shown in Figure 2.10 consists of V_b to express the SOC, resistance R_s that is modeled based on the conductivity of the electrolyte, inductance L_s which is often neglected due to its small value, and ac impedance Z_{ac} which is a complex equivalent circuit used to fit the impedance spectra. This ECM obtains additional characteristics of the battery dynamics such as diffusion, activation and concentration polarization. However, the impedance-based model is unable to predict dc response and battery run-time as it can only work under constant SOC and ambient temperature conditions [53][59][66]. There is a proportional relationship between the complexity of the model and the accuracy in such way as the complexity increases, the accuracy of the model increases as well [30]. The accuracy of the battery models can be increased further by taking into account more characteristics. The temperature has a high influence on the battery characteristics such as OCV and the battery capacity. Modeling the battery parameters such as the internal resistance, OCV, and hysteresis as function of temperature and SOC can improve the accuracy of the battery model. The higher accuracy of the model the more accurate the SOC prediction becomes [61][64].

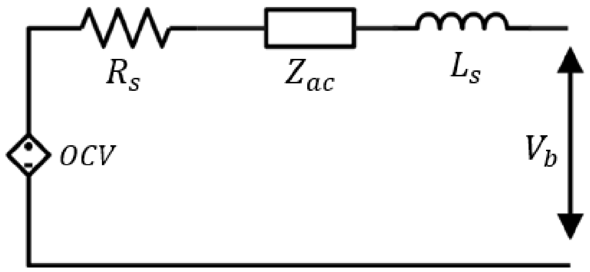

Figure 2.10 Impedance model [59].

2.3.1.4 Battery Pack Modeling

The BESS consists of a large number of battery cells connected both in series and parallel to meet the voltage and current (capacity) requirements. The connection of the batteries is based on a hierarchical order, where the battery cell is the simplest element. A group of a few connected battery cells is called "battery modules". Similarly, multiple strings of the battery modules are connected to form the "battery pack". In ideal case, there is no variation between the cells of the battery pack and all battery cells are assumed identical to each other. Thus, despite the connection topology used, the battery pack capacity as well as the voltage are proportional to those of a single cell. Large battery banks are formed by connecting multiple battery packs that contain multiple modules of cells which are connected either in series or parallel, as shown in Figure 2.11.

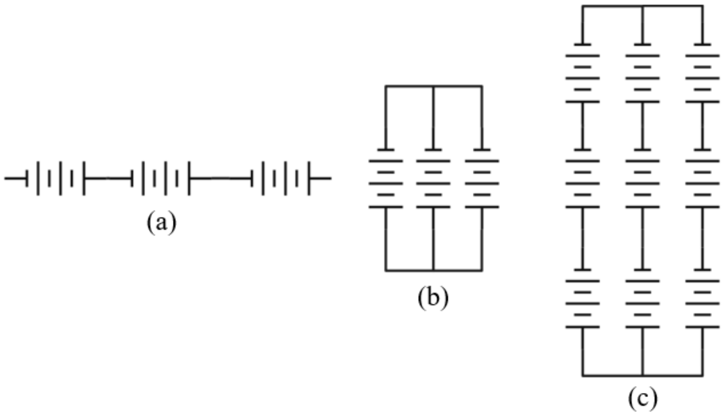

Figure 2.11 Battery cell connections: (a) series connection, (b) parallel connection, (c) series/parallel connections.

Multiple cells are connected in series to obtain higher voltage level by adding up the voltage of each cell and in parallel to stack up higher capacity. When multiple cells are connected in series as shown in Figure 2.12, the voltage of each cell is added up to calculate the overall OCV (OCV_{series}) as expressed in Equation (2.16), where m is the number of the cells connected in series and OCV_j is the OCV of the j^{th} cell. Equation (2.17) shows the total internal resistance ($R_{i,series}$) when multiple cells are connected in series, where $R_{i,j}$ denotes the R_i corresponding to the j^{th}cell. Equation (2.18) shows the total equivalent polarization resistance ($R_{p,series}$) when multiple cells are connected in series, where $R_{p,j}$ denotes the R_p corresponding to the j^{th}cell. The equivalent capacity ($C_{n,series}$) of the multiple cells connected in series is shown in Equation (2.19). As seen, $C_{n,series}$ is equal to the capacity of each cell ($C_{n,j}$). This is true if all cells are identical. However, in real case, the variation in cell capacity always exists due to manufacturing diversity and different ambient temperature of the battery cells. Hence, this variation in battery cells causes overcharge and over discharge leading to a significant degradation in both capacity and life cycle of the battery pack [67][68]. The cell with the lowest capacity determines the capacity of the entire string. Series connected cells discharge at the same rate until it reaches the cut-off voltage. Nevertheless, this cut-off voltage is limited by the cut-off voltage of the weakest cell in such a way that only the weakest cell reaches its cutoff voltage. The terminal voltage ($V_{Tseries}$) of the series battery string can be defined in Equation (2.20), where V_p is the polarization voltage across the RC network.

$$OCV_{series} = mOCV = OCV_1 + OCV_2 + \cdots + OCV_m \tag{2.16}$$

$$R_{i,series} = mR_i = R_{i,1} + R_{i,2} + \cdots + R_{i,m} \tag{2.17}$$

$$R_{p,series} = mR_p = R_{p,1} + R_{p,2} + \cdots + R_{p,m} \tag{2.18}$$

$$C_{n,series} = C_{n,1} = C_{n,2} = C_{n,m} \tag{2.19}$$

$$V_{Tseries} = mV_T = m(OCV - V_p - R_i i) \tag{2.20}$$

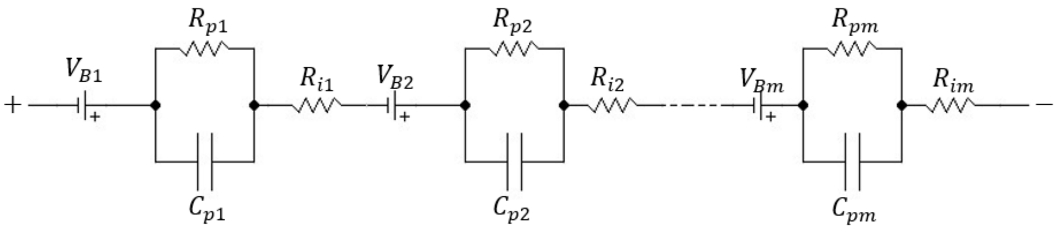

Figure 2.12 The model of series connected battery cells.

Figure 2.13 depicts the model of parallel connected battery cells. In parallel connection, the OCV of each battery cell is equal to each other as shown in Equation (2.21). The equivalent internal resistance of parallel connected battery cells ($R_{i,parallel}$) is given in Equation (2.22), where n is the number of parallel connected cells. On the other hand, the equivalent polarization resistance ($R_{p,parallel}$) and capacitance ($C_{n,parallel}$) of parallel connected battery cells are given in Equation (2.23) and (2.24), respectively.

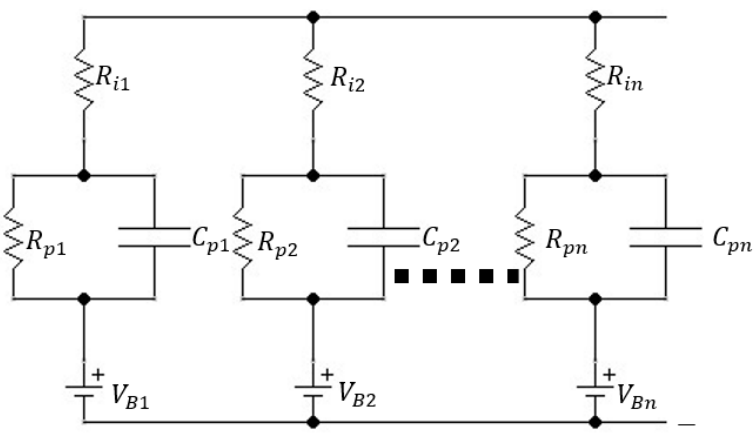

Figure 2.13 The model of parallel connected battery cells.

The terminal voltage V_T in the parallel configuration can be expressed in Equation (2.25) as a function of the OCV, the current flowing through each parallel connected cell i_k, and the n number of parallel connections. Evidently, the terminal voltage is inversely proportional to the number of parallel connected cell as it decreases with more cells connected in parallel. The discharge current rate in parallel connected cell is unequal and expressed as a decreasing function of the output voltage.

$$OCV_{parallel} = OCV_1 = OCV_2 = OCV_m \tag{2.21}$$

$$R_{i,parallel} = \frac{R_i}{n} = (\frac{1}{R_{i,1}} + \frac{1}{R_{i,2}} + \cdots + \frac{1}{R_{i,n}})^{-1} \tag{2.22}$$

$$R_{p,parallel} = \frac{R_p}{n} = (\frac{1}{R_{p,1}} + \frac{1}{R_{p,2}} + \cdots + \frac{1}{R_{p,n}})^{-1} \tag{2.23}$$

$$C_{n,parallel} = nC_n = C_{n,1} + C_{n,2} + \cdots + C_{n,} \tag{2.24}$$

$$OCV - \frac{OCV}{n} + \frac{V_T}{n} = OCV - \frac{V_p}{n} - \frac{R_i}{n} i_k \tag{2.25}$$

In order to obtain safe and optimum performance of the battery, a multi-cell battery model should be built to reflect the characteristics of voltage, capacity, and the current distribution between cells. Moreover, these characteristics depend on several factors such as connections of the cells, cell-to-cell variations, and discharge current rate [68]. The modeling of the battery packs in the literature is generally based on three modeling methods. The first method is to model each individual cell and create pack model based on the accumulative series/parallel connections of the cells [68] [69]. Despite the high accuracy of this method, it is associated with great complexity, because all the differences among the cells are treated individually [69][70]. Hence, it is only suitable for applications of lower number of battery cells [71]. As for the second modeling method, the cell model is scaled into a simplified battery pack model and treated as a single cell model. In this method, the cell inconsistency issues related to the battery to the battery pack is included in the pack model. Also, this method has faster simulation speed compared to the first method making it suitable for simulation and design of utility scale BESS [69]. The third method builds a well-battery pack model than can grasp the total behavior of the pack from different aspects. In this method, the battery pack model includes the battery cells characteristics along with the thermal impact on them. The advantages of this approach are the relatively fast simulation speed with less computational effort. In addition, capability to capture the non-idealities characteristics in battery pack such as weak cells and interconnection impedances is also available in this approach [69][71]. The cell-to-cell variation is a serious dilemma in batteries that could cause

SOC imbalance between the batteries by limiting the available capacity and reduces the lifetime. Ideally, all battery cells are considered to have uniform capacity and the effects of the packaging elements on the battery pack is neglected. Accordingly, the parameters of the pack model are varied based on the series and parallel connection of the multiple cells. On the other hand, the differences in capacity and internal resistances of the multiple-cells have to be considered in real case in order to model the battery pack. In this case, the capacity of each cell must be priory determined [70]. The study in [72] presents a screening method that is used to sort the battery cells with similar characteristics together to minimize the effects of cell variations. This can be done over two steps. In the first step, the cells with similar discharging capacities are grouped after being measured several times at different discharge current rates. In the second step, the selected cells from the first step are subjected to pulse-type charging/discharging current at a diversity of SOC points to choose cells that have similar variances. After the screening process is applied, the battery pack can be modelled by extending the model from single cell to multi-cell battery such that the parameters of the battery pack for series string of simple or Thevenin multi-cell models can be expressed. Battery packs with series connected cells suffer from a serious reliability issue since a fault in a single cell causes the entire pack to cease operation. On the other hand, parallel connected cells are able to continue the operation even during a fault in a single cell, but the imbalance of the charging/discharging current rates among the cells could lead to cells mismatch. A battery pack having cells connected both in series and parallel can be considered as a more robust design with all the features of the series and parallel connectivity. However, this arrangement is also accompanied with all their drawbacks. For example, a single fault will cause failure in one series string but the rest of parallel connected strings will be unaffected. Also, the battery pack capacity will also be limited by the weakest cell.

2.3.1.5 Battery Cell Arrangements

There are different ways to attain series/parallel battery pack models depending on the wiring order of the series and parallel modules as well as the cell arrangements inside the pack. The parallel cell module (PCM) and series cell module (SCM) named by Plett and Klein are considered as the most common wiring arrangements in the literature [68]. In PCM, the cells are wired in parallel forming modules of parallel connected cells then the modules are wired in series. As a result, this approach is able to ease out any variation in the resistance and capacities of the cells such that the battery packs continuously operate even with significant parameters variation. If a single cell introduces leakage current a fault can occur. The battery can still be functional but with less terminal voltage amplitude in case of short-circuit fault in a single cell as all cells in the module are affected by the same fault. SCM, on the other hand, at first, the cells are connected in series, then the modules are wired in parallel. This configuration allows the modules to self-balance when no load is connected. When a single cell is subjected to open-circuit fault, the entire string associated with the faulty cell is disconnected from the pack. Whereas, a short-circuit fault in a single cell subjects all the cells in the same string to higher voltage in order to keep up with the bus voltage of the battery pack. The study in [68] involves 4 different cells connection topologies including SCMs and PCMs, as shown in Figure 2.14. It is focused on inspecting the relationship between the maximum capacity of the battery and the cells arrangement in case of mismatch in the cell's parameters. It is then found out that the battery pack with PCM arrangement provides higher capacity and reduces the statistical dispersion. Also, it is highlighted that the battery pack capacity can be even lower than the weakest cell and the first cell to reach the cut-off voltage is not necessarily the weakest cell. There is an extensive number of arrangements for wiring the cells inside the battery pack. The appropriate arrangement of the cells is critical such that different arrangements can lead to huge variation in the capacity of the battery pack inferring that batteries arrangement has large impact on the overall battery performance. The number of possible arrangements n for wiring the battery cells or modules can be estimated based on the number of parallel connections p having s cells as follows;

$$n = \frac{(p*s)!}{p!(s!)^p} \tag{2.26}$$

2.3.1.6 Battery Charging Methods

Conventionally, a battery is charged by injecting electrical current into the battery when its SOC falls below 20% of its maximum capacity. How fast the battery is charged to its maximum capacity depends on the current amplitude flowing into the battery as high currents achieve faster charging. However, batteries cannot sustain large currents for long time duration due to temperature increase that could be harmful for the batteries. Also, while charging, the batteries current and voltage should be kept within their rated thresholds values to guarantee the battery safety. Therefore, an appropriate charging technique has to be selected to safely charge the battery at reasonable rate while maintaining the temperature, voltage, and current within their rated values to avoid faster battery aging and drop in performance. There are different charging techniques that are available in literature. The most basic charging methods are constant current (CC) charging and constant voltage (CV) charging. In CC charging, as the name implies, the battery is charged at low rate of CC until a predetermined threshold value is reached. The charging current rate is considered as the key factor that influences the behavior of the battery in this approach. Faster charging can be attained with higher current rates at the cost of reducing the lifetime of the battery. For charging with lower current rates, high-capacity utilization can be realized but the charging speed will be significantly reduced. Therefore, an optimum current rate has to be determined in order to implement CC efficiently in such manner the battery can be charged at reasonable speed without accelerating the aging of the battery [31]. CV charging is another basic common charging method that charges the battery while maintaining a constant output voltage. By adopting CV charging method, the life time of the batteries can be further prolonged due to the prevention of overvoltage and irreversible side reactions. The charging speed in CV approach is a function of SOC and current rate such that the charging current is higher when charging the battery from lower SOC and as SOC increases during charging the current progressively decreases as the battery is gets closer to full charge. Moreover, the charging speed can be reasonably fast when charging between 0.15% and 80% SOC and get significantly slower beyond 90% SOC. Furthermore, large current rates are required during the initial stages of CV charging operating to maintain constant output voltage, the battery lattice will be more exposed to collapsing and the battery poles could be broken. For CV charging, the most difficult aspect is determining an appropriate voltage value that can achieve balance between electrolyte decomposition, capacity utilization, and charging speed [31][73]. Constant current-constant voltage (CC-CV) is a comprehensive charging technique that combines both CC and CV charging.

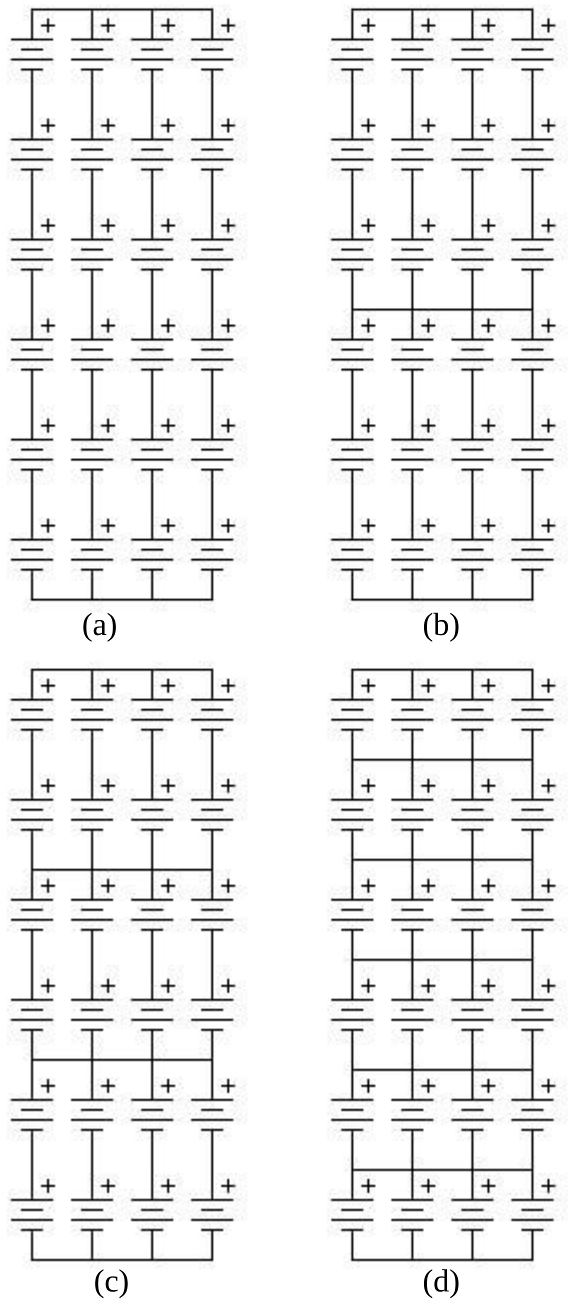

Figure 2.14 Different battery module arrangements [68].

The operation of CC-CV approach is divided into 3 stages as shown in Figure 2.15. The first stage is called “trickle-charge”. This stage is only activated in case the battery is subjected to over discharge. The main objective of this stage is to check the operating status of the battery by supplying the battery a constant charging current for a predetermined period and analyzing the battery voltage slope [74][75]. If the battery is found out to be damaged the charging is aborted. Otherwise, the second charging stage is initiated. During second stage, CC is applied to charge the battery at constant current and stops when the battery voltage hits its maximum threshold value that is usually around 70% SOC. If CC charging continues further the battery voltage will rise above its rated maximum voltage exposing the battery to excessive heating which could severely damage the battery. Therefore, the charging is switched to the third stage employing CV charging keeping the battery voltage at its maximum rated value while the charging current gradually decreases until it falls to trickle-charging level which is usually around 10% of the maximum charging current. When the battery is fully charged CV charging is terminated [75].

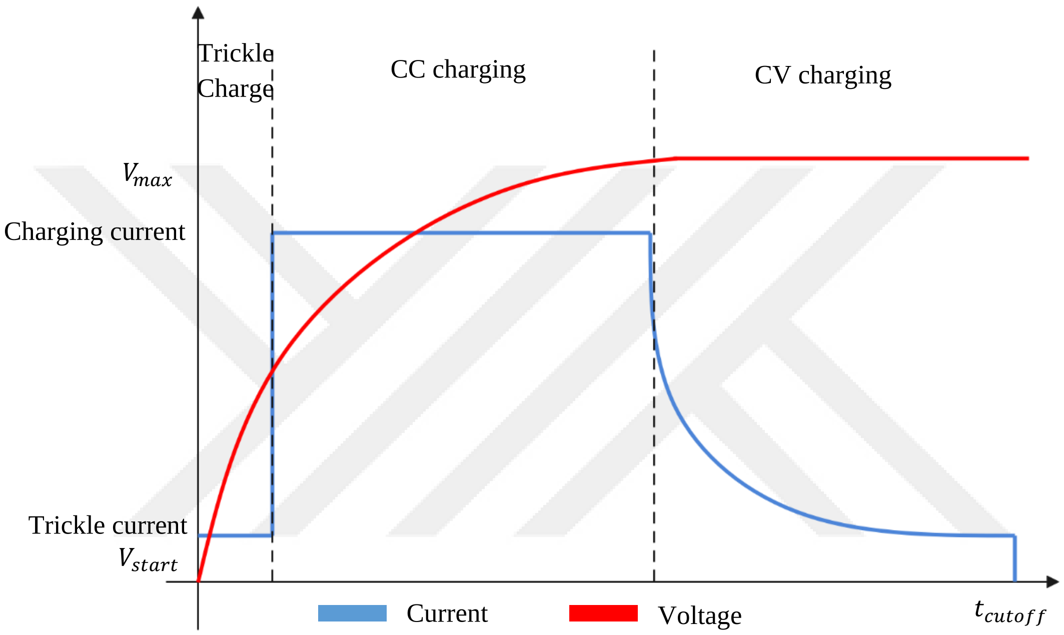

Figure 2.15 CC-CV charging graph.

The aforementioned approach is the standard CC-CV charging method that was firstly used for Lead-acid battery charging as it is highly recommended in the industry. It can be applied to other battery technologies with few minor adjustments. Li-ion battery has higher terminal voltage and charging acceptance than Lead-acid battery, thus larger constant current rates are required for charging Li-ion battery usually set between 0.5-3.0 C [31]. The utilization of CC-CV charging method is much better than using CC and CV charging individually as it is capable to compromise between the weaknesses of each basic charging mode. For example, CV charging mode can compensate any capacity losses that occur in the CC phase due to large electrochemical polarization. On the other hand, CC charging mode is able to compensate for the slow charging speed of CV mode. Moreover, executing both CC and CV charging modes means the challenges of finding a proper CC rate and CV threshold still remains [31]. More advanced CC-CV charging techniques can be applied to improve the charging performance of the standard CC-CV approach by involving more charging stages or by adjusting the duration of each charging stage [75]. In [76], faster charging was obtained by applying a CC stage for longer duration in such a way that the duration of CV stage where charging is slowed down is shortened. This is achieved by setting the reference threshold voltage slightly above the maximum voltage. Another charging approach that can improve the battery charging speed and lifetime corresponding to the CV stage in the conventional CC-CV method is the multi-stage constant current (MSCC). In this technique, the charging duration is divided into multiple CC levels in a descending staircase pattern as shown in Figure 2.16. Whenever the battery voltage hits the threshold voltage, the current is descended to the next level. This occurs repeatedly until all predefined current stages are fulfilled [31][73]. This method is applicable for charging Ni-Mh, Lead-acid, and Li-ion batteries. The main challenge for this approach is determining the number of current levels and its corresponding amplitudes. Several studies were conducted to search for an optimum charging pattern for MSCC. In [77], particle swarm optimization method was used to find an optimum 5 stages charging pattern. In [78], a fast-charging pattern based on 5 stages MSCC capable for charging Li-ion battery to 75% SOC in only 40 minutes was found by adopting Taguchi-based algorithm. An alternative fast charging strategy is the pulse charging. In this method, the battery is charged by applying a pulsating current pulsing between 1 sec and milliseconds depending on the charging frequency. Also, the charging current rate can be controlled by adjusting the pulse duty cycle [73][75]. The battery charging behavior based on pulse charging scheme is depicted in Figure 2.17. Observably, as pulsing current is charging or discharging the battery, the voltage slightly surges above the maximum threshold as a means to allow the battery fully sustain the charging current. Once the pulse current is in OFF state, the battery voltage starts recovering and settles a bit above its original value prior to the pulsing current charge and this occurs repeatedly. The time required for the battery voltage to recover after surging above its maximum threshold depends on the corresponding battery SOC as SOC increases during charging the battery. Meanwhile, the voltage recovery time increases as well. Therefore, this relationship can be used as an indicator to determine when the battery is near fully charged to stop the battery charging [75]. The large charging currents can be applied in the form of pulses but not consistently due to the fact that the amount of charge that can be stored or drawn from the battery gets lesser as charging current rate increases. Thus, besides the charge constraint, if the battery continues charging faster than the chemical reactions, it will result in excessive heating in battery leading to undesirable effects on the battery safety and performance such as capacity fade and polarization [73]. However, applying large charging currents in the form of pulses will not be as harmful as constant charging, since the battery is allowed to rest in between charging pulses achieving even ion distribution in battery electrolyte as well as accelerating the battery charging [73][74].The study in [79] investigates the impact of inductor current ripples associated with pulsing charging/discharging on the aging of Li-ion battery which ends up concluding that those current ripples are irrelevant to faster battery aging.

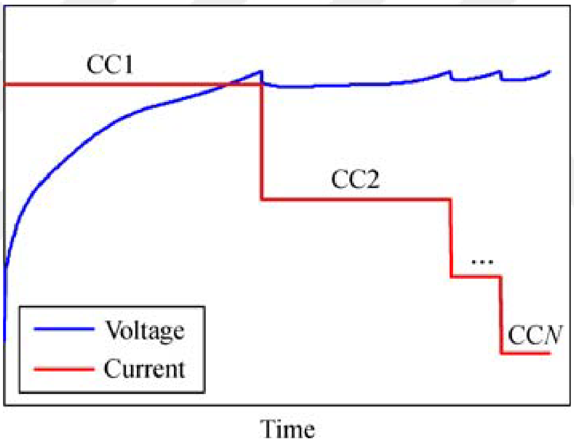

Figure 2.16 MSCC charging [31].

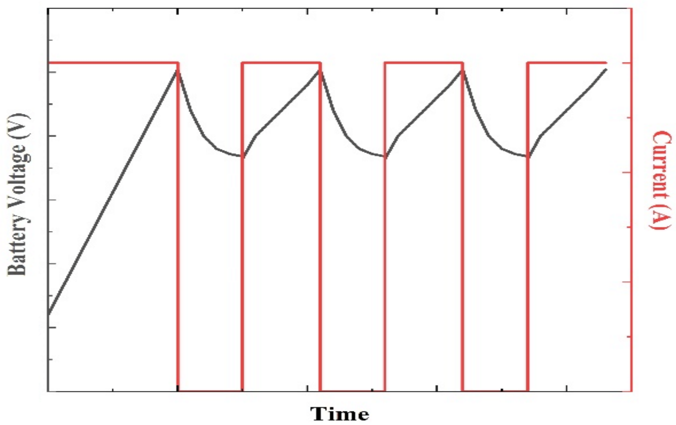

Figure 2.17 Pulse charging [145].

The charging of the battery considering different cell arrangements in the battery pack is studied in [80]. In that study, 3 Li-ion battery cells with different initial SOC values are connected to a charger to deliver a constant current and voltage needed to charge the battery pack. When the battery cells are connected in series, to ensure the charging speed of the Li-ion battery pack, it is first charged by CC, as the terminal voltage exceeds the threshold voltage. The charger switches to charging by CV as soon as one of the cells reaches 100% of its nominal capacity. Additionally, the charging stops to prevent over charging. Even though the series charging can achieve fast charging with consistent charging current, the battery cells are more vulnerable to SOC imbalance that could limit the overall capacity of the battery pack. This situation can also lead to overcharging or undercharging. In a similar manner, when the parallel connected cells are subjected to parallel charging, the charging current is distributed between the cells based on their SOC, as the cell with the lowest capacity is charged with higher current amplitude. Such an action realizes better energy balance in the battery pack, but at the cost of increasing the polarization effects. Later, a comprehensive approach is proposed that can realize both series and parallel charging to achieve fast charging and energy balance in the battery pack by adding switching devices across the battery terminals to interchange between the two charging modes.

2.3.2 Battery Management System (BMS)

The BMS is a control and optimization system which is crucial for proper functioning the BESS to protect batteries from electrical and thermal issues such as variance in discharging current among cells, SOC imbalance, and overheat. A general schematic of BMS is depicted in Figure 2.18 [67]. The main function of the BMS is SOC balancing using different SOC balancing algorithms. Monitoring voltage, current, SOH, temperature of each cell/whole pack, internal faults, protecting the batteries from over-charging/discharging are other functions of a BMS [67]. In real case, the influence of the BMS on the battery parameters is minor and can be neglected. Since, it appears as a small resistance and has non-significant influence on the voltage source as well as the value of the polarization resistance [71].

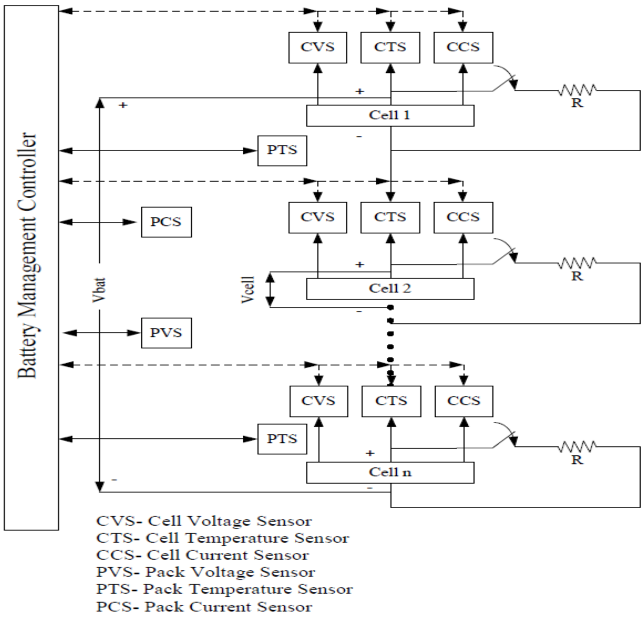

Figure 2.18 General schematic of BMS [67].

2.3.3 Power Conversion System (PCS)

PCS utilizes power electronic converters to act as an interface between the ESS and the grid. PCS also provides an electrical isolation between the ESS and the grid and allows power flow in both directions for charging and discharging of the ESS. PCS can also be managed for providing ancillary services to the grid and the electrical market. There are a variety of converter topologies which depend on the type and the final application of the energy storage technologies used. The PCS for mostly all different types of energy storage technologies are usually composed of a coupling transformer that boosts the voltage from hundreds of volts to medium voltage (MV) level of distribution network, a filter to eliminate the harmonics at the ac side, grid-side converter (DC/AC converter) to connect the ESS to the ac grid, and a switching gear that protects the whole system which trips when a fault occurs to isolate the ESS from the grid [6][81]. Conventional power electronic converters can operate for a long time (over 20 years) while maintaining constant low thermal cycles and temperature profile [82]. The bidirectional configuration of the power electronic converters is the most common one in the literature to be used in the ESS. Since, these converters control to power flow in both directions. Therefore, there is no need to use a separate converter for each direction of the power flow. This attribute reduces the size and cost of the system and remarkably increases the performance and efficiency [83]. The power electronics topologies used for ESS can be classified into 3 categories: Standard topologies, multilevel topologies, and multiport topologies. The standard converters are also referred as two-port converters in which its input is connected to the ESS and its output is connected to the load or grid. There are two structures for the convenient power converters that is the single stage structure and the double stage structure. In the single stage, only a single power converter is used at the grid side of the ESS to control the power flow between the electric grid and the ESS to manage the charging and discharging processes. In case of double stage structure, an additional power electronic converter is employed at the storage side, mostly a dc/dc converter to individually or collectively manage the charge and discharge processes. The multilevel topologies are capable of providing more output voltage levels, high voltage amplitude, and large output power with minimized harmonic content. Therefore, multilevel topologies are suitable for MV and high voltage applications (HVDC) and utility scale BESS applications. Finally, the multi-port topology is a type of power electronics structure that interfaces between different types of energy storage devices or ES to multiple loads such as PV-BESS integration [81] [84].

2.3.3.1 Single-Stage Converters

Single-stage converters are considered as the most simple and efficient for connecting ESS to the ac grid. In this kind of converters, the batteries or storage units are directly interfaced with the bidirectional dc-ac dc-link to transfer energy between the storage system and the grid [84][85]. They are usually used in non-isolated connections. Despite high efficiency, single-stage converters exhibit floating voltage in the dc-link which depends on the characteristics of the batteries or storage device. Consequently, the dc voltage should be greater than ac voltage. The ratio is approximately 1.5 times. This imposes a constraint on the voltage of the battery pack which has to be designed with higher nominal voltage in order to inject current in the grid when the batteries are fully discharged [4][85]. A typical single-stage power converter consists of a bidirectional ac-dc converter with a line frequency transformer. The most common and mature topology is the two-level H-bridge converter which is shown in Figure 2.19 [6][84]. The IGBT is recommended for this topology as the power switch. The voltage and the power rating of this topology or three-level one can be further increased by connecting semiconductor switches in series and in parallel, respectively. Moreover, applying this approach may increase the total cost and require more expensive output filters since low switching frequency is needed to reduce the switching losses [6][81][84].

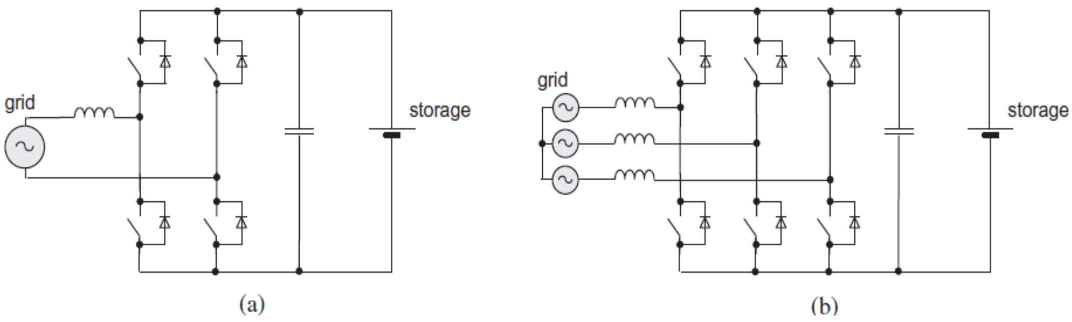

Figure 2.19 Bidirectional two-level converter (a) single phase (b) three-phase [84].

The z-source inverter (ZSI) overcomes some issues that exist in traditional two-level inverter such as shoot-through problem that affects the converter reliability by providing a boost function invulnerable to shoot-through. The quasi-ZSI is an improved form of ZSI in such that the ratings of passive components are reduced and a continuous input current is supplied [84]. Both ZSI and quasi-ZSI have wide regulation freedom due to utilizing shoot through states for the voltage boost function. However, both of them have a unidirectional power flow capability. In order to achieve bidirectional power flow, an additional power switch is connected across the diode as shown in Figure 2.20 to handle the current in the rectifier mode operation [84].

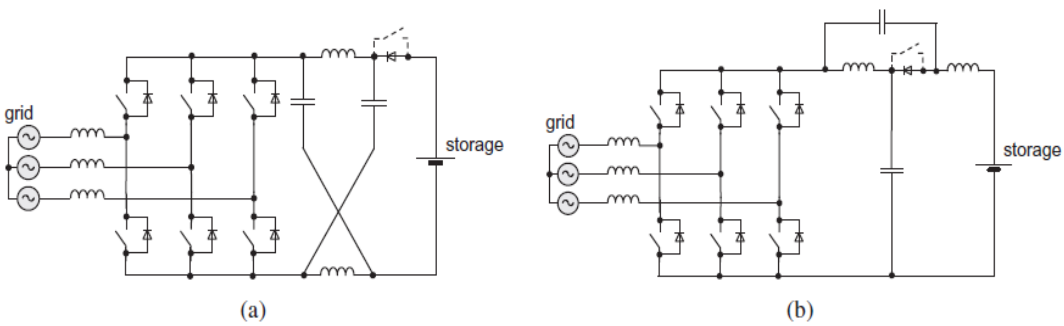

Figure 2.20 (a) Three-phase bidirectional ZSI, (b) three-phase bidirectional quasi-ZSI [84].

Another alternative approach is utilizing bidirectional matrix converters. This topology comprises of controlled four-quadrant bidirectional switches in an array structure to provide variable output voltage with variable frequency. An example of matrix converters is the ZSI and quasi-ZSI three-phase bidirectional ac-dc converters as shown in Fig 2.21. These converters can attain a variable ac output voltage and frequency in the inversion mode and a regulated output dc voltage from varying voltage and frequency ac source in the rectification mode [84][86]. In [87], a single-stage isolated matrix based bidirectional ac-dc converter is presented for energy storage. This converter comprises of six bidirectional matrix switches at the primary side, a high frequency transformer to process the high frequency ac voltage, and four switches at the secondary side that are capable of zero voltage switching to provide high efficiency. Moreover, the matrix-based topology provides higher power density and power conversion efficiency in single-stage topologies.

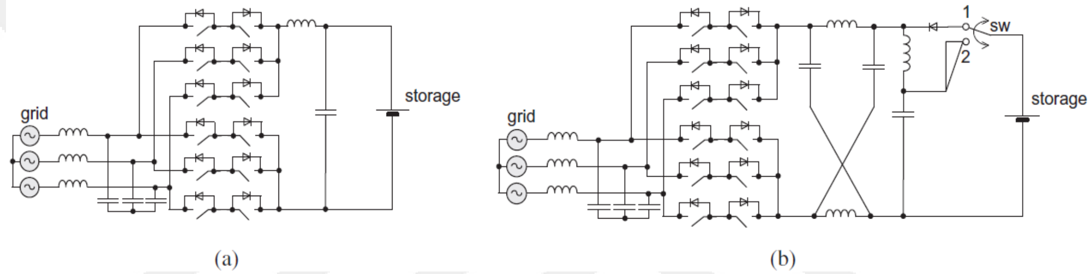

Figure 2.21 Three-phase impedance source matrix based bidirectional ac-dc converters: (a) ZSI (b) quasi-ZSI [84].

The overall advantages of the single-stage topologies are reduced losses, lower device count, and low cost. However, this topology is limited to low voltage storage systems. Since multiple storage modules are required to be connected in series to attain higher voltage levels. However, a failure of a single unit could cause a failure for the whole system which is considered a major disadvantage. There are three main categories for the control algorithms that can be used for single-stage converters: voltage source current controlled, voltage source voltage controlled, and space vector controlled. The space vector controlled is the most common control algorithm among the others which consists of two control loops: inner loop for ac current and outer loop for voltage. The three-phase input current is converted into complex d-q vector space. This control algorithm demands good computation power from the control due to the transformations back and forth from d-q frame into abc frame [84].

2.3.3.2 Two-Stage Topologies

The two-stage topologies provide more flexibility in developing the voltage range of the storage device in which the dc voltage is allowed to be below or above the ac voltage of the grid [4][82]. This is achieved by connecting a dc/dc converter at the storage side to process the power absorbed or delivered by the batteries by controlling the voltage at the dc link [13][83]. The bidirectional dc/dc converters are divided into two major categories which are the non-isolated topology and the isolated topology [83][84]. The non-isolated topology has a simple configuration since it does not include a transformer. The power is transferred without any magnetic isolation thus this topology does not exhibit any magnetic interference that is accompanied with the galvanic isolation. On the other hand, the isolated topology provides galvanic isolation and employ a higher frequency transformer that offers higher step-up voltage gain ratio than the non-isolated topology. In both of these topologies, dc voltage is converted to ac voltage waveform through the high-frequency transformer and then rectified back to dc waveform [83].

2.3.3.2.1 Non-isolated DC/DC converters

The bidirectional half-bridge (buck and boost) topology is shown in Figure 2.22. This topology is the simplest and commonly used converter type known for high efficiency which is over 90% [84]. The bidirectional half-bridge converter acts as a buck converter when charging the batteries and acts as a boost converter when discharging the batteries. The buck-boost converter shown in Figure 2.23 is similar to the typical bidirectional half-bridge topology [83][84]. However, this converter is capable of operating in buck and boost modes in both power flow directions with negative output voltage that make it a suitable for applications where the voltage varies in wide range [13][83][84]. The bidirectional CUK converter shown in Figure 2.24 has a similar concept of the buck-boost which is also a symmetrical topology that is capable of step-up/step-down the voltage in both directions with reversed output voltage. This converter has the ability to provide continuous input and output currents and also capable of eliminating the input and output current ripples [83][84]. The disadvantages of the CUK converter are the large inductor requirement and high voltage rating transfer capacitor [84]. The conventional bidirectional dc/dc converter has limited boosting capability and in order to increase the dc-link voltage, several storage devices are required to be connected in series. The cascaded DC-DC topology is an alternative solution to improve the voltage boosting capability and reduce the current to operate in higher power ratings. In this topology, multiple DC-DC converter is connected in cascaded structure to achieve higher voltage gain ratio with the same duty cycle of the switch. An example of cascaded dc/dc converters is the double bidirectional half-bridge converter as shown in Figure 2.22 (b) and the cascaded buck-boost bidirectional converter as shown in Figure 2.23 (b) [83][84].

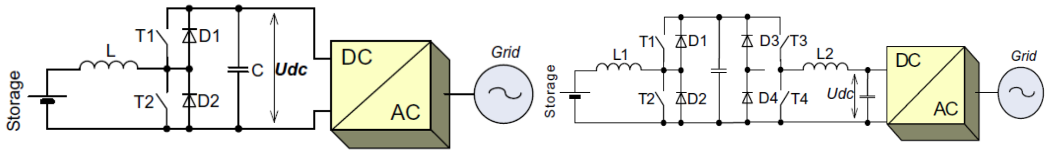

Figure 2.22 (a) Bidirectional half-bridge dc/dc converter, (b) Double bidirectional half-bridge dc/dc converter [83][84].

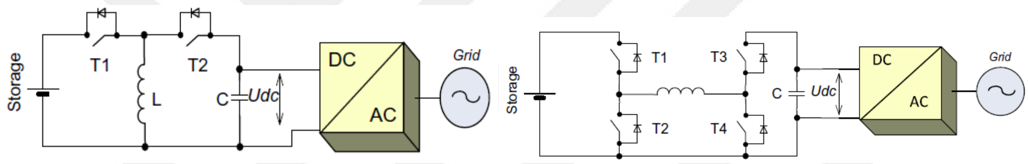

Figure 2.23 (a) Bidirectional buck-boost dc/dc converter, (b) Double bidirectional buck-boost dc/dc converter [83][84].

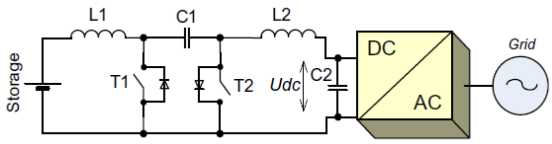

Figure 2.24 Bidirectional CUK converter [83][84].

2.3.3.2.2 Isolated DC/DC converters

Generally galvanic isolation adds an extra degree of freedom granting higher voltage boosting capability [83]. However, in certain cases, the galvanic isolation as a safety measure to deliver power safely to sensitive loads are vulnerable to noise and faults [13][83]. Isolation can be applied to some of the aforementioned non-isolated topologies to further improve the voltage boost ability. For example, fly-back converter as shown in Figure 2.25 can be obtained by adding isolation to buck-boost converter by replacing the inductor of the buck-boost converter with a transformer. Similarly, including isolation for CUK converter (Fig 2.26) can provide more benefits to the original design such as eliminating input/output current ripples [38]. The back-to-back bidirectional topologies such as half-bridge, full-bridge, and dual-active bridge (DAB) converters are the most popular isolated topologies that use high-frequency transformer for isolation. The DAB is the most common among the back-to-back converters. The conventional DAB converter as shown in Fig 2.27 is comprised of two full-bridge converters separated by high-frequency transformer. The DAB includes total 8 switches, 4 in each full-bridge which allow for its utilization in high power application, since the number of switches is proportional to the bidirectional converters power capacity. However, including additional switches result in more switching losses which can be dealt with by utilizing soft-switching techniques and low loss switches such as silicon-carbide (SiC) or gallium nitride (GaN) [81][83]. During charging, DAB converter operates in buck mode where the full-bridge on the grid side acts as an DC-AC inverter then the high-frequency transformer steps up the voltage. Finally, the full-bridge on the storage side acts as an ac-dc rectifier. This process is reversed in case of discharging [13][83]. Figure 2.28 shows a comprehensive approach of the DAB converter combined with bidirectional buck-boost converter to achieve maximum efficiency. The buck-boost converter regulates the battery voltage and keeps it constant allowing the DAB converter to function in one operating point. This is a commonly used topology of DAB converter especially for high power applications [84]. Another back-to-back topology is the dual half-bridge (DHB) (Fig 2.29). This topology has half number of switches of the DAB, which makes it more preferable for lower power applications. However, having half the number of switches of DAB doubles the current flowing in the switches. The DHB is divided into two groups: voltage-fed and current-fed DHB. Voltage fed converters are well-known circuits for converting high voltages at the input to low voltages at the output in high-power switch mode power supply. Because the boosting action is only accomplished by the winding ratio in voltage-fed converters, a high winding ratio between the primary and secondary sides of the high-frequency transformer is required. This also leads the snubber to be increased to manage the surge at turn-off switching instants. Moreover, voltage fed converters might not be ideal option as it requires larger number of electrolyte capacitors to handle the current ripples. Current-fed DHB on the other hand, includes an inductor which helps reducing the current ripple and capacitor size. Also active boosting action can be performed with a lower winding ratio [146-147]. The current-fed DHB can improve the life cycle and performance of the energy storage devices by performing SOC estimation under dynamic environment. Also, using a current-fed DHB can further improve the transformer efficiency through boosting the dc capacitor voltage. Moreover, the current-fed DHB is considered as more beneficial than voltage-fed DHB [84].

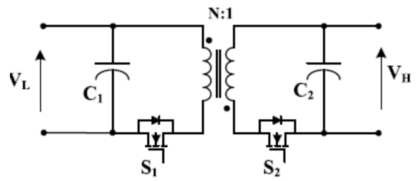

Figure 2.25 Fly-back converter [83].

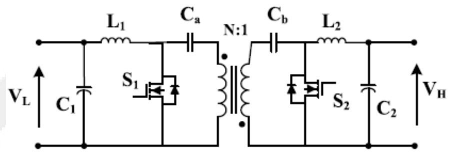

Figure 2.26 Isolated bidirectional CUK converter [83].

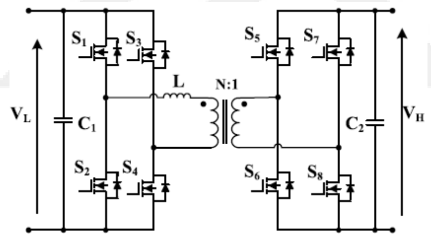

Figure 2.27 Dual active-bridge (DAB) [83].

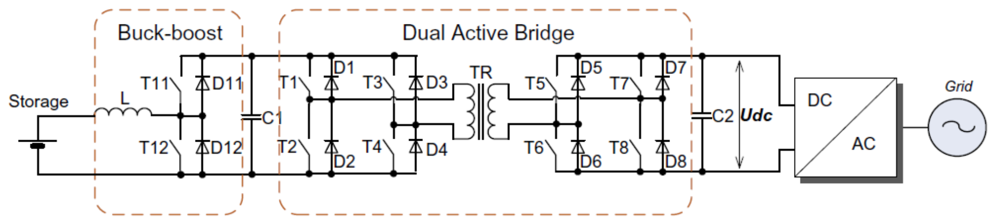

Figure 2.28 Bidirectional buck-boost combined with DAB [84].

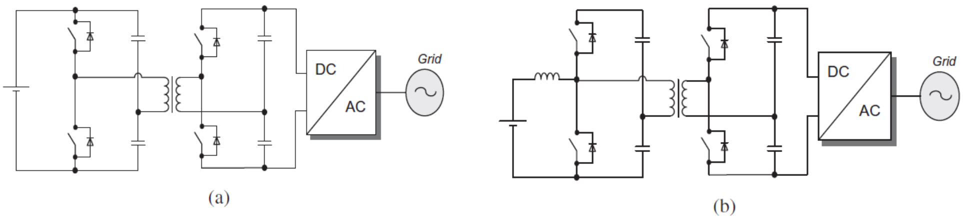

Figure 2.29 Dual half-bridge converters (a) Voltage-fed DHB (b) Current-fed DHB [84].

The main purpose of the bidirectional DC-DC converter is to maintain a constant dc bus voltage along with regulating the charge/discharge current. There are two main control algorithms implemented for DC-DC converters. These are voltage mode control (VMC) and current mode control (CMC). VMC is simple and flexible which can be implemented in any all kinds of dc/dc converters. VMC is based on fixed frequency pulse width modulation (PWM) control methods and can be implemented with phase shift modulation [84]. The main objective of VMC is to control the dc-link voltage. The CMC overcomes the VMC with faster response time and short-circuits protection [81]. The CMC controls the charging/discharging current of the battery. There are three sub-variations of the CMC. These are peak, average, and hysteretic. Moreover, all of the aforementioned control algorithms can be implemented for the isolated topologies except for peak and hysteretic CMC [81][84]. The utilization of bidirectional DC-DC converters in two stage topologies can solve several issues in the ESS and reach an optimized design. One of the issues is the variation of the battery voltage which is resolved by controlling the dc link by using bidirectional DC-DC converters [81]. Another issue is the increased number of batteries in the string to meet the required string voltage which can be solved by the boost ability of the DC-DC converters [81]. The traditional method to comply with the voltage and power requirements of the BESS is the series connection battery packs to increase the output voltage level and the parallel connection of battery packs to increase the output current [88]. An alternative approach is the array connection of battery power modules (BPM). Each BPM comprises of battery pack connected with a bidirectional DC-DC converter. Similarly, BPM can be connected in series configuration to boost the voltage rating and in parallel configuration to increase the current rating. Furthermore, this approach can deal with the imbalance in the battery bank in such the power flow of each pack can be individually regulated. Additionally, a balanced charging and discharging can be achieved by stopping the connected converters or turning off some of the mechanical switches to isolate the that are fully charged, over discharged, and damaged batteries from the BESS [81][89]. In [88], a series connection of isolated DC-DC converters is proposed to achieve a direct connection to MV grid. In this paper, series connection of DAB cells is proposed to dramatically boost the output voltage to 11 kV. The paper also proposes a method to reduce the device count and the number of semiconductors used by replacing the DC-DC converters in the BPM with two contactors. However, double-stage topologies include additional losses from power switching devices and increases the total cost of the PCS and BESS.

2.3.3.3 Multilevel Topologies

The multilevel topologies are considered as a practical solution for the utilization of BESS in MV range without using transformers. The main objective of the converters based on multilevel topology is to obtain an ac voltage from several dc voltage levels. Generally, these converters comprise of branches of series connected modules and inductor. Instead of switching all modules at the same time, the multilevel converters are capable of switching only the connected modules, thus reducing the harmonic filtering requirements and the switching losses. CHB, modular multilevel converter (MMC), and neutral-point clamped (NPC) converters are the most common multilevel topologies [83][90]. The three-phase CHB shown in Figure 2.30 comprises of three phase legs. Each leg consists of a series connected H-bridge cells to boost the battery voltage to MV range without the use of a transformer. The utilization of this topology helps to improve the robustness and reliability of the system by equally distribution of the battery modules among the converter cells and achieving shorter battery strings. Since a failure in a single battery cell inside the string could cause a failure of the entire string. Another merit of CHB is that in case of fault, in a single cell, the operation of the other healthy cells will not be affected [81][84]. The output voltage levels n can be described in Equation (2.27) where k is the number of H-bridge cells connected in series. The voltage level scales with the number of connected cells in series [91].

$$n = 2k + 1 \tag{2.27}$$

The CHB converter can either be connected in delta or star-configuration. Due to short-circuit and circulating current problems, star-connection is usually preferred [82][92]. The inclusion of a DC-DC converter in the CHB structure can decouple the power variation of the dc-link from the battery which achieves an operation over a wide modulation index for the grid-side converter [84][90]. The optimum modulation technique for the CHB converter is optimum harmonic stepped waveform which can efficiently eliminate the harmonics and obtain lower switching losses. Adding more converter cells with lower rated semiconductors can decrease the conduction losses that increase proportionally with the number of connected cells [82][92].

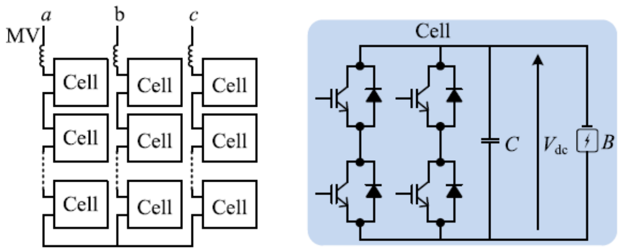

Figure 2.30 Three-phase CHB converter and H-bridge cell circuit [81].

MMC shown in Figure 2.31 is another cascaded approach for interfacing of BESS with MV grid similar to the concept of CHB but with two branches of 6 phase legs. The MMC can be integrated with BESS to interface the MV grid in two manners. Either in centralized manner where MMC is directly connected to the MV dc link or in a distributed configuration in which battery modules is distributed among the sub-modules (SM) forming the arms of the converters. In regard to the centralized case the SM is connected to a common dc-link that is associated with a long battery string where the voltage of the dc-link is equals the sum of two branch voltages [81][90]. However, using long battery strings deny the main benefits of the cascaded structures and result in the flow of low-order current harmonics through the batteries. Therefore, the distributed structure is a more beneficial approach for the integration of mmc in BESS implementation [81]. The main function of the mmc is to divide the high total voltage into smaller steps that can be managed between the low-voltage sub modules that acts as independent voltage sources allowing for scalability of the total voltage rating. In addition to scaling the total voltage, this scalability provides high reliability by adding more modules to compensate the failure of the other modules. The MMC comprises of cascaded modules that includes H-bridge modules that consist of semiconductor switches, capacitor, and diodes. Furthermore, forming a balanced voltage divider along with balancing SOC of the capacitors within the SMs in such way the terminal voltage has less constraints compared to the other multilevel topologies [92]. Moreover, SOC balancing is done by injecting circulating currents in the converter phase-legs which could lead to an increase in the switching and conduction losses [81]. Another feature of the MMC is its flexibility in changing the total voltage during the operation with minimum number of semiconductors ensuring low switching losses [92]. However, compared to the CHB, MMC has double number of switching devices, Also MMC has 6 branches compared to the 3 branches in CHB which introduce more complexity and cost. Nevertheless, MMC is a still valuable approach for other applications such as HVDC transmission [81][90].

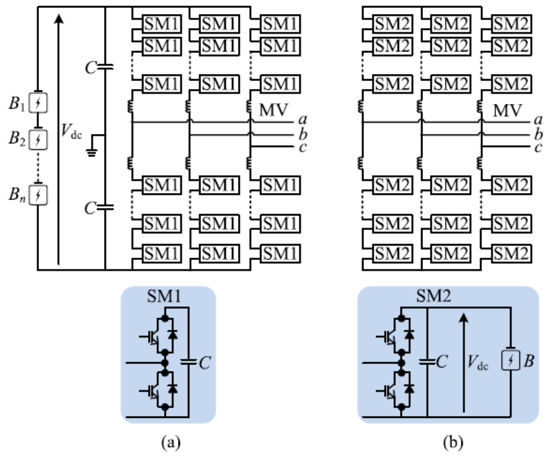

Figure 2.31 MMC converter and corresponding SMs (a) Centralized configuration (b) Distributed configuration [81].

NPC inverter was proposed in 1981 by Nabae, Takahashi, and Akagi which was basically a three-level diode clamped inverter [84][95]. In this topology, dc voltage is divided into several levels by connection a series of capacitors in a string allowing the capacitors to be recharged as a group. The main feature of the NPC converter is that all phase legs share a common dc-link bus that is subdivided by $(m-1)$ capacitors depending on output phase voltage level m which lessens the capacitance requirements. However, one disadvantage of the NPC is that due to average dc levels, the capacitors tend to overcharge or discharge hence requiring a charge-balance control for the capacitors [84][95]. The three-level NPC and active NPC (ANPC) converters are shown in Figure 2.32. Consequently, with an optimum switching state sequence and commutations, the loss among the devices can be well distributed granting higher utilization of semiconductor switch [84]. ANPC converter provides partial modularity and expanded redundancy. Thus, it is an efficient approach for direct coupling of high voltage batteries with reduced components of power electronics. However, due to the voltage variation of the batteries, it is necessary for the overrating of the power electronics switches [82].

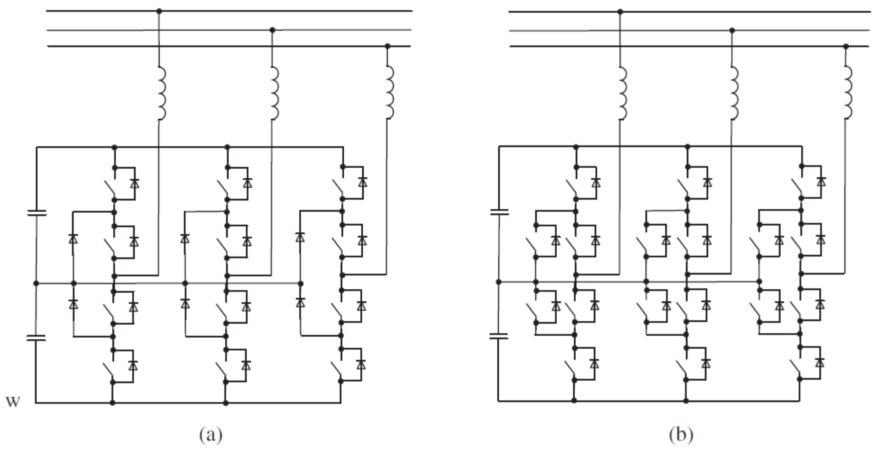

Figure 2.32 Three-level diode clamped inverters (a) NPC (b) ANPC [84][85].

The flying capacitor (FC) was introduced by Meynord and Foch as an alternative topology to the NPC [95]. Figure 2.33 shows the structure of a three-phase FC inverter which shows how capacitors are used to divide the dc side voltage compared to the clamping diodes in NPC inverter [84][95]. In contrary to the NPC inverters, it is not necessary for ON state switches to be in sequential series. Moreover, FC inverter has phase redundancies that balance the voltage levels of the capacitors. Another merit of FC inverter is that the real and reactive power flow can be controlled. However, the drawback of the FC is the complexity in tracking the voltage levels of all capacitors and recharging them at the same voltage level [95].

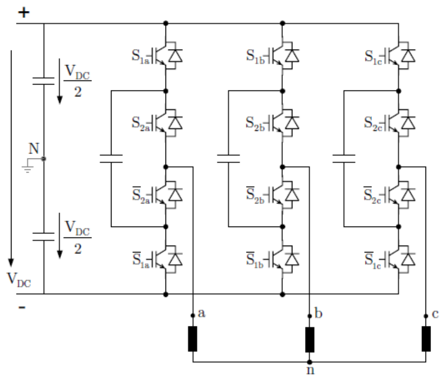

Figure 2.33 Three-level FC inverter [84][85].

2.3.3.4 Multiport Topologies

The conventional converter topologies are considered as two-port converters having ES port as the input and load port as the output. On the other hand, multiport topologies add more flexibility to the ESS allowing more independent ESs or multiple loads to be processed by the PCS simultaneously. Moreover, having multiple ESs to share a common dc bus is considered as more efficient approach than having the ES coupled at the ac grid. This approach can be applied in BESS providing redundancy by interfacing several independent battery strings [4][84]. Figure 2.34 presents three different configurations for connecting the multiple energy storage sources. Figure 2.34 (a) presents that the two ESs are connected in parallel coupling the common dc-link directly. This case is the uncontrolled configuration such that it is not possible to regulate the power flow of each element independently. In addition, the ESs should be in the same voltage range. Otherwise, voltage variations in the dc-links will appear due to variation in SOC between the ESs. The semi-controlled configuration shown in Figure 2.34 (b) has better controllability and also eliminates the current limiting impedances requirement by connecting DC-DC converter to ES1 in order to control the power flow and regulate the terminal voltage of ES1 as it is different from the voltages of ES2 and dc-link. Nevertheless, due to the variation in SOC of ES2, the variation in dc-link voltage remains. Lastly, the fully-controlled configuration is shown in Figure 2.34 (c). In this configuration, each ES is associated with DC-DC converter allowing for full controllability of the power flow and the voltage of each ES can be individually regulated. Thus, the issue of the voltage variation in the dc-link is resolved [81].

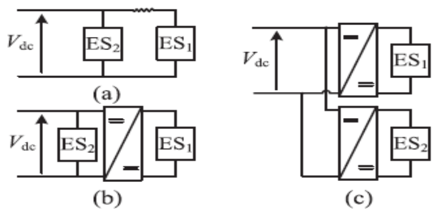

Figure 2.34 Typical connection configuration of multiple ESs: (a) Direct connected (b) Half controlled and (c) Fully controlled [81].

In [85], a comparison study was conducted between three-level NPC, three-level ANPC, three-level FC, and five-level CHB topologies based on efficiency, common mode voltage, and output redundancy in order to design a 5 MV converter for direction connection of a battery group to a 4.16 kV ac grid. The comparison was conducted by simulation studies based on commercially available modules. Space vector PWM modulation was used with level-shift for NPC and phase-shift for the other converters. Moreover, by using level-shift modulation in the NPC, the output line voltage is reduced to half of dc-link voltage, compared to the output line voltage of three-level FC and three-level ANPC, as shown in Figure 2.35. The filter sizes were also compared. The NPC topology requires the minimum size output filter such as 1230μH. Three-level ANPC topology requires an output filter of 3250μH and three-level FC topology requires an output filter of 1720μH. The common voltage in three-level NPC converter reaches up to the one third of dc link voltage compared to one-sixth of dc link voltage in case of three-level ANPC and three-level FC topologies. This result increases higher common mode current over switching dead times. Five-level CHB has a similar line voltage ripple to that of FC and ANPC converters. The five-level CHB exhibits higher output redundancy that results in the smallest output filter such as 980μH compared to the other converters. Figure 2.35 displays a bar graph comparing the loss distribution of the four converters for an average dc-link voltage. Accordingly, NPC is the most efficient one with 0.91% losses. The losses of the CHB and NPC converter are calculated as 0.93%. However, despite the small output filter, a large amount of gate drives and control signals is needed. FC converter has relatively low efficiency with 1.56% of losses due to the low power rating of its switches which apparently lead to relatively lower efficiency compared with the other topologies.

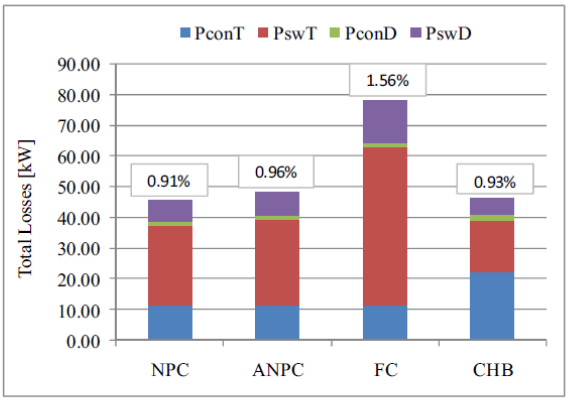

Figure 2.35 Converter loss distribution [85].

CHB and MMC converters were compared in [90] in terms of efficiency, voltage, and energy variations. The double-stage CHB including DC-DC converter (CHBDCDC) adds a DC-DC converter to the conventional CHB converter which changes the voltage variation in the modules. Both the CHB and CHBDCDC lack dc-link capacitors to deal with the energy variations. Hence, a frequency filter is essential in order to minimize the harmonic content of the battery current. In contrary to the MMLCHB that does not allow the generation of negative voltage in addition to the restriction on the battery voltage being twice higher than the maximum voltage, the MMLCFB uses full-bridge modules granting negative branch voltages and allowing the output voltage to be higher than half the dc-link voltage. Based on the simulation results of this study the CHB is a more feasible option in BESS implementation than the MMC having battery efficiency and requiring lower number of modules and semiconductor switches. In addition, it provides better battery manipulation. It can be seen from Figure 2.36 that CHB converter outperforms than MMC converters. CHB converter shows better performance than CHBDCDC, but the efficiency linearly decreases as the battery voltage variation increases. There is a point where CHBDCDC has better efficiency than CHB. Therefore, the utilization of CHBDCDC can be considered when a large variation in battery voltage is concerned. Moreover, the reduction of battery voltage variation by using CHBDCDC was proved in a laboratory experiment [90].

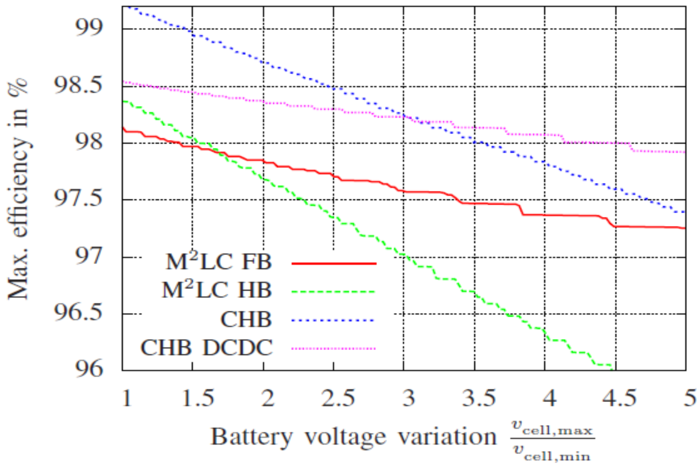

Figure 2.36 Maximum possible efficiency for real power application depending on battery voltage variance [90].

A more general comparison about efficiency and cost was conducted including two/three-level converters in a 22 kV grid-connected 30MW BESS application [81]. Figure 2.37 (a) presents a bar graph comparing the power loss of the different topologies at 0.8 pu power level. Moreover, this comparison was evaluated considering a continuous operation of BESS for load-leveling and peak shaving under intermittent RES generation. It can be noted from Figure 35 that two-level converters have the lowest efficiency as a result of increased switching frequency. In fact, most of the two-level converter losses come from the high frequency transformer. On the contrary, the three-level converter has relatively better efficiency and is slightly affected by the switching frequency increase. The MMC and CHB have the highest efficiencies among the other converters due to the low switching frequency. Accordingly, the CHB and MMC converters outperform the other configurations with better quality of output sinusoidal waveform and smaller filter requirements. MMC has 3% higher efficiency than CHB under heavy loads. Yet CHB outperforms MMC converter under light load conditions. It should be also noted how a high share of the power losses come from adding DC-DC converters, which can be considered as a reason for not including it in practical applications. Figure 2.37 (b) illustrates the cost evaluation of five different converter configurations with the CHB having the lowest cost compared to other converters. The high frequency transformer in the two-level converter serves 40% of the total cost which is saved in the CHB. Contrarily, MMC for its relatively bulk capacitance is the most expensive power conversion system [81].

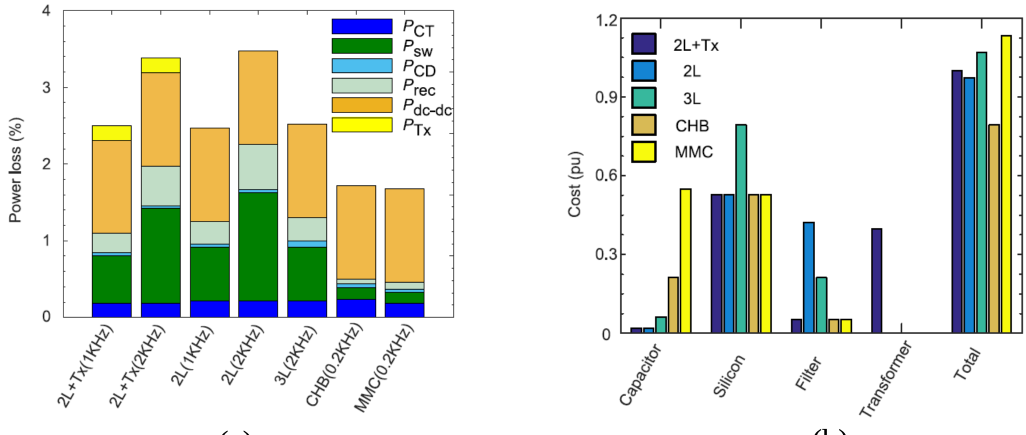

(a) (b)

Figure 2.37 General comparison of power electronic converters topologies for BESS operation (a) Power loss evaluation (b) Cost evaluation [81].

Multilevel power converter is a more favorable choice for designing large scale BESS as it provides more scalability in power and voltage with a smaller number of series battery connections. Excess amount of series connections can lead in reliability issues. There are many other approaches and designs that can be applied to design large scale BESS. For instance [96][97] propose series/parallel connected battery modules which are interfaced with a DC-DC converter and ac-dc converter to obtain higher voltage levels with high reliability. Reconfigurable battery packs utilize switches to reconfigure the battery cells connections in order to improve the battery performance and efficiency. In [98], a new modular reconfigurable battery pack is introduced which consists of single or several cascaded reconfigurable battery modules connected to a H-bridge converter. Each battery pack needs only one power electronic switch to charge and discharge the battery cells. Such a design allows better control over the battery cells and disconnects only the faulty cell without disrupting the BESS operation. Consequently, this design features fault-tolerance and high-reliability with least power switch requirements. A review on different kinds of reconfigurable battery techniques and designs are presented in [99]. Power blocks can be used as a means to minimize the size of the battery pack by splitting the battery modules among a smaller power block increasing the design reliability. In case of a battery cell failure, only the corresponding series string to the faulty cell are disconnected [100][101]. Another design is the intelligent battery pack which connects two MOSFETs to the battery cell or module: one in parallel and one in series. In case of fault in a particular cell or module, this strategy utilizes the set of

MOSFETs to bypass the faulty unit without disrupting the BESS operation [102][103]. Ref [40] compares between power block design, intelligent battery pack design, and CHB topology for large-scale BESS application rated at 11 kV and 1MWh. The designs were evaluated in terms of cell losses and the power electronic devices based on Markov-based modeling. It was concluded that intelligent battery pack and CHB designs are more favorable due to their fault-tolerant and built-in SOC capabilities. The cost of the protection device is a major factor in the assessment of the converter topology to be used in BESS integration. Some features of the protection measures in each topology are as follows: For the topologies that use a series connection of devices to attain high-voltage dc-link, a high voltage dc breaker is required. However, cheaper low-voltage dc breakers can be employed for the cascaded and two/three-level parallel connected converters. In cascaded topologies, the second harmonic oscillation in instantaneous power is a major issue that can be solved by employing large dc capacitors to absorb these harmonics. For parallel connected two/three-level converters, a significant amount of ac switchgear and bus bars are required to step up the ac voltage [81]. The main objective of adding an additional DC-DC stage is for better regulation of the batteries. However, there is a trade off in cost, efficiency, and battery safety when considering the addition of DC-DC stage in the system. The reason why the conventional converters are favored in industrial solutions is that in case that DC-DC stage is only needed for isolation purposes, the cost of the DC-DC converters will only by applicable to CHB and MMC converters. Low-order harmonics naturally occurs in CHB and MMC converters which can negatively affect both the life expectancy and safety of the batteries. Therefore, by employing DC-DC converters, the safety and life of the batteries can be preserved. As mentioned before, the battery technology plays a significant role in deciding the converter topology. An example of this is the Lithium-titante that has high tolerance to low order harmonics. So, the use of DC-DC converter is no more required for CHB, MMC as well as other converters. Another example is the usage of CHB configuration for flow batteries. Since, flow battery has high capacity compared to other batteries, it is difficult to distribute the flow battery among the CHB cells [81].

2.3.4 Filter and Transformer

A filter is usually the combination of L and C components used to mitigate the harmonics associated with high frequency switching in power converters. The filter can be connected to the input, output, or both side of the power converters. In a BESS application, as the simplest case, a single choke inductor connected with a resistance, or an advanced type such as LCL filter can be arranged. On the other hand, a transformer is essential for grid-connected BESS applications to step-up or step-down the voltage level of the BESS output. The transformer sizing and rating depend on the scale of the BESS and the topology of the power electronic converters being used. The transformer is usually required for two or three level converters. But in case when multilevel converters are utilized, a transformer connection is not generally necessary, as higher voltage level can be attained at the converter output. Also, with the use of multilevel converter topology in BESS applications, the transformer rating and size can be reduced to couple with MV networks, hence the costs are reduced.

2.4 PCS Operation and Control

In this study, double-stage PCS is considered to interface the BESS with the distribution grid, CHB is chosen to provide bidirectional dc/ac conversion between the BESS and the grid which includes a non-isolated bi-directional buck-boost half-bridge converter is connected to each H-bridge module to obtain higher voltage levels and regulate the charging and discharging of the batteries. Thus, only the operation and control of related to the aforementioned topologies will be discussed in this subsection.

2.4.1 Bi-directional DC-DC Converter Operation and Control

As mentioned before, the main objective of the DC-DC converter is to buck and boost the voltage at the dc-link and regulate the charging and discharging processes of the batteries. This converter is depicted in Figure 2.38. It is comprised of two power switches with anti-parallel diodes, a dc-link capacitor to reduce the voltage ripples at the dc-link, and an inductor at the storage side. This converter is capable of operating in two modes depending on the system power flow and the switching states. It can either operate in buck or in boost mode. As shown in Figure 2.39, when the converter is operating in buck mode, the power flow direction goes toward the battery while switch S1 is ON and S2 is OFF in the first period permitting the power flow. But on the second period, both S1 and S2 is OFF and the current flows in a closed circuit. On the other hand, as shown in Figure 2.40, when the battery discharges (Boost mode) and the power flow is to the direction of the load or grid, switch S2 will be ON while S1 is OFF allowing the current to flow in closed circuit passing through the inductor as the inductor is charged. In the second period when both S1 and S2 is OFF, the current flows towards the load while releasing the energy stored in the inductor simultaneously with the battery which in turn results in higher capacitor voltage at the output. The control of the DC-DC converter switches is achieved by controlling the duty cycle d which can be expressed in Equation (2.28). The duty cycle d is the ratio of the ON time (T_{ON}) over the total switching cycle (T_S). Since S1 and S2 cannot be both ON simultaneously, the duty cycle for each switch must be the complementary of the other one. There are many approaches available in the literature to control the buck-boost DC-DC converters. The most common control approach is the cascaded PI control scheme as shown in Figure 2.41. This approach consists of two control loops: an inner control loop that controls the inductor current and generates the duty cycle values that later modulate through PWM, and an outer loop that controls the dc-link voltage. Usually, the inner loop is five to ten times faster than the outer loop to deny any kind of noise or disturbance before it influences the outer voltage loop. This approach was applied in [104] for controlling bidirectional DC-DC converter in two-stage BESS and further improved in [105] by adding a feed forward controller to minimize the voltage fluctuations at the dc-link capacitor. Other approaches such as non-linear control was applied in [106-109] by using exact ES-FBL to regulate different DC-DC converters. Based on these studies, a non-linear model of the bidirectional DC-DC converter will be introduced in Chapter 3 which is controlled by ES-FBL control scheme.

$$d = \frac{T_{ON}}{T_s} \tag{2.28}$$

The PWM scheme compares a low-frequency reference signal with a high-frequency carrier signal, being usually a sawtooth or a ramp signal. With this comparison, switching pulses (logic 1 or logic 0) are produced as shown in Figure 2.42. $V_{control}$

and $\hat{V}_s$ is the control voltage and the peak of the carrier sawtooth waveform, respectively. The frequency of the carrier signal determines the switching frequency of the semiconductors. For buck-boost converters, the duty cycle d can be expressed as a function of the output voltage (V_{out}) and input voltage (V_{in}) as follows:

$$\frac{V_{out}}{V_{in}} = \frac{D}{(1-D)} \tag{2.29}$$

In case of bidirectional DC-DC converter, d of each switch is the complementary of the other one in such a way that only a single switch is in ON state while the other is OFF.

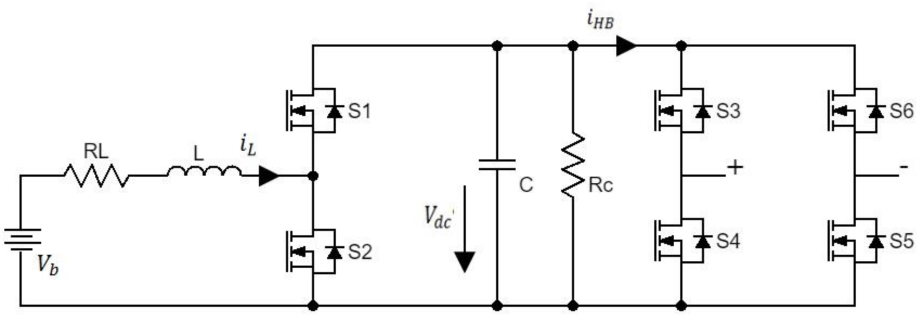

Figure 2.38 Bidirectional DC-DC converter connected to CHB cell.

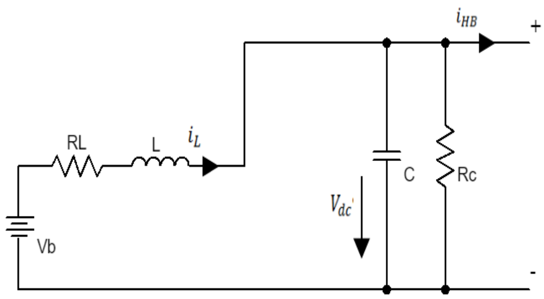

Figure 2.39 Bi-directional DC-DC converter equivalent circuit in buck mode.

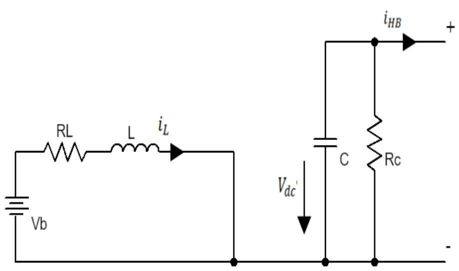

Figure 2.40 Bi-directional DC-DC converter equivalent circuit in boost mode.

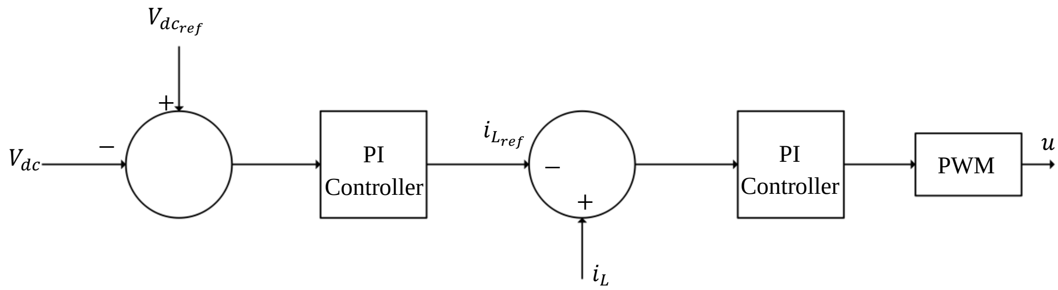

Figure 2.41 Cascaded PI controller.

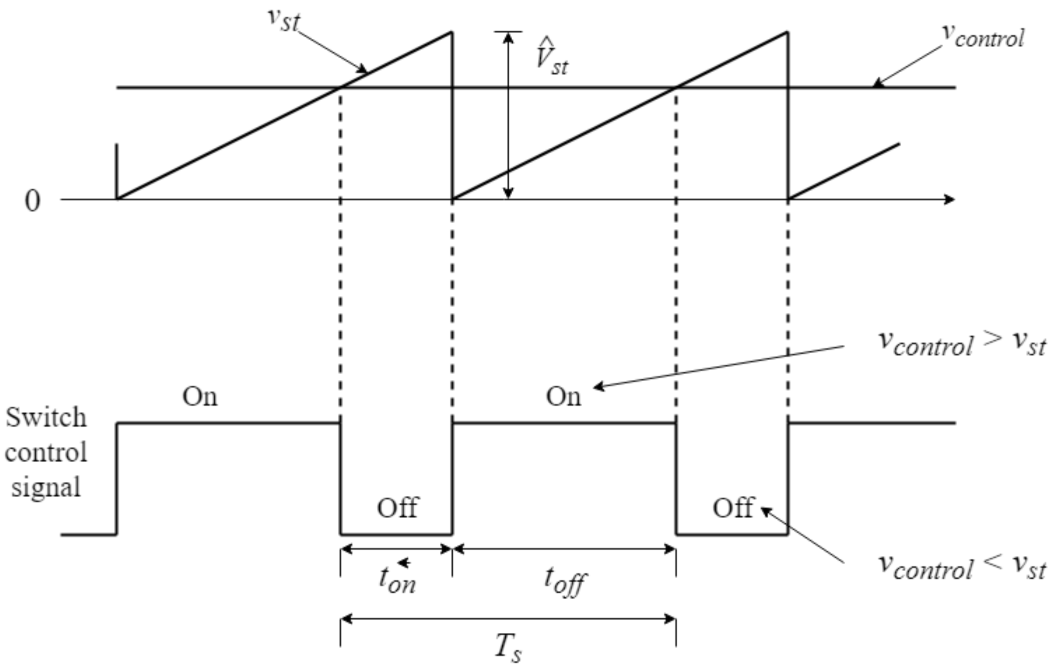

Figure 2.42 The switching pulse generation of PWM scheme [110].

2.4.2 CHB Operation and Control

2.4.2.1 CHB Principle of Operation

CHB has gained much attraction from researchers especially for MV applications due to its ability to accumulate different voltage levels and operate in both directions of power flow (both inverter and rectifier operation) with low harmonic distortion. This type of multilevel inverters is practical and deems to be useful for ESS such as batteries or SC. The CHB structure mitigates the number of series connected batteries, since each H-bridge SM is connected to a dc-source such as battery to accumulate the voltage. Thus, in case of a fault at the dc-source, the system will not cease its operation but rather bypass the faulty SM that contains the faulty dc-source.

The number of voltage levels n at the output of a CHB converter is related to the number of SM's N and expressed in Equation (2.30). Also, the level number l of line voltage in three-phase configuration can be expressed in Equation (2.31);

$$n = 2N + 1 \tag{2.30}$$

$$l = 2n - 1 \tag{2.31}$$

As shown in Figure 2.43, each converter cell contains a four-switch H-bridge inverter connected to a dc-link capacitor and a bidirectional DC-DC converter that is connected to a battery bank or ES device on the on other end. A single H-bridge converter can generate the output voltage as $+V_o$, $-V_o$, and 0. The output of the CHB is the peak ac phase voltage which is the summation of the dc-link voltage of each H-bridge cell and can be expressed in Equation (2.32) when the losses of the switching devices are negligible [95].

$$V_o = V_{dc1}S_1 + V_{dc2}S_2 + \cdots + V_{dcj}S_j \tag{2.32}$$

$$V_o = \sum_{j=1}^{N} V_{dcj}\, S_j$$

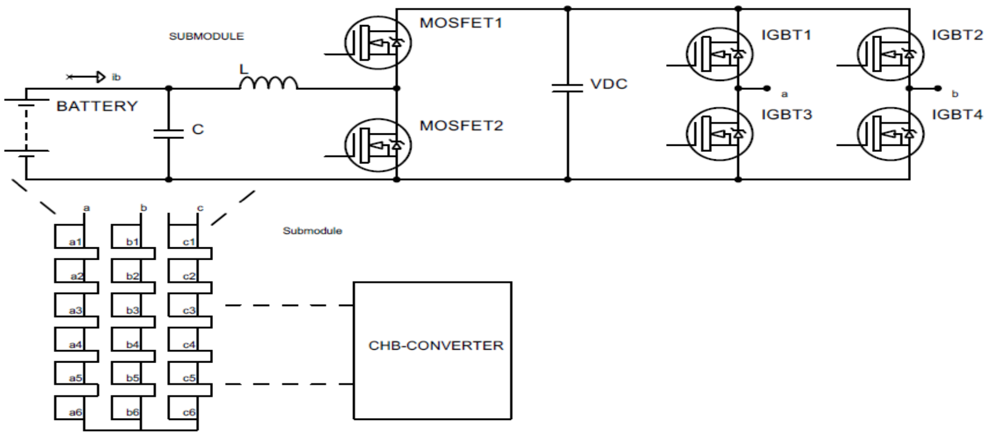

Figure 2.43 CHB cell.

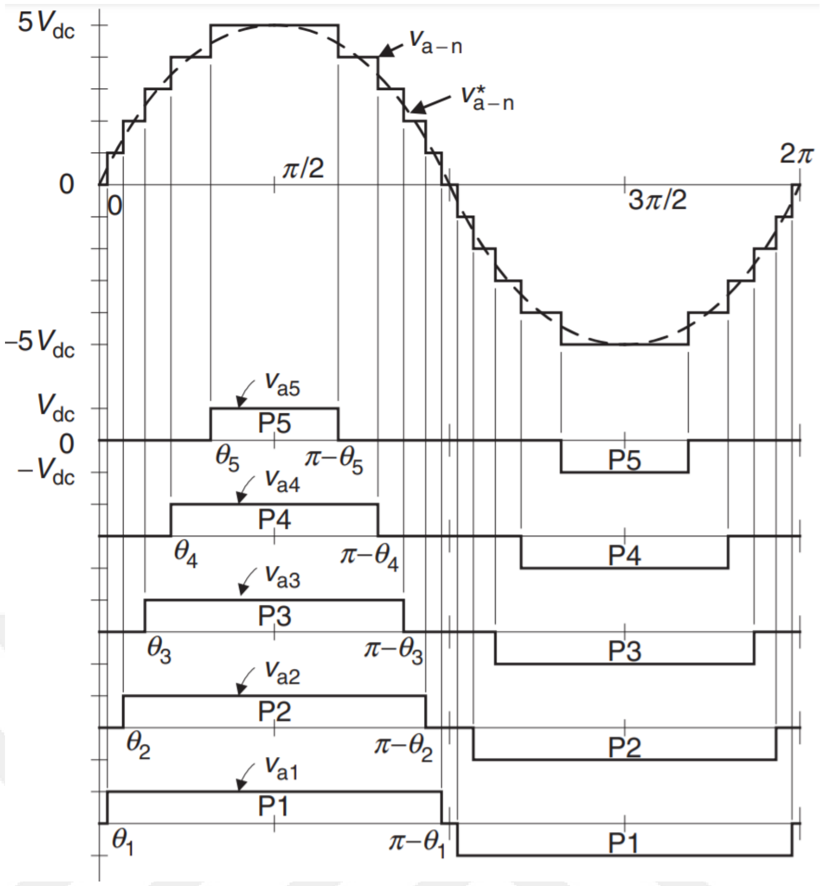

Figure 2.44 Stepped staircase waveform of a 11-level CHB [95].

An example of the output voltage waveform of 11-level CHB can be seen in Figure 2.44. Such a waveform is called "stepped staircase waveform" as each step represents a unique voltage level. The Fourier transform of such waveform and the magnitudes of the Fourier coefficients when normalized with respect to V_{dc} are demonstrated in Equations (2.33) and (2.34), respectively.

$$V(wt) = \frac{4V_{dc}}{\pi}\sum_{n}[\cos(n\theta_1 + \cos n\theta_2 + \cdots + \cos\theta_n] * \frac{\sin(wt)}{n}, n = 1,3,5,7 \quad (2.33)$$

$$H(n) = \frac{4}{\pi n}[\cos(n\theta_1 + \cos n\theta_2 + \cdots + \cos n\theta_s] * \frac{\sin(wt)}{n}, n = 1,3,5,7 \quad (2.34)$$

where $\theta_1, \theta_2, \ldots, \theta_n$ is called the "conditioning angle" which are chosen to keep a minimum total harmonic distortion (THD) of the voltage commonly chosen to eliminate lower frequency harmonics such as 5, 7, 11, and 13, it can also be noted that CHB output voltage does not exhibit even harmonics. w is the angular frequency, V_{dc} is the output voltage, and n is the harmonic order. In three-phase systems, the output of each CHB phase can be connected either in delta or star configuration. Accordingly, the line voltage can be expressed as the difference between two phase voltages as follows:

$$V_{ab} = V_{an} - V_{bn} \tag{2.35}$$

where V_{ab} is the line-to-line (line) voltage, V_{an} and V_{bn} is the line-to-neutral voltage of phase-A and phase-B, respectively. The benefits of three-phase CHB converter are that all triplen harmonic components in the line voltage are eliminated [111]. The following three voltages can be obtained from a single H-bridge cell such as $+V_o$, $-V_o$, and 0, which depend on the ON/OFF states of the switches at the given time. The CHB converter is able to generate multilevel voltages by a cascaded connection of multiple H-bridge SMs and control each cell switch individually to regulate the output voltage. For each H-bridge, a pair of switches is turned ON and OFF simultaneously to provide a unique voltage output. The Boolean state of each switch can be either logic 1 (ON) or logic 0 (OFF). When the H-bridge operates in forward direction to produce $+V_o$ positive voltage, the switches T1 and T4 is ON simultaneously as depicted in Figure 2.45. On the other hand, when the H-bridge operates in reverse direction, the negative voltage $-V_o$ is obtained when both switches T2 and T3 are ON at the same time. However, zero voltage level can be obtained when either T1 and T2 or T3 and T4 are ON.

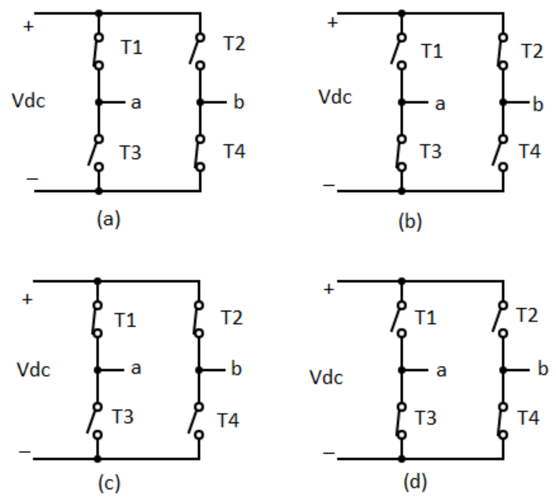

Figure 2.45 H-bridge inverter switching states.

Consequently, higher voltage levels can be obtained by controlling the switch positions of each SM connected in the CHB inverter. For example, a 11-level CHB has five SMs by controlling the states of the switches. So, a total of 11 voltage levels can be attained as depicted in Figure 2.44. The switching states of the 11-level CHB inverter are shown in Table 2.3. Generally, CHB topology can be operated either as symmetrical or asymmetrical which means that the dc-source voltage in each SM can be either equal or unequal, respectively. In the pre-mentioned explanation and examples, the symmetrical topology is considered in which the dc-sources are assumed to be equal in each SM. However, in asymmetrical topology, unequal dc-sources are used in each SM which provides higher voltage levels with less semiconductor requirements compared to the symmetrical operation [112]. However, utilizing asymmetrical topology in a BESS means that the battery bank in each CHB cell will be unequal which can result in discrepancies for the charging/discharging of each battery bank and will eventually lead to variations in the internal resistances between the batteries that can finally cause SOC imbalance.

Table 2.3 Switching states for 11-level CHB converter.

Switching states required	**Output voltage**
All SMs with $(S1, S4)_n$ must be ON	+5V
Four SMs with $(S1, S4)_n$ must be ON	+4V
Three SMs with $(S1, S4)_n$ must be ON	+3V
Two SMs with $(S1, S4)_n$ must be ON	+2V
One SM with $(S1, S4)_n$ must be ON	+V
All SMs with $(S1, S2)_n$ OR $(S3, S4)_n$ must be ON	0
Single SM with $(S2, S3)_n$ must be ON	-V
Two SMs with $(S2, S3)_n$ must be ON	-2V
Three SMs with $(S2, S3)_n$ must be ON	-3V
Four SMs with $(S2, S3)_n$ must be ON	-4V
All SMs with $(S2, S3)_n$ must be ON	-5V

To keep the battery parameters is difficult and requires complex control algorithms. The highest voltage level m that can be attained with unequal dc sources CHB can be given by

$$m = 3^n \tag{2.36}$$

where n is the number H-bridge cells. The number of the switching devices N_{sw} either in symmetrical or asymmetrical operation can be calculated as follows:

$$N_{sw} = 4n \quad (2.37)$$

Equation (2.38) can be used to express the maximum output voltage $V_{o,max}$ of CHB converter with unequal dc-sources by excluding the zero-level voltage and divide by two for the negative voltage, given as follows:

$$V_{o,max} = \left(\frac{3^n - 1}{2}\right) V_{dc} \quad (2.38)$$

The functionality of the batteries in the BESS in different kinds of systems can be controlled with different types of control strategies such as voltage-oriented control that decouples the components in *dq0* rotating reference frame. This control scheme controls both active power P and reactive power Q, respectively. Hysteresis control scheme is also available which controls the load current within a defined hysteresis band [113].

2.4.2.2 PCS Control

Simply, the control of the CHB or any PCS in general is the control of the power transfer between the ES and the grid while meeting the grid or network regulations. There are many control schemes to control the PCS interfacing with the grid. One of the most popular control strategies is the direct power control. As the name suggests, this control strategy grants direct control over active and reactive power by creating an optimum switching table from the instantaneous errors between active and reactive power references and their corresponding measured values [114]. Vector oriented control scheme is another control scheme that is vastly used in the literature. In this control strategy, three-phase quantities are transformed from the stationary frame to the synchronously rotating dq0 reference frame to simplify the computations and grant a straighter forward control over active (d-axis) and reactive (q-axis) components. Additionally, with this transformation, independent control of active and reactive power is possible by independently regulating the (d-axis) and (q-axis) current respectively. The block diagram of this control scheme is illustrated in

Figure 2.47. As seen, PI controllers are used to control the *d* and *q*-axis current components to generate the reference signal. Then, both of these signals are used to generate the switching signals of the semiconductors through PWM scheme. The grid phase angle has to be tracked in order to achieve synchronization between the power converter and the grid, A typical approach for synchronizing utility networks and grid-connected power electronics converters is the phase-locked loop (PLL). In such applications, the PLL's role is critical in detecting the utility phase angle accurately and quickly enough to provide the grid-connected inverter's reference signal. The common method to realize PLL on three-phase system is by using synchronous frame PLL. The block diagram of synchronous frame PLL is shown in Figure 2.46 The instantaneous phase angle θ is detected by synchronizing the reference frame with the three-phase voltage vector (v_a, v_b, and v_c). To be locked to the phase angle of utility voltage vector, the Proportional–Integral (PI) controller drives v_q to be zero, as given by the reference $v_q{}^*$which gives the angular speed quantities. Finally phase angle θ can be simply derived by integrating the angular velocity [148].

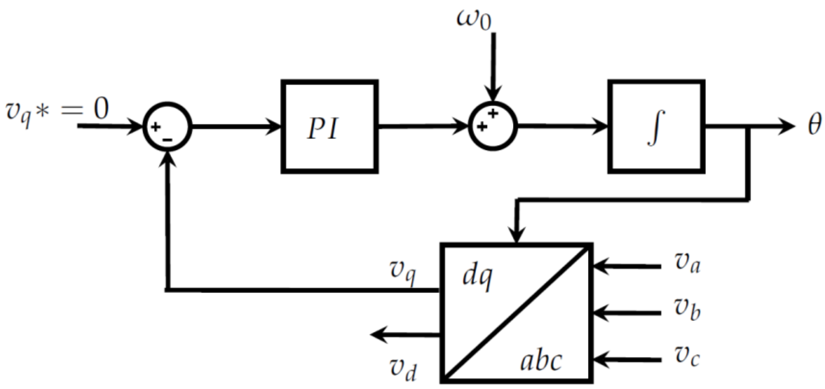

Figure 2.46 Phase-Locked Loop (PLL) block diagram [148].

Considering the CHB-BESS shown in Figure 2.47, an expression can be derived to define the voltage and current expressions as follows:

$$V_{abc} = V_{iabc} - L_f \frac{di_{abc}}{dt} - R_f i_{abc} \quad (2.39)$$

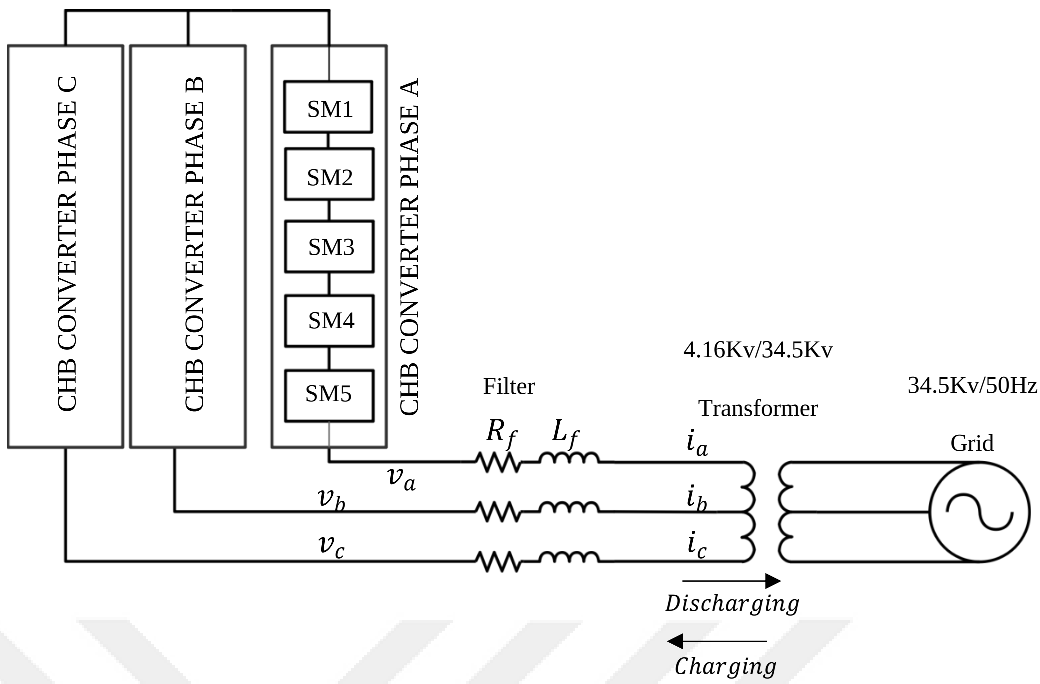

Figure 2.47 Grid connected 11 level CHB based BESS circuit diagram

where V_{abc} is the line-to-neutral grid voltage, V_{iabc} is the line-to-neutral inverter output voltage, L_f and R_f is the filter inductance and resistance, and i_{abc} is the phase current. In order to apply vector current control scheme to the system, Equation (2.39) has to be transformed into the synchronous rotating *dq0* reference frame by using Park Transformation, as follows [115]:

$$\begin{bmatrix} x_d \\ x_q \\ x_0 \end{bmatrix} = \frac{2}{3} \begin{bmatrix} \cos\theta & \cos(\theta - \frac{2\pi}{3}) & \cos(\theta + \frac{2\pi}{3}) \\ -\sin\theta & -\sin(\theta - \frac{2\pi}{3}) & -\sin(\theta + \frac{2\pi}{3}) \\ \frac{1}{2} & \frac{1}{2} & \frac{1}{2} \end{bmatrix} \begin{bmatrix} x_a \\ x_b \\ x_c \end{bmatrix} \tag{2.40}$$

Then the following decoupled equations are obtained as follows:

$$V_d = V_{i_d} + L_f \omega i_q - R_f i_d - L_f \frac{di_d}{dt} \tag{2.41}$$

$$V_q = V_{i_q} - L_f \omega i_d - R_f i_q - L_f \frac{di_q}{dt} \tag{2.42}$$

where V_d and V_q represents the *dq* components of the grid voltage, i_d and i_q are the dq currents, and ω is the angular frequency. After transforming the system to the rotating dq0 reference frame, as the currents are decoupled into *d*-axis and *q*-axis components, the control of the active and reactive power is simplified. The instantaneous powers can be calculated in *dq0* reference frame as follows:

$$P = \frac{3}{2}\left(V_d i_d + V_q i_q\right) \tag{2.43}$$

$$Q = \frac{3}{2}\left(V_q i_d - V_d i_q\right) \tag{2.44}$$

By aligning V_d on the grid reference voltage vector, V_q becomes zero and the power equations are simplified as follows:

$$P = \frac{3}{2} V_d i_d \tag{2.45}$$

$$Q = -\frac{3}{2} V_d i_q \tag{2.46}$$

With this way, P and Q, respectively, can be controlled independently by i_d and i_q. Consequently, the reference values of *d*-axis and *q*-axis current components ($i_d{}^*, i_q{}^*$) can be calculated using active and reactive power reference values (P^*, Q^*) as follows:

$$i_d^* = \frac{2P^*}{3V_d} \tag{2.47}$$

$$i_q^* = -\frac{2Q^*}{3V_d} \tag{2.48}$$

As shown in Figure 2.48, each reference current component and its corresponding measured counterpart is compared and regulated via PI controller. The output of the PI controller is added to the feedforward terms given in Equations (2.41) and (2.42) to generate the reference voltage signals that will be later used to manage the PWM scheme to generate the firing pulses for the switching devices.

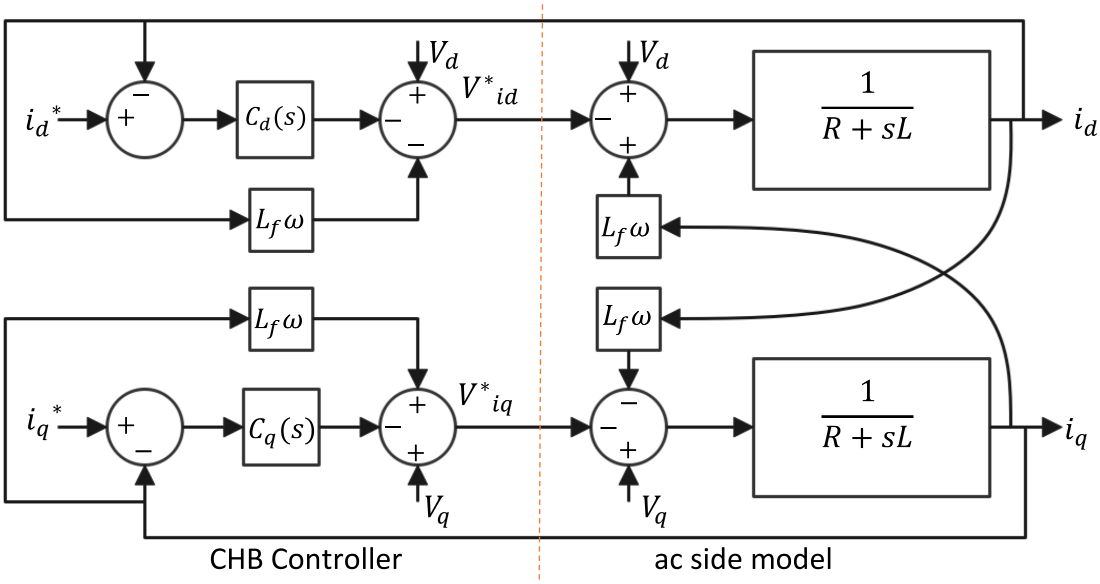

Figure 2.48 Decoupled current control scheme and ac side mathematical model.

From control theory perspective, the transfer function of each PI controller (C_d, C_q) can be expressed as follows:

$$C_d = C_q = \frac{k_p s + k_i}{s} = k_p\left(\frac{1+Ts}{Ts}\right) \tag{2.49}$$

where k_p and k_i is defined as the proportional gain and integral gain, respectively, and $Ts = \frac{K_p}{K_i}$ is the time constant. The CHB-BESS can be modeled as an ideal voltage source with a time delay equals half of the switching cycle due to the fact that in order to generate the PWM signals, the reference and carrier waves are compared. This process depends on the current value and a slight error could result in a delay in the system that could be as significant as one switching cycle. Thus, the average value of half the switching cycle is used as follows:

$$G_{PWM}(s) = \frac{1}{1+sT_d} \tag{2.50}$$

where $T_d = \frac{T_s}{2}$ is defined as the averaged time delay. The system given in Equations (2.41) and (2.42) is modeled in synchronous rotating *dq0* frame that reflects the behavior of multi-input/multi-output nonlinear coupled system. Hence, it is difficult to obtain decoupling with conventional linear control strategy. The terms associated with the angular frequency $L_f \omega i_d$ and $L_f \omega i_q$ provide cross-coupling for both axes. These terms can be considered as disturbance and the whole system can be split into two parts: a current compensating part and a voltage feed-forward compensating part that can be rewritten as follows:

$$V_{i_d} \underbrace{= V_d - L_f \omega i_q}_{feedforward\ compensating\ term} + \underbrace{R_f i_d + L_f \frac{di_d}{dt}}_{current\ compensating\ term} \quad (2.51)$$

$$V_{i_q} = \underbrace{V_q + L_f \omega i_d}_{feedforward\ compensating\ term} + \underbrace{R_f i_q + L_f \frac{di_q}{dt}}_{current\ compensating\ term} \quad (2.52)$$

Once the inverter voltage for both *d* and *q* axes are cross-coupled, as voltage feedforward term is disregarded as disturbance, the system is rewritten as follows:

$$V_{i_d} = R_f i_d + L_f \frac{di_d}{dt} \quad (2.53)$$

$$V_{i_q} = R_f i_q + L_f \frac{di_q}{dt} \quad (2.54)$$

By applying Laplace transform to Equations (2.52) and (2.53), the equations become:

$$V_{i_d}(s) = sL_f I_d(s) + R_f I_d(s) \quad (2.55)$$

$$V_{i_q}(s) = sL_f I_q(s) + R_f I_q(s) \quad (2.56)$$

Now, the system is successfully decoupled and each current component can be independently controlled. Then, the transfer function can be obtained as follows:

$$G_{filter}(S) = \frac{I_q(s)}{V_{i_d}(s)} = \frac{I_d(s)}{V_{i_q}(s)} = \frac{1}{R_f}\left(\frac{1}{1+s\tau}\right) \quad (2.57)$$

where $\tau = \frac{L_f}{R_f}$ is the time constant. There are various modulation techniques available for CHB based inverters. The modulation techniques used for CHB can be classified into fundamental frequency switching techniques such as space vector control and selective harmonic elimination control), and high-switching frequency PWM such as space-vector PWM, selective harmonic elimination PWM, and sinusoidal pulse width modulation (SPWM) [95]. The SPWM is the most commonly used modulation strategy to generate the switching patterns due to its high efficiency and simple implementation compared to other techniques. Also, it can easily eliminate lower order harmonics [116]. The basic principle of SPWM is that a reference signal usually a sinusoidal modulating waveform is compared with a carrier waveform usually a triangular wave. By comparing these wo waveforms, the firing signals for the semiconductor switches are generated. A multi-carrier SPWM technique can be categorized as follows:

1- Phase-shifted SPWM
2- Level-shifted SPWM
3- Hybrid SPWM

The modulation index m, amplitude modulation index m_a, and the frequency modulation index m_f can be defined as follows:

$$m = \frac{V_{ref}}{\sum_{n=1}^{N} V_{dc}} \quad (2.58)$$

$$m_a = \frac{V_m}{V_{cr}} \quad (2.59)$$

$$m_f = \frac{f_{cr}}{f_m} \quad (2.60)$$

The modulation index m is defined as the ration between the amplitude of the modulation signal to the measured signal in the converter that is later compared with $(n-1)$ carrier waves to generate $2(n-1)$ firing pulses that drives the CHB switches. The amplitude modulation index m_a is defined as the ratio of the peak voltage of the modulating wave V_m to the peak value of V_{cr} of the carrier wave. The frequency modulation index m_f it is the ratio of the carrier wave to the fundamental frequency of the modulating wave [95][116]. In phase-shifted SPWM, each adjacent carrier wave is phase shifted from another one by a ratio of $\emptyset = \frac{360}{n-1}$, where n is the level count. However, the amplitude and frequency of all carrier waves are the same. An illustrated example of a five-level CHB carrier waves are shown in Figure 2.49. Each carrier wave is shifted by 90°.

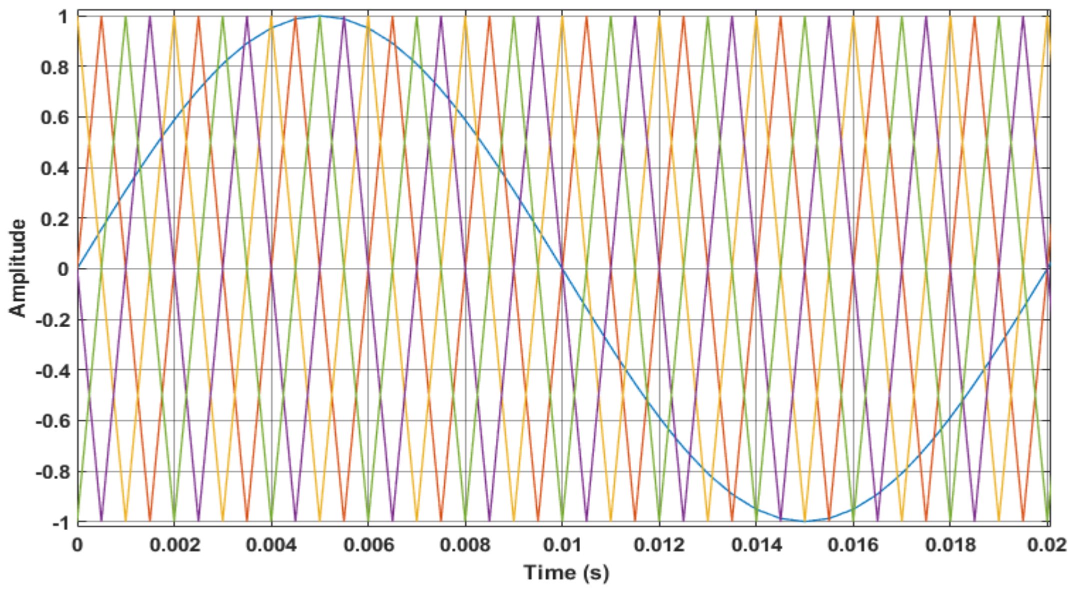

Figure 2.49 Phase-shift SPWM.

The level-shifted SPWM modulation scheme is classified as:

1- In-phase disposition
2- Phase opposition disposition
3- Alternate phase opposition disposition

In-phase disposition SPWM scheme is well-suited for CHB inverter due to its lower harmonic distortion at high modulation indices compared with the other SPWM techniques. In this method, all amplitudes and frequency are same for all carrier waves with no phase shift between them. However, the carrier waves start at different offset values. The orientation of the carrier waves in-phase disposition SPWM is shown in Figure 2.50. A comprehensive hybrid SPWM modulation scheme that combines phase-shift and level-shift modulation schemes is presented in [116]. This is achieved by applying phase shift between all carrier waves while assigning different offset for each individual carrier wave. The hybrid SPWM demonstrated low THD at the output voltage compared to other modulation schemes.

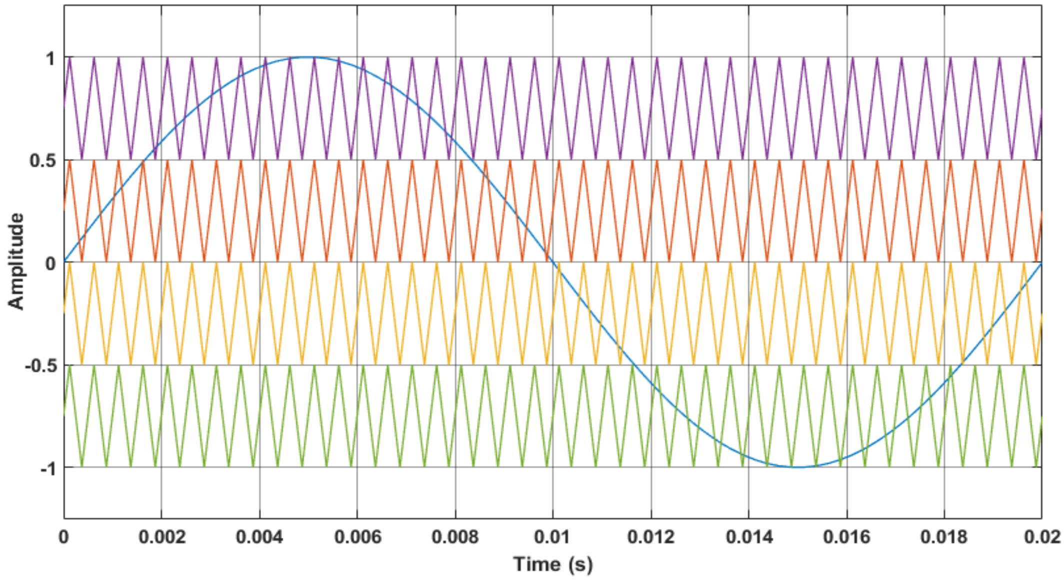

Figure 2.50 Level-shifted in-phase disposition SPWM.

2.4.2.3 CHB SOC Balance

The previously mentioned modulation methods cause SOC imbalance during operation due to uneven distribution of power among the CHB SMs. Even with even distribution, SOC imbalance is inevitable due to other factors such as aging, parameters variation, switching losses, and manufacturing diversity. Therefore, a balancing algorithm is essential in order to ensure SOC balance between ES units to realize optimum capacity utilization and improve the reliability of the system. The key principle of SOC balancing algorithms is to balance the power distribution in the CHB cells. The CHB balancing methods is divided into phase-to-phase balancing schemes which aim to equalize the average SOC of each CHB leg, and in-phase balancing that balances the SOC of all CHB cells inside single phase or branch. For phase-to-phase balancing, the most common approach for CHB based BESS is clustered balancing. The main concept of this strategy is to maintain an equal average SOC values between all phases by injecting zero sequence voltage to the reference voltage of each phase. This adds more power to the phases with less SOC until all phases are balanced [117][118][119]. Ref [120] achieves phase-to-phase balancing in a different way by adding a six-switch balancing circuit embedded with a battery unit to the neutral point of the hybrid-CHB to interchange power between phases until all phases are balanced. The main aim of in-phase SOC balancing algorithms is to achieve SOC balance between all CHB cells inside an individual phase. For in-phase SOC balancing, the balancing algorithms depends on the modulation method used. A common SOC balancing strategy for level-shifted PWM is reconfiguration of carrier waves by rearranging the carrier wave offset in such a way that the cells with the highest SOC will have lower offset to discharge more power while cells with lower SOC set at higher offset to discharge less power. The exact opposite is applicable in case of charging where cells with higher SOC is set at higher offsets compared to lower SOC cells. This strategy is further improved by proposing a modulation range instead of fixed offset. This includes the battery voltage variation related to the open circuit SOC relation allowing for better balancing even if different batteries in the CHB cells are considered without the need of any dc-link voltage balancing [121]. Both in-phase and phase-to-phase SOC balancing in CHB induce no losses in energy since it is achieved without any external circuits or additional hardware.

2.5 BESS Operation and Control

In order to exchange power with the grid, BESS is equipped with power electronic converters as current controlled devices while synchronizing the current phasor with the phase angle of the grid voltage. Grid-tied BESS is modeled based on the control mode used to control the interfaced power electronic converter which can be classified into either grid-following mode or grid-forming mode. In grid-following mode, the PCS behaves as current source that exchanges active and reactive power with the grid based on predetermined power and current references. The majority of today's converters adopt grid-following mode. This control mode uses PLL to keep the track of grid voltage phase-angle in order to synchronize with the grid. However, grid-following based converters are limited to grid-tied mode and cannot be utilized for islanded operation. In grid-forming mode, the converter is modeled as ac voltage source that behaves like a synchronous generator. The main differences between the two modes are that grid-forming has the ability to regulate both voltage and frequency in islanded and grid-tied operations and its synchronization method is mostly related to the concept of active power transfer and swing equation [122][123]. The CHB-BESS considered in this thesis adopts grid-following mode in such a way that the active and reactive power imported and exported from the BESS are managed by controlling the converter current components using vector control which is previously discussed. During charging operation, CHB consumes a predetermined value of active or reactive power from the grid by modifying the phase angle and modulation index of the voltage reference signal. Each battery unit charges with a predefined set-point dependent on total active/reactive power set-point divided by the number of operating CHB cells at the time. Meanwhile, the voltage and energy at the dc-link rises during charging. Hence, by adding DC-DC converter to the dc-side, the voltage at the dc-link capacitor can be maintained by transferring energy at the dc-link to the battery units. Similarly, when the BESS is discharging the CHB injects power to the grid by modifying the reference voltage modulation index and phase and angle, and each battery bank discharge rate is dependent on the predetermined active/reactive power set points and the operating CHB cells. During discharging, the voltage at the dc-link is maintained by transferring energy from the battery into the dc-link capacitor. The CHB based BESS structure and its control scheme proposed in this thesis are illustrated in Figure 2.51. Observably, PI controllers are adopted for controlling the current loops at the point of common coupling (PCC) while the exact state feedback linearization (ES-FBL) method is used to regulate the DC-DC converter which will be discussed in the next chapter.

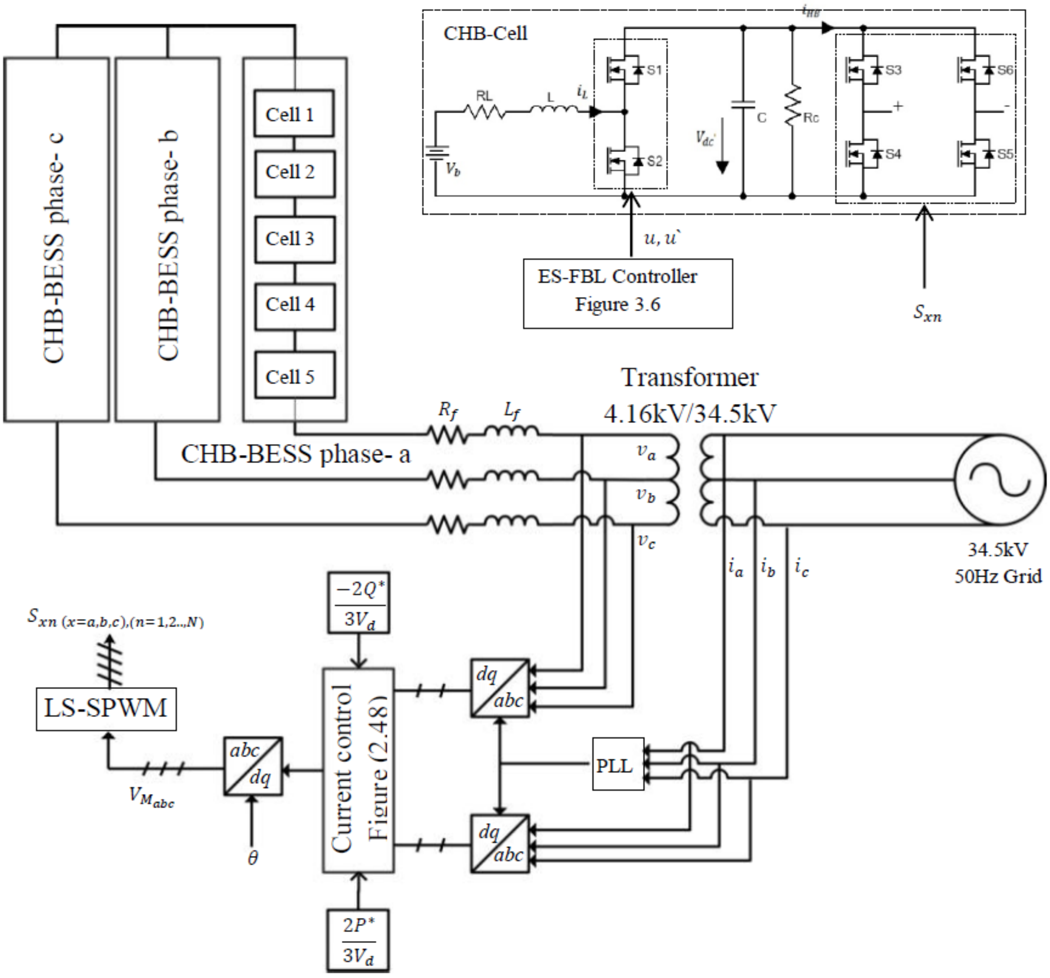

Figure 2.51 BESS-CHB structure and its control scheme proposed in the thesis.

2.6 BESS Cost Assessment and Analysis

The cost of BESS has witnessed great decline over the past three decades as the prices of Li-ion batteries has dropped 90% of its original price since its commercialization three decades ago. The price of Li-ion is on a falling trend as shown in Figure 2.52. Since, Li-ion battery technology continues to mature and the adoption of Li-ion batteries for energy storage increases day by day [143].

Figure 2.52 Li-ion cost over the past decade [143].

It is necessary to make a cost analysis study before proceeding to implement any ESS in order to acquire the most benefits and profits out of the ESS and avoid any financial losses. As shown in Figure 2.53, the costs of an ESS can be categorized into ESS capital costs, operating and maintenance costs, decommissioning costs, and performance metrics. A general cost model describing the annual life-cycle costs C_{LC} ($/Kw-yr) of ESS can be derived as follows:

$$C_{LC} = C_I + C_{O\&M} + C_R + C_{EoL} \tag{2.61}$$

where C_I is the capital cost which includes the capital costs of the storage units such as battery modules, PCS such as inverters, DC-DC converters, and etc, and the balance of plant components such as transformers, cables, protection, cooling system, and other related components. $C_{O\&M}$ weights the costs related to all the operation and maintenance performed throughout the lifetime of the ESS including replacement parts, labor, warranty and insurance costs and other relevant costs. C_R weights the costs of estimated replacement for the components that wear over time due to aging effects. C_{EoL} represents the costs of storage end life including the costs of recycling/disposal, disassembly/removal, and the costs of disconnection from the grid [6]. Considering the detailed cost assessment and analysis illustrated in Figure 2.53, the total installation cost can be estimated as 1793 $/kW and 448 $/kWh for an installation of 1 MW power capacity operated over 4 hours. Furthermore, the installation cost estimation for 1 MWh LFP BESS can be nearly around 448000 $ excluding operation and other costs.

		Lithium-ion LFP						
		1 MW / 4 hr		10 MW / 4 hr		100 MW / 4 hr		
Parameter	Units	2020	2030	2020	2030	2020	2030	
ESS Installed Cost / Energy Storage System / Storage System: Storage Block	$/kWh	[164 - 200] 182	[87 - 128] 109	[156 - 191] 174	[83 - 122] 104	[149 - 182] 165	[79 - 116] 99	
ESS Installed Cost / Energy Storage System / Storage System: Storage Balance of System	$/kWh	[38 - 47] 42	[25 - 35] 30	[36 - 44] 40	[24 - 33] 28	[35 - 42] 38	[23 - 32] 27	
ESS Installed Cost / Energy Storage System: Power Equipment	$/kW	[76 - 93] 85	[59 - 77] 73	[66 - 80] 73	[51 - 66] 63	[57 - 69] 63	[44 - 57] 54	
ESS Installed Cost / Energy Storage System: Controls & Communication	$/kW	[36 - 44] 40	[24 - 33] 28	[7 - 9] 8	[5 - 6] 5	[1 - 2] 2	[1 - 1] 1	
ESS Installed Cost / Energy Storage System: System Integration	$/kWh	[37 - 56] 50	[37 - 46] 36	[35 - 52] 47	[35 - 42] 33	[33 - 49] 44	[33 - 40] 31	
ESS Installed Cost: Engineering, Procurement, and Construction	$/kWh	[48 - 74] 61	[45 - 56] 50	[44 - 68] 56	[42 - 51] 46	[42 - 64] 53	[39 - 48] 43	
ESS Installed Cost: Project Development	$/kWh	[57 - 90] 73	[54 - 67] 60	[52 - 83] 67	[50 - 61] 55	[49 - 78] 63	[47 - 58] 52	
ESS Installed Cost: Grid Integration	$/kW	[28 - 34] 31	[23 - 28] 25	[22 - 27] 25	[18 - 23] 20	[18 - 22] 20	[15 - 18] 16	
Total ESS Installed Cost*	$/kW	[1517 - 2040] $1,793	[1105 - 1460] $1,266	[1389 - 1868] $1,643	[1008 - 1334] $1,156	[1302 - 1752] $1,541	[944 - 1249] $1,081	
Total ESS Installed Cost*	$/kWh	[379 - 510] $448	[276 - 365] $317	[347 - 467] $411	[252 - 333] $289	[326 - 438] $385	[236 - 312] $270	
Operating Costs: Fixed O&M	$/kW-yr	[3.96 - 4.84] 4.40	[3.26 - 4] 3.61	[3.63 - 4.43] 4.03	[2.98 - 3.67] 3.30	[3.41 - 4.16] 3.79	[2.8 - 3.44] 3.10	
Operating Costs: Variable O&M	$/MWh	0.5125		0.5125		0.5125		
Operating Costs: System RTE Losses ($/kWh)	$/kWh	0.005	0.004	0.005	0.004	0.005	0.004	
Performance Metrics: Round Trip Efficiency	%	86%	88%	86%	88%	86%	88%	
Performance Metrics: Response Time	sec	1-4		1-4		1-4		
Performance Metrics: Cycle Life	#	2,000	2,100	2,000	2,100	2,000	2,100	
Performance Metrics: Calendar Life	yrs	10		10		10		
Performance Metrics: Duration Corresponding to Cycle Life**	yrs	5.77	6.06	5.77	6.06	5.77	6.06	

Figure 2.53 LFP cost estimation and prediction for 2020 and 2030 [144].

2.7 Results

In this chapter, the overall BESS concept was discussed and reviewed from different aspects. Different types of battery technologies were reviewed and assessed. Different topologies for modeling battery cells and packs were reviewed. Multiple PCS topologies used for ES are reviewed. Important studies related to multilevel converter topologies for BESS applications, specifically CHB was highlighted. Half-bridge bidirectional DC-DC converter and CHB operation and control were discussed. Finally, the control and operation of the overall BESS were summarized.

CHAPTER III

BESS DESIGN, MODELING, AND SIMULATION

In this chapter, the design details of 1 MWh BESS are given in detail. The design is based on symmetrical Y-connected CHB converter connected to a 34.5 kV distribution grid through an L filter to mitigate the harmonics at PCC and a coupling transformer. The chapter starts by designing the BESS-CHB to meet the capacity and voltage requirements. Next, the battery unit incorporated in each CHB cell is modeled. Then, the DC-DC converter embedded to each battery is modeled using a non-linear modeling approach which is utilized to design a ES-FBL controller to regulate the charging and discharging of the battery. Finally, the CHB-BESS is modelled and controlled using the pre-described vector-oriented control scheme in order to perform a simulation study for the BESS under different case studies.

3.1 BESS Design

The main basis for designing a BESS is to meet the capacity and voltage requirements that are usually determined by more complex studies for sizing and allocation of the BESS in distribution networks which is out of the scope of this study. In this study, the desired energy capacity and voltage is decided as 1 MWh and 34.5 kV, respectively. In order to meet the voltage requirement, a MV transformer is needed. Moreover, as we adopt CHB as the power converter, the usage of transformer can be neglected by adding a significant number of CHB cells instead. However, due to the high computational requirements accompanied with large number of CHB, a transformer with a rating of 4.16 kV/34.5 kV is used. As mentioned in previous chapters, the voltage of the battery pack V_p is the sum of the nominal voltage of n number battery modules connected in series. The total output voltage is the sum of each active CHB SM that contain multiple battery packs connected both in series and parallel. Depending on the battery SOC, the battery voltage may vary between minimum and maximum limits. Therefore, it is more feasible to consider a minimum voltage in designing N number of CHB cells for BESS to ensure no voltage drops occur at the ac side. Thus, the number of CHB cells can be calculated as follows:

$$N \geq \frac{\sqrt{2} \cdot V_{LL}}{\sqrt{3} \cdot V_{b,min}} \tag{3.1}$$

where V_{LL} is the line-to-line voltage at the PCC, and $V_{b,min}$ is the minimum battery bank voltage. A redundancy in CHB cells is always preferred to compromise for any system failure or shortening. The inclusion of some voltage factors in the design such as grid voltage deviation factor K_V (usually 15% voltage deviation) and the voltage drop at the filter inductor K_L which is around 5% can improve the robustness of the CHB design. Hence, Equation (3.1) can be rewritten as shown below:

$$N \geq \frac{\sqrt{2} \cdot V_{LL} \cdot K_V \cdot K_L}{\sqrt{3} \cdot V_{b,min}} \tag{3.2}$$

By adding a DC-DC converter to the SM, the design of the battery and CHB gains more flexibility by allowing for the system to attain the voltage required at each CHB branch with less series battery connections and a smaller number of CHB SMs. By replacing the $V_{b,min}$ term with the dc-link voltage V_{dc} in Equations (3.1) and (3.2), it can be rewritten as follows:

$$N \geq \frac{\sqrt{2} \cdot V_{LL}}{\sqrt{3} \cdot V_{dc}} \tag{3.3}$$

$$N \geq \frac{\sqrt{2} \cdot V_{LL} \cdot K_V \cdot K_L}{\sqrt{3} \cdot V_{dc}} \tag{3.4}$$

To make the DC-DC converter controller effective, the minimum dc-link voltage has to be maintained higher than the maximum battery voltage under all operating conditions. The capacity of the BESS, on the other hand, is determined by the parallel connections of M battery modules. The total energy of the BESS will be the sum of each battery bank energy at each individual SM inside the CHB. Thereby, assuming the same battery is used in all SMs, the minimum energy and capacity of each SM or battery bank can be then calculated as follows:

$$E_b = \frac{E_{bess}}{3 \cdot N} \tag{3.5}$$

$$C_b = \frac{E_{bess}}{3 \cdot N \cdot V_{dc}} \quad (3.6)$$

where, E_b is the battery bank energy in each SM, E_{bess} is the total energy of the BESS, and N is the number of SMs used in each CHB phase or branch multiplied by three for a three-phase system. However, the number of CHB cells is a design problem which has to be designed beforehand to meet the voltage requirements of the BESS. Upon designing the preceding parameters, the number of the batteries and its n series and m parallel connections can be designed to meet the general design based on the required dc-link voltage and the energy of each individual battery bank, respectively. Moreover, when the CHB is integrated with a bidirectional DC-DC converter, there will be a variety of battery series/parallel connection settings and combination to meet the design specification. In this thesis, the voltage deviation and drop factors in Equation (3.4) are considered in the design stage such that a redundant SM in each CHB branch is added to introduce more robustness and reliability. Also, half-bridge buck-boost bidirectional DC-DC converter is used in each SM to control the charging/discharging operations of the batteries. The parameters of the CHB-BESS design used in this thesis are listed in Table 3.1.

3.2 BESS Modeling

3.2.1 Battery Model

The standard LifePO4 battery module is considered in this thesis. The specification of this battery module is listed in Table 3.1 The generic battery model available in the simulation environment is used as shown in Figure 3.1 [126]. This model is suitable to be updated to simulate different kinds of secondary batteries.

Table 3.1 The specifications of the CHB-BESS design.

Total number of SM in CHB topology	6
Total number of voltage levels at the output of CHB	11 levels
Total number of battery banks	18
Total number of battery modules per bank	24
Total number of battery modules	432
Total number of battery cells	6912

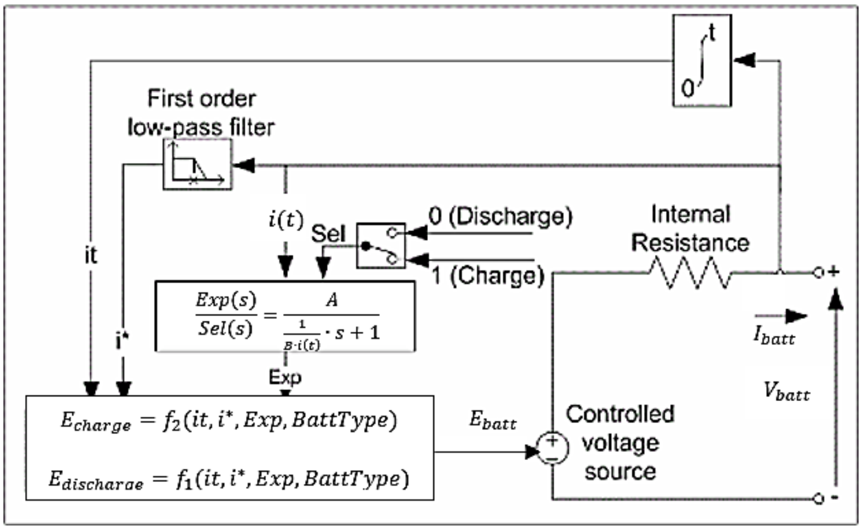

Figure 3.1 The generic battery model used in simulation environment [126].

The charging and discharging voltage of the Li-ion battery for this generic model can be expressed as a function of current as follows:

$$V_{Bdischarge} = E_o - K\left(\frac{Q}{Q-\int idt}\right)i - R_i i - K\left(\frac{Q}{Q-\int idt}\right)\int i\,dt + Ae^{-B\int idt} \quad (3.7)$$

$$V_{Bcharge} = E_o - K\left(\frac{Q}{0.1Q+\int idt}\right)i - R_i i - K\left(\frac{Q}{Q-\int idt}\right)\int i\,dt + Ae^{-B\int idt} \quad (3.8)$$

where A is the exponential voltage and B is the exponential capacity in Ah^{-1}. Two more terms are added to the Shepherd model. The fourth term in Equations (3.7) and (3.8) denotes the polarization properties associated with the overvoltage. This term, when combined with E_o, can produce a more accurate relationship for the non-linearity of OCV related to the SOC variance. The fifth term represents dynamic voltage, which changes exponentially with SOC and can be seen as discharge curves given in Figure 3.2 to indicate non-linear hysteresis when charging and discharging.

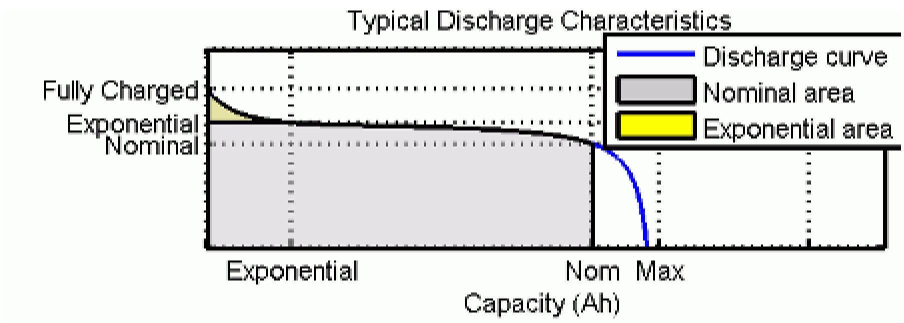

Figure 3.2 Generic battery model discharge curve [126].

The aforementioned model assumes the followings:

1- Internal resistance R_i is assumed to be constant during charging/discharging cycles and does not change with current amplitude in the model given by Equations (3.7) and (3.8).
2- The ideal case is assumed in which both charging and discharging processes have identical characteristics. The parameters are retrieved from the discharge characteristics.
3- The Peukert effect is negligible as the capacity does not vary with the current amplitude.
4- The self-discharge is negligible, since it can be derived by placing large resistance in parallel with the battery terminals.
5- The battery memory effect is not considered.

Based on those assumptions, the generic battery model is favorable when the aforementioned effects and characteristics are not a matter of concern. This model is preferred in large-scale BESS applications where tremendous numbers of battery cells are included in CHB based BESS that requires large number of batteries and switching components that impose heavy computational burden for simulation. The specification of each battery pack used in the thesis is listed in Table 3.2.

Table 3.2 The specifications of the battery module.

Battery type	LiFePo4
Voltage min. / nom. / max.	44.0 V / 51.2 V / 58.4 V
Stored energy	2.56 kWh / 50 Ah
Number of cells per module	16

Table 3.3 Battery pack parameters.

Battery type	Li-ion
Nominal voltage	410 V
Rated capacity	150 Ah
Cutoff voltage	307.5 V
Fully charged voltage	477.2 V
Internal resistance	0.027 Ω

3.2.2 Bi-directional DC-DC Converter Model and its Control

Figure 3.3 shows the primary circuit of the CHB converter cell. A battery is connected to a bidirectional buck-boost DC-DC converter that is coupled to an H-bridge inverter through a dc-link capacitor. The bidirectional DC-DC converter works in both forward and reverse power flow from the battery to the grid or vice versa, as the name implies. The DC-DC converter is capable of managing the battery charging and discharging modes. As a result, the voltage level design for the batteries becomes more flexible.

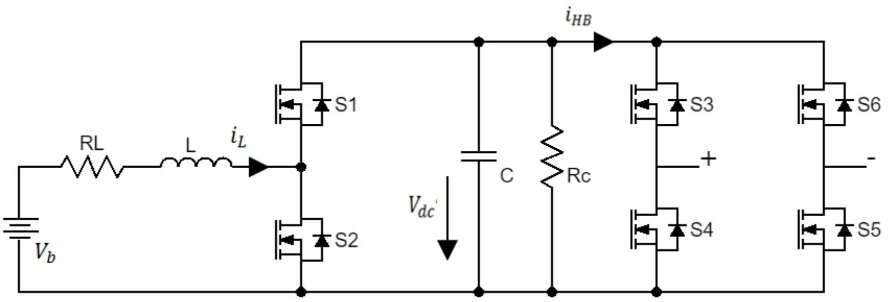

Figure 3.3 CHB SM including battery, DC-DC converter, H-bridge inverter.

Kirchhoff's voltage and current laws are used to derive the equations defining the dynamics of the bidirectional DC-DC converter in both buck and boost modes. The equivalent circuit of bidirectional DC-DC converter in buck-mode is shown in Figure 3.4. In this mode, switches S1 and S2 are turned ON and OFF, respectively. In buck mode, the dynamics of the DC-DC converter can be characterized using the following equations:

$$L\frac{di_L}{dt} = V_b - i_L R_L - V_{dc} \tag{3.9}$$

$$C\frac{dV_{dc}}{dt} = i_L - \frac{V_{dc}}{R_c} - i_{HB} \tag{3.10}$$

where L is the inductance on the battery side, C is the dc-link capacitance, R_L and R_C are the internal resistance of the inductance and capacitance, respectively, V_b and V_{dc} are the battery and dc-link voltage, respectively, i_L is the inductance current, and i_{HB} is the current of H-bridge inverter.

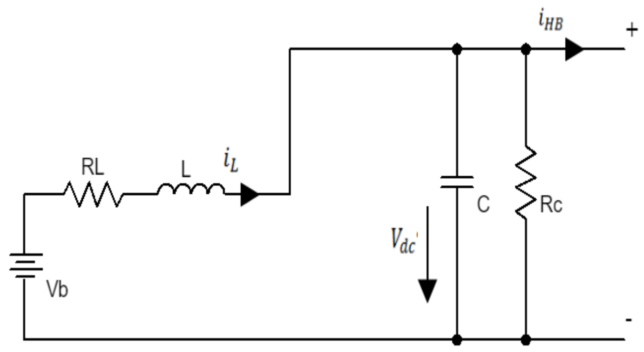

Figure 3.4 The equivalent circuit of bidirectional DC-DC converter in buck-mode.

When switch S1 is turned OFF and switch S2 is turned ON, the equivalent circuit of DC-DC converter reduces to the one shown in Figure 3.5. In this mode, the DC-DC converter operates in boost mode. The dynamics of the DC-DC converter can be characterized using the following equations:

$$L\frac{di_L}{dt} = V_b - i_L R_L \tag{3.11}$$

$$C\frac{dV_{dc}}{dt} = -\frac{V_{dc}}{R_c} - i_{HB} \tag{3.12}$$

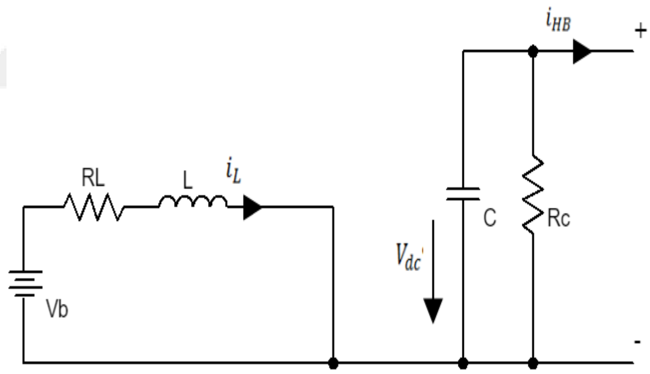

Figure 3.5 The equivalent circuit of bidirectional DC-DC converter in boost-mode.

Equations (3.9)-(3.12) can be reduced to a couple of equations, since the bidirectional DC-DC converter operates in the continuous mode of conduction. Thus, averaging state-space approach can be used to get a PWM bi-directional buck-boost converter model using the converter duty cycle d. Then the averaged equations can be written as bellow:

$$L\frac{di_L}{dt} = V_b - i_L R_L - (1-d)V_{dc} \tag{3.13}$$

$$C\frac{dV_{dc}}{dt} = (1-d)i_L - \frac{V_{dc}}{R_c} - i_{HB} \tag{3.14}$$

A non-linear state-space model can be acquired from Equations (3.13) and (3.14) by selecting the inductance current i_L and the dc-link voltage V_{dc} as state variables and the duty cycle d as the system input. Hence the state-space representation of the system can be expressed as follows:

$$\dot{x} = f(x) + g(x)u, \quad u = d$$
$$y = h(x), x = [i_L \; V_{dc}] \tag{3.15}$$
$$f(x) = \begin{bmatrix} \frac{V_b}{L} - \frac{R_L x_1}{L} - \frac{x_2}{L} \\ \frac{x_1}{C} - \frac{x_2}{CR_c} - \frac{i_{HB}}{C} \end{bmatrix}, g(x) = \begin{bmatrix} \frac{x_2}{L} \\ \frac{-x_1}{C} \end{bmatrix} \tag{3.16}$$

In general, buck-boost dc-dc converters are usually known to be unable to directly control the dc-link capacitor voltage, since the open-loop transfer function for the converter is non-minimum phase. The dc-link voltage should therefore be indirectly controlled by selecting the inductive current i_L as the system output. The system is then transformed into a minimum phase, as the dc-link voltage becomes controllable. So, the bidirectional DC-DC converter state-space average model can be described as follows:

$$\dot{x} = f(x) + g(x)u,$$
$$u = d \,, y = h(x) = x_1 - i_{l_{ref}}, x = [i_L \; V_{dc}] \tag{3.17}$$

Here the error which is between the measured and the reference value of the inductor current is chosen as the output of the system. After redefining the state-variables and selecting the errors as the new state-variables, the following equation is obtained:

$$e = [e_1 \quad e_2] = [x_1 - i_{l_{ref}}, x_2 - V_{dc_{ref}}] \tag{3.18}$$

where e is the error vector, $x_1$and $x_2$is the state variables defined in equation 3.15, $i_{l_{ref}}$ is the reference inductor current, and $V_{dc_{ref}}$ is the reference dc-link voltage value. Then, Equations (3.16-3.17) can be rewritten as follows:

$$\dot{\boldsymbol{e}} = \boldsymbol{f}(\boldsymbol{e}) + \boldsymbol{g}(\boldsymbol{e})\boldsymbol{u}, \quad \boldsymbol{u} = \boldsymbol{d}$$
$$\boldsymbol{y} = \boldsymbol{h}(\boldsymbol{e}), = \boldsymbol{e_1} \tag{3.19}$$

$$
\boldsymbol{f}(\boldsymbol{e}) = \begin{bmatrix} \frac{\boldsymbol{V_b}}{\boldsymbol{L}} - \frac{\boldsymbol{R_L}(\boldsymbol{e_1} + \boldsymbol{i_{l_{ref}}})}{\boldsymbol{L}} - \frac{(\boldsymbol{e_2} + \boldsymbol{V_{dc_{ref}}})}{\boldsymbol{L}} \\ \frac{\left(\boldsymbol{e_1} + \boldsymbol{i_{l_{ref}}}\right)}{\boldsymbol{C}} - \frac{(\boldsymbol{e_2} + \boldsymbol{V_{dc_{ref}}})}{\boldsymbol{C}\boldsymbol{R_c}} - \frac{\boldsymbol{i_{HB}}}{\boldsymbol{C}} \end{bmatrix}
$$

$$
\boldsymbol{g}(\boldsymbol{e}) = \begin{bmatrix} \frac{(e_2 + V_{dc_{ref}})}{L} \\ \frac{-(e_1 + i_{l_{ref}})}{C} \end{bmatrix} \tag{3.20}
$$

Moreover, the inductor current reference $i_{l_{ref}}$ can be derived from Equation (3.14) as follows:

$$
i_{l_{ref}} = \frac{V_{dc_{ref}} + v_b}{V_{dc_{ref}}} \left(\frac{V_{dc_{ref}}}{\boldsymbol{R_c}} + \boldsymbol{i_{HB}}\right) \tag{3.21}
$$

3.2.2.1 Exact State Feedback Linearization (ES-FBL)

The ES-FBL approach is able to use the suitable state variable definition to convert the non-linear model into a new linear model. The method proposed is somewhat different from common linearization methods. Small signal analysis, for example, is limited to linearize the system only around a single operating point. Whereas, ES-FBL has the benefits of linearizing the model across the whole operating range of the model compared to other methods such as small-signal linearization [124][125]. The following theorem must be examined in advance before attempting to apply the proposed approach for controlling the bidirectional DC-DC converter.

Theorem 1: The following two conditions have to be met to ensure that ES-FBL controls the affine SISO non-linear system given in Equation (3.20).

Condition 1.1: Throughout every x that is in closure of x°, the rank of the matrix $[g \ \ ad_f g, \dots, ad_{f^{n-2}} g\ ]$ has to be the same as the dimension n of the system, where $ad_f g$ is the lie bracket operative.

Condition 1.2: When $x = x^{\circ}$, the vector field set $D = \{g \ \ , ad_f g, \dots, ad_{f^{n-2}} g\ \}$ has to be involutory.

If the aforementioned conditions are satisfied, there must be an output function $W(X)$ that brings the relative degree r to be equal to the system's dimension n, and satisfy the expression $L_g W(X) = 0$. The term $L_g W(X)$ represents the lie derivative operator of $W(X)$ along g. Furthermore, the coordinate transformation shown below can be used to generate new coordinates z_n:

$$Z = \begin{bmatrix} z_1 \\ z_2 \\ \vdots \\ z_n \end{bmatrix} = \varphi(x) = \begin{bmatrix} h(x) \\ L_f h(x) \\ \vdots \\ L_{f^n h(x)} \end{bmatrix} \tag{3.22}$$

With the use of the above coordinate transformation, a new linear system can be obtained from a nonlinear system, expressed as follows:

$$\begin{aligned} \dot{z_1} &= z_2 \\ \dot{z_2} &= z_3 \\ &\vdots \\ \dot{z}_{n-1} &= L_{f^n h(x)} + L_g L_{f^{n-1}}\, h(x)u \end{aligned} \tag{3.23}$$

where z_n is the new state variables of the new linear system, $L_{f^n h(x)}$ is the lie derivative of the output $h(x)$ with respect to f^n, and $L_{f^{n-1}}\, h(x)u$ is the lie derivative of $h(x)u$ with respect to f^{n-1} and $L_g L_{f^{n-1}}\, h(x)u$ term is the lie derivative of the $L_{f^{n-1}}\, h(x)u$ term with respect to g.
Accordingly, a new control input can be introduced in the new linear system as:

$$v = \alpha(x) + \beta(x)u \tag{3.24}$$

where $\alpha(x) = L_{f^n} h(x)$ and $\beta(x) = L_g L_{f^{n-1}}\, h(x)$. Summarily, a linear configuration can be realized from the original nonlinear system as:

$$\dot{Z} = AZ + Bv \tag{3.25}$$

Finally, Equation (3.25) can be used to develop a new nonlinear system control law in which the control input is defined as:

$$u = \frac{-\alpha(x) + v}{\beta(x)} \tag{3.26}$$

3.2.2.2 Bidirectional DC-DC Converter Controller Design

We refer to Theorem (1) to determine whether the nonlinear system specified in Equation (3.20) complies with the aforementioned conditions of the ES-FBL in order to design ES-FBL controller. Therefore, by applying the lie bracket operative of g along f we get;

$$ad_f g = \frac{dg(e)}{de} f(e) - \frac{df(e)}{de}$$
$$g(e) \begin{bmatrix} \frac{dg_1}{de_1} & \frac{dg_1}{de_2} \\ \frac{dg_2}{de_1} & \frac{dg_2}{de_2} \end{bmatrix} \begin{bmatrix} f_1(e) \\ f_2(e) \end{bmatrix} - \begin{bmatrix} \frac{df_1}{de_1} & \frac{df_1}{de_2} \\ \frac{df_2}{de_1} & \frac{df_2}{de_2} \end{bmatrix} \begin{bmatrix} g_1(e) \\ g_2(e) \end{bmatrix} \tag{3.27}$$

Substitution of Equation (3.20) in Equation (3.27) yields:

$$ad_f g = \begin{bmatrix} \frac{-e_2 + V_{dc_{ref}}}{LCR_c} - i_{HB} + \frac{R_L}{L} \frac{(e_2 + V_{dc_{ref}})}{L} \\ \frac{-V_b}{LC} + \frac{R_L(e_1 + i_{l_{ref}})}{LC} - \frac{-(e_1 + i_{l_{ref}})}{R_c C^2} \end{bmatrix} \tag{3.28}$$

According to Equation (3.28), the rank of the matrix $Rank\begin{bmatrix} g & ad_f g \end{bmatrix} = 2$. This is equal to the dimension n of the nonlinear system. As a result, Theorem (1) is satisfied, and the ES-FBL can be used to solve the nonlinear system provided in Equation (3.20). Following that, the relative degree must be checked to see if it matches with the dimension n of the nonlinear system given in Equation (3.16). The lie derivative operator $L_g h(e)$ can be used to demonstrate this check as follows:

$$L_g h(\mathrm{e}) = \frac{\mathrm{d}h}{\mathrm{dt}} g(e) = \begin{bmatrix} 1 & 0 \end{bmatrix} \begin{bmatrix} \frac{(e_2 + V_{dc_{ref}})}{L} \\ \frac{-(e_1 + i_{l_{ref}})}{C} \end{bmatrix} = \frac{1}{L}\left(e_2 + V_{dc_{ref}}\right) \neq 0 \tag{3.29}$$

Equation (3.29) shows that the relative degree r is not equal to the dimension n of the non-linear system given in Equation (3.16). Thus, there is a $W(e)$ virtual output that could be designed to meet the condition ($L_g\, W(e) = 0$), which has been found to be:

$$W(\mathrm{e}) = \mathrm{L}e_1{}^2 + Ce_2{}^2 + 2Li_{l_{ref}}e_1 + 2CV_{dc_{ref}}e_2 \tag{3.30}$$

Thereby, the nonlinear system of bidirectional buck-boost converter provided in Equation (3.20) can be expressed in a linear form as in Equation (3.23):

$$\dot{Z} = \begin{bmatrix} 0 & 1 \\ 0 & 0 \end{bmatrix} Z + \begin{bmatrix} 0 \\ 1 \end{bmatrix} v \tag{3.31}$$

$$Z = \begin{bmatrix} W(e) \\ L_f W(e) \end{bmatrix} \tag{3.32}$$

And the full state feedback controller v can be defined as

$$v = -(K_1 Z_1 + K_2 Z_2) \tag{3.33}$$

Since the liner system given in Equation (3.33) is a 2nd order system;

$$\dot{Z}_1 + K_2 \dot{Z}_1 + K_1 Z_1 = 0 \tag{3.34}$$

By substituting the error terms e_1 and e_2 with the state variables x_1 and x_2. Accordingly, $L_f W(e), \alpha(e), and\ \beta(e)$ becomes:

$$L_f W(e) = 2V_b x_1 - \frac{2x_2{}^2}{R_c} - 2i_{HB} x_2 - 2R_L x_1{}^2 \tag{3.35}$$

$$\alpha(e) = L_{f^2} W(e) = \frac{2V_b(V_b - x_2 - 3R_L x_1)}{L} + \frac{4x_2}{CR_c}$$

$$\times \left(-x_1 + 1.5i_{HB} + \frac{x_2}{Rc}\right) + \frac{2i_{HB}}{C} \times (-x_1 + +i_{HB}) + \frac{4R_L x_1}{L} \times (R_L + x_1) \tag{3.36}$$

$$\beta(e) = L_g L_f \mathrm{W(e)} = \frac{2V_b x_2}{L} + \frac{4x_2 x_1}{CR_c} + \frac{2i_{HB} x_2}{C} - \frac{4R_L x_1 x_2}{L} \tag{3.37}$$

Finally, by substituting Equations (3.36) and (3.37) in the control input u in Equation (3.26), the new control law is obtained as:

$$u = \frac{-L_{f^2} W(e) + v}{L_g L_f \mathrm{W(e)}} \tag{3.38}$$

Finally, the control block diagram of the ES-FBL of the bi-directional DC-DC converter is illustrated in Figure 3.6.

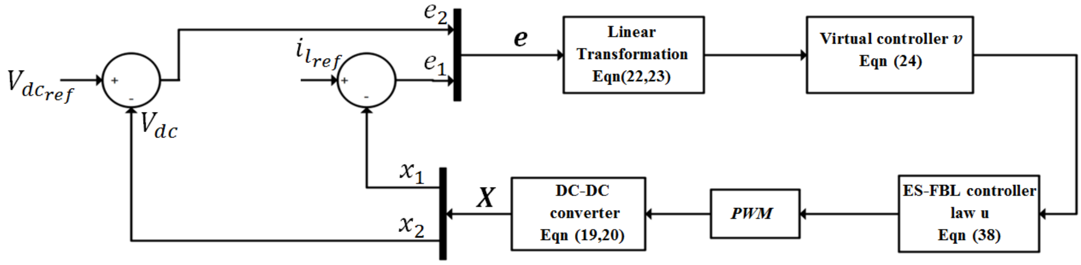

Figure 3.6 ES-FBL control diagram of the DC-DC converter proposed in the thesis.

Referring to the circuit of the bidirectional DC-DC converter shown in Figure 3.3, the natural vibration frequency and the RC constant can be calculated as:

$$\omega_o = \frac{1}{\sqrt{LC}}, \omega_1 = \frac{1}{R_c C} \tag{3.39}$$

Accordingly, as the system given in Equation (3.25) is a second order system, the selection of the controller gains $[K_1\ K_2\ ]$ in Equation (3.34) can be determined based on classic control theory of second order systems by defining the control gains as $K_1 = \omega_n{}^2 = \frac{K}{LC}$ and $K_2 = 2z\sqrt{K_1}$ where z is the damping ratio.

3.2.3 CHB-BESS Model

As was previously mentioned, the CHB topology is chosen to interface the BESS with the grid. The main objective of the CHB is to interface the ESS with the grid to exchange energy and power. Thus, the CHB converter and the grid are modeled as an ideal voltage source as shown in Figure 3.7. Moreover, by adopting this approach, the switching losses and the high frequency effects caused by the switching devices in the CHB is neglected. Furthermore, the ideal voltage sources considered are connected through an inductive filter.

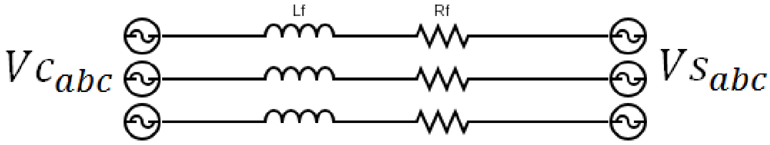

Figure 3.7 Simplified schematic of the system.

The peak output voltage of each phase of CHB can be described in Equation (3.40) as a function of modulation index ($m_x, x = a, b, c$), the sum of dc-link voltages for each operating CHB cell ($\sum_{i=1}^{N} V_{dc,i} S_i$) where S_i is the switching function corresponding to the SM i, and converter phase angle θ_c.

$$V_a = m_a \sum_{i=1}^{N} V_{dc,i} S_i \cdot \cos(\theta_c)$$
$$V_b = m_b \sum_{i=1}^{N} V_{dc,i} S_i \cdot \cos\left(\theta_c - \frac{2\pi}{3}\right)$$
$$V_c = m_c \sum_{i=1}^{N} V_{dc,i} S_i \cdot \cos\left(\theta_c + \frac{2\pi}{3}\right) \tag{3.40}$$

Assuming all the losses related to switching and dc-link capacitor is negligible based on the power conversion law, the power balance between the BESS and the PCC can be expressed as follows:

$$P_{ac} = P_{dc}$$
$$\sqrt{3}\, V_{ac} i_{ac} = \sum_{x=a,b,c} \sum_{i=1}^{N} V_{b,i} i_{l,i} S_i \tag{3.41}$$

In Equation (3.41), the left side is defined as the power of the ac side and the right side as the power of the dc side, where V_{ac} is the line-to-line voltage at PCC and i_{ac} is the line current. Based on the power flow the current components in dc and ac sides, the current polarity will be negative during charging operation and positive during discharging operation of the BESS. By assembling the voltage output given in Equation (3.40) and placing them in Equation (2.39), it can be transformed to *dq0* reference frame to be utilized in the vector current control strategy mentioned in the previous chapter. The ac side of Equation (3.41) can be rewritten along with the voltage expression at the PCC in the synchronous rotating reference frame as follows:

$$\frac{3}{2}\left(V_d i_d + V_q i_q\right) = \sum_{x=a,b,c} \sum_{i=1}^{N} V_{b,i} i_{l,i} S_i \tag{3.42}$$

$$V_{i_d} = V_d - L_f \omega i_q + R_f i_d + L_f \frac{di_d}{dt} \tag{3.43}$$

$$V_{i_q} = V_d + L_f \omega i_d + R_f i_q + L_f \frac{di_q}{dt} \tag{3.44}$$

Where V_d and V_q are the d and q components of the grid voltage respectively, i_d and i_q are the d and q components of the line currents respectively, $V_{b,i}$ and $i_{l,i}$ is the battery voltage and inductor current respectively corresponding to the i^{th} SM of x phase. V_{i_d} and V_{i_q} are the d and q components of the inverter voltage respectively, L_f is the filter inductance, and R_f is the filter resistance. Based upon the above equations, the vector control strategy discussed in Chapter 2 can be adopted to control the power exchange between BESS and grid at PCC. The main control of the CHB-BESS is divided into two parts: current control and voltage control. For the current control part, the amplitude and the direction of the line current is controlled by adjusting the phase angle of the converter such that the phase angle set is at leading when injecting current into the grid by discharging the batteries, and lagging when the batteries are charging as the power is consumed from the grid. The voltage control, on the other hand, controls the voltage amplitude by adjusting the modulation index of the reference signals. In the thesis, the firing pulses for the semiconductor switches of the CHB are produced using level-shifted PWM due to its low THD at the output voltage. The charging/discharging current rates of the BESS are determined by the active/reactive power references from Equation (2.46) and (2.47). Since level-shifted PWM is selected, the SOC of the batteries can be balanced using an offset interchanging approach whose flowchart is depicted in Figure 3.8. Additionally, the overall control process of the CHB-BESS is simplified in Figure 3.9.

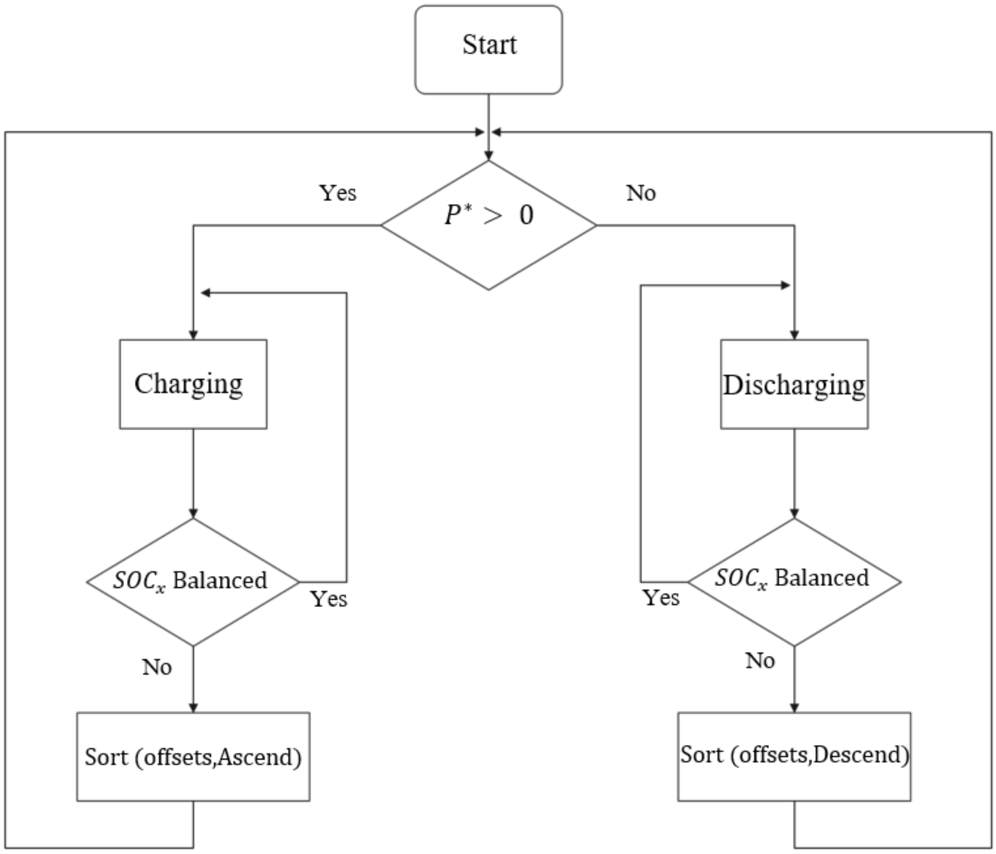

Figure 3.8 The flowchart of in-phase LS-SPWM SOC balancing.

In the SOC balancing scheme, the SMs with the least SOC value is assigned with higher offsets for their corresponding carrier waves compared to the reference signal during discharging. In contrast, when BESS is charging, the carrier waves corresponding to SMs with the lowest SOC values is assigned with lower offsets, while the higher offset is assigned to SM with higher SOC values. This led the batteries to charge and discharge at different rates until all batteries have balanced and nearly equal SOC value. In this thesis a redundant CHB SM is included in the design which is considered a more practical design such that in case of fault occurrence in a single SM, only the faulted SM is by passed with no need to bypass SM's in the other phase branches as there will be no significant voltage drop at the output. However, the fault-tolerance test in this thesis considers only faults associated with batteries excluding faults related to switches and other components. Additionally, the fault diagnosis is out of the thesis. Thereby, only the appropriate action after the fault detection in a battery cell in single SM is investigated. Furthermore, assuming fault occurrence in a single battery bank, the battery is then open-circuited by triggering the safety switches inside the battery bank. In order to bypass the SM associated with the faulty battery bank, the following switching pairs given in Figure 2.45 must be ON (T1, T2), (T3, T4), (T1, T3) or (T2, T4) simultaneously. Using redundant cell design adds more reliability to the system such that the voltage drop can be avoided and disconnecting a single SM in the other CHB branches will not be necessary. However, the addition of redundant SM means that more components and switches are used which increases the total cost of the system.

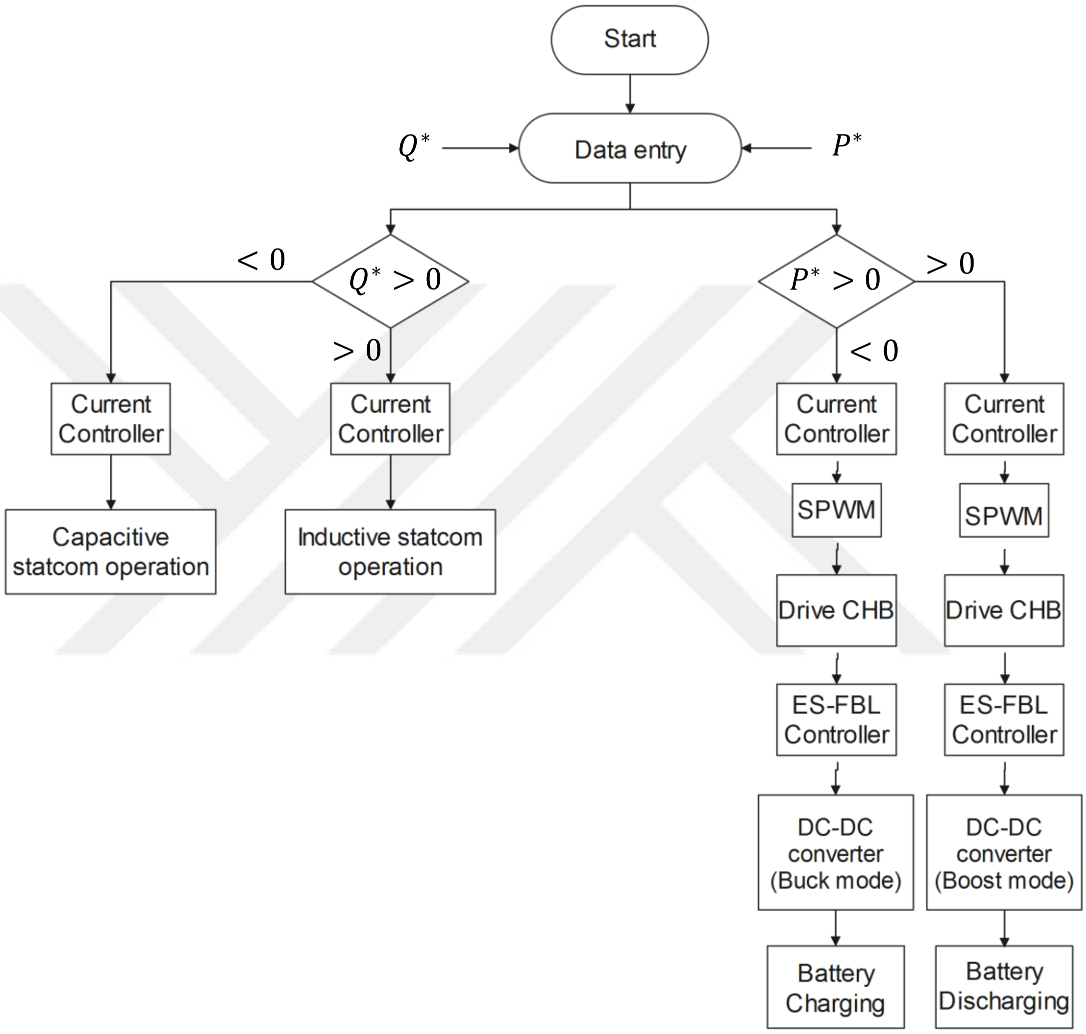

Figure 3.9 Flowchart of the overall control process

3.3 Simulation Studies

Considering the battery and system specification listed in Table 3.1 and 3.2 respectively, the two-stage CHB-BESS model presented in Fig. 2.52 is used to perform different simulation studies which were carried out on a PC with Intel core i7 2.6Ghz processor© and 16 GB RAM. In order to validate the effectiveness of the proposed non-linear controller embedded with decoupled current control, the following case studies and the parameters are performed/investigated:

1- Active power consumption from the grid (BESS charging)
2- Active power injection into the grid (BESS discharging)
3- STATCOM operation to inject inductive and capacitive reactive power into the grid while charging BESS
4- STATCOM operation to inject inductive and capacitive reactive power into the grid while discharging BESS
5- Fault tolerant test

Table 3.4 Parameters of grid-tied CHB-BESS proposed in the thesis.

Parameter	**Symbol**	**Value**
Grid line-to-line voltage	$V_{g,LL}$	34.5 kV
Grid frequency	f_g	50 Hz
PCC line-to-line voltage	$V_{i,LL}$	4.16 kV
Base power at PCC	S	1 MVA
Filter resistance	R_f	3.14 mΩ
Filter inductance	L_f	0.5 mH
Battery voltage	V_b	410 V
dc-link voltage	V_{dc}	680 V
dc-link capacitance	C_{dc}	7 mF
capacitor internal resistance	R_{dc}	10 kΩ
Energy storage cell inductance	L	0.36 mH
Inductance internal resistance	R_L	0.1 Ω
CHB switching frequency	f_{sw}	2 kHz
DC-DC converter switching frequency	f_{dc-dc}	10 kHz

In the first two case studies, the BESS is operated to test the capability of exchanging active power with the grid by controlling the synchronous rotating currents i_d and i_q through decoupled current control by setting arbitrary reference values for the active and reactive power references while setting the reactive power reference to zero. At first, the simulation is conducted for charging phase with the initial SOC of the batteries set at 50%, then the simulation was performed to discharge the batteries with an initial SOC of 80%. Similarly, in the third and fourth case studies, the BESS is operated to test the capability of exchanging reactive power with the grid by controlling the synchronous rotating currents i_d and i_q through decoupled current control by setting arbitrary reference values for the active and reactive power references and setting a constant value for active power. At first, the simulation is conducted for charging phase with the initial SOC of the batteries set at 50%, then the simulation was performed to discharge the batteries with an initial SOC of 80%. In the final case study, a fault is assumed in the battery bank of an individual SM resulting an open-circuit in the battery bank and the SM associated with the faulty battery is bypassed. This case demonstrates the effect of fault on redundant cell CHB design.

3.4 Results

The design approach and the necessary calculations for developing a CHB based BESS were mentioned in this Chapter. Following that the battery, DC-DC converter, and CHB converter were modeled individually. The battery was modeled after the built-in generic battery model available in the simulation environment. The DC-DC converter was described using a non-linear model and a ES-FBL control scheme was presented for controlling the DC-DC converter to regulate the charging/discharging processes of the battery. Finally, the CHB-BESS model was discussed in order to implement vector current oriented control that was previously mentioned in the last chapter.

CHAPTER IV

SIMULATION RESULTS AND DISCUSSION

This chapter reports the results and findings of the simulation performed on the designed system in Chapter 3 for 1 MWh rated BESS-CHB. The objective of the simulations conducted in this thesis is to demonstrate and verify the performance and capability of the designed CHB based BESS operating under different conditions. In this chapter, the graphs and tables are utilized to present the recorded results and measurements. In the appropriate places of this chapter, the key points for these results are discussed. The battery charging and discharging behavior depends on the active and reactive power set points of the main CHB current vector controller, and the ES-FBL non-linear controller for the DC-DC converter. The nominal discharge current and arbitrary discharge currents curve are shown in Figure 4.1. These curves can be extracted to give a general idea on the battery dynamic behavior under different discharging currents. As seen, the open-circuit voltage of the battery has a proportional relationship with the battery SOC, as it decreases during discharging and increases when charging. The battery bank can be fully discharged in one hour if it were to discharge at 1C rate which nearly equals 150 A discharging current.

4.1 Case 1: Active Power Control (Charging)

In this simulation scenario, positive arbitrary active power set points are applied to the respective controller to consume active power from the grid while maintaining a constant zero reactive power to ensure unity power factor operation of the BESS. The dynamic performances of the active and reactive power controllers are shown in Figure 4.2. The simulation starts by setting the active power reference to 1 pu at t=0 s which is followed successfully after short transients as shown in Figure 4.2. At t=1.5 s, the active power reference is decreased to 0.7 pu followed by another decrease to 0.5 pu at t= 1.8 s until it is set to 0 pu at t=2 s. Then, it is set back to 1 pu at t = 2.2 s which is finally increased to 1.5 pu at t=2.5 s until to the end of the simulation.

It is observed that the active power controller was able to successfully follow the given reference set points for the active power with a fast response and zero steady-state error.

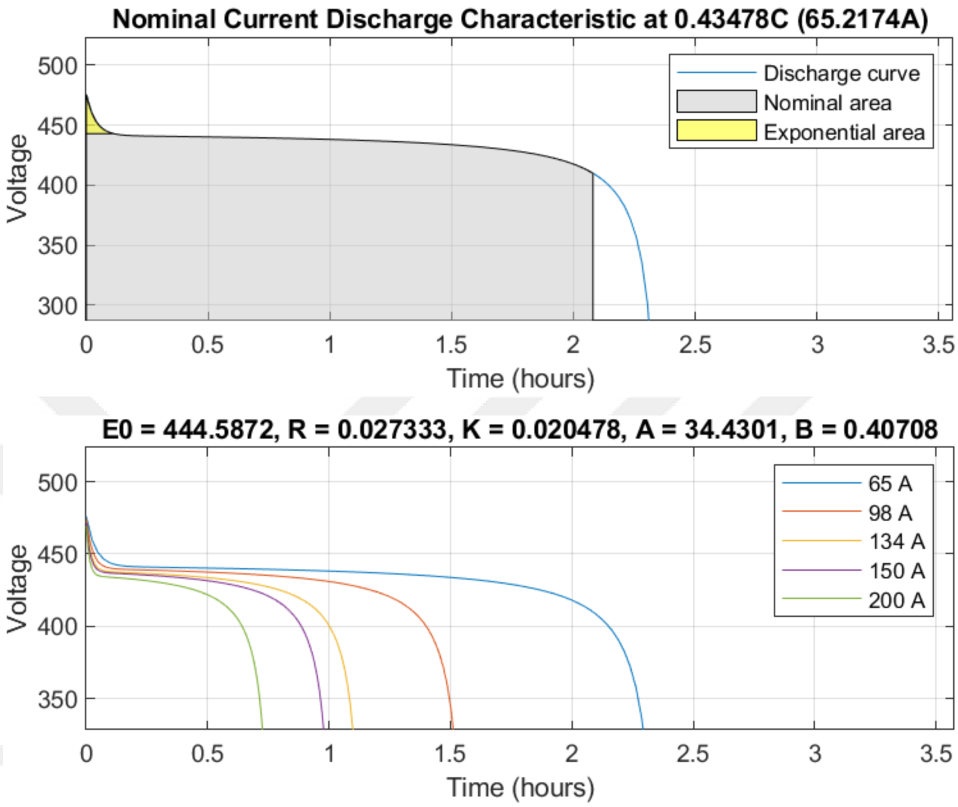

Figure 4.1 The battery model discharge curve (a) nominal discharge current curve, (b) arbitrary discharge currents curve.

The output voltage and current of phase-A of CHB-BESS is recorded and shown in Figure 4.3. As can be seen, the output voltage consists of 11-levels meaning only 5 out of 6 SMs are switching at the time while one module is redundant and kept inoperative until it is needed to operate to compensate for a faulty cell or to response to excessive power demand. However, considering in-phase SOC balancing, this redundant SM will always be operating such that 5 out of 6 SMs are operating while taking the place of redundant SM to maintain equal and balanced SOC even with the redundant SM.

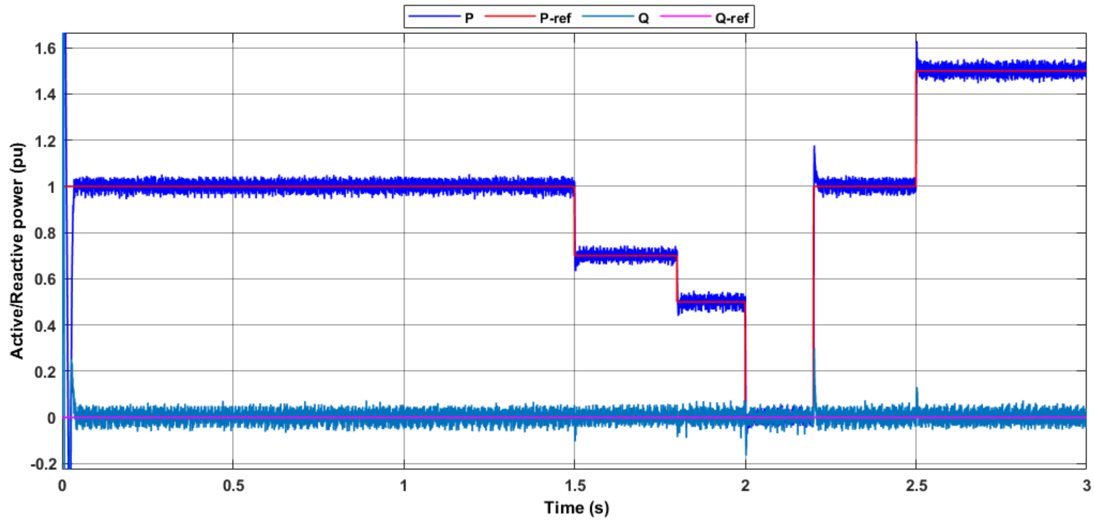

Figure 4.2 The dynamic performances of the active and reactive power controllers.

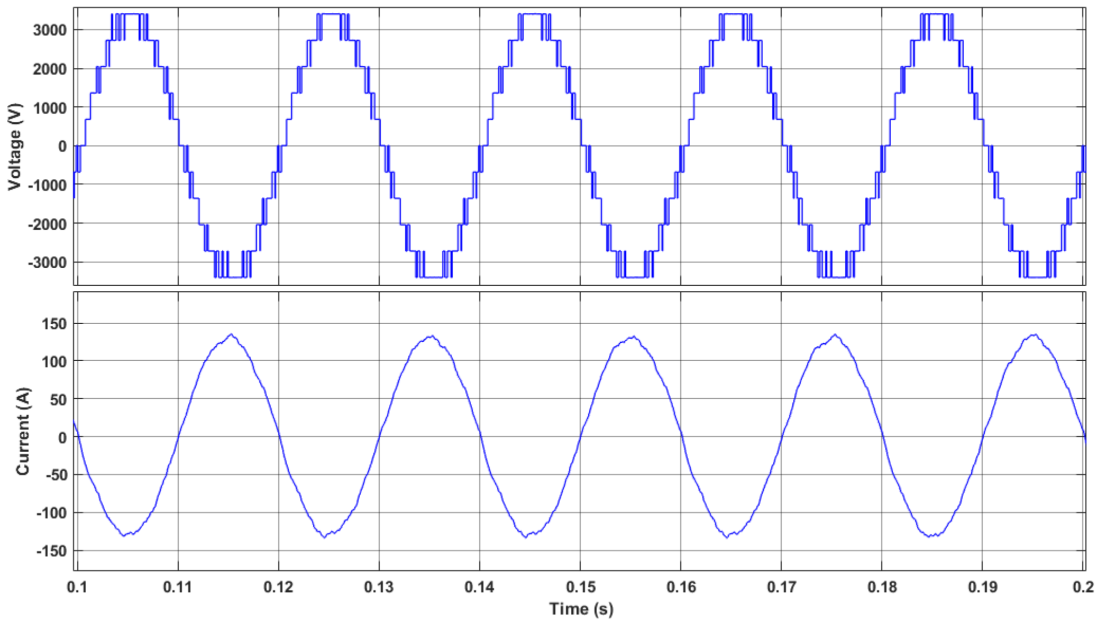

Figure 4.3 The output voltage and current of phase-A of 11-level CHB.

Three-phase voltage and current profile at PCC is depicted in Figure 4.4. As it appears that both the voltage and current waveforms exhibit acceptable sinusoidal form as the voltage and current are completely in phase indicating unity power factor operation and the BESS is behaving as a pure resistive load while drawing active power to charge the batteries. As shown in Figure 4.5, THD of the PCC voltage is obtained as 3.91% during the first simulation period when active power is at 1 pu. The THD of the PCC current, on the other hand, is obtained as 2.63%. The recorded THD values are listed in Table 4.1 and compared with the standards of IEE 519 for systems with bus voltage of 69kV and below. Accordingly, the obtained THD for both the voltage and current at the PCC are considered acceptable and within the IEEE 519 regulations. Those THD values can be further improved if more voltage levels are added in the CHB by including more SMs.

Table 4.1 Total Harmonic Distortion During Charging Operation.

Description	Voltage THD in %	Current THD in %
11-level CHB	3.91	2.63
IEEE 519 Maximum Standard	5	5

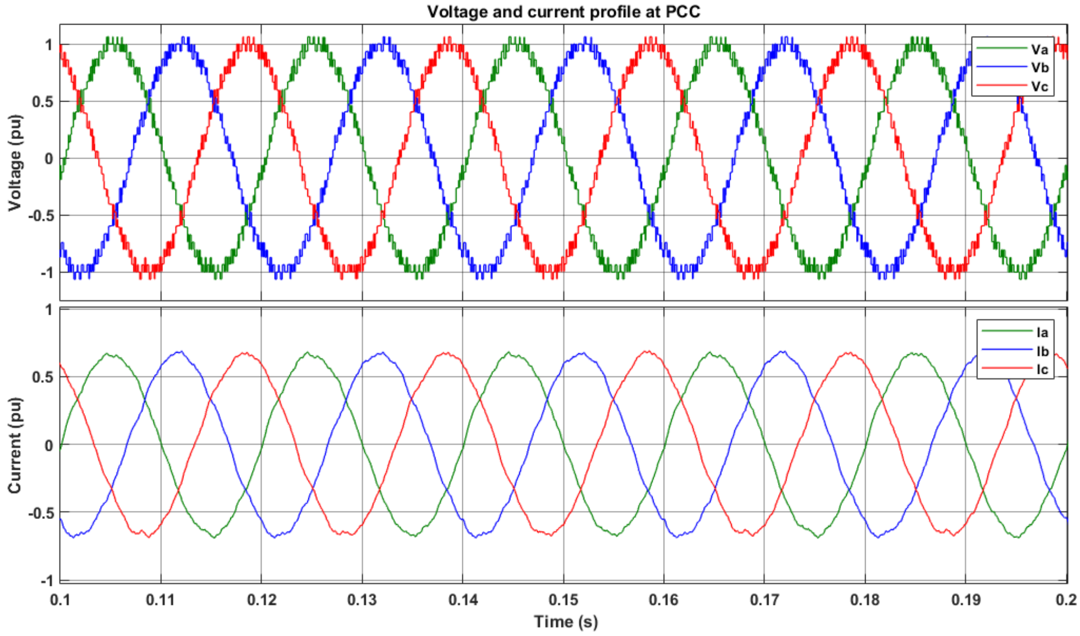

Figure 4.4 Three-phase voltage and current profiles at PCC.

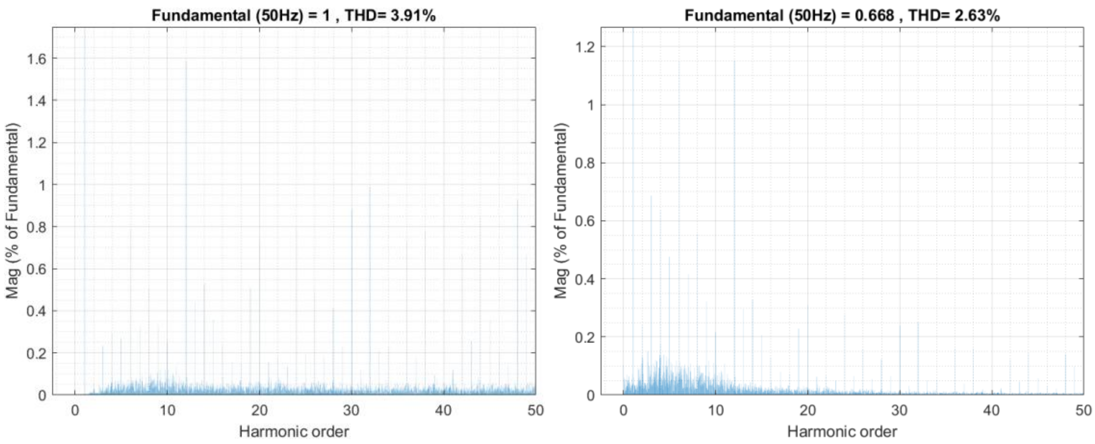

Figure 4.5 THD analysis during charging (a) voltage (b) current waveforms.

Due to the excessive amount of simulation data, only the batteries and other elements associated with phase-A is recorded and demonstrated for different case studies.

Table 4.2 Initial SOC of the battery modules.

Battery	SOC (%)
B1	50.01
B2	50.02
B3	50
B4	50.015
B5	50.03
B6	49.99

The initial values of each battery in phase-A are given in Table 4.2. Due to the short time period of the simulation, the initial SOC of each battery bank is set nearly equal with difference in two decimals to demonstrate the SOC balancing capability of the in-phase balancing scheme. The SOC of the battery banks for phase-A without in-phase balancing scheme is demonstrated in Figure 4.6. It is obvious that each battery SOC keeps on charging on the same pace with no regard to other battery SOC which eventually leads to unbalanced SOC and the difference gap in SOC between each battery keeps growing until a significant difference emerges limiting the whole BESS operation capability. Additionally, the redundant battery is observed at the bottom of the graph discharging at negligible rate due to either DC-DC converter switching or nearly negligible over modulation. On the other hand, in-phase SOC balancing allows to charge all the batteries at the same rate reaching nearly equal SOC for all batteries. This behavior is shown in Figure 4.7. It is observed that all batteries including the redundant battery are utilized. It starts charging with all the batteries while the battery with the highest SOC is stopped charging. Thus, allowing to reduce the strain on the batteries while charging.

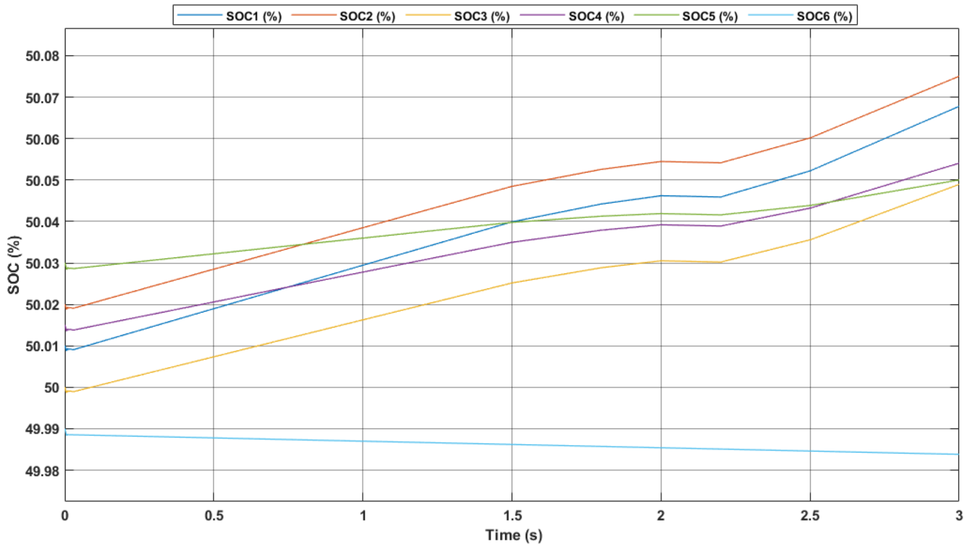

Figure 4.6 The SOC of the batteries for phase-A without in-phase balancing scheme.

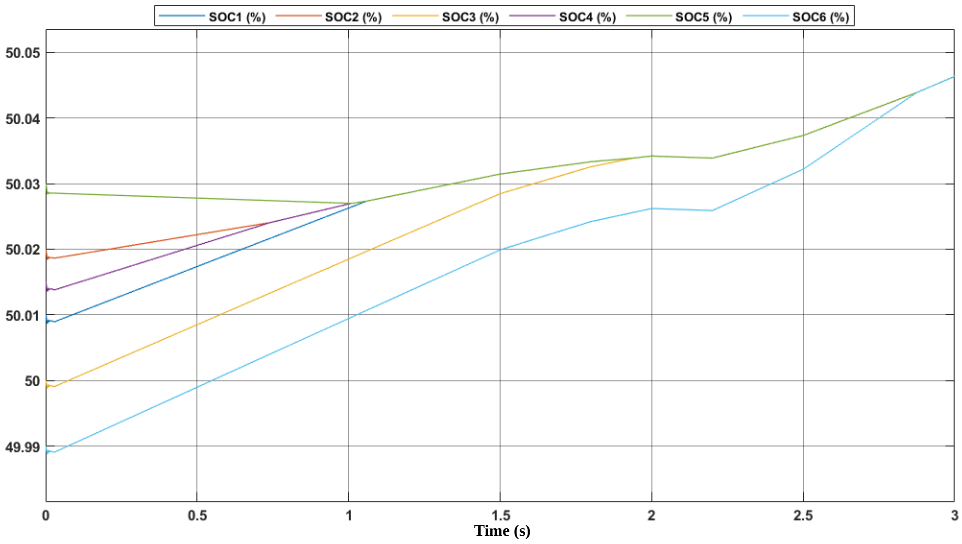

Figure 4.7 The SOC of the batteries for phase-A with in-phase balancing scheme.

The dc-link voltage was fixed at 680 V for all SMs to generate the required 11-level output voltage to meet the voltage requirement of 4160 V (line-to-line) at PCC. This was carried out using ES-FBL control scheme to regulate the dc-link voltage at each SM through linearizing the dc side model under all operation conditions that showed spectacular performance in maintaining the desired voltage throughout the simulation period with varying the power set points as seen in Figure 4.8.

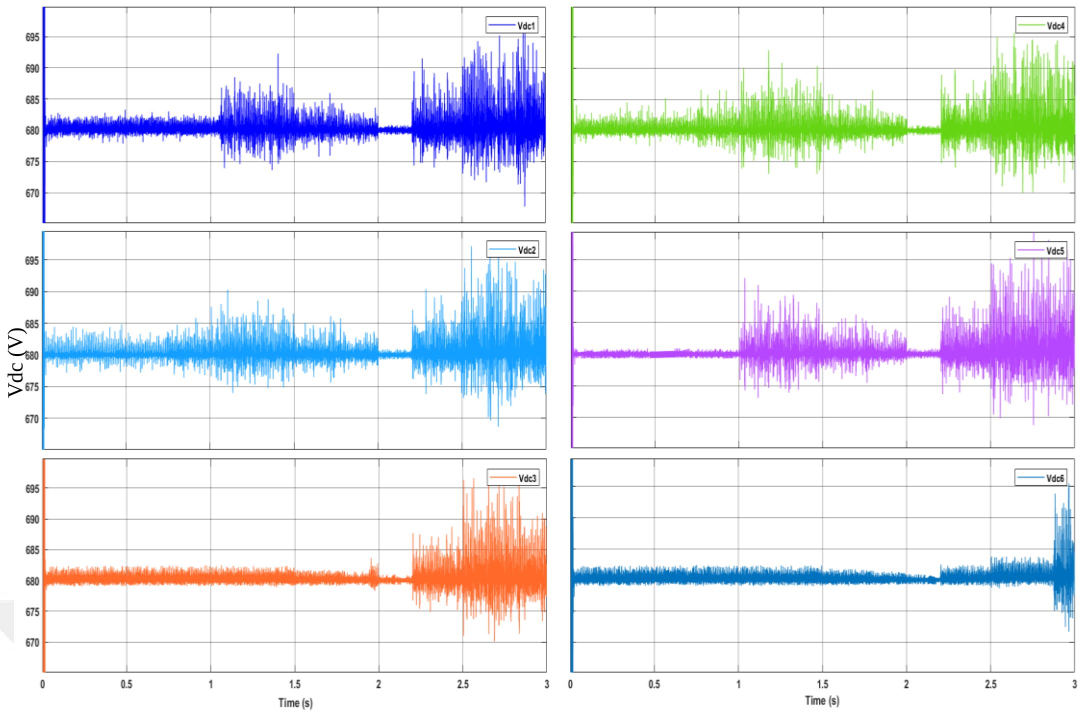

Figure 4.8 DC-link voltages of CHB SMs for phase-A.

There was a minimum amount of voltage throughout the simulation time. However, there were some fluctuations at the dc-link voltages for all SMs when the system was consuming 1.5pu active power at t=2.5 s which is not significant. Also, there were some minor voltage fluctuations between t=1 s and t=2 s for Vdc1, Vdc2, Vdc4, and Vdc5 that are caused from interchanging the carrier waves offsets in the in-phase SOC balancing scheme as seen in Figure 4.7. Where, Vdc1, Vdc2, Vdc3, Vdc4, Vdc5, and Vdc6 are the dc-link voltages numbered corresponding to the SM in phase a branch of the CHB. Looking at the current and voltage behaviors of battery 1 in Figure 4.9, it is quite evident that the battery exhibits pulsating charging behavior caused by DC-DC converter switching, as the battery is charging at pulsating current and the voltage slightly increases until it settles at certain value. Here, the current is charging at an average current of -134 A between t=0 s and t=1.2 s and settles at nearly 447 Volt of average battery voltage. The minus current indicates that the battery is charging while the positive current discharges the battery. Moreover, looking at battery 2 and battery 5 in Figure 4.10 and Figure 4.13 respectively, it is clear that those batteries are charging lesser than the other batteries due to their higher SOC values. On the other hand, batteries 3 and 6 are charging the most throughout the charging operation due to their lowest SOC values compared to other batteries. As the batteries continue to charge, it can be seen that the charging current starts varying throughout the operation due to the SOC balancing. For example, as battery 1 becomes the most charged battery at nearly t=1.2 s, the charging rate of it dramatically reduced while battery 5 starts charging in its place. This operation continues to maintain SOC balance between all the battery units.

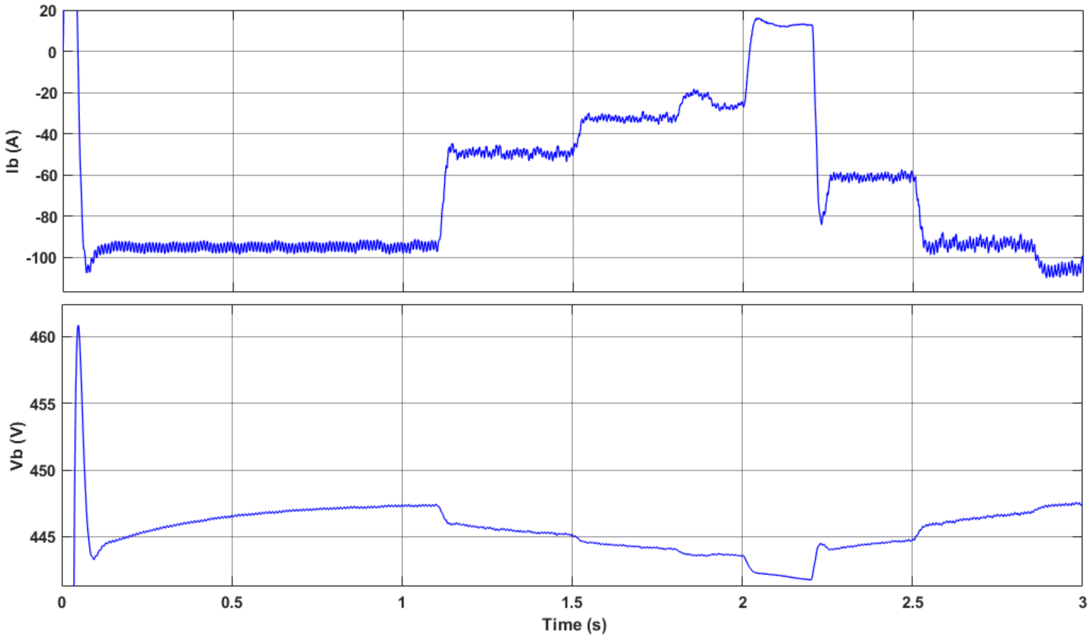

Figure 4.9 The current and voltage waveforms of battery 1.

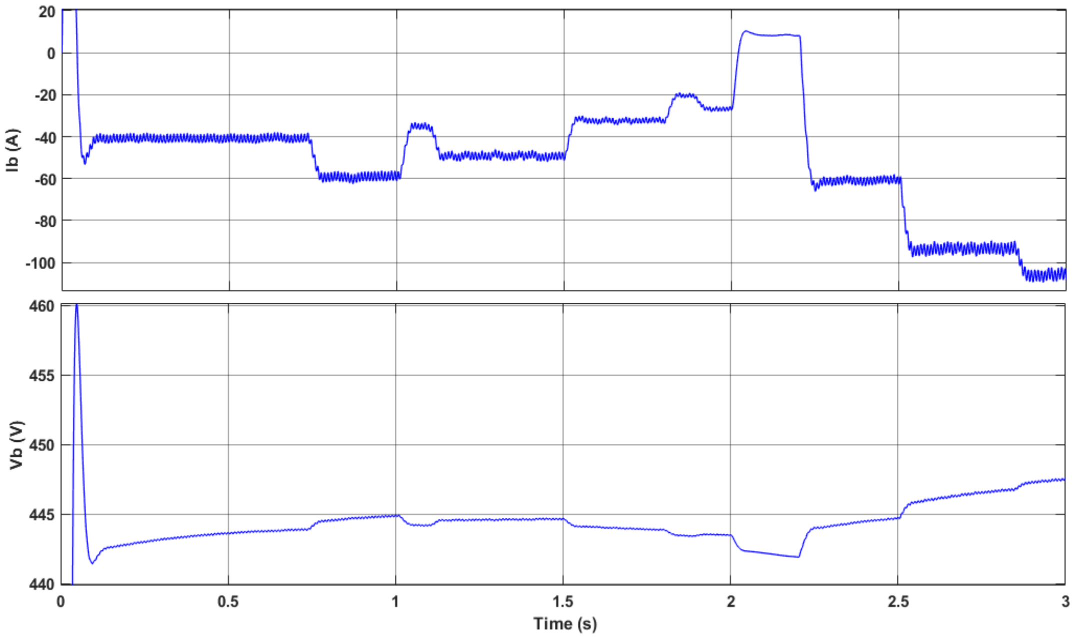

Figure 4.10 The current and voltage waveforms of battery 2.

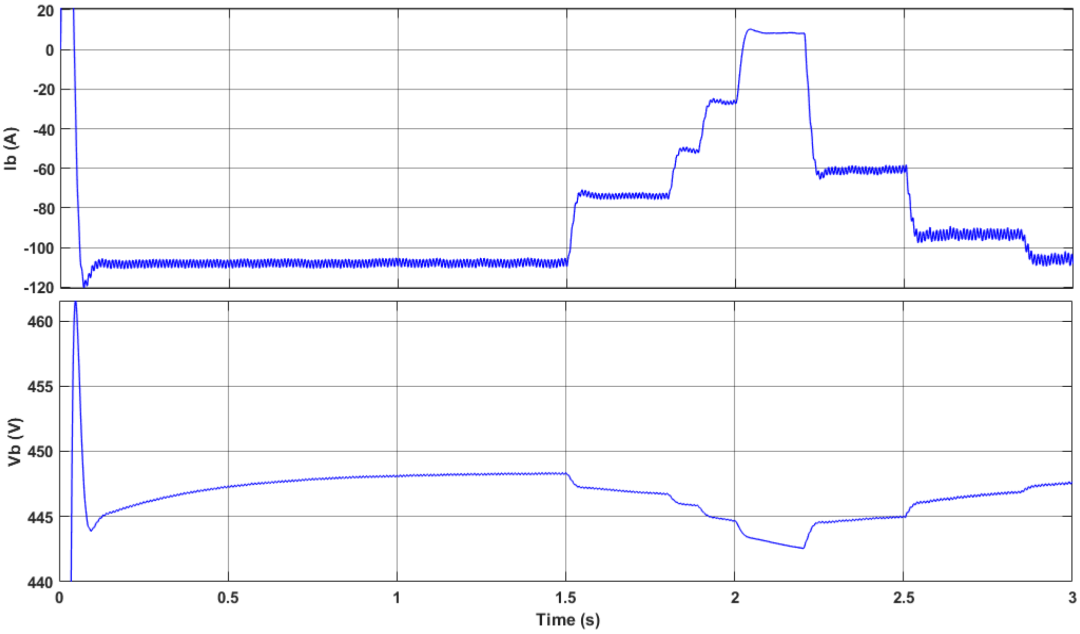

Figure 4.11 The current and voltage waveforms of battery 3.

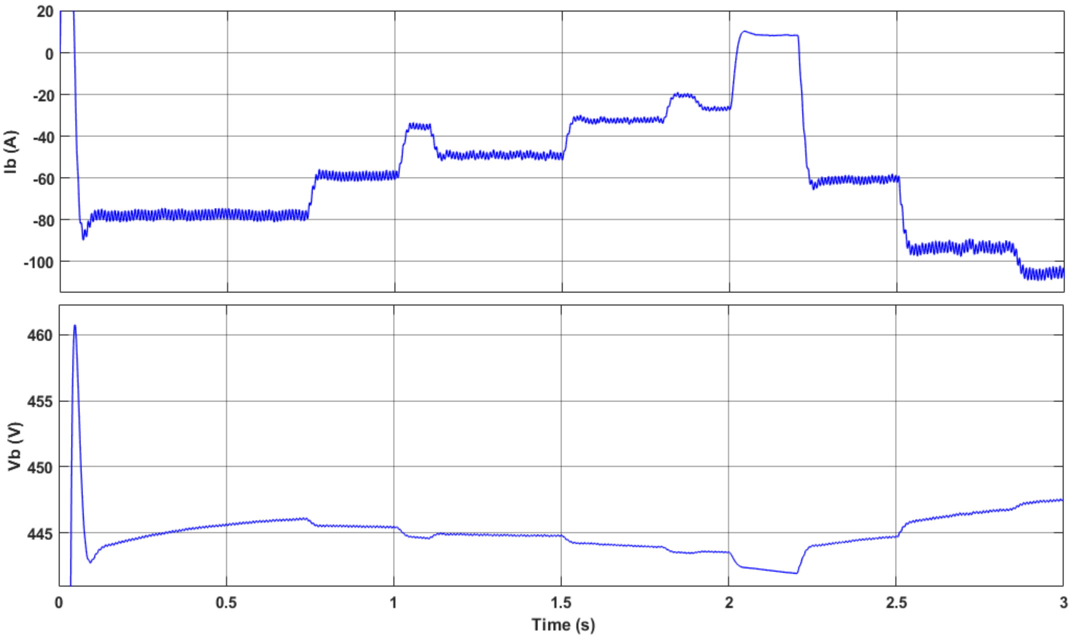

Figure 4.12 The current and voltage waveforms of battery 4.

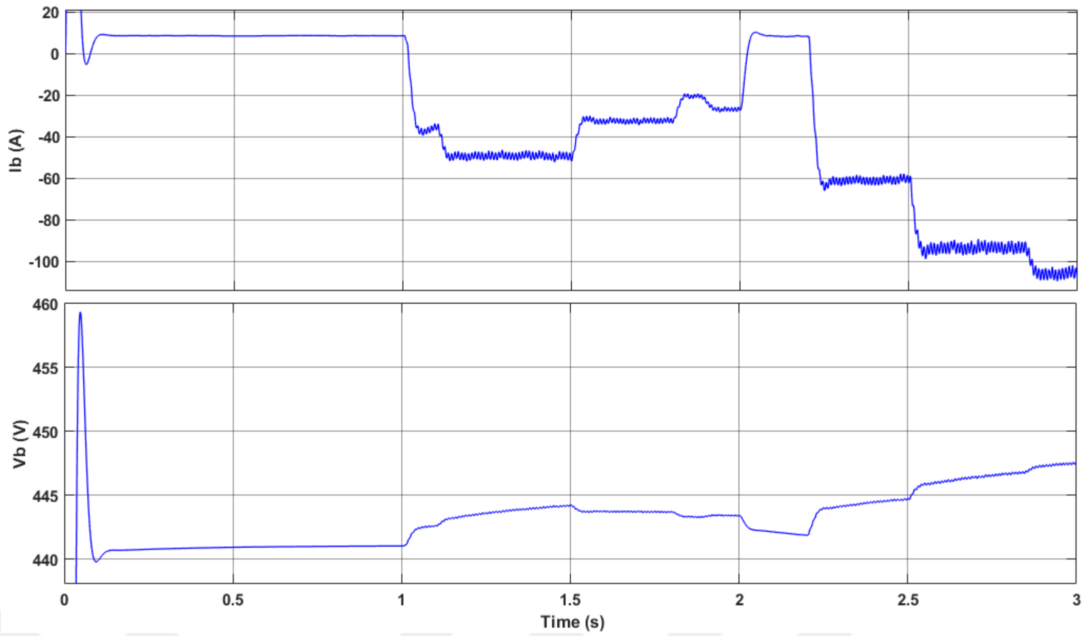

Figure 4.13 The current and voltage waveforms of battery 5.

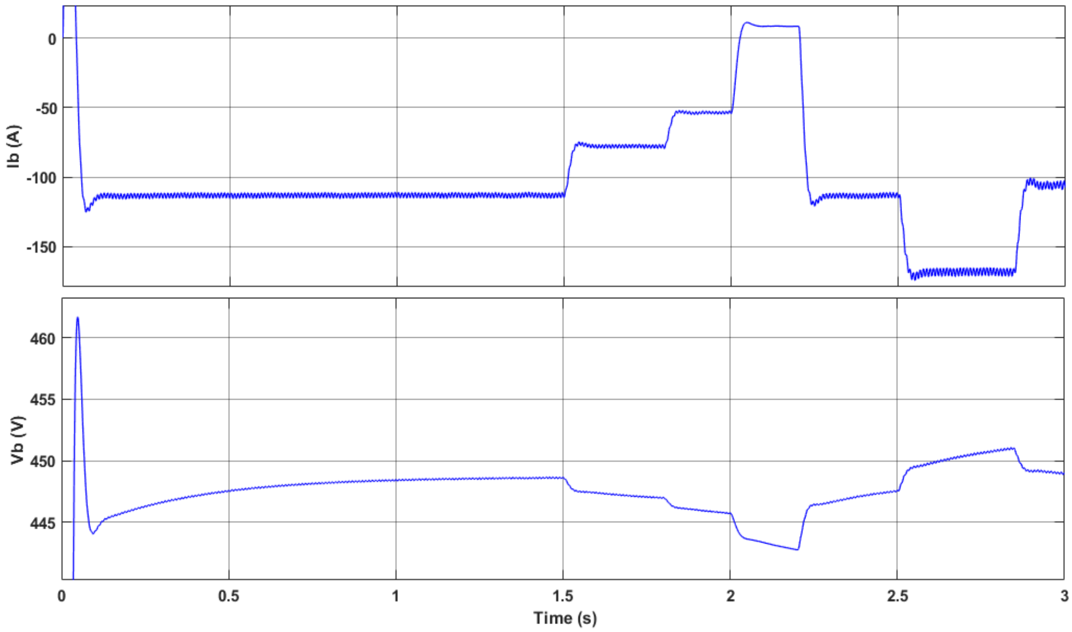

Figure 4.14 The current and voltage waveforms of battery 6.

4.2 Case 2: Active Power Control (Discharging)

In this case study, the simulation settings are same as in the first case study, but the initial SOC of each battery module is given near 80%, as listed in Table 4.3.

Table 4.3 Initial SOC of the battery modules.

Battery	SOC (%)
B1	80.01
B2	80.02
B3	80
B4	80.015
B5	80.03
B6	79.99

Arbitrary negative active power set points are given to the respective controller to inject active power into the grid to realize BESS discharging while maintaining constant zero reactive power to ensure unity power factor operation. The simulation starts by setting the active power reference to -1 pu at t=0 s which is followed successfully after short transients as shown in Figure 4.15. At t=1.5 s, the active power reference is decreased to -0.7 pu followed by another decreased to -0.5 pu at t= 1.8 s until it set to 0 pu at t=2 s. The system is set back to 1 pu at t = -2.2 s which is finally increased to -1.5 pu at t= 2.5 s until the end of the simulation. It is observed that the controller was able to successfully follow the given reference set point for the active power with a fast response and zero steady-state error.

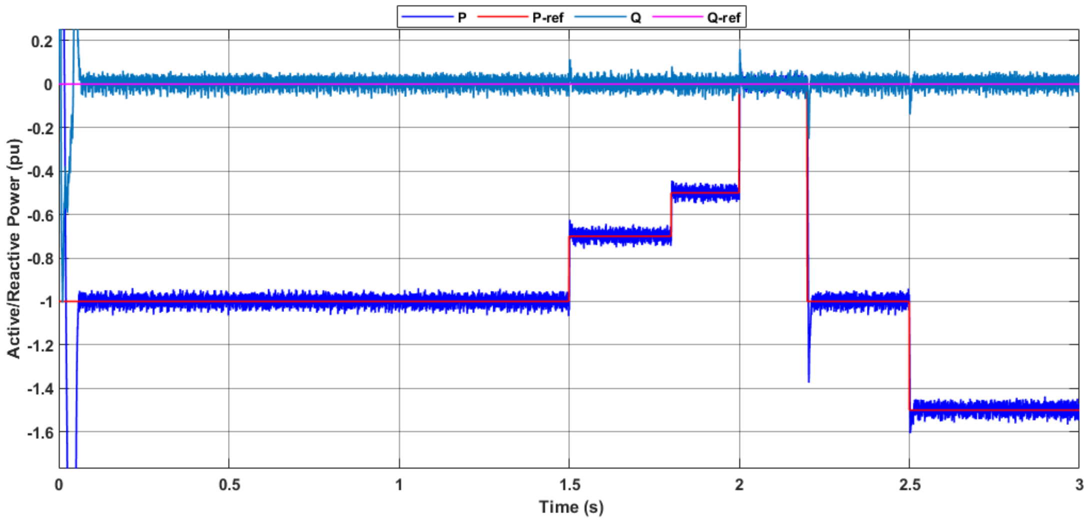

Figure 4.15 The dynamic performances of the active and reactive power controllers.

The output voltage and current for phase-A of CHB-BESS is recorded and shown in Figure 4.16, bearing the same concept during charging. Three-phase voltage and current profile at PCC are depicted in Figure 4.17. As it appears, both the voltage and current waveforms exhibit acceptable sinusoidal form with the voltage and current waveforms are 180° out of phase which indicates unity power factor operation. BESS is behaving as an active power generator. According to Figure 4.18, the THD of the voltage is recorded as 4.24% during the first simulation period when active power is at -1 pu. The current THD, on the other hand, is obtained as 2.97%. The recorded THD values during discharging operation are listed in Table 4.4 and compared with the standards of IEE 519 for systems with bus voltage of 69kV and below. Accordingly, the obtained THD for both the voltage and current at the PCC are considered acceptable and within the IEEE 519 regulations. Those THD values can be further improved if more voltage levels are added in the CHB by including more SMs.

Table 4.4 Total Harmonic Distortion During Discharging Operation.

Description	Voltage THD in %	Current THD in %
11-level CHB	4.24	2.97
IEEE 519 Maximum Standard	5	5

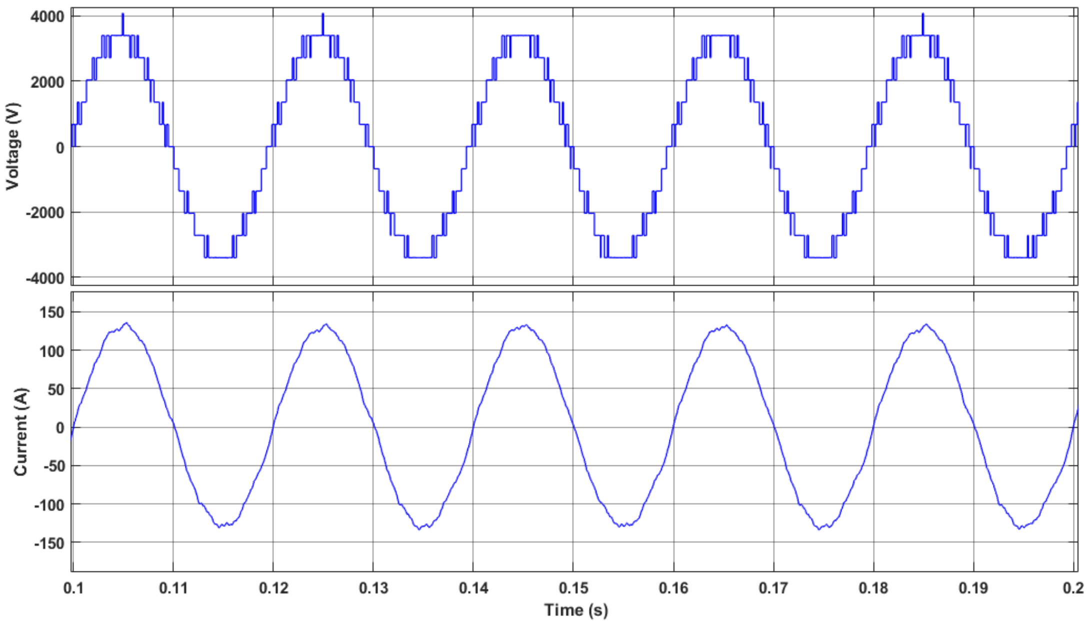

Figure 4.16 The output voltage and current of phase-A of 11-level CHB.

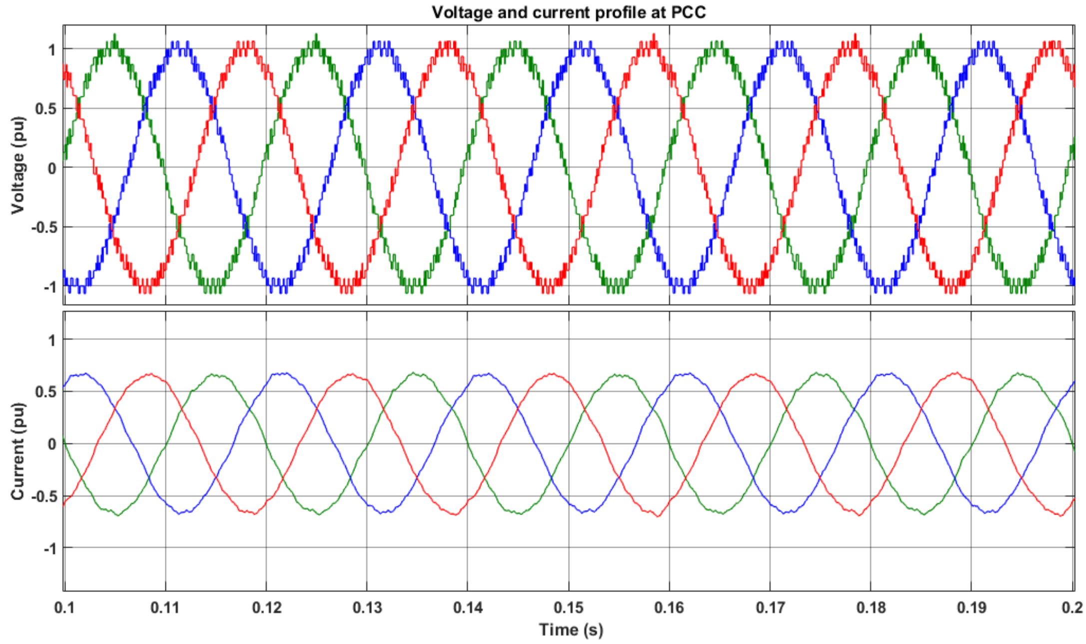

Figure 4.17 Three-phase voltage and current profiles at PCC.

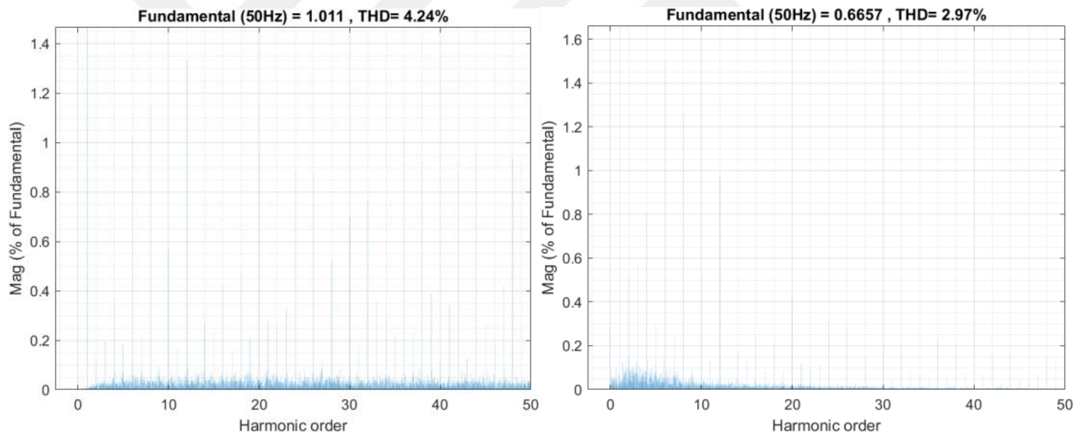

Figure 4.18 THD analysis during discharging (a) voltage (b) current waveforms.

The initial SOC values presented in Table 4.3 are considered in this case study. The SOC of the battery banks for phase-A without in-phase balancing scheme is demonstrated in Figure 4.19. It is obvious that each battery SOC keeps on discharging on the same pace with no regard to other battery SOC which eventually leads to unbalanced SOC. The difference gap in SOC between each battery keeps growing until a significant difference emerges limiting the whole BESS operation capability. Additionally, the redundant battery is inoperative as its SOC is nearly constant. On the other hand, by including in-phase SOC balancing allows to discharge all the batteries at the same rate reaching nearly equal SOC for all batteries as shown in Figure 4.20. Also, it enables for the utilization of all batteries including the redundant battery as it starts discharging with all the other battery while the battery with the least SOC takes the place and stops discharging, thus, allowing to reduce the strain on the batteries while discharging.

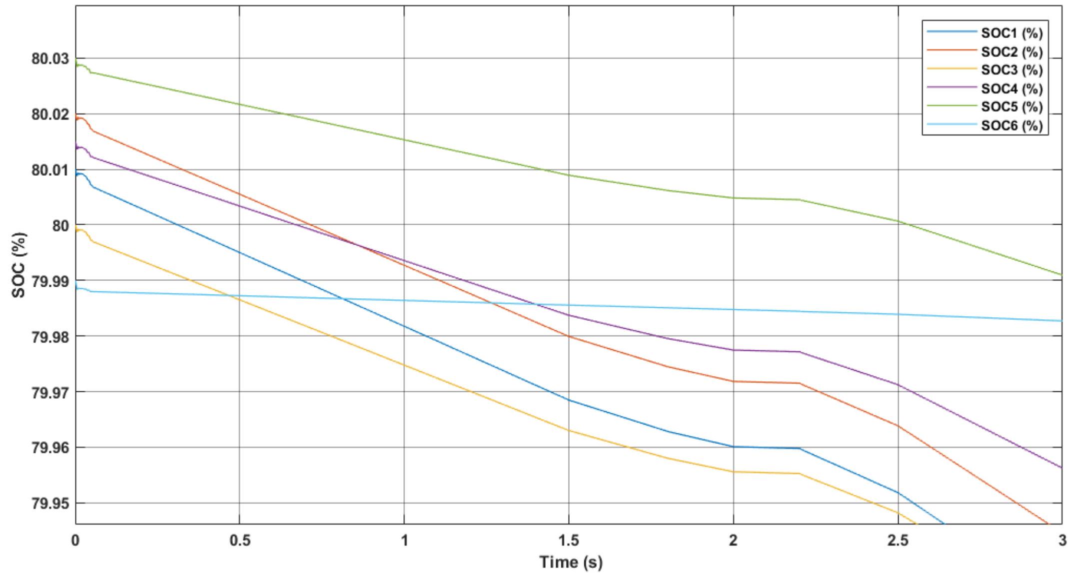

Figure 4.19 The SOC of the batteries for phase-A without in-phase balancing scheme.

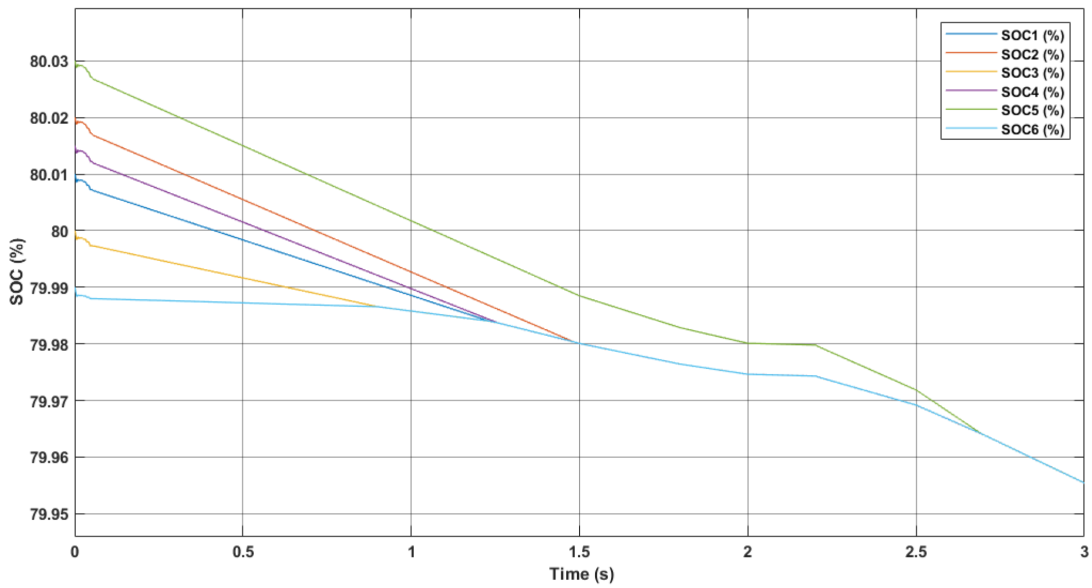

Figure 4.20 The SOC of the batteries for phase-A with in-phase balancing scheme.

The dc-link voltage was fixed at 680 V for all SMs to generate the required 11-level output voltage to meet the voltage requirement of 4160 V (line-to-line) at the PCC. This was realized using ES-FBL control scheme to regulate dc-link voltage at each SM through linearizing the dc side model under all operation conditions that showed spectacular performance in maintaining the desired voltage throughout the simulation period with varying power set points, as seen in Figure 4.21. There was a minimum amount of voltage throughout the simulation time. However, there were some fluctuations at the dc-link voltages for all SMs when the BESS were injecting 1.5pu active power at t=2.5 s which is not significant. There were minor voltage fluctuations at t=1.3 s for Vdc1 and Vdc4, as their carrier waves were frequently interchanged at that time. Similarly, Vdc3 and Vdc6 introduced trivial noise between t=0.9 s and t=1.5 s due to SOC balancing operation.

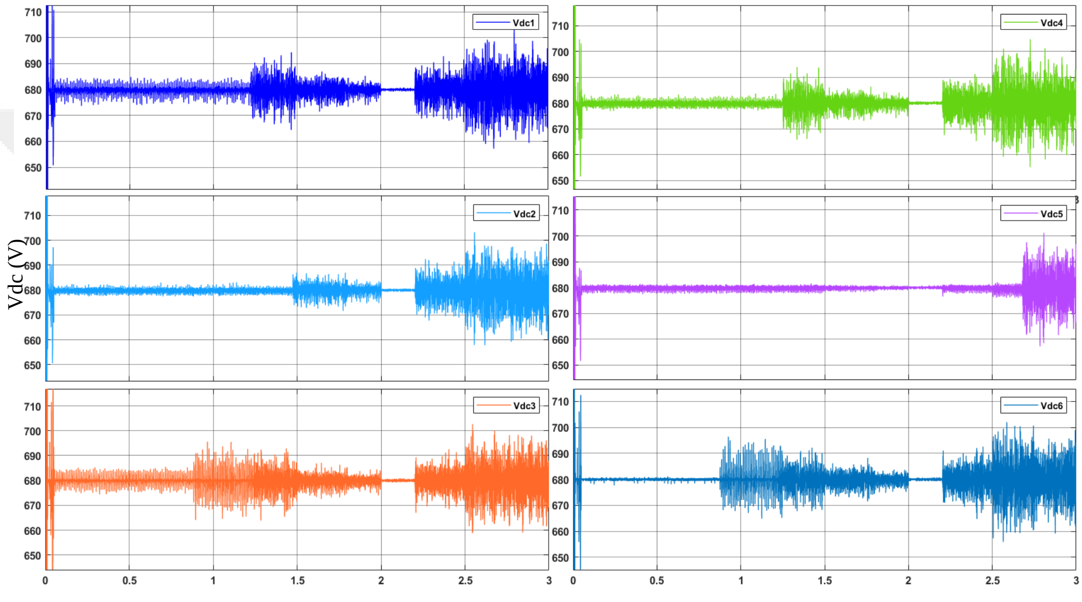

Figure 4.21 DC-link voltages of CHB SMs for phase-A.

Looking at the current and voltage behaviors of battery 1 in Figure 4.22, it is quite evident that the battery exhibits pulsating discharging behavior caused by DC-DC converter switching as the battery is discharging at pulsating current and the voltage slightly decreases until it settles at certain value. Here, the current is discharging at average current of 134 A between t=0 s and t=1.3 s and the voltage settles at nearly 435 Volt of average battery voltage, a minus current indicates that the battery is charging while positive current discharges the battery. Moreover, looking at battery3 and battery6 in Figure 4.10 and Figure 4.13, respectively, it is clear that those batteries are discharging lesser than the other batteries due to their lower SOC values. On the other hand, batteries 2 and 5 are discharging the most throughout the discharging process due to their highest SOC values compared to other batteries. As this operation continues, the discharging current for each battery keeps on varying based on their SOC to maintain SOC balance between all the battery units.

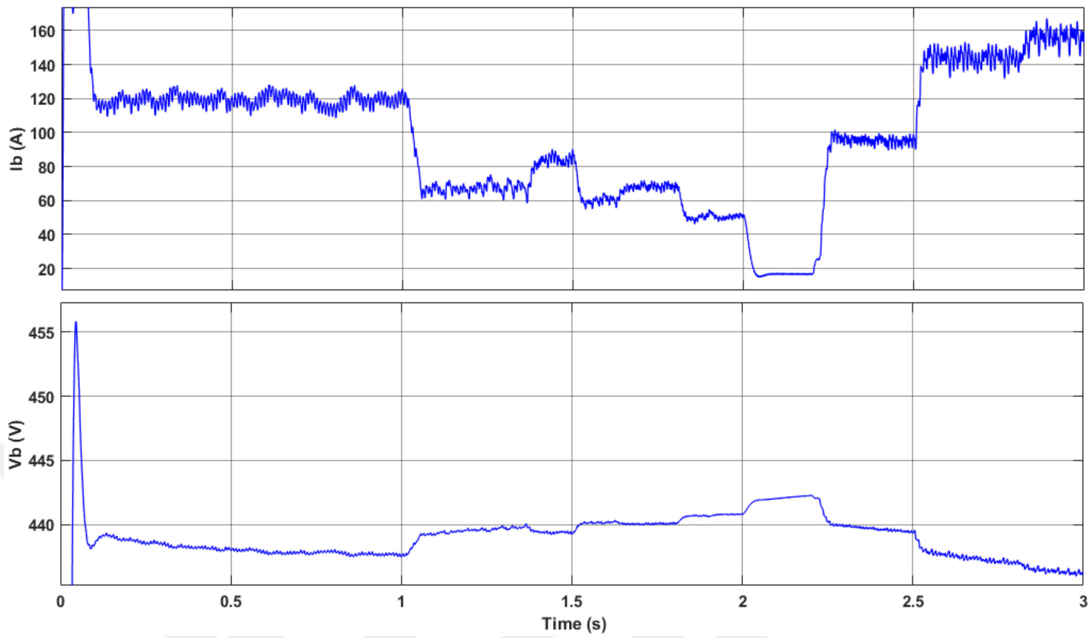

Figure 4.22 The current and voltage waveforms of battery 1.

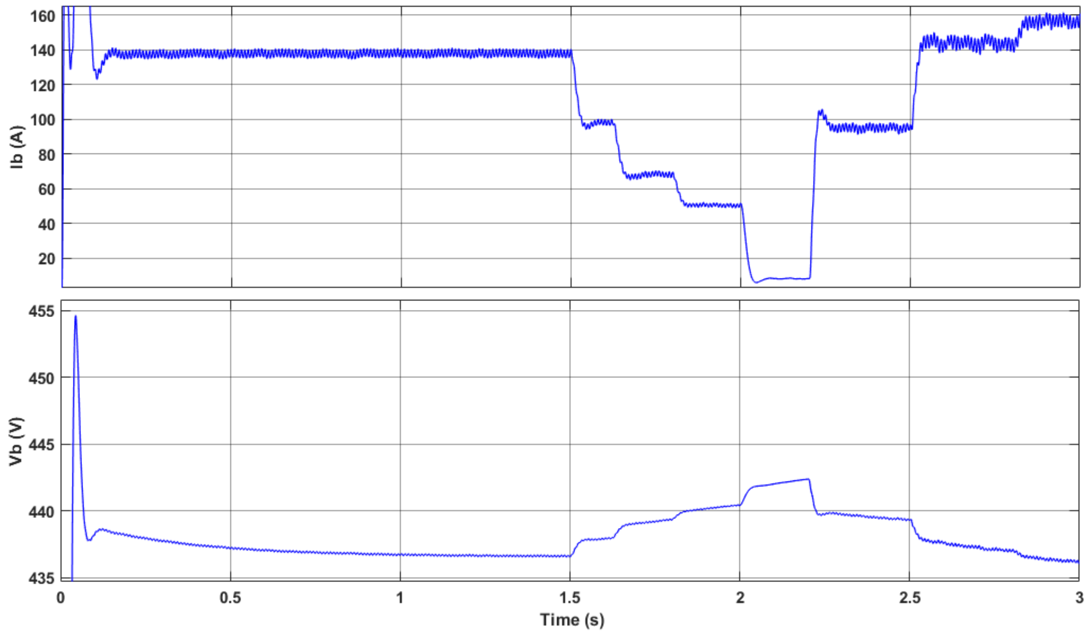

Figure 4.23 The current and voltage waveforms of battery 2.

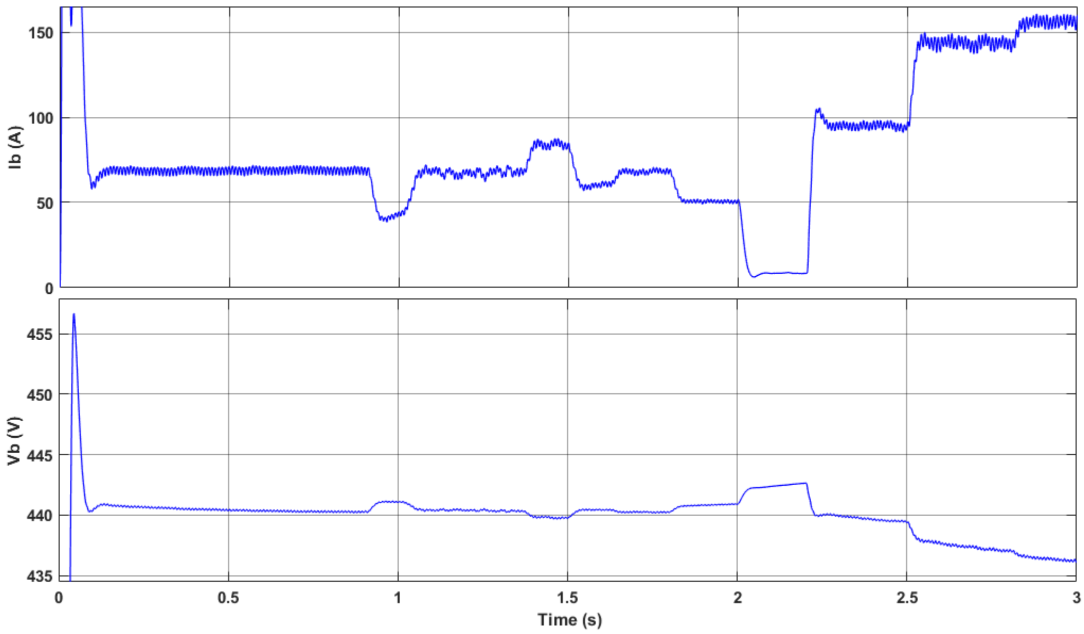

Figure 4.24 The current and voltage waveforms of battery 3.

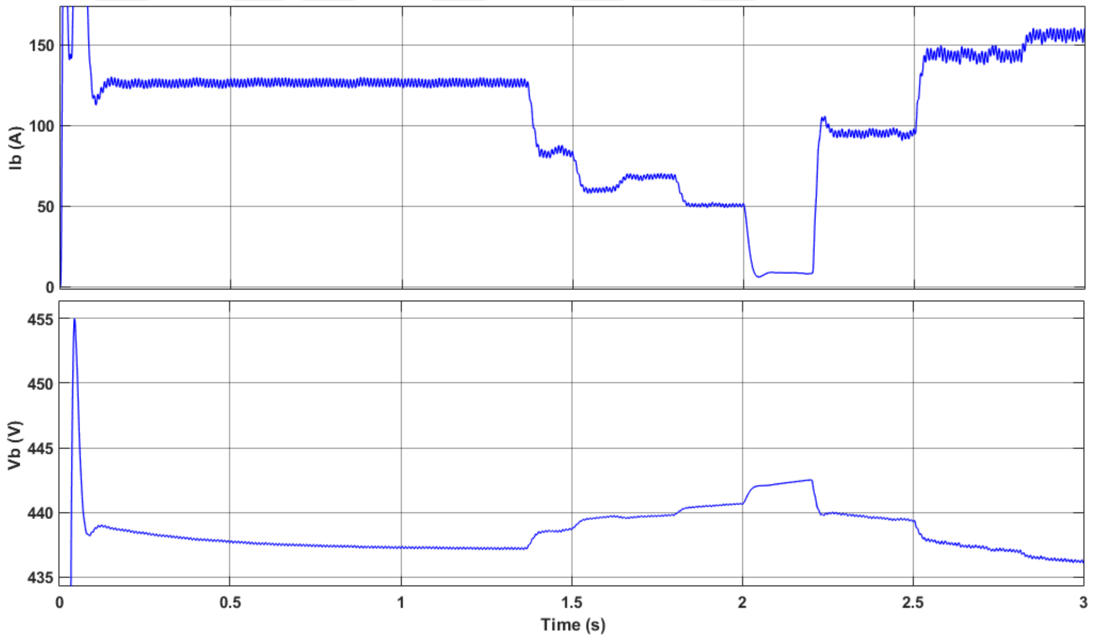

Figure 4.25 The current and voltage waveforms of battery 4.

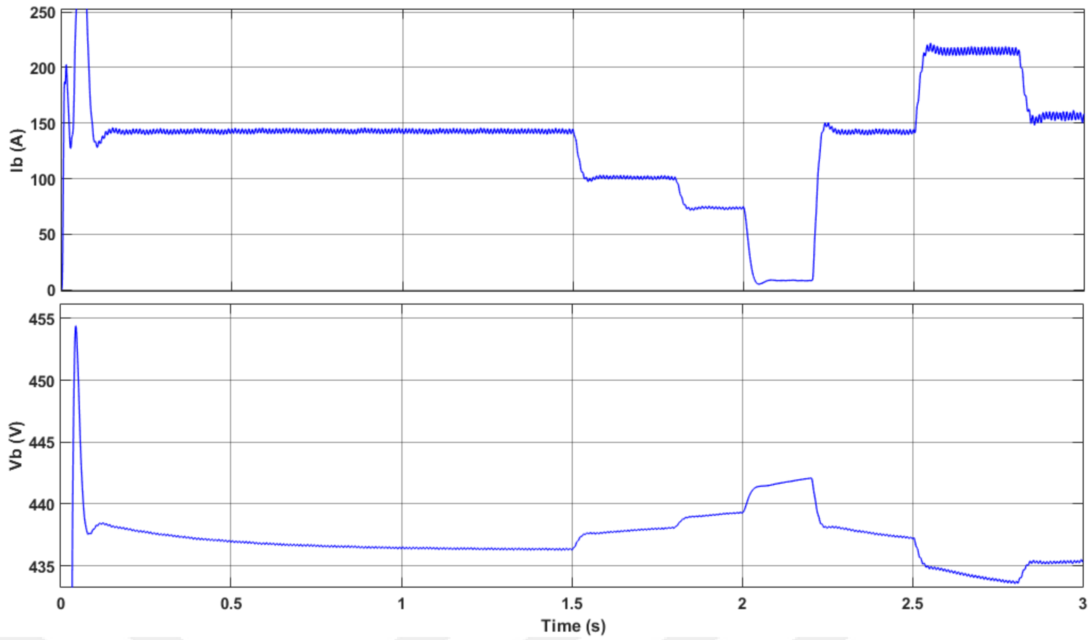

Figure 4.26 The current and voltage waveforms of battery 5.

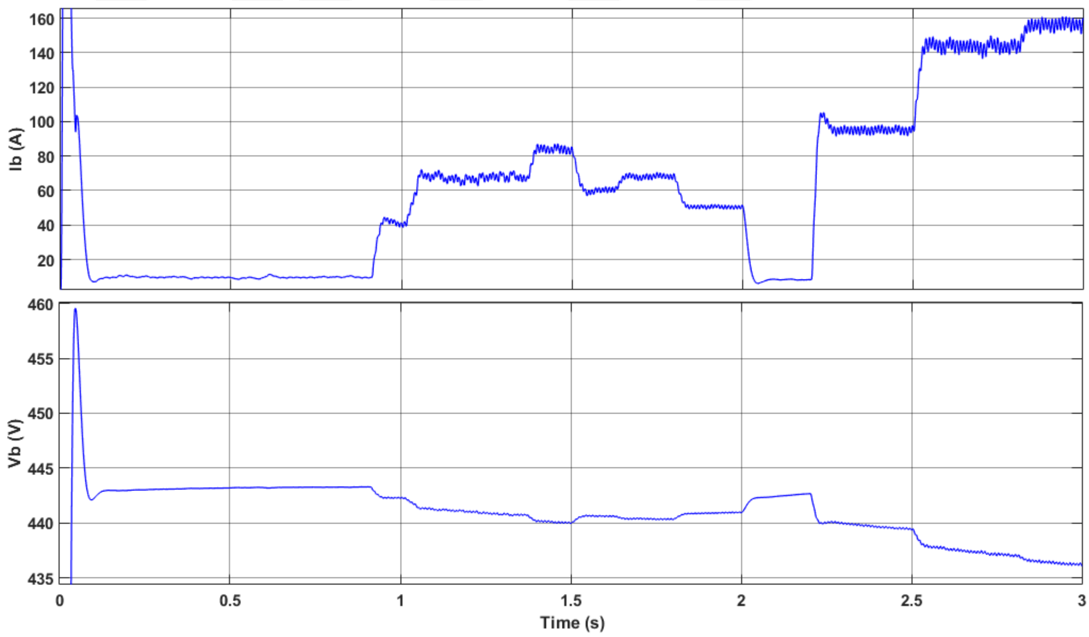

Figure 4.27 The current and voltage waveforms of battery 6.

4.3 Case 3: STATCOM Operation (Charging)

In this case study, the performance and capability of the CHB-BESS for STATCOM operation to inject both inductive and capacitive reactive power into the grid while charging the batteries is tested and verified through simulation. The SOC initial values are set the same as given in Table 4.2. Observably from Figure 4.28, the arbitrary reactive power set points are given to the respective controller to inject capacitive and inductive reactive power into the grid, while the active power is fixed throughout the operation. The simulation starts by setting the active power reference to 0.5 pu for the entire simulation period while reactive power is set to zero. At t=0.3 s, the inductive reactive power of 0.3 pu is injected into the grid followed by an increase to 1 pu at t=0.8 s, that is later reduced to 0 pu at t=1.7 s. Subsequently, at t=1.8 s, the CHB starts injecting capacitive reactive power into the grid at -0.5 pu followed by an increase to -1 pu at t=2.3 s, which continues until the simulation ends at t=3 s. Conclusively, the controller was able to successfully track the given reference set point for both the active and reactive powers with a fast response and zero steady-state error.

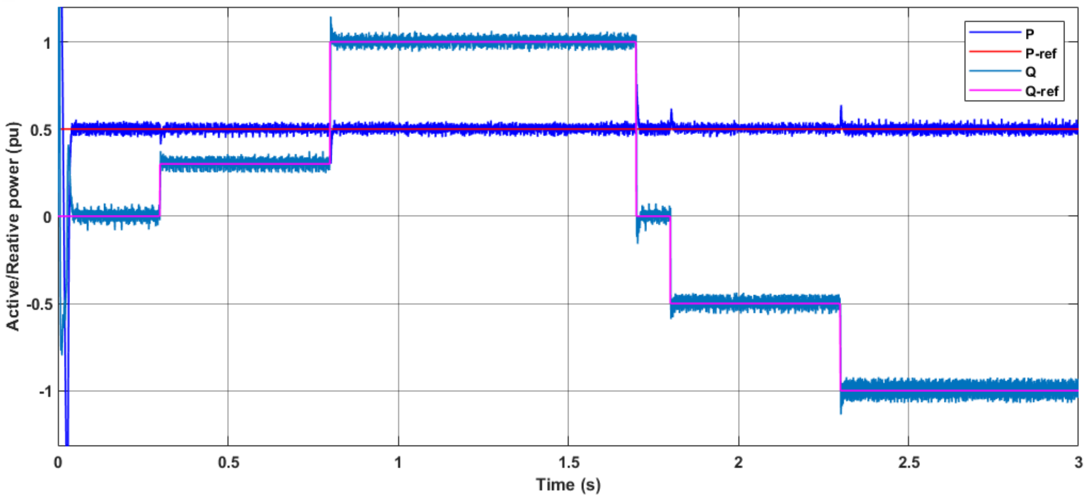

Figure 4.28 The dynamic performances of the active and reactive power controllers.

The output voltage and current for phase-A of 11-level CHB-BESS is recorded and shown in Figure 4.29 for inductive reactive power operation and in Figure 4.30, for capacitive reactive power operation, respectively. As expected, when the BESS is injecting inductive reactive power, the voltage slightly drops. Oppositely, the voltage rises slightly during capacitive STATCOM operation. These results clearly show that the BESS can smoothly participate in voltage support to help maintain the grid voltage within its code limits if it is used in real case scenario. Three-phase voltage and current profile at PCC are depicted in Figure 4.31 and Figure 4.32, for both inductive and capacitive STATCOM operations, respectively. Obviously, it can be noted that power factor is lagging during inductive STATCOM operation, while it is leading during capacitive STATCOM operation.

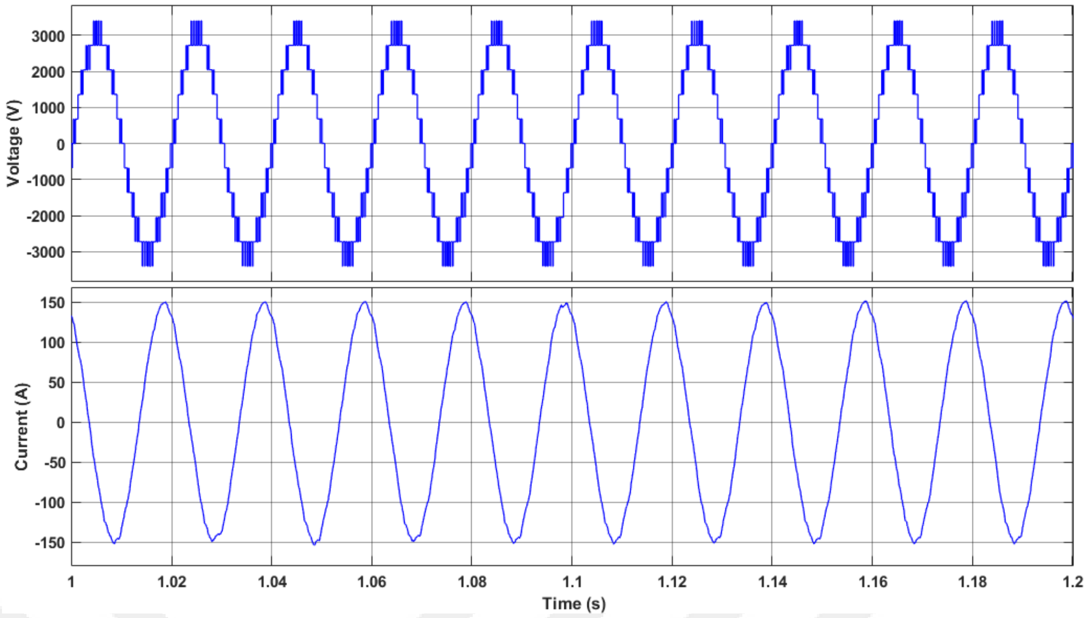

Figure 4.29 The output voltage and current of phase-A of 11-level CHB during inductive STATCOM operation.

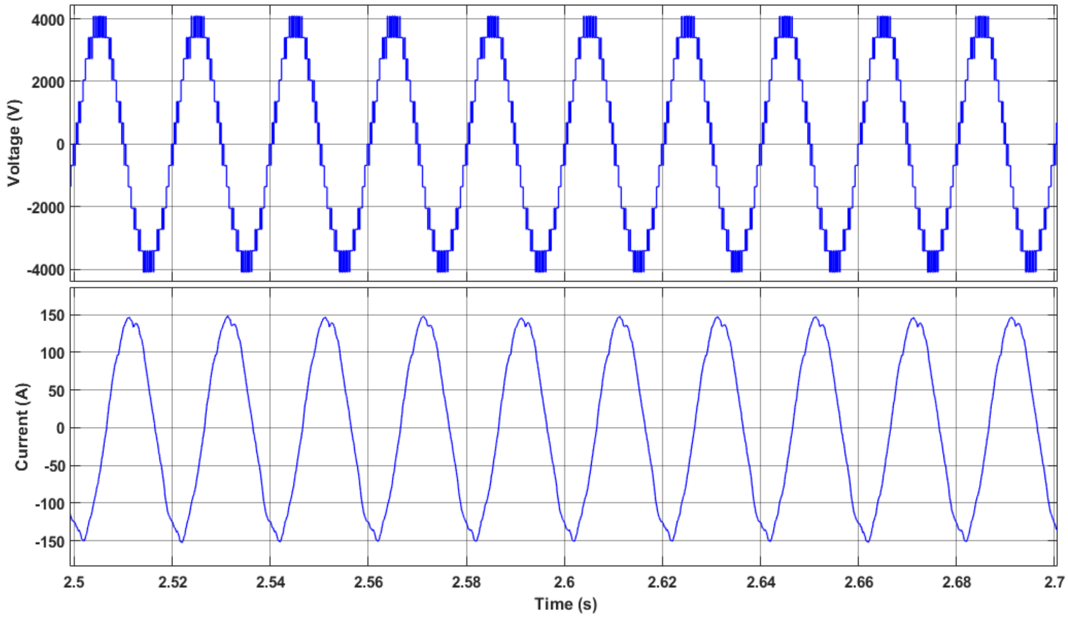

Figure 4.30 The output voltage and current of phase-A of 11-level CHB during capacitive STATCOM operation.

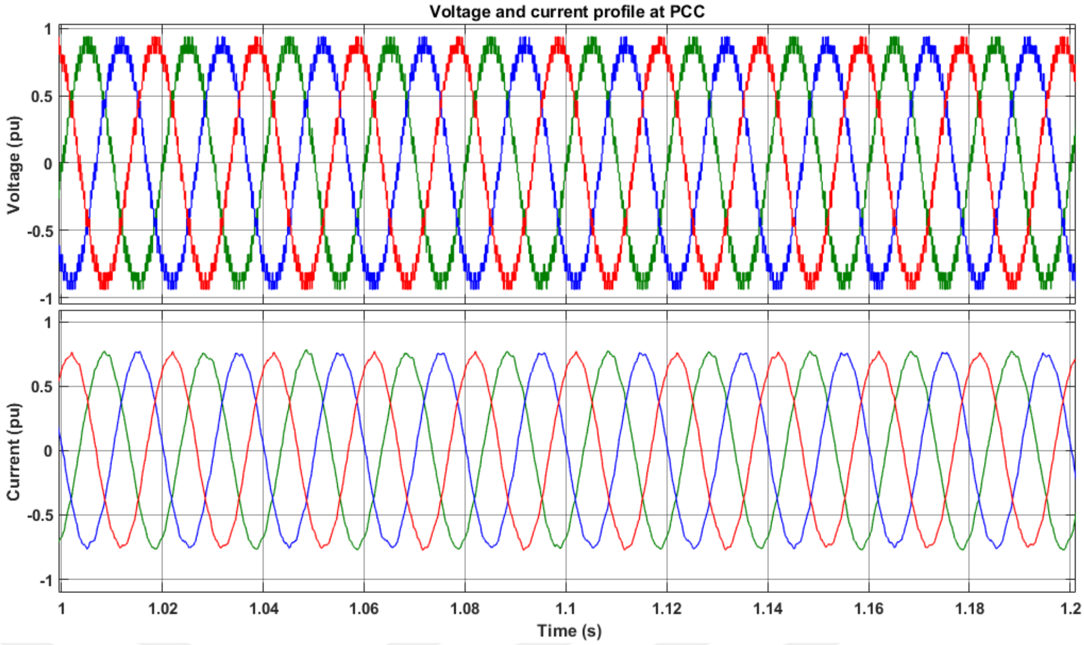

Figure 4.31 Three-phase voltage and current profiles at PCC during inductive STATCOM operation.

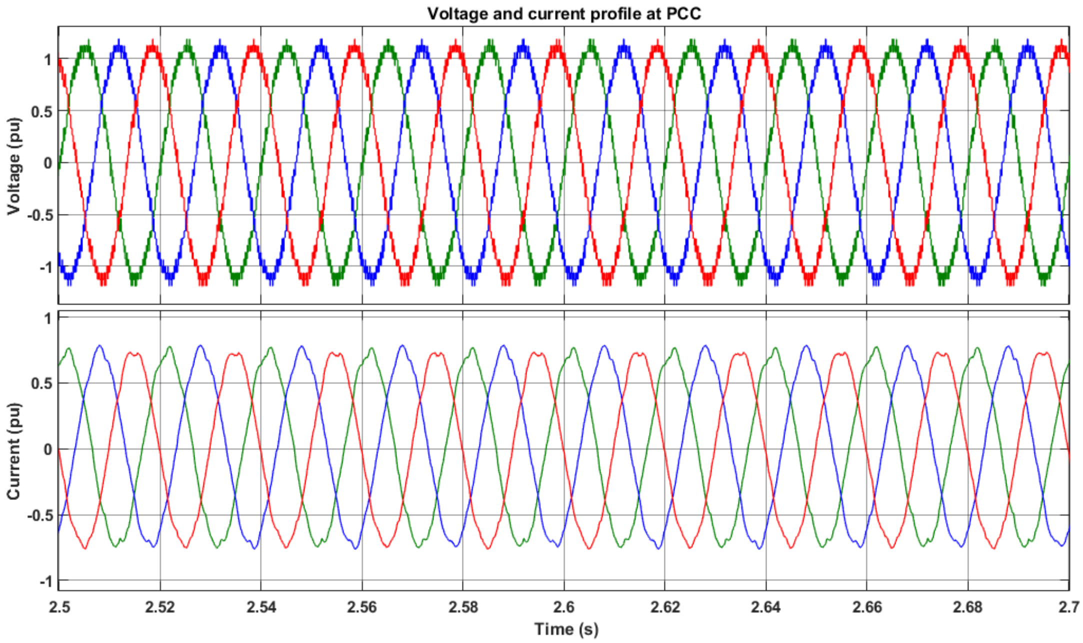

Figure 4.32 Three-phase voltage and current profiles at PCC during capacitive STATCOM operation.

Figure 4.33 shows the dc-link voltages for all SMs. It is clearly observed that the waveforms are stable within their reference values throughout the simulation period within both the inductive STATCOM operation from t=0.3 s. to t=1.7 s, and the capacitive STATCOM operation from t=1.8 s to t=3 s.

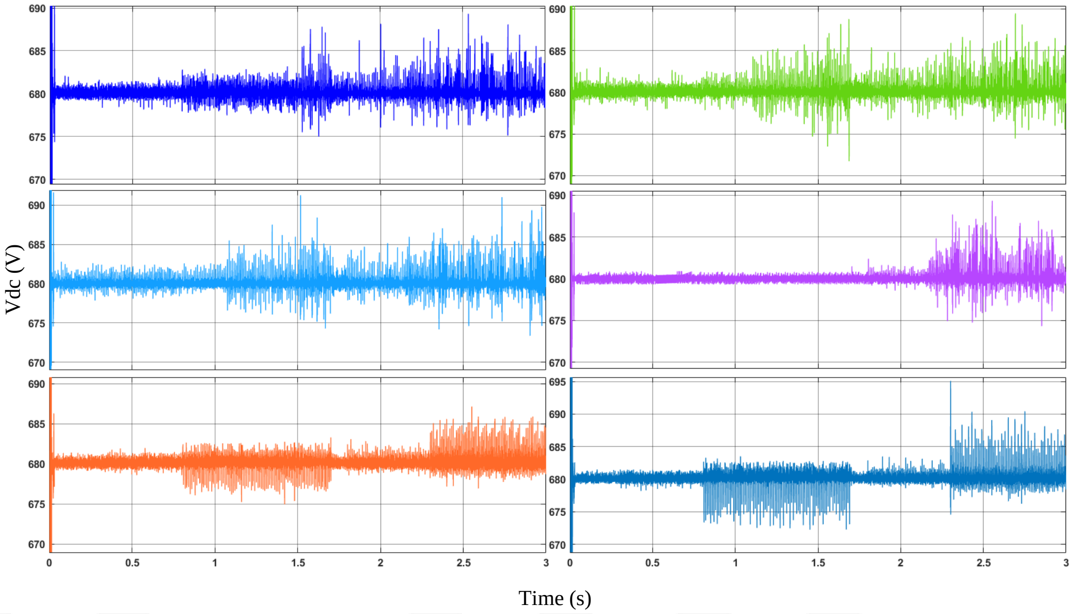

Figure 4.33 DC-link voltages of CHB SMs for phase-A.

As the active power is fixed at 0.5 pu, the batteries are expected to charge at a constant rate while the SOC balancing scheme is ON which can be observed in Figure 4.34.

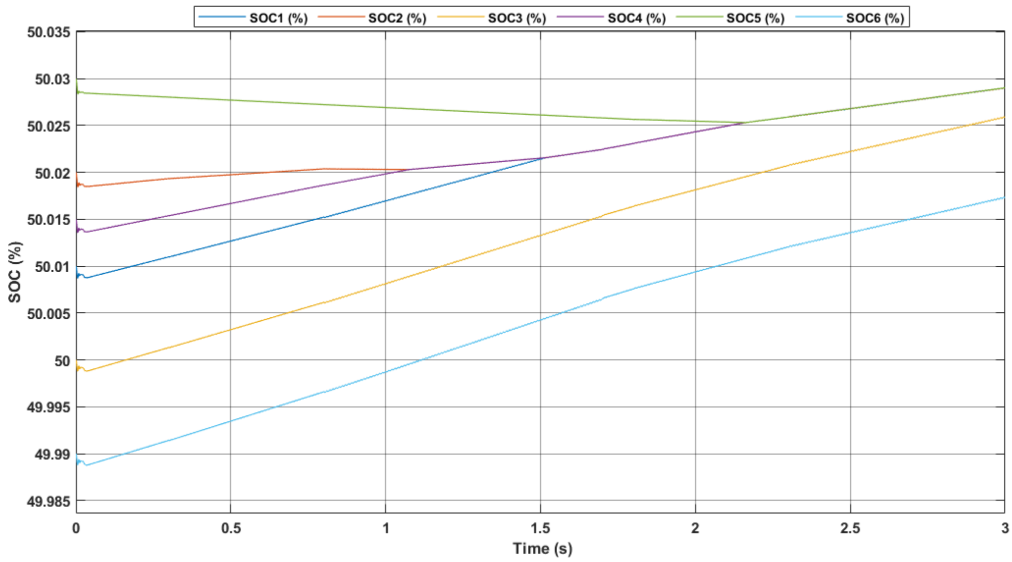

Figure 4.34 The SOC of the batteries for phase-A with in-phase balancing scheme.

Figure (4.35)-(4.40) shows the current and voltage waveforms for batteries 1 to 6. It can be seen that the most batteries charge at low rate and only battery 3 and 6 are charging during the entire simulation period due to their lower SOC values compared to the other batteries.

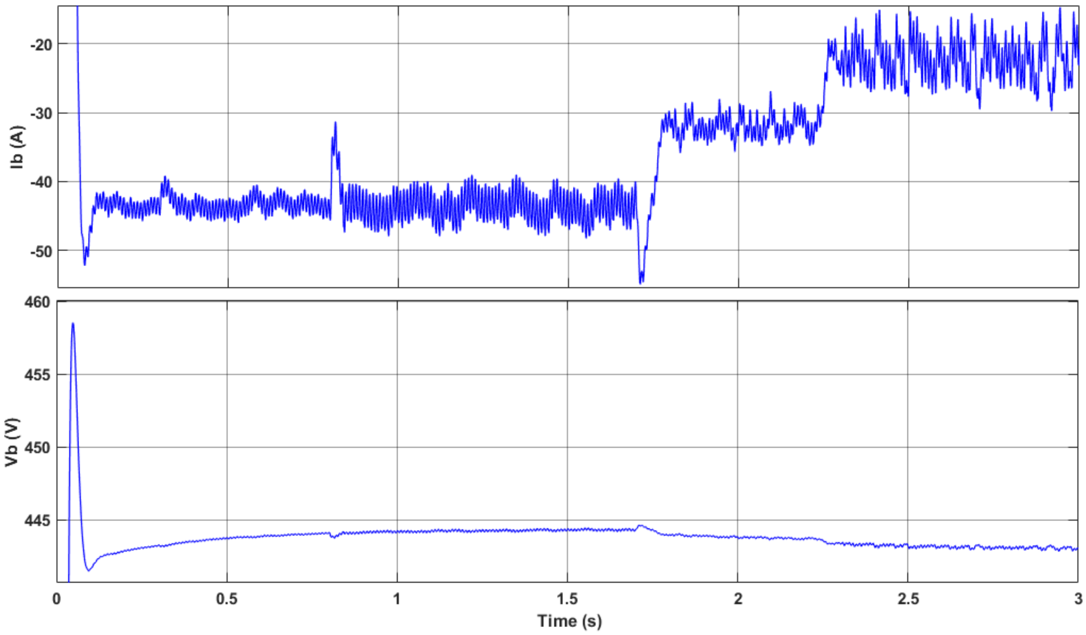

Figure 4.35 The current and voltage waveforms of battery 1.

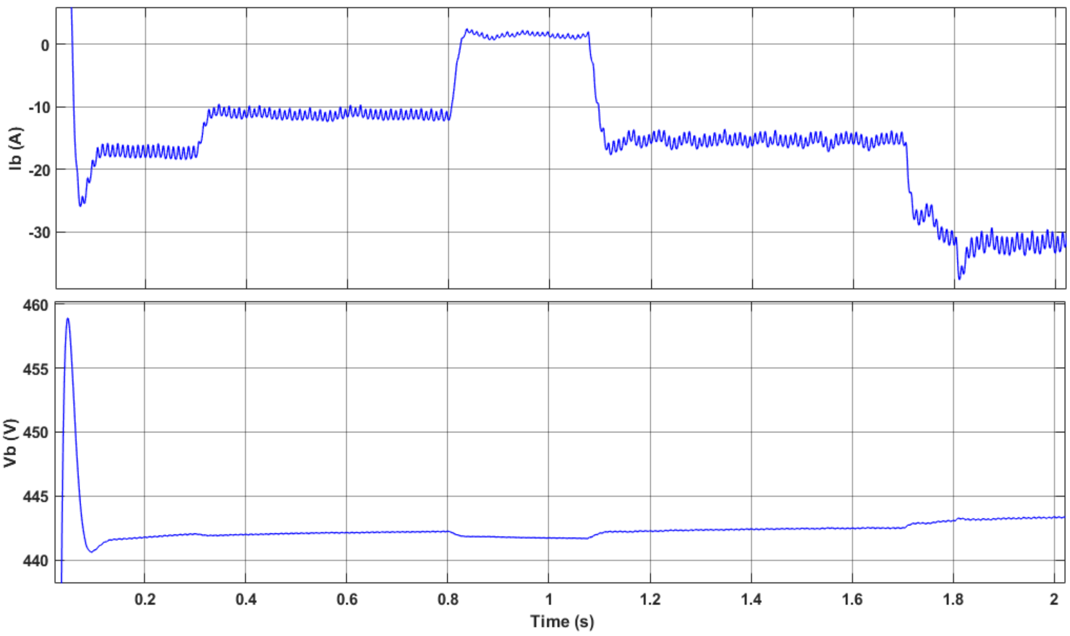

Figure 4.36 The current and voltage waveforms of battery 2.

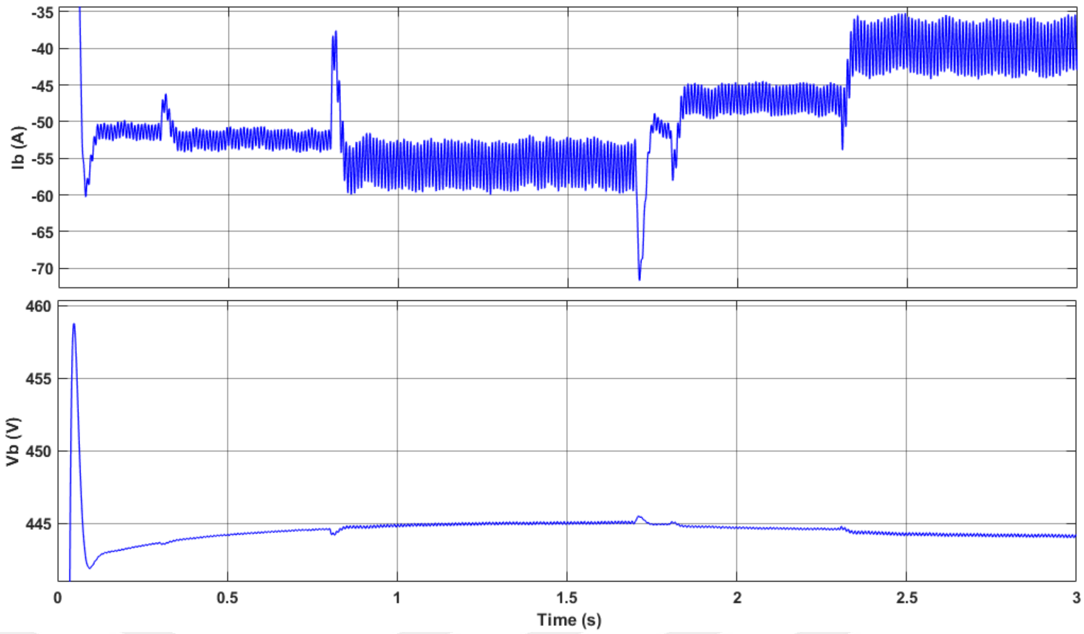

Figure 4.37 The current and voltage waveforms of battery 3.

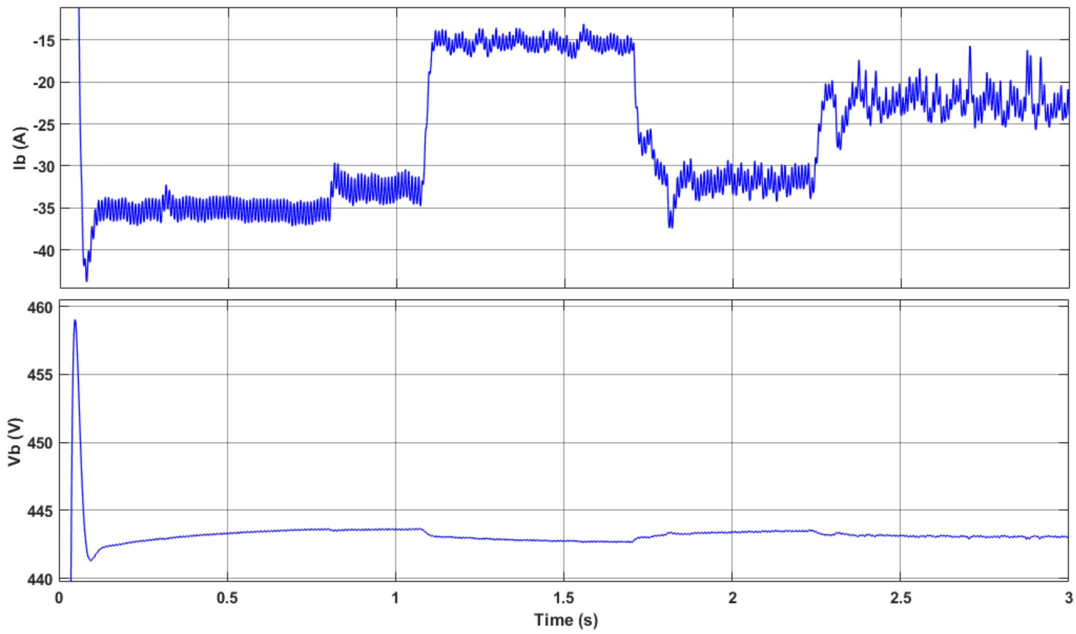

Figure 4.38 The current and voltage waveforms of battery 4.

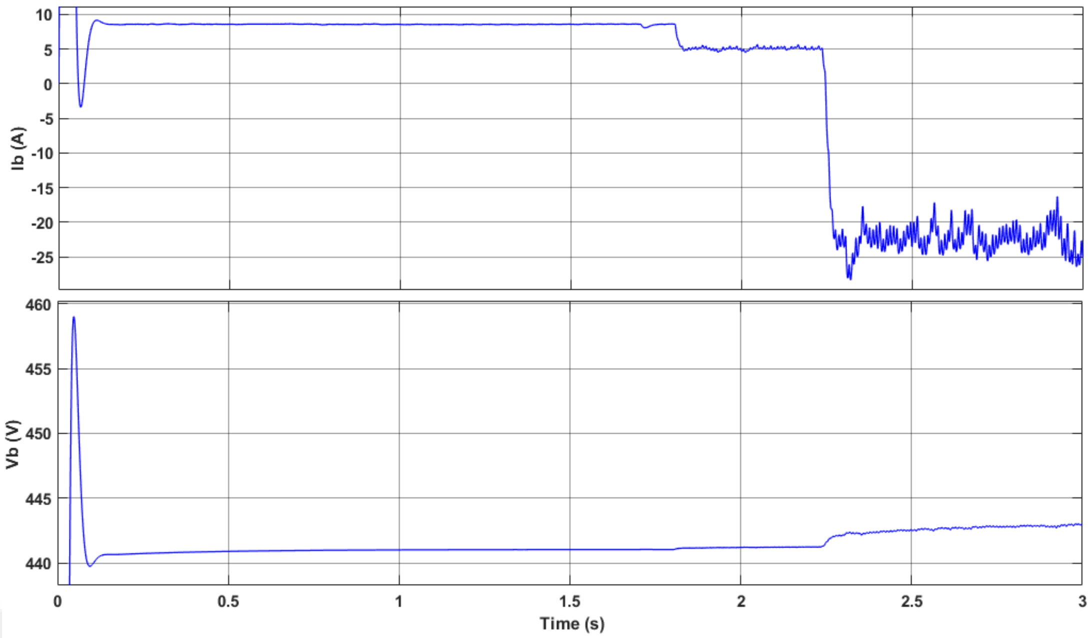

Figure 4.39 The current and voltage waveforms of battery 5.

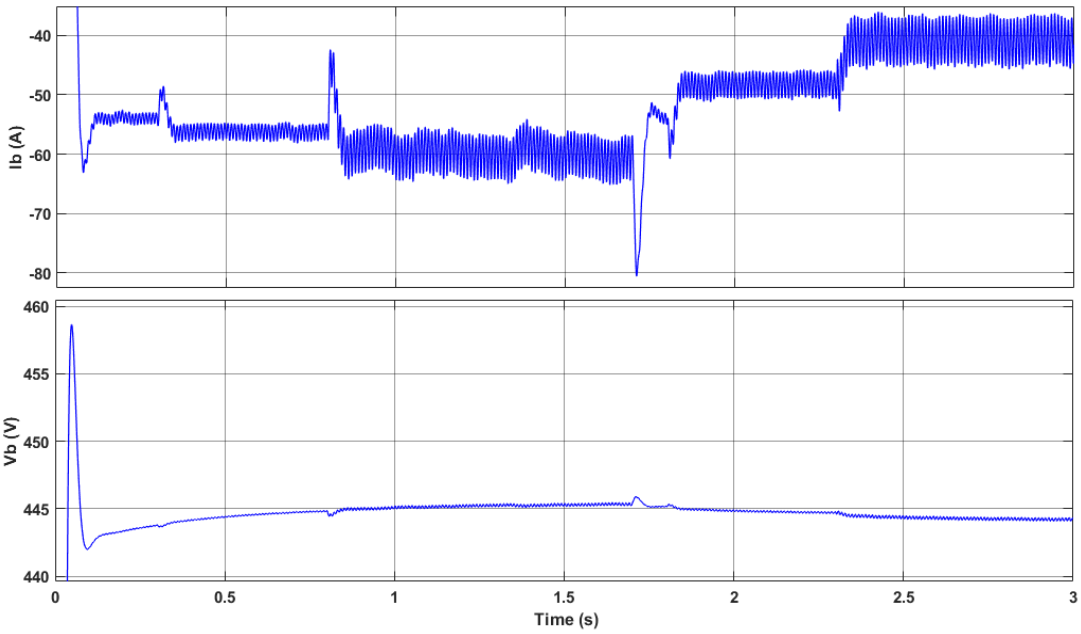

Figure 4.40 The current and voltage waveforms of battery 6.

4.4 Case 4: STATCOM Operation (Discharging)

In this case study, the performance and capability of the CHB-BESS for STATCOM operation to inject both inductive and capacitive reactive power into the grid while discharging the batteries are tested and verified through simulations. The SOC initial values are set the same as the ones listed in Table 4.3. Figure 4.41 shows the controller performance of the BESS in this mode of operation. Arbitrary reactive power set points are applied to the controller to inject capacitive and inductive reactive power into the grid while the active power is fixed throughout the operation. The simulation starts by setting the active power reference to -0.5 pu for the entire simulation period while reactive power is set to zero. At t=0.3 s, an inductive reactive power of 0.3 pu is injected into the grid followed by an increase to 1 pu at t=0.8 s that is later reduced to 0 pu at t=1.7 s. Subsequently, at t=1.8 s, CHB start injecting capacitive reactive power into the grid at -0.5 pu followed by an increase to -1 pu at t=2.3 s which continues until the simulation ends. Conclusively, it seen that the controller was able to successfully track the given reference set point for both the active and reactive powers with a fast response and zero steady-state error.

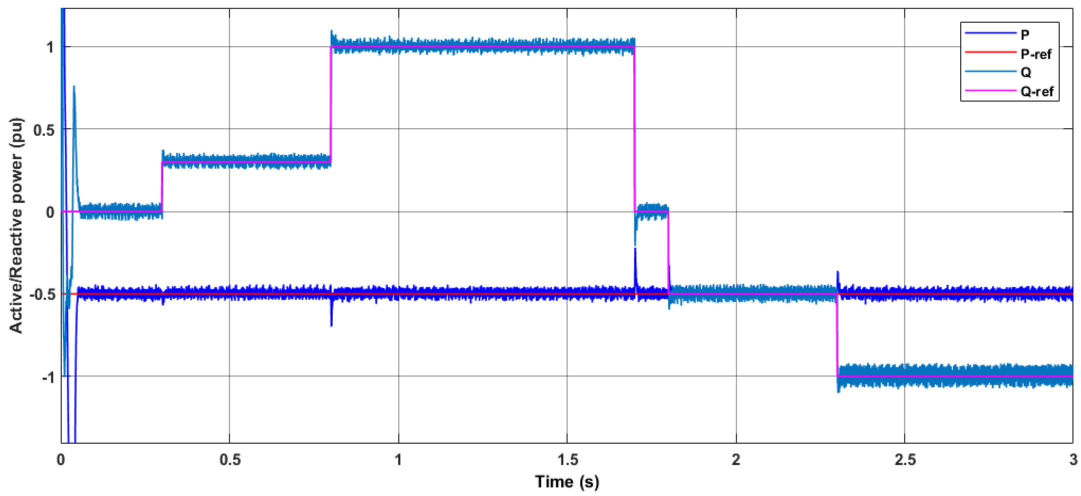

Figure 4.41 The dynamic performances of the active and reactive power controllers.

Figures 4.42 and 4.43 shows three-phase voltage and current profiles at PCC for the 11-level CHB-BESS during inductive and capacitive STATCOM operations during discharging, respectively. Similar to the previous case studies, the voltage drops during inductive reactive power injection with a leading power factor. In contrast, a slight voltage rise occurs as capacitive reactive power is injected into the grid with a lagging power factor. The dc-link voltages for phase-A SMs are depicted in Figure 4.44. Accordingly, it is observed that the ES-FBL control scheme was able to maintain the voltage at the dc-link capacitor at 680 V throughout the simulation time under different conditions. However, there are some noises introduced between t=0.8 s-1.7 s and t=2.3 s-3 s, which is caused mainly by a slight residual error between the reference and measured values of the inductor current for the DC-DC converter controller.

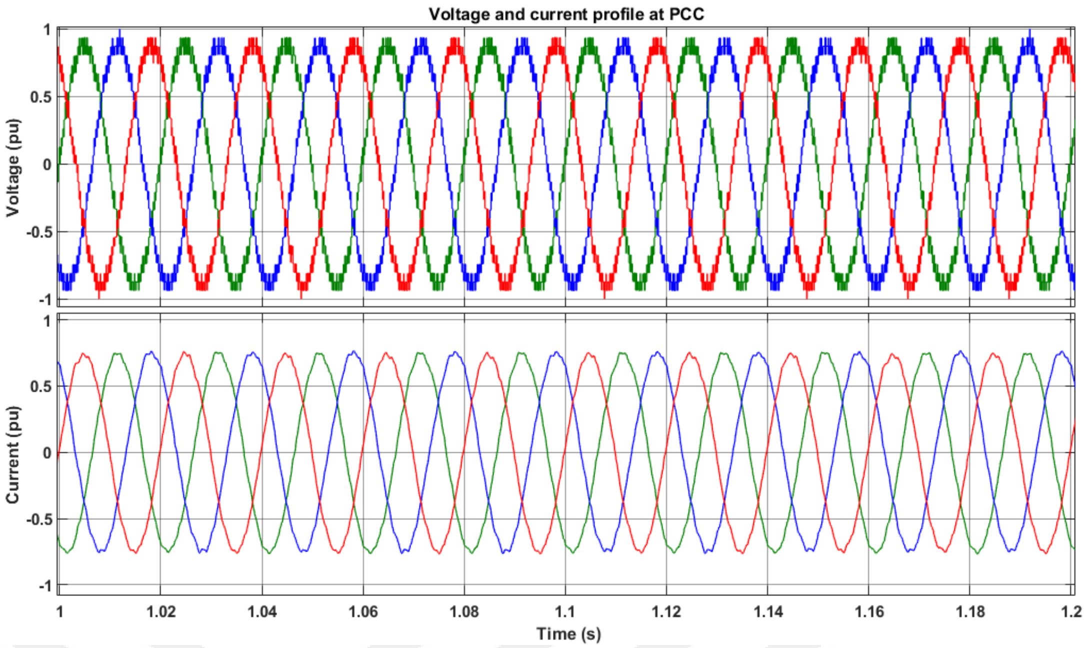

Figure 4.42 Three-phase voltage and current profiles at PCC during inductive STATCOM operation.

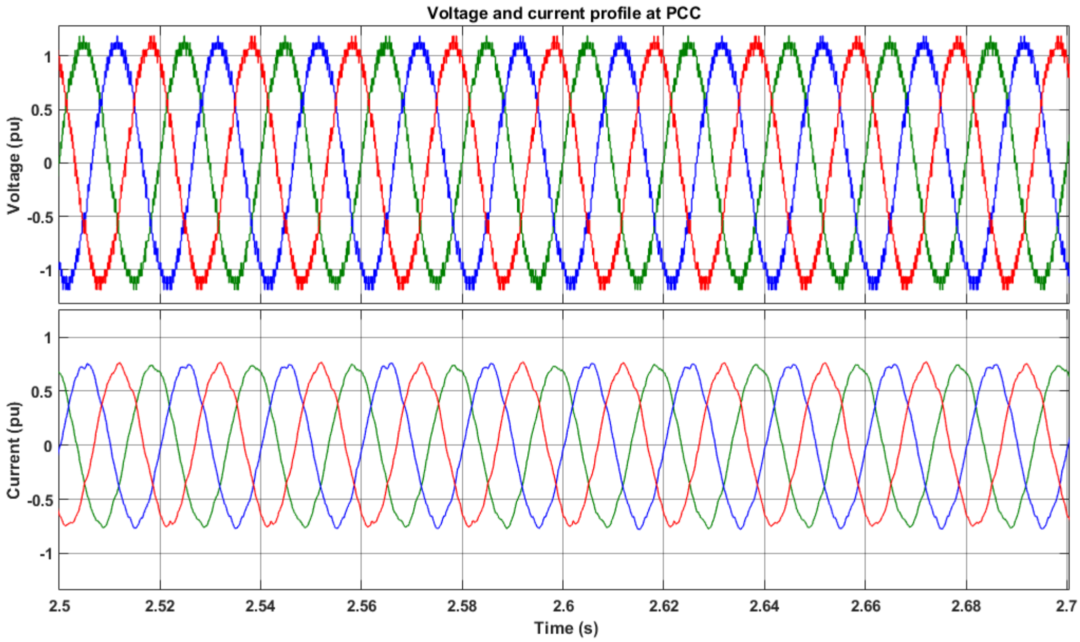

Figure 4.43 Three-phase voltage and current profiles at PCC during capacitive STATCOM operation.

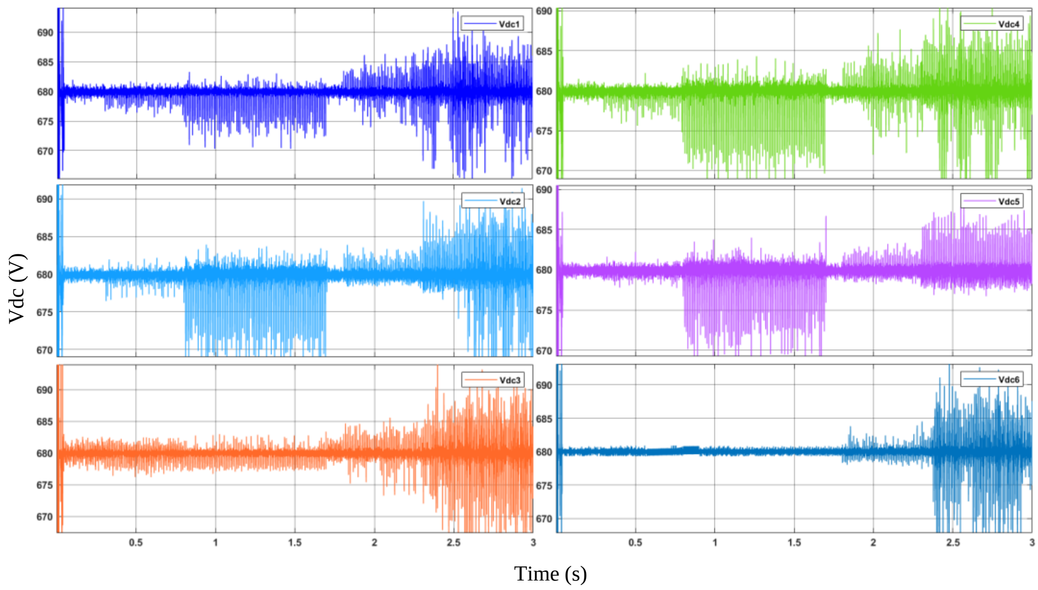

Figure 4.44 DC-link voltages of CHB SMs for phase-A.

As the active power is fixed at -0.5 pu, throughout the simulation, nearly all the batteries discharge at steady constant rate while SOC in-phase balancing is ON as shown in Figure 4.45.

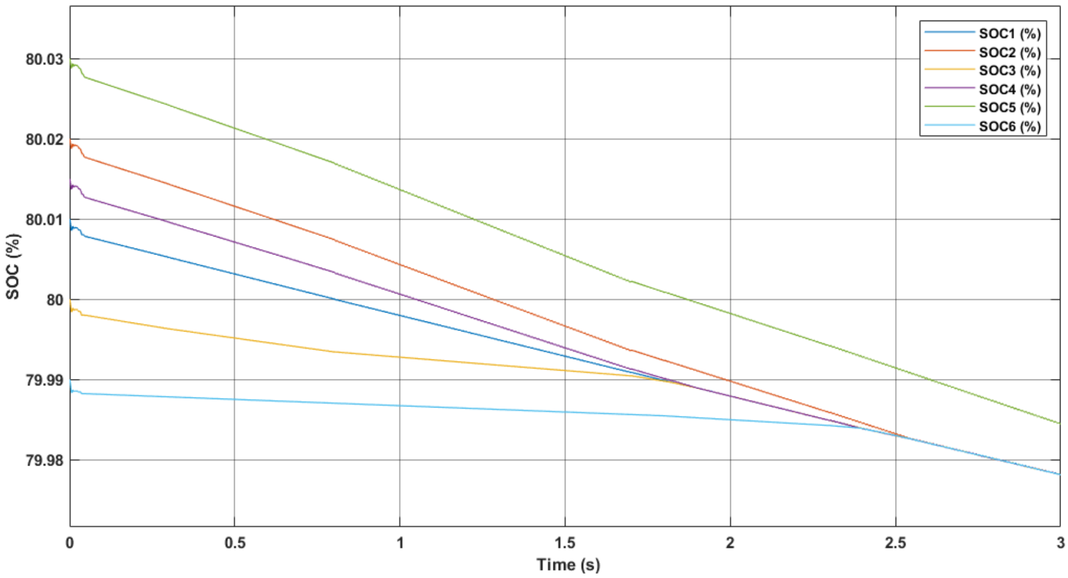

Figure 4.45 The SOC of the batteries for phase-A with in-phase balancing scheme.

Nearly, all batteries discharge at the same rate as shown in Figure 4.46-4.51, except for battery 3 and 6 which nearly does not discharge at all due to their lower SOC compared to the rest of the batteries. Generally, in case 3 and 4, the batteries only charge and discharge based on the active power, as the reactive power has almost no impact on the charging/discharging characteristics, since reactive power is associated with the converter switches and other reactive elements such as inductors and capacitors inside the system.

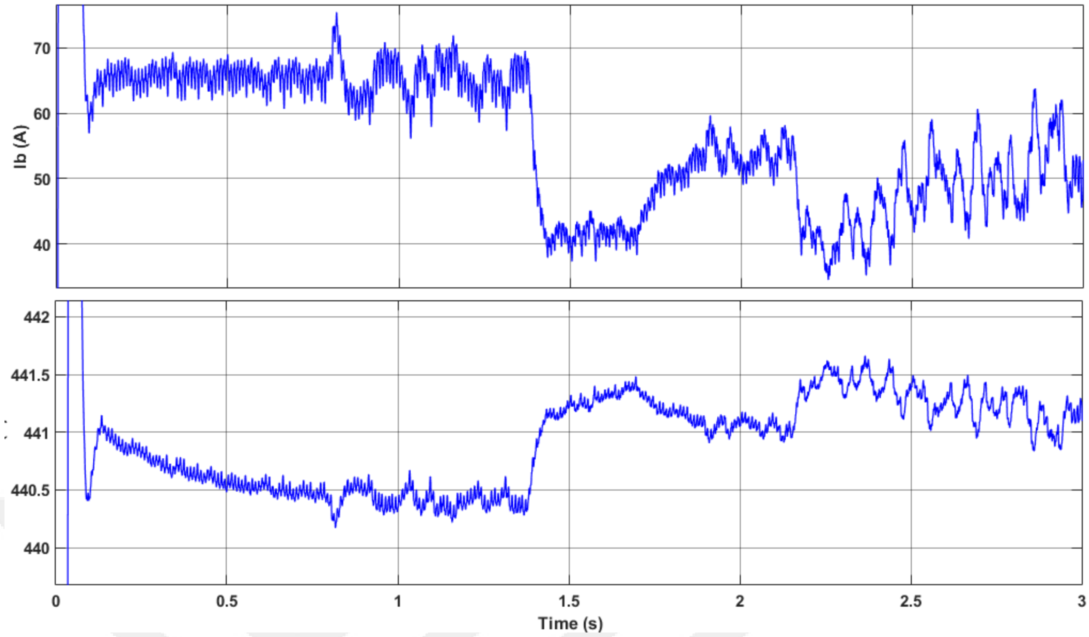

Figure 4. 46 The current and voltage waveforms of battery 1.

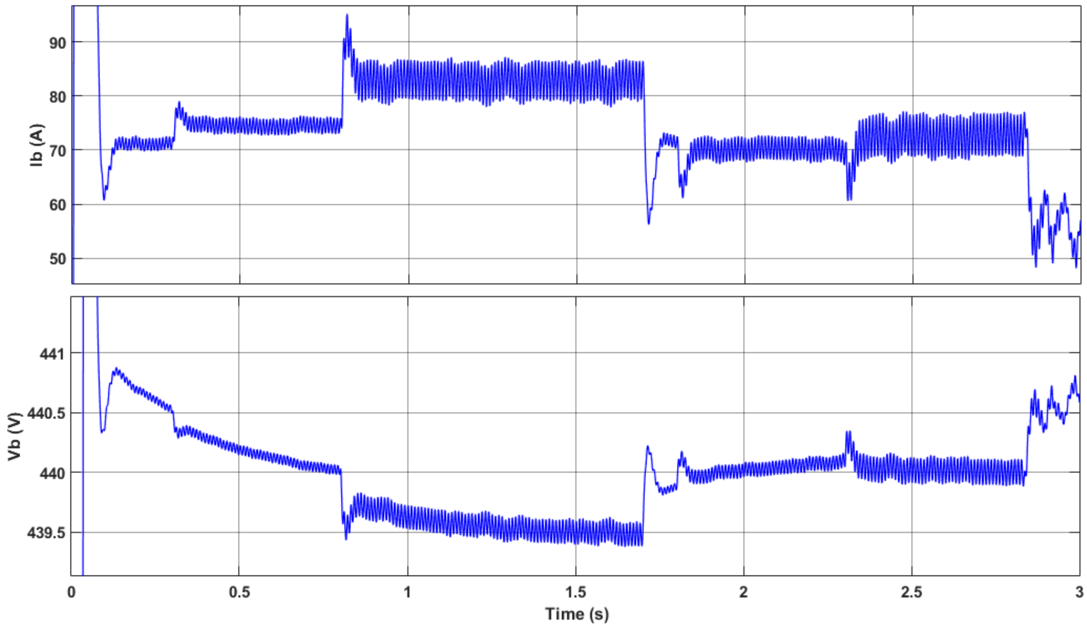

Figure 4.47 The current and voltage waveforms of battery 2.

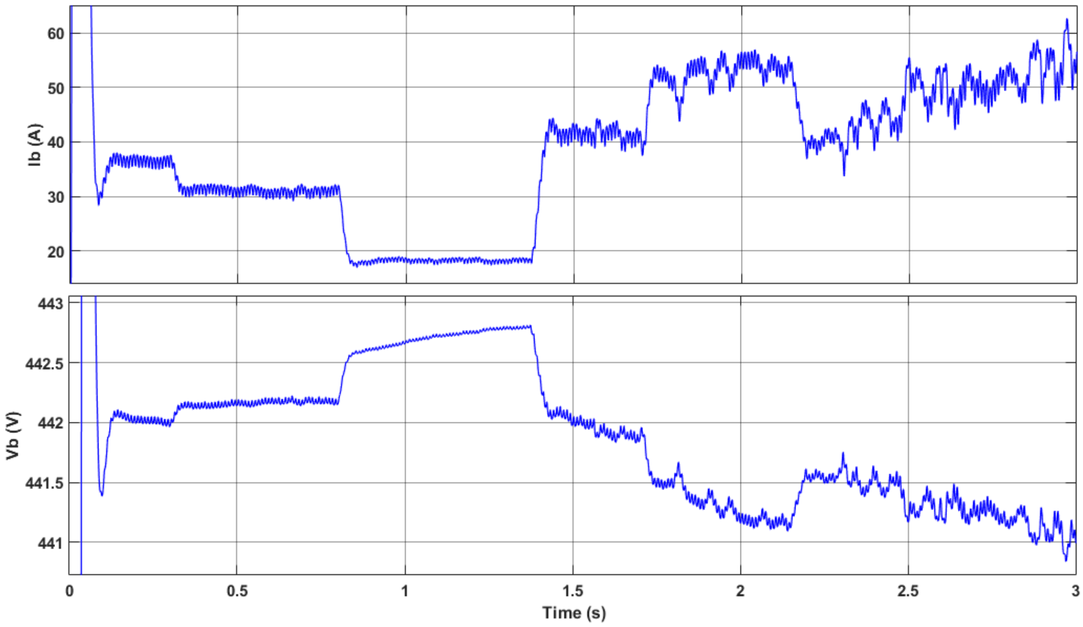

Figure 4.48 The current and voltage waveforms of battery 3.

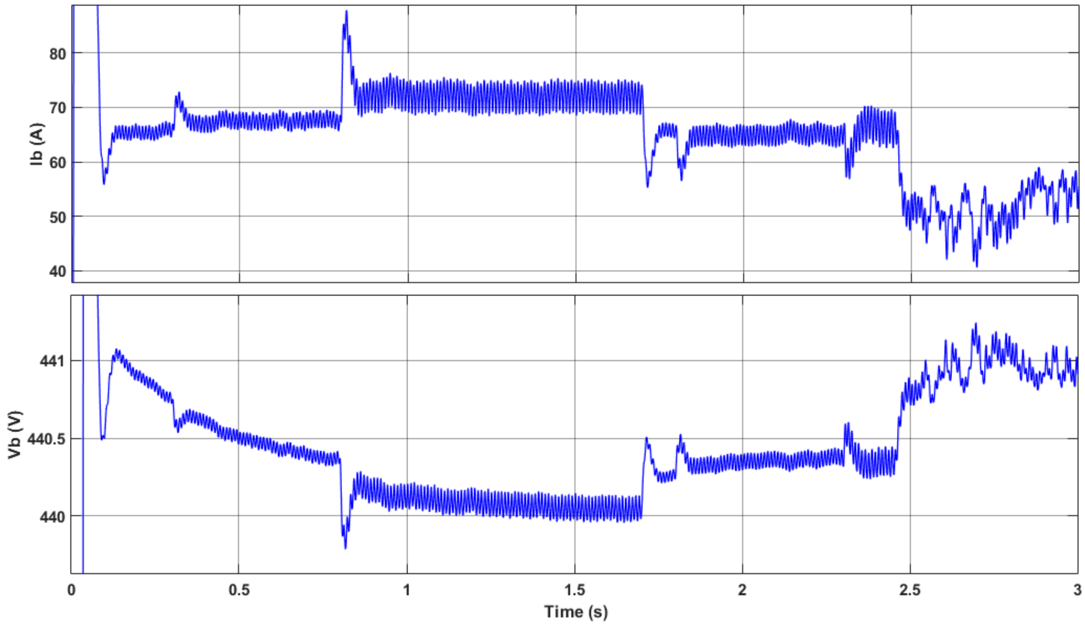

Figure 4.49 The current and voltage waveforms of battery 4.

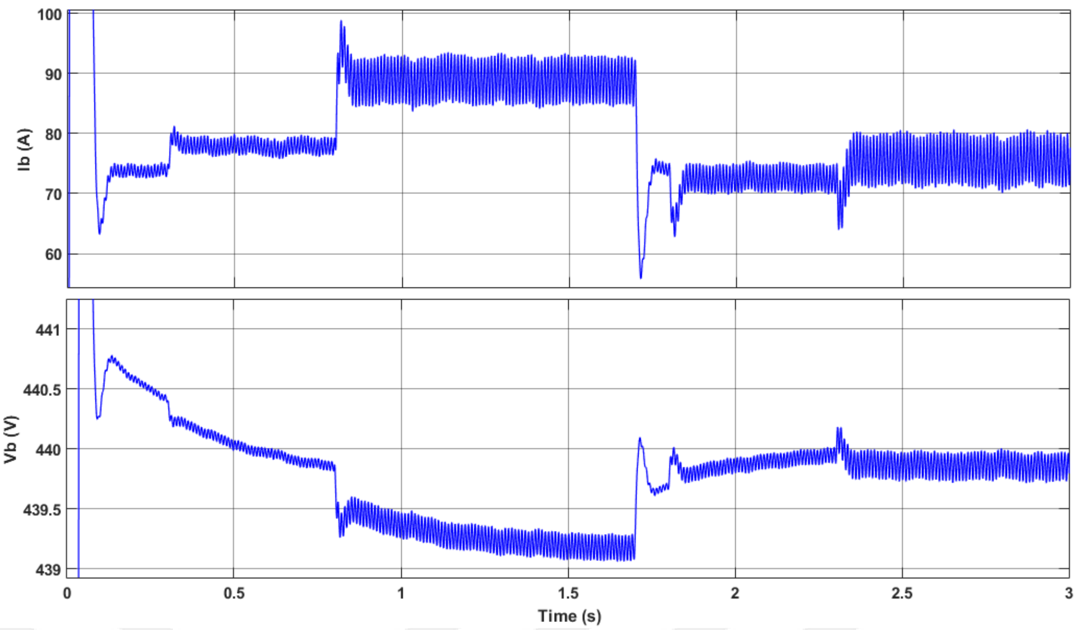

Figure 4.50 The current and voltage waveforms of battery 5.

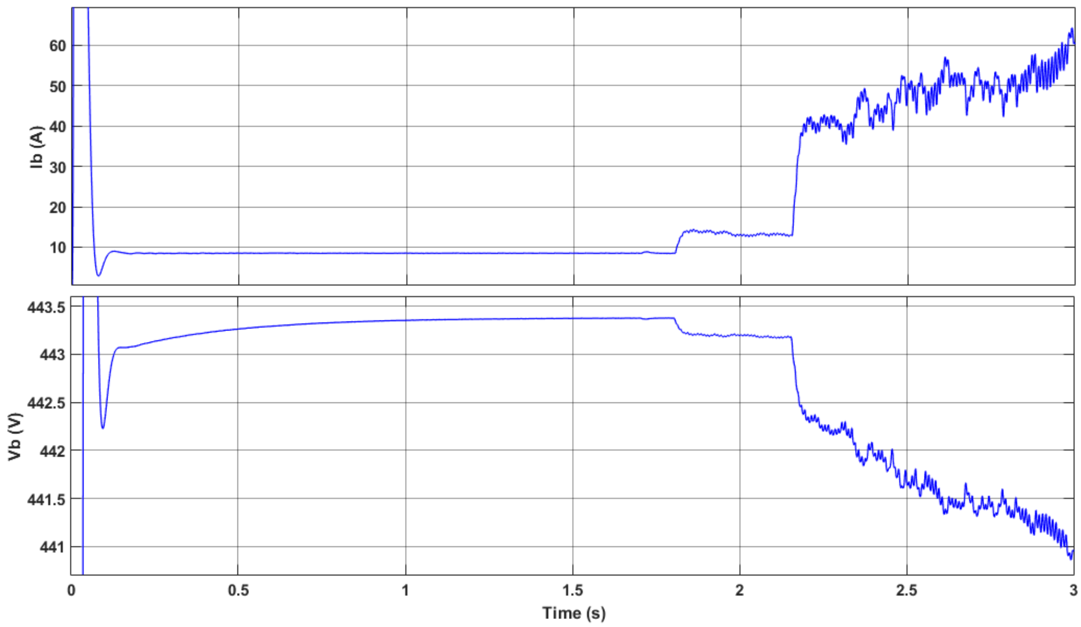

Figure 4.51 The current and voltage waveforms of battery 6.

4.5 Case 5: Fault Tolerant Test

In order to demonstrate the effectiveness of employing an additional SM in each phase, a fault in a single SM of branch A is assumed. The fault considered is related only to the battery bank which is assumed to be instantly detected and dealt with accordingly. The system is simulated for discharging at constant active power at 1 pu, while reactive power is also fixed at 0 pu over a duration of 2 s. The initial SOC of each battery bank is listed in Table 4.3. At t = 1.1 s, a fault transpires in battery bank of SM 6 which is instantly detected and the battery bank is open-circuited while the SM is bypassed. Figure 4.52 shows the voltage of current for phase-A branch. It is apparent that the fault has no effect on the voltage and current due to the redundancy SMs used in the design. However, in real case, a slight voltage drop can occur until the fault is diagnosed and the appropriate action is taken.

Table 4.5 Initial SOC of the battery modules.

Battery	SOC (%)
B1	80.01
B2	79.99
B3	80
B4	80.015
B5	80.03
B6	80.02

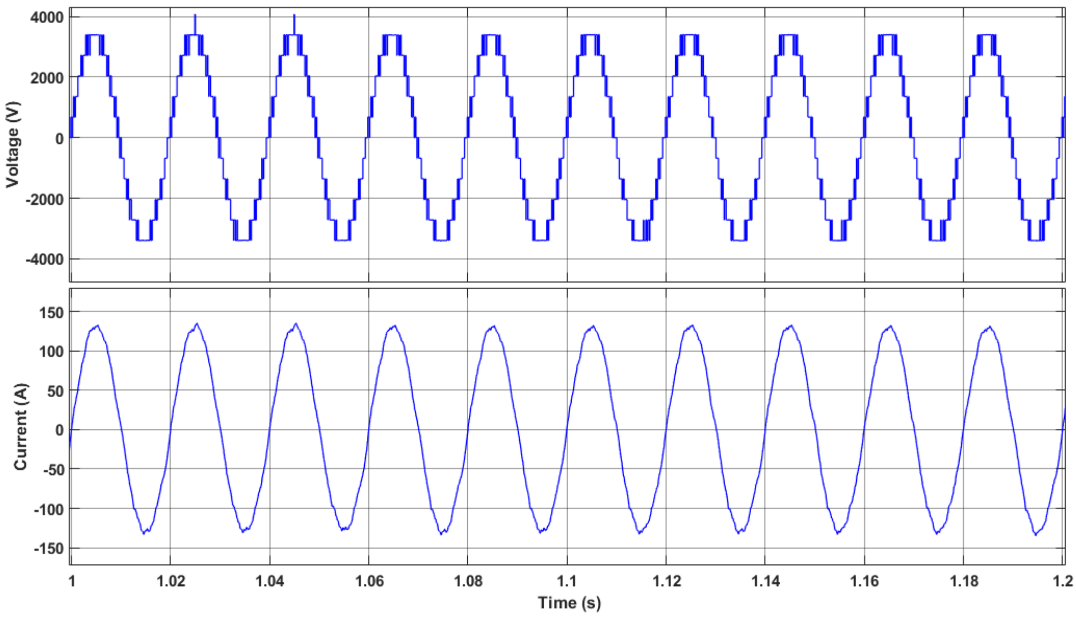

Figure 4.52 Voltage and current waveforms of phase-A of 11-level CHB.

Figure 4.53 shows the dc-link voltages of phase-a SMs. It is evident that the other SMs are not affected by the fault of the SM 6 and the voltage of faulty SM is gradually, as the energy stored inside the capacitor is dissipating.

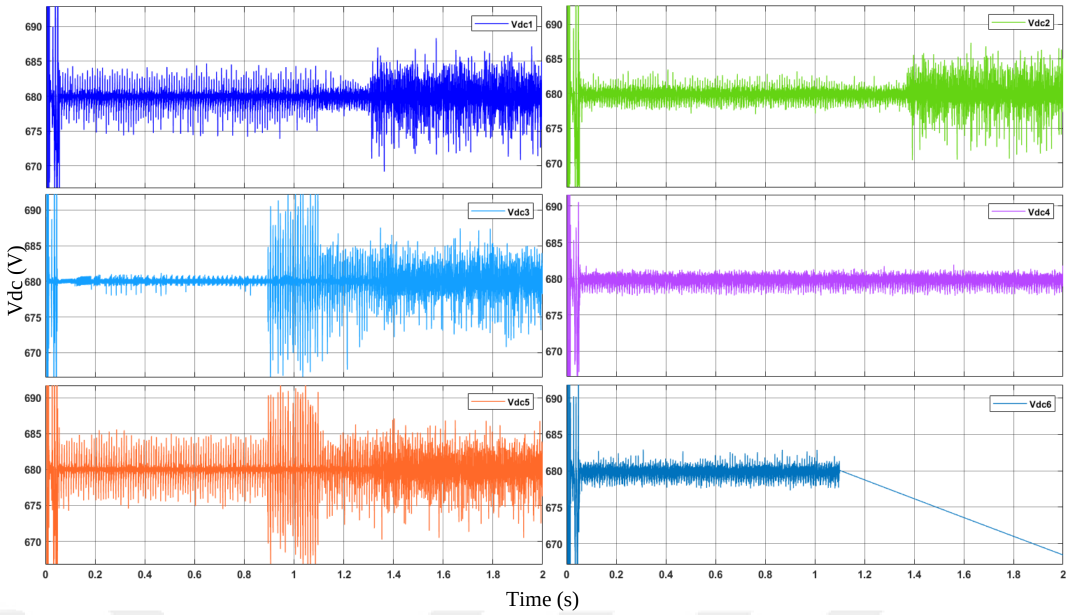

Figure 4.53 DC-link voltages of CHB SMs for phase-A.

The SOC measurements of phase-A is shown in Figure 4.54. It is obvious that SM 6 completely stops charging at the fault occurrence. Also, the other SMs that are discharging at lower rate, start discharging at higher rates to compensate for the bypassed SM 6.

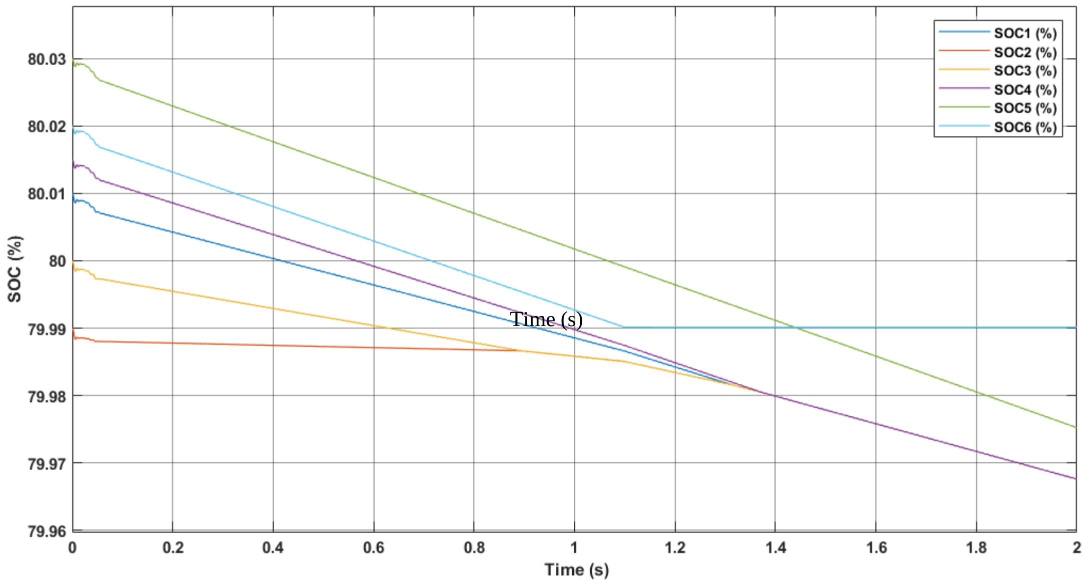

Figure 4.54 SOC measurements of phase-A with in-phase SOC balancing scheme.

As seen from Figure 4.55, the faulty battery bank completely stops charging at t = 1.1 s, reducing the battery current to zero and the battery voltage is settled at its open-circuit voltage.

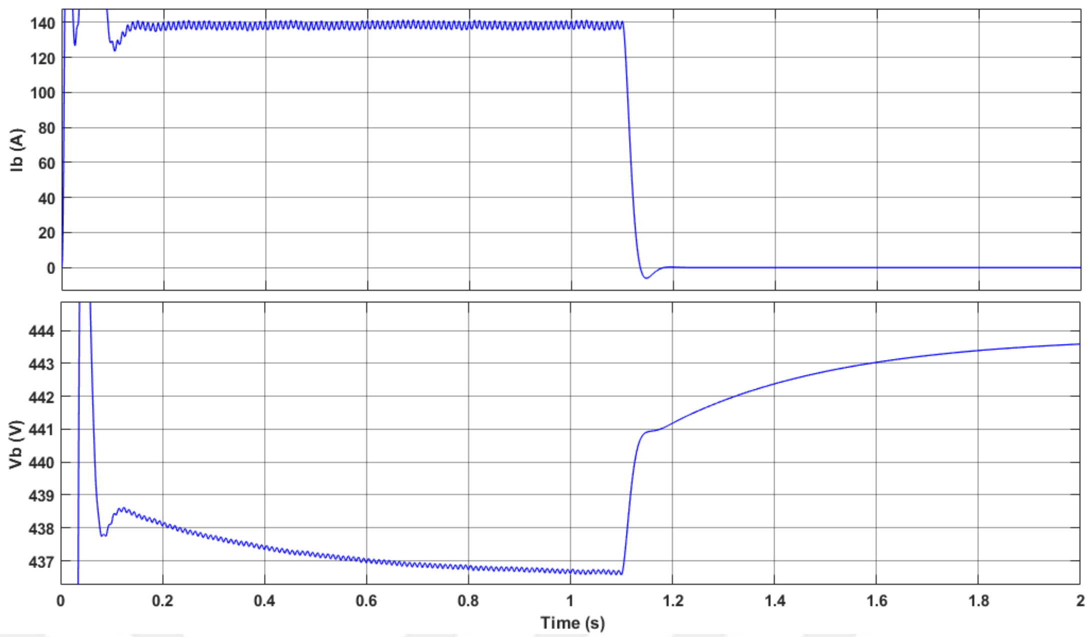

Figure 4.55 Faulty battery characteristics.

4.5 Results

This chapter introduced results and discussion for simulation studies that were conducted for different scenarios starting by testing the designed 1 MWh CHB-BESS for exchanging active power during charging and discharging the batteries in the process. It can be concluded that all the results showed satisfactory performance. Afterwards, the designed system was tested for STATCOM operation under charging and discharging modes of the batteries. The controllers demonstrated good performance in accomplishing STATCOM operation. Also, the SOC in-phase balancing scheme of CHB demonstrated its effectiveness in balancing all the battery SOC values without requiring any external hardware or complex control strategies. Finally, the system fault tolerance capability was tested by assuming a fault occurrence in individual SM in the CHB, which demonstrated the robustness and the reliability of the designed system.

CHAPTER V

CONCLUSIONS AND FUTURE PROSPECTS

5.1 Conclusions

This thesis gave an overview on the current literature on energy storage system in general and battery energy storage systems in detail. The battery energy storage system components, battery types, battery models, battery connections, battery charging methods, and control were reviewed in detail in order to design and model 1MWh BESS accordingly. 1 MWh BESS connected to 34.5 kV distribution grid was designed in this thesis used CHB as main grid converter to generate 4.16kV output voltage that is stepped up to 34.5 kV using a coupling transformer. The CHB were designed using 6 SM's in each phase branch in order to meet the voltage and capacity requirement including one redundant SM to increase the system safety and reliability in case of failure. Each CHB included battery bank connected to a DC-DC converter to regulate the charging and discharging of the battery and maintain stable dc-link voltage. ES-FBL nonlinear controller was proposed to control the DC-DC converter, while conventional PI controllers based on vector-oriented control were used to control the grid-connected converters to independently regulate active and reactive power by independently controlling the *dq* current components in rotation reference frame. Finally, simulating environment is used to verify the designed and modeled 1 MWh BESS by performing different case studies starting by testing the system capability to charge and discharge the BESS and exchange active/reactive powers with the grid and verifying the proposed ES-FBL nonlinear controller which showed impressive results in regulating the DC-DC converter by maintaining the dc-link voltage at the desired value under different circumstances at different simulation scenarios.

The key points of the conclusive results and contribution of this thesis is outlined as follows:

1- ESS literature Review: At the beginning of this thesis a literature review is presented on the different available ESS technologies, applications, and characteristics. Each ESS type has a distinct characteristic and is best suited to a limited number of applications. In this thesis BESS is the main focus which is characterized for its high efficiency, fast response time, and long-life cycle making it more suitable for broad range of applications such as providing grid ancillary services and RES integration. ESS literature review was presented in chapter 1 of this thesis.

2- Review of past BESS installations and simulations: Actual projects of operating BESS of various power and energy ratings that uses different BESS technologies were reviewed. Also, different studies that design and simulate BESS were reviewed along with studies that cover different subjects related to sizing and allocation of BESS. This part was shown in chapter 2.

3- BESS literature review: BESS was investigated in terms of its structure, topology, components, and control systems. The main components of a BESS are batteries, DC-DC converters, and PCS. The differences between different types of batteries, as well as the construction, operating principle, and control system of a DC-DC converter and a PCS, were evaluated and investigated. According to previous evaluations and assessments LFP battery was selected in this study, while half-bridge DC-DC converter was selected to regulate the dc-link voltage and battery operation. For interfacing the BESS with the grid CHB was selected due to its high reliability and efficiency in handling utility scale BESS. BESS literature review was given in chapter 2.

4- BESS Design: The design of BESS involves the calculation of the required batteries and their series/parallel connections in order to meet the capacity and voltage requirements of the system. In this thesis CHB PCS topology is chosen which helps mitigate the number of series connected batteries increasing the reliability of the system as in case of a fault in a battery cell only the SM associated with the faulty cell will be by passed without the need to cease the BESS operation. Also, the multi-level voltage generated by CHB improve the THD and reduce the filter size at PCC. The design of CHB based BESS is discussed in chapter 3.

5- <u>BESS cost assessment:</u> The cost of Li-ion batteries is in continues decreases due to the increasing demand over the past decade. For future evaluation and experimentation purposes the cost of the 1MWh designed in this thesis is assessed and approximated to cost around 448,000$ which includes only the installation cost. This part is included in chapter 2.

6- <u>BESS Modeling:</u> The modeling of the BESS components was done separately in this study. The dc side of the BESS was modeled using non-linear model which was used to develop a ES-FBL controller to regulate the dc-link voltage. While the ac side of the CHB-BESS was modeled as ideal voltage source that is controlled using current vector-oriented strategy using PI controllers to regulate the *d* and *q* components of the line currents as means to control the active/reactive power exchange between the BESS and CHB. Different battery cell and battery packs models and modeling methods was reviewed in chapter 2, in this thesis the generic battery model available in the library of the simulating environment is used to model the battery banks designed in this thesis which is considered practical for modeling large scale BESS. This part was discussed in chapter 3.

7- <u>BESS simulation:</u> A simulation was carried out on the simulating platform using the generic battery model in its library–the CHB-BESS designed and modeled in this thesis was built and simulated for different case studies. Those simulation proved the capability of the designed system and controllers to exchange both active and reactive with a 34.5kV grid with minimum error and fast transients. The performance of the ES-FBL proposed in this thesis for regulating the dc-link voltage showed stable and robust behavior in maintaining the desired dc-link voltage throughout different circumstances. The behavior of the batteries current and voltage showed an expected result during both charging and discharging. SOC balancing among the SM inside a single phase of the CHB was achieved by utilizing SOC in-phase balancing scheme by interchanging the carrier waves offsets of each SM which allows for more efficient utilization of all the SM including the redundant SM. Also, a fault-tolerance case study was investigated which showed that having a redundant SM in the CHB design is more reliable and efficient as the system operation will not be affected in case of bypassing a faulted cell and there is no need to bypass other SM in the other phases. BESS simulation was presented in chapter 4.

5.2 Future Works and Prospects

The research in this thesis was limited to design and model the BESS and test its performance and operation for normal test scenarios. In future studies we recommend the follows:

1- To implement the BESS designed in this thesis and simulate it for real case scenarios considering real actual distribution networks to further improve the operation of distribution networks and load handling by using BESS for different kind of applications.

2- An experimental study of the CHB based BESS designed in this thesis is recommended to be build and tested in laboratory environment to further investigate the CHB bases BESS and make further improvements.

3- An experimental study involving the ES-FBL proposed in this thesis is recommended to build and test bidirectional DC-DC converters controlled using the pre-mentioned approach to regulate dc-link voltage and the battery charging/discharging operations.

4- In this study the BESS connected to the grid was composed of multiple battery banks, DC-DC converter, and H-bridge converters. The battery banks were modeled as single battery model blocks using the generic model which is close to the Shepherd and R_i model that does not reflect all the dynamics of the battery such as self-discharge, temperature, and internal resistance. A more detailed battery models is recommended to be adopted for for future studies for large scale BESS.

5- As soft computing techniques and artificial intelligence are emerging as main trend in the literature, a study concerning the optimization of BESS and CHB structures is essential especially using reinforcement learning algorithms which can show high performance in the optimization problems. Therefore, potential studies on using reinforcement learning algorithms to control and optimize the BESS for different kind of operations are recommended.

6- In this thesis SOC estimation and faults associated with switches and other components was not investigated in direct manner, in future study SOC estimation using soft computing techniques is recommended along with fault tolerance studies regarding faults in switches and other components in CHB based BESS.

7- In order to implement BESS in distribution networks finding the most feasible nodes in the network is crucial. Thus, study of the sizing and allocation of BESS in distribution network is essential.

REFERENCES

[1] H. E. Oliveira Farias, L. Neves Canha. (2018). Battery Energy Storage Systems (BESS) Overview of Key Market Technologies, *IEEE PES Transmission & Distribution Conference and Exhibition - Latin America (T&D-LA)*. 1-5.

[2] S. Vazquez, S. M. Lukic, E. Galvan, L. G. Franquelo, J. M. Carrasco. (2010). Energy Storage Systems for Transport and Grid Applications, *IEEE Transactions on Industrial Electronics*. **57(12)**, 3881-3895.

[3] C. Wannasut, K. Hongesombut. (2014). A study of BESS application for the diferral of power distribution system investment, *International Conference on Information Science*, Electronics and Electrical Engineering. 1624-1628.

[4] R. H. Byrne, T. A. Nguyen, D. A. Copp, B. R. Chalamala, I. Gyuk. (2018). Energy Management and Optimization Methods for Grid Energy Storage Systems, *in IEEE Access*. **6**, 13231-13260.

[5] Mathew Aneke, Meihong Wang. (2016). Energy storage technologies and real life applications – A state of the art review, *Applied Energy*. **179**, 350-377.

[6] Francisco Díaz-González, Andreas Sumper, Oriol Gomis-Bellmunt. (2016). *Energy Storage in Power Systems*. WILEY: UK.

[7] Kumar, Nishant. (2015). Superconducting Magnetic Energy Storage (SMES) System.

[8] Mairaj ud din Mufti, Shameem Ahmad Lone, Shiekh Javed Iqbal, Muzzafar Ahmad, Mudasir Ismail. (2009). Super-capacitor based energy storage system for improved load frequency control, *Electric Power Systems Research.* **(1)**, 226-233.

[9] Prashant Gorakhnath. Patil, Kotha Venkateshwarlu, Mohan Tukaram Patel. (2015). Application of Super Capacitor Energy Storage in Microgrid System, *International Journal of Science, Engineering and Technology Research (IJSETR)*. **4(3)**, 589-594.

[10] Shengqi Zhang, Y. Mishra, G. Nourbakhsh, G. Ledwich. (2013). The application of BESS in load shedding scheme, *Australasian Universities Power Engineering Conference (AUPEC)*. 1-6.

[11] H. Qian, J. Zhang, J. Lai. (2010). A grid-tie battery energy storage system, *IEEE 12th Workshop on Control and Modeling for Power Electronics (COMPEL)*. 1-5.

[12] M. Shatnawi, N. A. Qaydi, N. Aljaberi, M. Aljaberi. (2018). Hydrogen-Based Energy Storage Systems: A Review, *7th International Conference on Renewable Energy Research and Applications (ICRERA)*. 697-700.

[13] N. Kondrath. (2017). Bidirectional DC-DC converter topologies and control strategies for interfacing energy storage systems in microgrids: An overview, *2017 IEEE International Conference on Smart Energy Grid Engineering (SEGE)*. 341-345.

[14] Omid Palizban, Kimmo Kauhaniemi. (2016). Energy storage systems in modern grids—*Matrix of technologies and applications,Journal of Energy Storage*. **6**, 248-259.

[15] Istvan Taczi. Energy regulators regional association. (2016). Overview of the Energy Storage Possibilities to Support the Electrical Power System.: https://erranet.org, 07.2016.

[16] Asian Development bank. (2018). *Handbook on battery energy storage system*.

[17] X. Li, S. Wang. (2019). A review on energy management, operation control and application methods for grid battery energy storage systems, *in CSEE Journal of Power and Energy Systems*.

[18] Arangarajan, Vinayagam, M.T.O., Amanullah, Chandran, Jaideep, Shafiullah, Gm, Stojcevski, Alex. (2015). Role of energy storage in the power system network.

[19] H. Ibrahim, A. Ilinca, J. Perron. (2008). Energy storage systems—Characteristics and comparisons, Renewable and Sustainable Energy Reviews. **12(5)**, 1221-1250.

[20] X. Zhou, Y. Lin, Y. Ma. (2015). the overview of energy storage technology, *IEEE International Conference on Mechatronics and Automation (ICMA)*. 43-48.

[21] Rancilio, Giuliano, Lucas, Alexandre, Kotsakis, Evangelos, Fulli, Gianluca, Merlo, Marco, Delfanti, Maurizio, Masera, Marcelo. (2019). Modeling a Large-Scale Battery Energy Storage System for Power Grid Application Analysis. *Energies*. **12**.

[22] A. S. Subburaj, W. B. Ray, S. B. Bayne. (2014). Comparison study of the controllers for grid connected battery system. *IEEE NewNEB DC Utility Power Conference and Exhibition (NewNEB).* 1-6.

[23] N. Miller, D. Manz, J. Roedel, P. Marken, E. Kronbeck. (2010). Utility scale Battery Energy Storage Systems, *IEEE PES General Meeting*. 1-7.

[24] International energy agency (IEA) 2019, Installed capacity of utility-scale battery storage systems in the New Policies Scenario, 2020-2040.: https:// iea.org, 02.03.2021.

[25] N. Chatrung. (2019). Battery Energy Storage System (BESS) and Development of Grid Scale BESS in EGAT, *IEEE PES GTD Grand International Conference and Exposition Asia (GTD Asia).* 589-593.

[26] J. Zhang, S. Ci. (2010). State of charge modeling of arbitrary cell connection, *2010 IEEE Energy Conversion Congress and Exposition*, 1635-1639.

[27] M. I. Wahyuddin, P. S. Priambodo , H. Sudibyo. (2018). State of Charge (SoC) Analysis and Modeling Battery Discharging Parameters. *2018 4th International Conference on Science and Technology (ICST).* 1-5.

[28] S. Li, B. Ke. (2011). Study of battery modeling using mathematical and circuit oriented approaches, *2011 IEEE Power and Energy Society General Meeting*. 1-8.

[29] Alfred Rufer. (2018). Energy Storage Systems and Components, *CRC Press*.

[30] Shufan Li, Chenglin Liao, Lifang Wang. (2014). Research progress of equivalent circuit models for SOC estimation of batteries in electric vehicles, *2014 IEEE Conference and Expo Transportation Electrification Asia-Pacific (ITEC Asia-Pacific*). 1-6.

[31] Liu, K., Li, K., Peng, Q. (2019). A brief review on key technologies in the battery management system of electric vehicles. Front, Mech. Eng. **14**, 47–64.

[32] yu, Zhihao, Huai, Ruituo, Xiao, Linjing. (2015). State-of-Charge Estimation for Lithium-Ion Batteries Using a Kalman Filter Based on Local Linearization. *Energies*. **8**. 7854-7873.

[33] P. Spagnol, S. Rossi, S. M. Savaresi. (2011). Kalman Filter SoC estimation for Li-Ion batteries, *2011 IEEE International Conference on Control Applications (CCA).* 587-592.

[34] Z. Luo, Y. Li, Y. Lou. (2015). An adaptive kalman filter to estimate state-of-charge of lithium-ion batteries, *2015 IEEE International Conference on Information and Automation.* 1227-1232.

[35] Chung, Dae-Won, Yang, Seung-Hak. (2018). SOC Estimation of Lithium-Ion Battery Based on Kalman Filter Algorithm for Energy Storage System in Microgrids. *E3S Web of Conferences*. **57**.

[36] F. Liu, T. Liu, Y. Fu. (2015). An Improved SoC Estimation Algorithm Based on Artificial Neural Network, *2015 8th International Symposium on Computational Intelligence and Design (ISCID).* 152-155.

[37] M. A. Hannan, M. S. H. Lipu, A. Hussain, M. H. Saad, A. Ayob. (2018). Neural Network Approach for Estimating State of Charge of Lithium-Ion

Battery Using Backtracking Search Algorithm, *in IEEE Access*. **6**, 10069-10079.

[38] H. Zhang, W. Na, J. Kim. (2018). State-of-Charge Estimation of the Lithium-Ion Battery Using Neural Network Based on an Improved Thevenin Circuit Model, *2018 IEEE Transportation Electrification Conference and Expo (ITEC)*. 342-346.

[39] S. Song, Z. Wei, H. Xia, M. Cen, C. Cai. (2018). State-of-charge (SOC) estimation using T-S Fuzzy Neural Network for Lithium Iron Phosphate Battery, *2018 26th International Conference on Systems Engineering (ICSEng)*. 1-5.

[40] E. Chatzinikolaou, D. J. Rogers. (2017). A Comparison of Grid-Connected Battery Energy Storage System Designs, *in IEEE Transactions on Power Electronics*. **32(9)**, 6913-6923.

[41] F. Liuyang, W. Keyou. (2015). The study of battery energy storage system deterioration and inconsistency, *2015 IEEE International Conference on Cyber Technology in Automation, Control, and Intelligent Systems (CYBER)*. 207-212.

[42] Pei Zhang, Changqing Du, Fuwu Yan, Jianqiang Kang. (2011). Influence of practical complications on energy efficiency of the vehicle's lithium-ion batteries, *2011 International Conference on Electric Information and Control Engineering*. 2278-2281.

[43] A. H. Fathima, K. Palanisamy. (2014). Battery energy storage applications in wind integrated systems — A review, *2014 International Conference on Smart Electric Grid (ISEG)*. 1-8.

[44] A. R. Sparacino, G. F. Reed, R. J. Kerestes, B. M. Grainger, Z. T. Smith. (2012). Survey of battery energy storage systems and modeling techniques, *2012 IEEE Power and Energy Society General Meeting*. 1-8.

[45] H. Keshan, J. Thornburg, T. S. Ustun. (2016). Comparison of lead-acid and lithium ion batteries for stationary storage in off-grid energy systems, *4th IET Clean Energy and Technology Conference (CEAT 2016)*. 1-7.

[46] R. M. Herritty, J. Midolo. (1998). Nickel cadmium batteries for photovoltaic applications, *Thirteenth Annual Battery Conference on Applications and Advances. Proceedings of the Conference*. 255-257.

[47] M. Disosway. (1998). Development of high power nickel-cadmium batteries for hybrid vehicles, *Thirteenth Annual Battery Conference on Applications and Advances. Proceedings of the Conference*. 19-23.

[48] J. McDowall. (1999). Nickel-cadmium batteries for energy storage applications, *Fourteenth Annual Battery Conference on Applications and Advances. Proceedings of the Conference (Cat. No.99TH8371)*. 303-308.

[49] Z. Wen. (2006). Study on Energy Storage Technology of Sodium Sulfur Battery and it's Application in Power System, *2006 International Conference on Power System Technology*. 1-4.

[50] T. Hatta. (2012). Applications of sodium-sulfur batteries, *PES T&D* 2012. 1-3.

[51] Y. R. Challapuram, G. M. Quintero, S. B. Bayne, A. S. Subburaj, M. A. Harral. (2019). Electrical Equivalent Model of Vanadium Redox Flow Battery, *2019 IEEE Green Technologies Conference (GreenTech).* 1-4.

[52] M. Vins, M. Sirovy. (2019). Sodium-Sulfur Batteries for Energy Storage Applications, *2019 20th International Scientific Conference on Electric Power Engineering (EPE).* 1-5.

[53] Y. Zhou, X. Li. (2015). Overview of lithium-ion battery SOC estimation, *2015 IEEE International Conference on Information and Automation*. 2454-2459.

[54] A. Stan, M. Świerczyński, D. Stroe, R. Teodorescu, S. J. Andreasen. (2014). Lithium ion battery chemistries from renewable energy storage to automotive and back-up power applications — An overview, 2014 *International Conference on Optimization of Electrical and Electronic Equipment (OPTIM)*. 713-720.

[55] Haisheng Chen, Thang Ngoc Cong, Wei Yang, Chunqing Tan, Yongliang Li, Yulong Ding. (2009). Progress in electrical energy storage system: *A critical review,Progress in Natural Science*. **19(3)**, 291-312.

[56] E. O. Ogunniyi, H. Pienaar. (2017). Overview of battery energy storage system advancement for renewable (photovoltaic) energy applications, 2017 *International Conference on the Domestic Use of Energy (DUE).* 233-239.

[57] Xing Luo, Jihong Wang, Mark Dooner, Jonathan Clarke. (2015). Overview of current development in electrical energy storage technologies and the application potential in power system operation, *Applied Energy*, **137**, 511-536.

[58] S. X. Chen, K. J. Tseng, S. S. Choi. (2009). Modeling of Lithium-Ion Battery for Energy Storage System Simulation, 2*009 Asia-Pacific Power and Energy Engineering Conference*, 1-4.

[59] K. Sun, Q. Shu. (2011). Overview of the types of battery models, *Proceedings of the 30th Chinese Control Conference*, 3644-3648.

[60] Meng, J., Luo, G., Ricco, M., Swierczynski, M., Stroe, Daniel-Ioan, Teodorescu, R. (2018). Overview of Lithium-Ion Battery Modeling Methods for State-of-Charge Estimation in Electrical Vehicles. *Applied Science*. **8**, 659.

[61] A. A. Hussein, I. Batarseh. (2011). An overview of generic battery models *2011 IEEE Power and Energy Society General Meeting*,. 1-6.

[62] B. Balagopal, M. Chow. (2016). Effect of anode conductivity degradation on the Thevenin Circuit Model of lithium ion batteries, *IECON 2016 - 42nd Annual Conference of the IEEE Industrial Electronics Society*, 2028-2033.

[63] W. Peng, Z. Yang, C. Liu, J. Xiu, Z. Zhang. (2018). An Improved PSO Algorithm for Battery Parameters Identification Optimization Based on Thevenin Battery Model, *2018 5th IEEE International Conference on Cloud Computing and Intelligence Systems (CCIS)*, 295-298.

[64] J. Wehbe, N. Karami. (2015). Battery equivalent circuits and brief summary of components value determination of lithium ion: A review, *2015 Third International Conference on Technological Advances in Electrical, Electronics and Computer Engineering (TAEECE),* 45-49.

[65] Bingyu Sang, Jinhang Hu, Guanjun Li, Jinhua Xue, Jilei Ye. (2016). Equivalent modeling method of battery energy storage system in multi-time scales, *2016 IEEE 8th International Power Electronics and Motion Control Conference (IPEMC-ECCE Asia)*, 252-256.

[66] M. K. Hossain, S. M. R. Islam. (2017). Battery Impedance Measurement Using Electrochemical Impedance Spectroscopy Board, *2017 2nd International Conference on Electrical & Electronic Engineering (ICEEE)*. 1-4.

[67] C. Sen, N. C. Kar. (2009). Battery pack modeling for the analysis of battery management system of a hybrid electric vehicle, *2009 IEEE Vehicle Power and Propulsion Conference*, 207-212.

[68] F. Baronti, R. Di Rienzo, N. Papazafiropulos, R. Roncella, R. Saletti. (2014). Investigation of series-parallel connections of multi-module batteries for electrified vehicles, *2014 IEEE International Electric Vehicle Conference (IEVC)*, 1-7.

[69] Jianwei Li, Michael S. Mazzola. (2013). Accurate battery pack modeling for automotive applications, *Journal of Power Sources*. **13**, 215-228.

[70] J. Lee, J. Ahn, B. K. Lee. (2017). A novel li-ion battery pack modeling considerging single cell information and capacity variation, *2017 IEEE Energy Conversion Congress and Exposition (ECCE)*. 5242-5247.

[71] B. Enache, M. E. Alexandru, L. Constantinescu. (2015). Extending the battery model from a single cell to a battery pack with BMS, *2015 7th International Conference on Electronics, Computers and Artificial Intelligence (ECAI)*. AE-5-AE-14.

[72] Jonghoon Kim, B.H. Cho. (2013). Screening process-based modeling of the multi-cell battery string in series and parallel connections for high accuracy state-of-charge estimation, *Energy*, **57**, 581-599.

[73] B. Arabsalmanabadi, N. Tashakor, A. Javadi, K. Al-Haddad. (2018). Charging Techniques in Lithium-Ion Battery Charger: Review and New Solution, *IECON 2018 - 44th Annual Conference of the IEEE Industrial Electronics Society*. 5731-5738.

[74] E. Ayoub, N. Karami. (2015). Review on the charging techniques of a Li-Ion battery, *2015 Third International Conference on Technological Advances in Electrical, Electronics and Computer Engineering (TAEECE)*. 50-55.

[75] B. Tar, A. Fayed. (2016). An overview of the fundamentals of battery chargers, *2016 IEEE 59th International Midwest Symposium on Circuits and Systems (MWSCAS)*. 1-4.

[76] Chia-Hsiang Lin et al. (2008). Fast charging technique for Li-Ion battery charger, *2008 15th IEEE International Conference on Electronics, Circuits and Systems*. 618-621.

[77] C. Liu, S. Wang, Y. Liu, M. Tsai. (2012). An optimum fast charging pattern search for Li-ion batteries using particle swarm optimization, *The 6th International Conference on Soft Computing and Intelligent Systems, and The 13th International Symposium on Advanced Intelligence Systems*. 727-732.

[78] Y. Liu, Y. Luo. (2010). Search for an Optimal Rapid-Charging Pattern for Li-Ion Batteries Using the Taguchi Approach," *in IEEE Transactions on Industrial Electronics*. **57(12)**, 3963-3971.

[79] S. De Breucker, K. Engelen, R. D'hulst, J. Driesen. (2013). Impact of current ripple on Li-ion battery ageing," *2013 World Electric Vehicle Symposium and Exhibition (EVS27)*. 1-9.

[80] Y. Zhang, S. Lu. (2018). Research on Series-Parallel Connection Switching Charging Method for Lithium Battery of Autonomous Underwater Vehicles, *2018 IEEE 8th International Conference on Underwater System Technology: Theory and Applications (USYS)*. 1-5.

[81] G. Wang et al. (2016). A Review of Power Electronics for Grid Connection of Utility-Scale Battery Energy Storage Systems, *in IEEE Transactions on Sustainable Energy*. **7(4)**, 1778-1790.

[82] M. Bragard, N. Soltau, S. Thomas, R. W. De Doncker. (2010). The Balance of Renewable Sources and User Demands in Grids: Power Electronics for Modular Battery Energy Storage Systems, *in IEEE Transactions on Power Electronics*. **25(12)**, 3049-3056.

[83] S. A. Gorji, H. G. Sahebi, M. Ektesabi, A. B. Rad. (2019). Topologies and Control Schemes of Bidirectional DC–DC Power Converters: An Overview, *in IEEE Access*. **7**, 117997-118019.

[84] V. Fernão Pires, Enrique Romero-Cadaval, D. Vinnikov, I. Roasto, J.F. Martins. (2014). Power converter interfaces for electrochemical energy storage systems – A review, *Energy Conversion and Management*. **86**, 453-475.

[85] I. Trintis, S. Munk-Nielsen, R. Teodorescu. (2010). Single stage grid converters for battery energy storage, *5th IET International Conference on Power Electronics, Machines and Drives (PEMD 2010).* 1-6.

[86] R. Kumar, A. V. Goyal, S. Srivastava, S. P. Singh, N. Singh. (2013) Modelling and simulation of matrix converter based DC-DC converter, *2013 International Conference on Energy Efficient Technologies for Sustainability*. 134-138.

[87] A. K. Singh, P. P. Deshpande, S. K. Panda. (2017). A single-stage isolated bidirectional matrix based AC-DC converter for energy storage, *IECON 2017 - 43rd Annual Conference of the IEEE Industrial Electronics Society*. 2744-2749.

[88] G. Wang, J. Pou, V. G. Agelidis. (2015). Reconfigurable battery energy storage system for utility-scale applications, *IECON 2015 - 41st Annual Conference of the IEEE Industrial Electronics Society*. 004086-004091.

[89] C. Moo, J. Jian, T. Wu, L. Yu, C. Hua. (2013) Battery power system with arrayed battery power modules, 2*013 International Conference on System Science and Engineering (ICSSE)*. 437-441.

[90] L. Baruschka, A. Mertens. (2011). Comparison of Cascaded H-Bridge and Modular Multilevel Converters for BESS application, *2011 IEEE Energy Conversion Congress and Exposition*. 909-916.

[91] R. Bououd, L. Sbita. (2017). An overview of chopper topologies, 2017 *International Conference on Green Energy Conversion Systems (GECS)*. 1-7.

[92] S. Thomas, M. Stieneker, R. W. De Doncker. (2011). Development of a modular high-power converter system for battery energy storage systems, *Proceedings of the 2011 14th European Conference on Power Electronics and Applications*. 1-10.

[93] K. Tian, S. Ali, Z. Huang, Z. Ling. (2019). Power control and experiment of 2MW/10kV cascaded H-bridge power conversion system for battery energy storage system, *8th Renewable Power Generation Conference (RPG 2019)*. 1-7.

[94] L. Zhi-Bin, C. Yang, M. Qin-Dong. G. Hai-Feng, Z. Bai-hua, L. Zhi-Gang. (2014). Design of 2MW/10kV cascaded power conversion system, IECON *2014 - 40th Annual Conference of the IEEE Industrial Electronics Society*. 4250-4255.

[95] Muhammad H. Rashid. (2011). *Power electronics handbook devices, circuits, and applications third edition*. Elsevier: USA.

[96] C. Moo, K. S. Ng, Y. Hsieh.June. (2008). Parallel Operation of Battery Power Modules, *in IEEE Transactions on Energy Conversion*. **23(2)**, 701-707.

[97] C. Moo, Kong-Soon Ng, Jin-Shin Hu. (2009). Operation of battery power modules with series output, *2009 IEEE International Conference on Industrial Technology*. 1-6.

[98] F. Chen, W. Qiao, L. Qu. (2017). A modular and reconfigurable battery system, *2017 IEEE Applied Power Electronics Conference and Exposition (APEC)*. 2131-2135.

[99] S. Ci, N. Lin, D. Wu. (2016). Reconfigurable Battery Techniques and Systems: A Survey, *in IEEE Access*. **4**, 1175-1189.

[100] M. T. Lawder et al. (2014). Battery Energy Storage System (BESS) and Battery Management System (BMS) for Grid-Scale Applications, *in Proceedings of the IEEE*. **102(6)**, 1014-1030.

[101] J. I. Y. Ota, T. Sato, H. Akagi. (2016). Enhancement of Performance, Availability, and Flexibility of a Battery Energy Storage System Based on a Modular Multilevel Cascaded Converter (MMCC-SSBC), *in IEEE Transactions on Power Electronics*. **31(4)**, 2791-2799.

[102] F. Baronti, G. Fantechi, R. Roncella, R. Saletti. (2012). Design of a module switch for battery pack reconfiguration in high-power applications," 2012 *IEEE International Symposium on Industrial Electronics*. 1330-1335.

[103] A. Manenti, A. Abba, A. Merati, S. M. Savaresi, A. Geraci. (2011). A New BMS Architecture Based on Cell Redundancy, *in IEEE Transactions on Industrial Electronics*. **58(9)**, 4314-4322.

[104] I. Trintis, S. Munk-Nielsen, R. Teodorescu. (2011). Cascaded H-bridge with bidirectional boost converters for energy storage, Proceedings of the 2011 *14th European Conference on Power Electronics and Applications*, Birmingham, UK. 1-9.

[105] T. Lahlou, D. Wittmann, M. Abdelrahem, H. Herzog. (2016). Stabilization of the DC-link voltage in a two stage cascaded H-Bridge multilevel converter for battery energy storage systems, *2016 IEEE International Energy Conference (ENERGYCON)*, Leuven, Belgium. 1-6.

[106] C. Yuan, Y. Huangfu, R. Ma, B. Zhao, H. Bai. (2019). Nonlinear PI and Finite-time Control for DC-DC Converter Based on Exact Feedback Linearization, *IECON 2019 - 45th Annual Conference of the IEEE Industrial Electronics Society*, Lisbon, Portugal. 6398-6403.

[107] D. -x. Shuai. (2014). State feedback exact linearization control of Buck-Boost converter, *2014 International Power Electronics and Application Conference and Exposition*, Shanghai, China. 1490-1494.

[108] Huijun Zheng, Dingxin Shuai. (2012). Nonlinear control of Boost converter by state feedback exact linearization, *2012 24th Chinese Control and Decision Conference (CCDC), Taiyuan*, China. 3502-3506.

[109] M. Salimi, S. Siami. (2015). Cascade nonlinear control of DC-DC buck/boost converter using exact feedback linearization, *2015 4th International Conference on Electric Power and Energy Conversion Systems (EPECS)*, Sharjah, United Arab Emirates. 1-5.

[110] Daniel Celius Zacharek, Filip Sundqvist. (2018). Design of Bidirectional DC/DC Battery Management System for Electrical Yacht, *Bachelor of Science Thesis in Electrical Engineering, Linköping University.*

[111] T. Daniel Raj, N. Kesavan Nair. (2016), Implementation of Cascaded H-Bridge Multi Level Inverter, *Middle-East Journal of Scientific Research*. **24(9)**, 2752-2759.

[112] Hassan, Othman. (2019). A Simple Staircase Modulation for A Cascaded H-Bridge Multilevel Inverter, *UofKEJ*. **9(2)**, 18-24.

[113] T. Lahlou, S. N. Malik, H. Herzog. (2017). Simulation and analysis of control and modulation schemes for a multilevel cascaded H-bridge inverter for use in a battery energy storage system, *2017 18th International Scientific Conference on Electric Power Engineering (EPE)*. 1-6.

[114] L. Xu, D. Zhi, L. Yao. (2007). Direct Power Control of Grid Connected Voltage Source Converters, *2007 IEEE Power Engineering Society General Meeting*. 1-6.

[115] Yoash Levron, Juri Belikov. (2017). Modeling power networks using dynamic phasors in the dq0 reference frame, *Electric Power Systems Research*. **144**, 233-242.

[116] D. Atkar, P. S. Udakhe, S. Chiriki, V. B. Borghate. (2016). Control of seven level cascaded H-Bridge inverter by hybrid SPWM technique, *2016 IEEE International Conference on Power Electronics*, *Drives and Energy Systems (PEDES)*.1-6.

[117] Jing-Hua ZHOU, Xiang JI, Xiao-Wei ZHANG, Ya-Ai CHEN, (2017). A Survey of Control Stratedy Based on Cascaded H-bridge Power Conversion System, *Proceedings of the 3rd Annual International Conference on Electronics, Electrical Engineering and Information Science (EEEIS 2017), Advances in Engineering Research (AER)*. **131**, 184-192.

[118] Zhibin Ling, Zhuoyang Zhang, Zhengxi Li, Yongqi Li. (2016). State-of-charge balancing control of battery energy storage system based on cascaded H-bridge multilevel inverter, *2016 IEEE 8th International Power Electronics and Motion Control Conference (IPEMC-ECCE Asia)*. 2310-2314.

[119] A. S. Gadalla, X. Yan, H. Hasabelrasul. (2018). State-of-charge balancing control strategy for battery energy storage systems based on a modern cascaded multilevel PWM converter, *2018 IEEE 12th International Conference on Compatibility, Power Electronics and Power Engineering (CPE-POWERENG 2018)*. 1-6.

[120] Z. Alaas, Caisheng Wang, Chenguang Jiang, Chen Duan, Jianfei Chen. (2017). Improved cascaded multilevel battery inverters with phase-to-phase SOC balancing capability, *2017 IEEE Transportation Electrification Conference and Expo (ITEC)*. 323-327.

[121] M. Herzog, A. W. Ebentheuer, T. Lahlou, H. Herzog. (2018). Management Algorithms for Cascaded H-Bridge Multilevel Inverters, *2018 53rd International Universities Power Engineering Conference (UPEC)*. 1-6.

[122] P. Roos. (2020). A Comparison of Grid-Forming and Grid-Following Control of VSCs. Dissertation.

[123] N. Sharma, S. Sankar. (2018). Modeling and Control of Battery Energy Storage System for Providing Grid Support Services," *2018 Clemson University Power Systems Conference (PSC)*. 1-5.

[124] Slotine, J.J.E. (1991). *Applied Nonlinear Control*. Prentice Hall: USA-New jersey.

[125] Hedrick, J.K, Girard, Anouck. (2005). *Control of nonlinear dynamic systems theory and applications*.

[126] Mathworks ®.Matlab/Simulink. Battery. https://www.mathworks.com/help/physmod/sps/powersys/ref/battery.html. 09.10.2020.

[127] B. Gundogdu, D. T. Gladwin. (2018). Bi-Directional Power Control of Grid-Tied Battery Energy Storage System Operating in Frequency Regulation, *2018 International Electrical Engineering Congress (iEECON)*. 1-4.

[128] N. Kawakami, Y. Iijima. (2012). Overview of battery energy storage systems for stabilization of renewable energy in Japan, *2012 International Conference on Renewable Energy Research and Applications (ICRERA)*. 1-5.

[129] Rancilio, Giuliano, Lucas, Alexandre, Kotsakis, Evangelos, Fulli, Gianluca, Merlo, Marco, Delfanti, Maurizio, Masera, Marcelo. (2019). Modeling a Large-Scale Battery Energy Storage System for Power Grid Application Analysis. *Energies*. **12**.

[130] Y. Zheng, Z. Y. Dong, K. Meng, F. J. Luo, H. Q. Tian, K. P. Wong. (2013). A control strategy of battery energy storage system and allocation in distribution systems, *2013 IEEE Power & Energy Society General Meeting*. 1-5.

[131] D. Hui, L. Tian, X. Yang, X. Niu, K. Zhao. (2014). The impact analysis of distribution grid based on Battery energy storage system, *2014 China International Conference on Electricity Distribution (CICED)*. 51-56.

[132] Chen, Yingying, Luo, Fengji, Zheng, Yu, Xu, Zhao, Wen, Junhao. (2016). Reliability Evaluation of Distribution Systems with Mobile Energy Storage Systems. *IET Renewable Power Generation*. **10**.

[133] Zheng, Y., Meng, K., Luo, F., Qiu, J., Zhao, J. (2018). Optimal integration of MBESSs/SBESSs in distribution systems with renewables. *IET Renewable Power Generation*. **12**, 1172-1179.

[134] M. Farrokhabadi, S. König, C. A. Cañizares, K. Bhattacharya, T. Leibfried. (March 2018). Battery Energy Storage System Models for Microgrid Stability Analysis and Dynamic Simulation, *in IEEE Transactions on Power Systems*. **33(2)**, 2301-2312.

[135] Y. Zheng et al. (July 2018). Optimal Operation of Battery Energy Storage System Considering Distribution System Uncertainty, *in IEEE Transactions on Sustainable Energy*. **9(3)**, 1051-1060.

[136] L. Wang, D. H. Liang, A. F. Crossland, P. C. Taylor, D. Jones, N. S. Wade. (Nov 2015). Coordination of Multiple Energy Storage Units in a Low-Voltage Distribution Network," *in IEEE Transactions on Smart Grid*. **6(6)**, 2906-2918.

[137] A. Dolara, F. Grimaccia, G. Magistrati, G. Marchegiani. (2016). Optimal management algorithm for battery energy storage system included in an islanded Micro-Grid, *2016 IEEE 16th International Conference on Environment and Electrical Engineering (EEEIC)*. 1-5.

[138] Y. J. Liu, G. W. Chang, L. Y. Hsu, K. K. Jen, C. S. Chung, J. H. Chen. (2015). Modeling and simulations of the low-voltage distribution system integrated with energy storage systems in Kinmen Island, *TENCON 2015 IEEE Region 10 Conference*. 1-5.

[139] N. Karthikeyan, B. R. Pokhrel, J. R. Pillai, B. Bak-Jensen. (2018). Utilization of Battery Storage for Flexible Power Management in Active Distribution Networks, *2018 IEEE Power & Energy Society General Meeting (PESGM)*. 1-5.

[140] J. Wang, S. Hashemi, S. You, C. Trœholt. (2017). Active and reactive power support of MV distribution systems using battery energy storage, *2017 IEEE International Conference on Industrial Technology (ICIT)*. 382-387.

[141] G. Hu, S. Li, C. Cai, Z. Wu, L. Li. (2017). Study on Modeling and Simulation of Photovoltaic Energy Storage Microgrid," *2017 4th International Conference on Information Science and Control Engineering (ICISCE).* 692-695.

[142] S. A. Helal, M. H. Ahmed, M. M. A. Salama, M. F. Shaaban. (2018). Optimal Scheduling of Battery Energy Storage Systems in Unbalanced Distribution Networks," *2018 IEEE Canadian Conference on Electrical & Computer Engineering (CCECE).* 1-4.

[143] Platte river power authority. Battery energy storage technology assessment. https://www.prpa.org/wp-content/uploads/2017/10/HDR-Battery-Energy-Storage-Assessment.pdf, 29.01.2021.

[144] Pacific Northwest national laboratory. 2020 Grid Energy Storage Technology Cost and Performance Assessment. https://www.pnnl.gov/sites/default/files/media/file/Final%20%20ESGC%20Cost%20Performance%20Report%2012-11-2020.pdf, 12.02.2021.

[145] Kosmadakis, Yannis, Elmasides, Costas. (2019). Towards performance enhancement of hybrid power supply systems based on renewable energy sources. *Energy Procedia*. **157**, 977-991.

[146] Jang, Su-Jin, Won, Chung-Yuen, Lee, Byoung-Kuk, Hur, Jin. (2007). Fuel Cell Generation System With a New Active Clamping Current-Fed Half-Bridge Converter. Energy Conversion, *IEEE Transactions on Energy Conversion*. **22**. 332-340.

[147] Mohr, M., Fuchs, F.-W. (2006). Voltage Fed and Current Fed Full Bridge Converter for the Use in Three Phase Grid Connected Fuel Cell Systems. *2006 CES/IEEE 5th International Power Electronics and Motion Control Conference*. 1-7.

[148] Rizqiawan, Arwindra, Hadi, Pradita, Fujita, Goro. (2019). Development of Grid-Connected Inverter Experiment Modules for Microgrid Learning. *Energies*. **12**, 476.

CIRRICULUM VITAE (CV)

EDUCATION

Degree	Field	University/School	Years
M.Sc.	Electrical and Electronic Engineering	Gaziantep University	2018-2021
B.Sc.	Electrical and Electronic Engineering	Gaziantep University	2013-2018
High School	-	Dubai National Charity School	2011-2013

RESEARCHS AND PROJECTS

1- B.Sc. Graduation Project, Automatic robot, Object scanner, Grab and Drop Robot, Spring 2017.
2- B.Sc. Oral Project On Wind Turbines And It's Generators, Spring 2016.

PUBLICATIONS

1- Al-khdhairi, Yousif M.S, Vural, Mete. (2021). Study on The Modeling and Simulation of a Grid-Connected Battery Energy Storage System Based on Cascaded H-Bridge Converter, *International Journal of Energy Applications and Technologies (IJEAT)* (Accepted on 7th September 2021).
2- Al-khdhairi, Yousif M.S, Vural, Mete. (2021). Nonlinear Control of a Two-Stage 1 Mwh Grid-Connected Battery Energy Storage System By Exact Linearization Via State Feedback, *IETE Journal of Research, SCI-E,* (Under Review).